UNIVERSITY OF CALIFORNIA, SAN DIEGO

Context specific regulation of synaptogenesis in *C. elegans*

A dissertation submitted in partial satisfaction of the requirements for the degree
Doctor of Philosophy

in

Biology

by

Naina Kurup

Committee in Charge:

Professor Yishi Jin, Chair
Professor Arshad Desai
Professor Shelley Halpain
Professor Subhojit Roy
Professor Yimin Zou

2017

The Dissertation of Naina Kurup is approved, and it is acceptable in quality and form for publication on microfilm and electronically:

Chair

University of California, San Diego

2017

DEDICATION

This dissertation is dedicated to my father, Dr. A. P. Chandrasekharan, who was overjoyed at the prospect of his daughter putting her endless hypothesizing to good use when she started her PhD.

TABLE OF CONTENTS

LIST OF FIGURES

LIST OF TABLES

ACKNOWLEDGEMENTS

I am greatly indebted to Dr.Yishi Jin for taking me on as a graduate student in her lab, and providing me with tremendous support and mentorship in matters both related and unrelated to my thesis research. My sincere gratitude to my thesis committee members, Dr. Arshad Desai, Dr. Shelley Halpain, Dr. Subhojit Roy and Dr. Yimin Zou for valuable discussions throughout my PhD, without which much of this work would not be possible. I would also like to thank the UCSD scientific community, in particular at the Department of Biological Sciences, for an enriching experience as a graduate student. I acknowledge the Latham & Watkins fellowship for funding my research from 2014-2015.

Members of the Jin and Chisholm labs both past and present have been a wonderful source of information and inspiration, both scientific and otherwise. Special thanks goes out to Seika Takayangi-Kiya, Marian Chuang and Panid Sharifnia for discussions on life, the universe and graduate school over long lunches in the sun. I'd also like to thank all the amazing people I met in San Diego during my PhD, who have helped me take my mind off of failed experiments in more ways than one, but are still tickled at the thought of my working with worms.

I am grateful to members of the UCSD Hillcrest Dialysis center, for their dedication and service to all their patients, including a rather inquisitive graduate student. I would also like to thank a wonderfully kind man, Deen Rozario, for the greatest gift of all. Finally, I'd like to thank my family for their encouragement and love throughout grad school, especially my mother during her repeated visits to San Diego for purposes of crisis management.

Chapter 1, in full, is a reprint of Kurup, N., & Jin, Y. (2016). Neural circuit rewiring : insights from DD synapse remodeling. *Worm*, *5*(1), e1129486, with permission of both authors. The dissertation author was the primary author.

Chapter 2, in full, is a reprint of of Kurup, N., Yan, D., Goncharov, A., & Jin, Y. (2015). Dynamic microtubules drive circuit rewiring in the absence of neurite remodeling *Current Biology*, *25*(12), 1594-1605; with permission of all the authors. The dissertation author was the

primary author.

Chapter 3, in full, is a reprint of of Kurup, N., Yan, D., Kono, K., & Jin, Y. (2017) Differential regulation of polarized synaptic vesicle trafficking and synapse stability in neural circuit rewiring in *Caenorhabditis elegans*. *PLOS Genetics, 13*(6): e1006844, with permission of all the authors. The dissertation author was the primary author.

Chapter 4, in full, is a reprint of Kurup, N., Goncharov, A., & Jin, Y. (submitted) Intermediate filaments modulate microtubule dynamics to facilitate synapse rewiring, with permission of all authors. The dissertation author was the primary author.

VITA

2007	Summer Intern, L. V. Prasad Eye Institute, Hyderabad, India
2008	Summer Intern under Dr. Moinak Banerjee, Rajiv Gandhi Center for Biotechnology, India
2009	Khorana Scholar under Dr. Alan Attie, University of Wisconsin-Madison
2010	Research fellow under Dr. Mitradas Panicker, National Center for Biological Sciences, Bangalore, India
2010	Master of Science (Hons.), Biological Sciences, Birla Institute of Technology and Science, Pilani, India
2010	Bachelor of Engineering (Hons.), Electrical and Electronics Engineering, Birla Institute of Technology and Science, Pilani, India
2017	Doctor of Philosophy, University of California, San Diego

PUBLICATIONS

Kurup N, Yan D, Kono K, Jin Y. Differential regulation of polarized synaptic vesicle trafficking and synapse stability in neural circuit rewiring in *Caenorhabditis elegans*. PLOS Genetics 2017 July; 13(6): e1006844.

Kurup N, Jin, Y. Neural circuit rewiring : insights from DD synapse remodeling. Worm 2016 Dec; 5(1), e1129486.

Kurup N, Yan D, Goncharov A, Jin Y. Dynamic microtubules drive circuit rewiring in the absence of neurite remodeling. Current Biology 2015 June; 25(12), 1594-1605.

Kurup N, Sharifnia P, Jin Y. Spatial and temporal dynamics of neurite regrowth. Curr. Opin. Neurobiol. 2013 Dec; 23(6):1011-7

ABSTRACTS

Kurup N, Jin Y. "The cellular mechanisms underlying *C. elegans* neural circuit rewiring" Keystone Symposia Conference on Axons: from cell biology to pathology, 2016. Poster

Kurup N, Yan D, Goncharov, A, Jin Y. "Temporal regulation of MT dynamics drives synapse remodeling." 20th International *C. elegans* meeting, 2015. Talk

Kurup N, Yan D, Goncharov A, Jin Y. "Dynamic microtubules promote synaptic remodeling in *C. elegans."* Cold Spring Harbor Conference on Axon Guidance, Synapse Formation and Regeneration, 2014. Talk

Kurup N, Jin Y. "Investigating the role of MT acetylation in trafficking and neurite development in *C. elegans"* Gordon Conference on Cell Biology of the Neuron, 2012. Poster

ABSTRACT OF THE DISSERTATION

Context specific regulation of synaptogenesis in *C. elegans*

by

Naina Kurup

Doctor of Philosophy in Biology

University of California, San Diego, 2017

Professor Yishi Jin, Chair

Synapses are the functional connections between neurons and their targets. Synapse degeneration or dysfunction underlie several neurodevelopmental and neurodegenerative disorders ranging from autism to Alzheimer's disease, making the study of synapse formation and maintenance highly relevant. Various types of synapses exist within the human nervous system, including *en passant* synapses, which form along the axon, and terminal synapses, which form at the ends of axons. The nervous system of the nematode *C. elegans* also forms *en passant* and terminal synapses, which when coupled with a transparent body, a known connectome and ease of genetic manipulation, makes it an ideal model for the study of synaptogenesis. In the first part of my dissertation, I elucidate the cellular mechanisms that regulate a unique synapse rewiring paradigm in *C. elegans* motor neurons, where pre-exisiting *en passant* synapses are completely eliminated and new synapses are formed without any alteration in overall axon morphology. My studies have identified a novel role for dynamic microtubules in facilitating this process, through the modulation of synaptic vesicle transport during remodeling. I also provide *in vivo* evidence for how molecular motors kinesin and dynein, which move towards opposite ends of the microtubule, engage in a tug-of-war to determine the

overall direction of motion of synaptic vesicles. In addition, I uncovered an unexpected role for intermediate filament proteins in regulating microtubule dynamics during synapse formation, and a novel kinase that regulates synapse maintenance after remodeling. Finally, I explore how post-translational modifications of tubulin alter long distance synaptic vesicle transport to terminal synapses, using the mechanosensory neurons in *C. elegans* as a model. Taken together, my dissertation enhances our current understanding of the different pathways regulating synapse dynamics.

Chapter 1

Introduction: Insights on synapse remodeling from neuron rewiring in *C. elegans*

Abstract

Nervous systems exhibit many forms of neuronal plasticity during growth, learning and memory consolidation, as well as in response to injury. Such plasticity can occur across entire nervous systems as with the case of insect metamorphosis, in individual classes of neurons, or even at the level of a single neuron. A striking example of neuronal plasticity in *C. elegans* is the synaptic rewiring of the GABAergic Dorsal D-type motor neurons during larval development, termed DD remodeling. DD remodeling entails multi-step coordination to concurrently eliminate pre-existing synapses and form new synapses on different neurites, without changing the overall morphology of the neuron. Here, we focus on recent advances in understanding the cellular and molecular mechanisms driving DD remodeling.

Introduction

Descriptions of the *C. elegans* nervous system generally include phrases like "invariant connectivity" or "stereotypic position of neurons". While such descriptions are accurate, little is said concerning how various forms of neuronal plasticity contribute toward establishing a functional adult *C. elegans* nervous system. The ventral nerve cord in adult worms contains 76 motor neurons that are grouped into eight classes by morphology, connectivity, and function (White et al., 1986), while the ventral nerve cord in juvenile L1 worms contains only 22 motor neurons belonging to three of these classes (Sulston et al., 1983; White, Albertson & Anness, 1978). The birth of motor neurons at the end of L1 and their integration into the embryonic nervous system is thus one example of global circuit plasticity in *C. elegans*.

First identified nearly four decades ago by John White and colleagues, another example of circuit plasticity in *C. elegans* is the switch in connectivity of the GABAergic Dorsal D (DD) motor neurons during locomotory circuit development (White, Albertson & Anness, 1978). Six DD neurons are positioned evenly along the ventral nerve cord and extend neurites in ventral and dorsal nerve cords, connected by circumferential commissures (White et al., 1986, Figure 1.1). In adult worms, DD neurons receive synaptic inputs from cholinergic motor neurons in the ventral nerve cord and form neuromuscular synapses to dorsal body wall muscles (White et al., 1986). However, in L1 worms, the ventrally innervating cholinergic neurons, as well as the closely related GABAergic Ventral D (VD) neurons are not yet born. This would leave the DD neurons without synaptic inputs and the ventral muscles without innervation. Intrigued by this paradox, White *et al.*, set out to reconstruct two L1 larvae using serial electron micrographs. They then discovered that L1 DD neurons formed neuromuscular synapses along their ventral neurites, and received synaptic inputs from dorsally innervating cholinergic neurons (White, Albertson & Anness, 1978). Their work defined the phenomenon of DD synapse remodeling, a complete switch in connectivity where DD neurons eliminate pre-existing synapses along their ventral neurites and reform synapses along their dorsal neurites by adulthood, surprisingly without major change in overall neuronal morphology (Figure 1A). The post-embryonically born VD neurons share similar axon morphology as DD neurons, innervate the ventral muscle and do not undergo remodeling (White al., 1986). Studies over the past two decades have revealed multiple genetic factors that regulate the timing of DD remodeling and changes in cellular components that facilitate this structural plasticity, shedding light on our understanding of the molecular mechanisms of synapse reorganization.

Factors that regulate the timing of DD remodeling

Using transgenic reporters to visualize DD neuron axons and synapses, it was determined that DD remodeling begins with new synapses forming at the anterior dorsal neurite

of DD1 (the DD neuron closest to the head of the worm) in mid-L1, approximately 10 hours post hatching in wild type animals cultured at 20^{o}C (Hallam & Jin, 1998). Elimination of pre-existing synapses and formation of new synapses proceed through the L1-L2 molt, and DD remodeling is complete by late L2. The heterochronic gene, *lin-14* (Ambros & Horvitz, 1984), was the first factor identified to regulate timing of DD remodeling (Hallam & Jin, 1998). *lin-14* expression decreases at the onset of remodeling, and a reduction in *lin-14* activity results in precocious remodeling (Hallam & Jin, 1998), indicating that *lin-14* acts to prevent remodeling.

The timing of DD remodeling coincides with the birth of the VD neurons, which form synapses to ventral body wall muscles, thereby replacing the larval DD synapses (Figure 1.1). However, the absence of VD or other ventral cholinergic motor neurons does not affect DD remodeling, as evidenced in *lin-6* mutants in which postembryonic cell division of late born motor neurons is blocked (Sulston et al., 1983; White, Albertson & Anness, 1978). In these mutants, DD remodeling proceeds normally, although their dorsal neurites maintain some larval synaptic inputs from cholinergic neurons (White, Albertson & Anness, 1978). The COUP-TF nuclear hormone receptor UNC-55 is expressed in the VD neurons and restricts them from remodeling their synapses (Walthall & Plunkett, 1995; Zhou & Walthall, 1998). Ectopic expression of UNC-55 in L1 DD neurons can prevent their remodeling, consistent with a model that lack of UNC-55 in DD neurons enables their ability to remodel (Shan et al., 2005). Transcriptional targets of UNC-55 include the Iroquois-like homeodomain protein IRX-1 and the Hunchback-like transcription factor HBL-1, both of which are normally expressed in the DD neurons and promote remodeling (Petersen et al., 2011; Thompson-Peer et al., 2012). Thus UNC-55 likely inhibits VD synapse remodeling through orchestrating a transcriptional repression program.

Another transcriptional regulator of DD synapse remodeling is the Pitx transcription factor, UNC-30, which is expressed in both DD and VD neurons and functions to specify their GABAergic fate (Eastman, Horvitz & Jin, 1999; Jin, Hoskins & Horvitz, 1994). UNC-30

promotes the expression of IRX-1 in DD neurons to facilitate remodeling (Petersen et al., 2011). Ultrastructural reconstruction of *unc-30* mutants, completed by John White three decades ago, revealed disruption of the synaptic patterns of both adult DD and VD neurons, as well as aberrant innervation of L1 DD neurons (Howell, White & Hobert, 2015). More recently, UNC-30 was shown to co-regulate transcriptional targets with LIN-14 in L1 DD neurons and with UNC-55 in VD neurons (Howell, White & Hobert, 2015). The transcriptional strategy involving UNC-30, LIN-14 and UNC-55 promotes the expression of the immunoglobin domain protein OIG-1, which acts to prevent aberrant remodeling in L1 DD neurons and VD neurons in both the larval and adult stages (Howell, White & Hobert, 2015).

The timing of DD remodeling is also dependent on global circuit activity, as genetic mutants that block or exaggerate synaptic transmission delay or advance the completion of rewiring, respectively (Thompson-Peer et al., 2012). However, DD remodeling is not dependent on GABA synaptic transmission (Jin, Jorgensen, Hartwieg & Horvitz, 1999). Changes in global circuit activity result in corresponding changes in the expression levels of the pro-remodeling gene HBL-1 (Thompson-Peer et al., 2012). The microRNA miR-84 can repress HBL-1 expression (Thompson-Peer et al., 2012), providing an additional layer of regulation on DD remodeling.

While recent studies on DD remodeling have focused largely on remodeling of pre-synaptic terminals, John White also observed remodeling of dendritic inputs from the dorsal to ventral DD neurite (White, Albertson & Anness, 1978). DD neurons receive cholinergic synaptic inputs, and express acetylcholine receptor subunits, including ACR-12 (Petrash et al., 2013), in their dendrites. In L1 DD neurons, OIG-1 prevents remodeling of ACR-12 (He et al., 2015). Expression of IRX-1 in DD neurons during remodeling represses OIG-1 to promote remodeling of ACR-12 (He et al., 2015). In L1 animals, the post-synaptic GABA-A receptor UNC-49 is expressed exclusively in the ventral muscles (Gally & Bessereau, 2003). Following the birth of the VD neurons in L2 animals, UNC-49 receptor clusters appear in both ventral and

dorsal muscles (Gally & Bessereau, 2003). Concurrent with DD remodeling, UNC-49 in the ventral body muscles switches from being depolarizing to hyperpolarizing in response to the GABA receptor agonist, muscimol (Han, Bellemer & Koelle, 2015). DD remodeling is thus a genetically programmed change in both circuit function and connectivity that occurs at a precise developmental time point, drawing parallels to critical period plasticity in mammalian nervous systems (Hensch, 2004). The various factors regulating the timing of DD remodeling are summarized in Figure 1.2. While these studies have elegantly elucidated the transcriptional regulation required to modulate circuit rewiring, the cellular changes during the execution of DD remodeling remain unclear.

The cellular changes that facilitate DD remodeling

In developing neurons, synapses are formed either concurrently with axon guidance and elongation, or at the end of axon guidance and target recognition, resulting in *en passant* or terminal synaptic boutons, respectively. In the worm locomotory circuit, synapses are *en passant* along neurites, which raises an interesting question as to how DD synapses are formed without axon growth to the new target. As the cytoskeleton is essential for both growth and transport along the neuron processes, we directed our attention to the role of the cellular transport machinery in facilitating DD remodeling.

Microtubules (MTs), polymers of α- and β- tubulin, are the primary cytoskeletal component involved in transport of synaptic material in neurons, and have distinct polarities in axons and dendrites across species. There is much speculation as to whether this difference in MT polarity is a cause or effect of neuronal polarity (Bass & Lin, 2011). Much to our surprise, we found that while DD neurites switch polarity after synapse remodeling, with the ventral neurite assuming a dendritic and dorsal neurite an axonal identity, their MT polarity remained unchanged (Kurup et al., 2015). This observation shows that neurite identity could be uncoupled from MT polarity, and suggests that the specificity of axonal and dendritic cargo might be

determined by factors besides the orientation of MTs.

Mature neurons contain highly stable MTs, and they also contain an additional population of dynamic MTs, which constantly grow and shrink from the MT plus end. One possible factor regulating cargo trafficking is the number of dynamic MTs, as we observed a dramatic increase in dynamic MTs during DD remodeling (Kurup et al., 2015). Indeed, DD remodeling was dependent on this increase in growing MTs, such that mutant animals with fewer dynamic MTs during remodeling failed to rewire their synapses to the dorsal neurite (Kurup et al., 2015). The increase in number of dynamic MTs facilitates synaptic vesicle transport mediated by plus-end directed motors UNC-104/Kinesin-3 (Park et al., 2011) and UNC-116/Kinesin-1 (Kurup et al., 2015) along the DD neuron commissure during remodeling. There is also evidence pointing to the involvement of the cyclin-dependent kinase CDK-5 in modulating UNC-104 activity during remodeling (Park et al., 2011). MT polarity remains plus-end out in all DD neuron processes during remodeling, including those in the dorsal neurites (Kurup et al., 2015). Thus a combination of UNC-104 and the minus end directed DHC-1/dynein is required to pattern the newly formed synapses along the dorsal DD neurite (Park et al., 2011). Concurrent to new synapse formation to dorsal muscles, existing synapses are eliminated from the ventral neurite of DD neurons, and some synaptic vesicle components appear to be recycled during new synapse formation (Park et al., 2011). Emerging evidence implicates both a cyclin Y homolog CYY-1 (Park et al., 2011), and the cell death pathway (Meng et al., 2015) in DD synapse elimination, but the link between the two pathways remains to be addressed.

We also found that activity of the conserved MAP3Kinase DLK-1 is required for new synapse formation during DD remodeling. In conditions where MT structure is compromised due to a genetic alteration in alpha-tubulin (Baran et al., 2010), loss of *dlk-1* completely blocks DD remodeling (Kurup et al., 2015). The DLK-1 promoter (~2 kb upstream from the TSS) contains binding sites for LIN-14 (Hristova et al., 2005), UNC-30 (Shan et al., 2005) and UNC-5 (Shan et al., 2005), suggesting possible regulation by these transcription factors. DLK-1

transcript levels are globally upregulated from mid L1-L2 stage (Grun et al., 2014), and a pulse of DLK-1 at the onset of DD remodeling facilitates new synapse formation (Kurup et al., 2015). DLK-1 localizes to the peri-synaptic region in adult DD neurons (Nakata et al.., 2005), and promotes MT growth and growth cone formation in regenerating axons (Ghosh-Roy et al., 2012; Hammarlund et al., 2009). During DD remodeling, DLK-1 mediates an increase in the number of dynamic MTs to facilitate synaptic vesicle transport, partly through downstream MT catastrophe factors like KLP-7/Kinesin-13 and SPAS-1/Spastin (Kurup et al., 2015; Roll-Mecak & McNally, 2010). However, loss of *dlk-1* alone only results in a slight delay in the completion of DD remodeling, whereas loss of dynamic MTs results in a complete block (Kurup et al., 2015). Collectively, these results indicate the existence of one or more redundant pathways that regulate MT growth during DD remodeling, and await further characterization.

Outlook

Compared to most other examples of large scale synapse rewiring involving neurite growth, retraction, or in some cases, even the death of inappropriately connected neurons (Sanes & Yamagata, 2009); DD remodeling appears to be unique. However, the discovery of this unique form of neural plasticity is primarily because of our complete understanding of the neural connectivity of C. *elegans*, made possible by work from John White and colleagues (White, Albertson & Anness, 1978; White et al., 1986). Increased technological capability to achieve single cell resolution in other organisms might lead to the description of similar rewiring paradigms. Indeed, an example of synapse refinement in the absence of axon growth was described in the mammalian central nervous system, where imaging of individual axonal arbors of retinal ganglion cells showed that retinogeniculate synapse remodeling can occur without axon retraction (Hong et al., 2014).

Four decades after John White's seminal work, we have learned a great deal about DD remodeling, which has provided a rich platform to study the temporal cues (Hallam & Jin, 1998;

He et al., 2015 Howell, White & Hobert, 2015; Petersen et al., 2011; Thompson-Peer et al., 2012; Walthall & Plunkett, 1995; Zhou & Walthall, 1998) as well as the cellular mechanisms that underlie this complete inversion of synaptic connectivity (Kurup et al., 2015; Meng et al., 2015; Park et al., 2011). Our findings have also revealed a novel role of dynamic MTs in regulating synaptic vesicle transport in the absence of neurite growth or pruning. A recurring theme from these studies is that DD remodeling is guarded by genetic redundancy involving multiple pathways. How each pathway interacts with the rest of the network to coordinate remodeling with such spatio-temporal precision remains a mystery. Since synapse loss is a primary pathophysiology of several neurodegenerative disorders (Koffie, Hyman & Spires-Jones, 2011; Milnerwood & Raymond, 2010), our current knowledge and future efforts in elucidating synapse formation and elimination during DD remodeling is important to ultimately understanding the molecular basis of such debilitating conditions.

Acknowledgments

This chapter is a reprint, in full, of Kurup, N., & Jin, Y. (2016). Neural circuit rewiring : insights from DD synapse remodeling. *Worm*, *5*(1), e1129486, with permission of both authors. The dissertation author was the primary author.

We thank members of our lab for their comments on the manuscript. Y.J. is an Investigator of the Howard Hughes Medical Institute. This work was supported by HHMI and an NIH grant (NINDS R01 035546 to Y. J.).

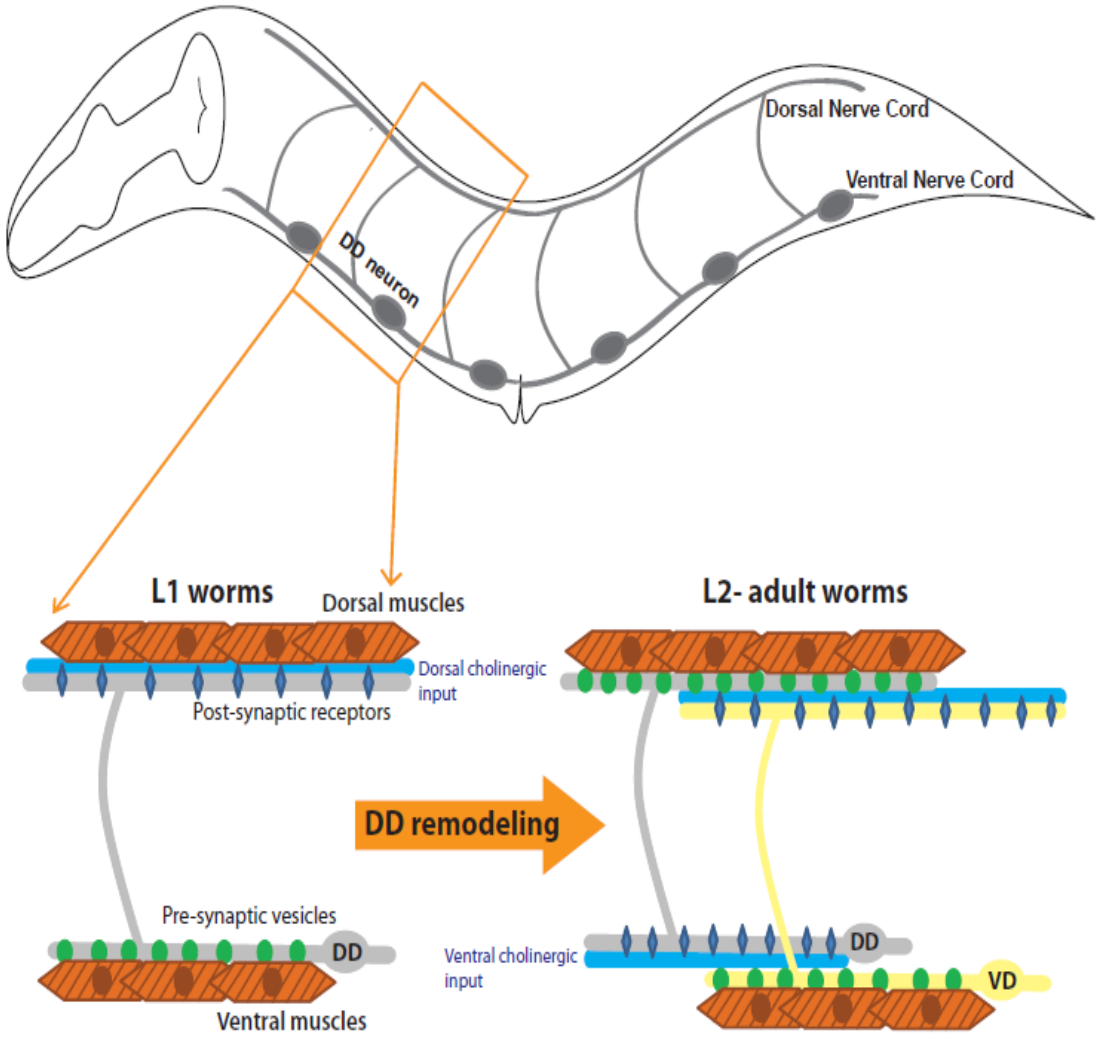

Figure 1.1 Schematic of DD synapse remodeling

(Top) Cartoon illustration of the *6 C.elegans* DD type motor neurons, which form cell bodies along the ventral nerve cord and extend process along the ventral and dorsal nerve cords, connected by a commissural branch. (Middle) In L1 worms (left) DD neurons form synapses (green circles) along the ventral neurites and receive cholinergic synaptic inputs (blue) in their dorsal neurites through the ACh receptor (blue diamonds). After DD remodeling in L2 and older animals (right), synapses along the ventral neurite are eliminated, and new synapses are formed with dorsal muscles. The VD neurons now synapse onto the ventral muscles and receive cholinergic synaptic input in ther dorsal neurites. DD neurons now receive cholinergic synaptic input in their ventral neurites (blue). (Bottom) Representative images of the synapses of a single wild type L1 (left) and adult (right) DD motor neuron, viewed using synaptobrevin (SNB) tagged to GFP, which labels synaptic vesicles. White asterisks denote DD neuron cell bodies.

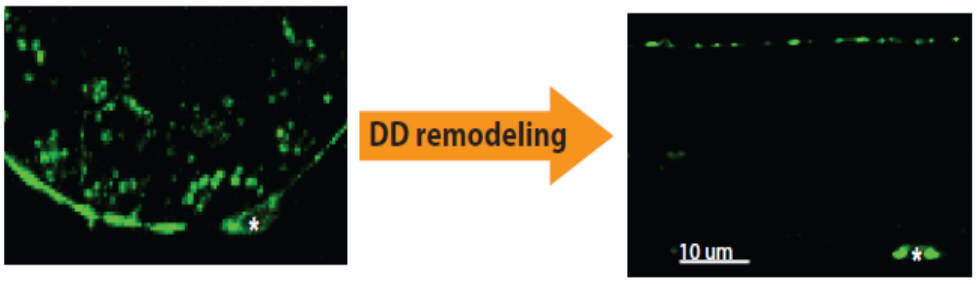

Figure 1.1 (continued) Schematic of DD synapse remodeling

(Top) Cartoon illustration of the *6 C.elegans* DD type motor neurons, which form cell bodies along the ventral nerve cord and extend process along the ventral and dorsal nerve cords, connected by a commissural branch. (Middle) In L1 worms (left) DD neurons form synapses (green circles) along the ventral neurites and receive cholinergic synaptic inputs (blue) in their dorsal neurites through the ACh receptor (blue diamonds). After DD remodeling in L2 and older animals (right), synapses along the ventral neurite are eliminated, and new synapses are formed with dorsal muscles. The VD neurons now synapse onto the ventral muscles and receive cholinergic synaptic input in ther dorsal neurites. DD neurons now receive cholinergic synaptic input in their ventral neurites (blue). (Bottom) Representative images of the synapses of a single wild type L1 (left) and adult (right) DD motor neuron, viewed using synaptobrevin (SNB) tagged to GFP, which labels synaptic vesicles. White asterisks denote DD neuron cell bodies.

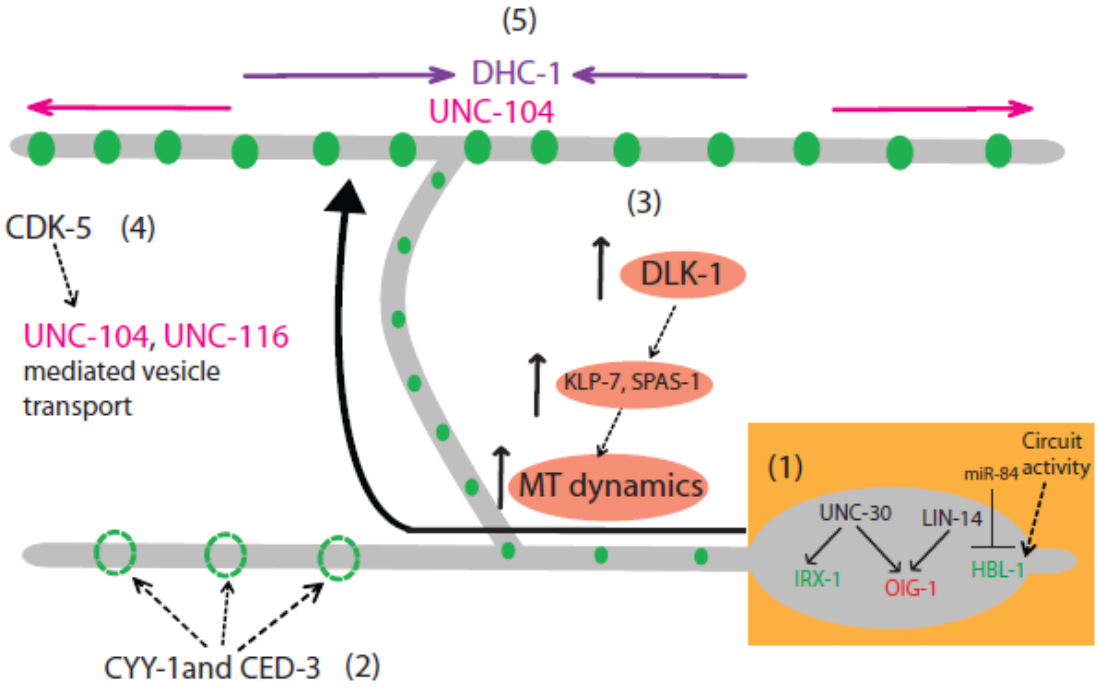

Figure 1.2 The mechanics of DD synapse remodeling

(1) A transcriptional program involving UNC-30, LIN-14, IRX-1 and HBL-1 modulates synapse remodeling in DD neurons, to regulate the expression of factors that promote (green) and inhibit (red) DD remodeling. (2) Ventral synapse elimination requires Cyclin-1/CYY-1 and components of the cell death pathway, including CED-3. (3) Activation of DLK-1 results in an increase in dynamic MTs through the activation of MT catastrophe factors like KLP-7 and SPAS-1. (4) Increased dynamic MTs facilitate UNC-116 mediated synaptic vesicle transport, and CDK-5 stimulates UNC-104 mediated synaptic vesicle transport to the dorsal neurite. (5) Patterning of newly formed synapses is achieved through coordinated activity of UNC-104 and DHC-1.

References

Ambros, V. & Horvitz, R. (1984) Heterochronic mutants of the nematode Caenorhabditis elegans. *Science, 226*(4673):409-16.

Baas, P. W., & Lin, S. (2011). Hooks and comets: The story of microtubule polarity orientation in the neuron. *Developmental neurobiology, 71*(6), 403-18.

Baran, R., Castelblanco, L., Tang, G., Shapiro, I., Goncharov, A., & Jin, Y. (2010). Motor neuron synapse and axon defects in a *C. elegans* alpha-tubulin mutant. *PloS one, 5*:e9655.

Eastman, C., Horvitz, H. R., & Jin, Y. (1999). Coordinated transcriptional regulation of the *unc-25* glutamic acid decarboxylase and the *unc-47* GABA vesicular transporter by the Caenorhabditis elegans UNC-30 homeodomain protein. *J. Neuroscience., 19*(15), 6225-6234.

Gally, C., & Bessereau, J.L. (2003). GABA is dispensable for the formation of junctional GABA receptor clusters in Caenorhabditis elegans. *J. Neurosci., 23*(7), 2591-2599.

Ghosh-Roy, A., Goncharov, A., Jin, Y., & Chisholm, A. D. (2012). Kinesin-13 and tubulin posttranslational modifications regulate microtubule growth in axon regeneration. *Developmental cell, 23*(4), 716-28.

Grun, D., Kirchner, M., Thierfelder, N., Stoeckius, M., & Selbach, M. (2014). Conservation of mRNA and protein expression during development of *C. elegans*. *Cell reports, 6*(3), 565-577.

Hallam, S. & Jin, Y. (1998) lin-14 regulates the timing of synaptic remodeling in Caenorhabditis elegans. *Nature, 395*, 644-647.

Hammarlund, M., Nix, P., Hauth, L., Jorgensen, E.M., & Bastiani. M. (2009). Axon regeneration requires a conserved MAP Kinase pathway. *Science, 323*, 802-806.

Han, B., Bellemer, A., & Koelle, M. R. (2015). An evolutionarily conserved switch in response to GABA affects development and behavior of the locomotor circuit of Caenorhabditis elegans. *Genetics, 199*, 1159-1172.

He, S., Philbrook, A., Mcwhirter, R., Gabel, C. V., Taub, D.G., Carter, M.H., Hanna, I.M., Francis, M. M., & Miller, D. M. III. (2015). Transcriptional control of synaptic remodeling through regulated expression of an Immunoglobulin superfamily protein. *Current Biology, 25*(19), 2541-2548.

Hensch, T. K. (2004). Critical period regulation. *Annual review of neuroscience, 27*, 549-79.

Hong, Y. K., Park, S., Litvina, E. Y., Morales, J., Sanes, J. R., & Chen, C. (2014). Refinement of the retinogeniculate synapse by bouton clustering. *Neuron, 84*(2), 332-339.

Howell, K., White, J. G., & Hobert, O. (2015). Spatiotemporal control of a novel synaptic organizer molecule. *Nature, 523*(7558), 83-87.

Hristova, M., Birse, D., Hong, Y., & Ambros, V. (2005). The Caenorhabditis elegans heterochronic regulator LIN-14 is a novel transcription factor that controls the developmental timing of transcription from the Insulin / Insulin-like growth factor Gene ins-33 by direct DNA binding. *Molecular and cellular biology*, *25*(24), 11059-11072.

Jin, Y., Hoskins, R. & Horvitz, H.R. (1994). Control of type-D GABAergic neuron differentiation by C. elegans UNC-30 homeodomain protein. *Nature, 372:780* –783.

Jin, Y., Jorgensen, E., Hartwieg, E., & Horvitz, H. R. (1999). The Caenorhabditis elegans gene unc-25 encodes glutamic acid decarboxylase and is required for synaptic transmission but not synaptic development. *J. Neurosci.*, *19*(2), 539-548.

Koffie, R.M., Hyman, B.T., & Spires-Jones, T.L. (2011). Alzheimer's disease : synapses gone cold. *Molecular Neurodegeneration*, *6*(1): 63.

Kurup, N., Yan, D., Goncharov, A., & Jin, Y. (2015). Dynamic microtubules drive circuit rewiring in the absence of neurite remodeling. *Current Biology*, *25*(12), 1594-1605.

Meng, L., Mulcahy, B., Cook, S. J., Neubauer, M., Wan, A., Jin, Y & Yan, D. (2015). The cell death pathway regulates synapse elimination through cleavage of gelsolin in Caenorhabditis elegans neurons. *Cell Reports*, *11*(11), 1737-1748.

Milnerwood, A. J., & Raymond, L. A. (2010). Early synaptic pathophysiology in neurodegeneration : insights from Huntington's disease. *Trends in Neurosciences*, *33*(11), 513-523

Nakata, K., Abrams, B., Grill, B., Goncharov, A., Huang, X., Chisholm, A. D., & Jin, Y. (2005). Regulation of a DLK-1 and p38 MAP kinase pathway by the ubiquitin ligase RPM-1 is required for presynaptic development. *Cell*, *120*(3), 407-20.

Park, M., Watanabe, S., Poon, V. Y. N., Ou, C.-Y., Jorgensen, E. M., & Shen, K. (2011). CYY-1/cyclin Y and CDK-5 differentially regulate synapse elimination and formation for rewiring neural circuits. *Neuron*, *70*(4), 742-57.

Petersen, S. C., Watson, J. D., Richmond, J. E., Sarov, M., Walthall, W. W., & Miller, D. M. (2011). A transcriptional program promotes remodeling of GABAergic synapses in Caenorhabditis elegans. *J. Neuroscience*, *31*(43), 15362-75.

Petrash, H. A., Philbrook, A., Haburcak, M., Barbagallo, B., & Francis, M. M. (2013). ACR-12 ionotropic acetylcholine receptor complexes regulate inhibitory motor neuron activity in Caenorhabditis elegans. *J. Neurosci.*, *33*(13), 5524-5532.

Roll-mecak, A., & Mcnally, F. J. (2010). Microtubule-severing enzymes. *Current Opinion in Cell Biology*, *22*, 96-103.

Sanes J.R and Yamagata M. (2009). Many paths to synaptic specificity. *Annu. Rev. Cell Dev. Biol.*, *25*, 161-95.

Shan, G., Kim, K., Li, C., & Walthall, W. W. (2005). Convergent genetic programs regulate similarities and differences between related motor neuron classes in Caenorhabditis elegans. *Developmental biology*, *280*(2), 494-503.

Sulston, J.E. , Schierenberg, E. , White, J.G. & Thomson, J.N. (1983). The embryonic cell lineage of the nematode *Caenorhabditis elegans*. *Dev. Biol., 100*:64–119.

Thompson-Peer, K. L., Bai, J., Hu, Z., & Kaplan, J. M. (2012). HBL-1 patterns synaptic remodeling in C. elegans. *Neuron, 73*(3), 453-465.

Walthall, W.W., & Plunkett, J.A.. (1995) Genetic transformation of the synaptic pattern of a motoneuron class in Caenorhabditis elegans. *J. Neurosci.15,* 1035– 1043.

White, J. G., Albertson, D. G. & Anness, M. A. R. (1978). Connectivity changes in a class of motorneurons during the development of a nematode. *Nature, 271***,** 764–766.

White, J. G., Southgate, E., Thomson, J. N., & Brenner, S. (1986). The Structure of the Nervous System of the Nematode Caenorhabditis elegans. *Philosophical Transactions of the Royal Society B: Biological Sciences*, *314*(1165), 1-340.

Zhou, H. M., & Walthall, W. W. (1998). UNC-55, an orphan nuclear hormone receptor, orchestrates synaptic specificity among two classes of motor neurons in Caenorhabditis elegans. *J. Neuroscience, 18*(24), 10438-44.

Chapter 2

Dynamic microtubules drive circuit rewiring in the absence of neurite remodeling

Abstract

A striking neuronal connectivity change in *C. elegans* involves the coordinated elimination of existing synapses and formation of synapses at new locations, without altering neuronal morphology. Here, we investigate the tripartite interaction between dynamic microtubules (MTs), kinesin-1, and vesicular cargo during this synapse remodeling. We find that a reduction in the dynamic MT population in motor neuron axons, resulting from genetic interaction between loss of function in the conserved MAPKKK *dlk-1* and an α-tubulin mutation, specifically blocks synapse remodeling. Using live imaging and pharmacological modulation of the MT cytoskeleton, we show that dynamic MTs are increased at the onset of remodeling and are critical for new synapse formation. DLK-1 acts during synapse remodeling, and its function involves MT catastrophe factors including kinesin-13/KLP-7 and spastin/SPAS-1. Through a forward genetic screen, we identify gain-of-function mutations in kinesin-1 that can compensate for reduced dynamic MTs to promote synaptic vesicle transport during remodeling. Our data provide *in vivo* evidence supporting the requirement of dynamic MTs for kinesin-1 dependent axonal transport and shed insight on the role of the MT cytoskeleton in facilitating neural circuit plasticity.

Introduction

Neural circuits undergo connectivity changes in response to various stimuli throughout the lifetime of an organism. Such changes can occur at many levels, including neurite growth and pruning, synapse formation and elimination, as well as strengthening and weakening of

existing synapses (Destexhe & Marder, 2004). Such structural plasticity is highly dependent on the cytoskeletal architecture of the neuron. Microtubules (MTs) are essential for neuronal polarity, neurite outgrowth and guidance (Conde & Cáceres, 2009). Studies of the *Drosophila* neuromuscular junction (NMJ), where MTs form loops within terminal synaptic boutons, have shown that Microtubule Associated Proteins (MAPs) like Futsch (Hummel et al., 2000; Roos et al., 2000) and Spartin (Nahm et al., 2013) regulate synapse growth by modulating MT stability. In the mammalian central nervous system, many synapses are formed *en passant* along the axons of neighboring nerve processes (Harris & Weinberg, 2012). In such neurons, where MTs generally run parallel to synapse boutons within the axon, how MTs affect synapse formation and maintenance remains to be understood.

In this study, we investigated how MTs affect the developmental rewiring of *C. elegans* GABAergic DD (Dorsal D type) neurons, referred to as DD remodeling (White, Albertson & Anness, 1978). Six DD motor neurons are positioned along the ventral nerve cord and extend neurites in ventral and dorsal nerve cords, connected by circumferential commissures (White et al., 1986). In the first larval (L1) stage, DD neurons form *en passant* synapses with the ventral body wall muscles. By the end of the second larval (L2) stage, these ventral synapses are eliminated, and new synapses are formed onto the dorsal body wall muscles, which are maintained for the rest of the lifetime of the animal (Hallam & Jin, 1998; Park et al., 2011; White et al., 1986; Zhou & Walthall, 1998). Importantly, the remodeling of synapses does not involve changes in axon morphology (Hallam & Jin, 1998). Thus, the elimination and reformation of synapses would possibly require the coordinated action of vesicular sorting and transport pathways, together with modifications in the underlying cytoskeleton. Recent work has shown a cyclin dependent kinase functions to promote new synapse formation in the dorsal neurites of the DD neurons, via the regulation of motor proteins UNC-104 (Kinesin-3) and DHC-1(Dynein) (Park et al., 2011). However, whether cytoskeletal changes are necessary for DD remodeling remains unknown.

The conserved DLK (Dual-Leucine zipper bearing MAP3K) family of kinases (DLK-1 in *C. elegans*) regulates several aspects of neuronal development and maintenance, including synapse and axon development, neuronal survival and axon regeneration (Bounoutas et al., 2011; Ghosh-Roy et al., 2012; Klinedinst et al., 2013; Nakata et al., 2005; Valakh et al., 2013; Welsbie et al., 2013; Yan et al., 2009). In *C. elegans*, DLK-1 regulates synapse development, neurite outgrowth and regeneration via a p38 MAP kinase pathway, with the transcription factor CEBP-1 as a downstream target (Nakata et al., 2005; Yan et al., 2009). Additionally, MT associated proteins (MAPs) such as the kinesin-13 homolog *klp-7* (Ghosh-Roy et al., 2012), have also been implicated in DLK-1 signaling in developing and mature neurons.

Recent studies in a variety of neuronal models have identified context-specific roles of DLK homologs in regulating MTs (Bounoutas et al., 2011; Klinedinst et al., 2013; Valakh et al., 2013). Here, using a gain-of-function mutation in α-tubulin (designated *tba-1(gf)*) (Baran et al., 2010) to perturb the MT cytoskeleton in animals lacking DLK-1 activity (designated *dlk-1(0)*), we have uncovered a specific role for DLK-1 and dynamic MTs in synapse remodeling. Remodeling is blocked in *tba-1(gf) dlk-1(0)* double mutants and transient expression of *dlk-1* during DD remodeling is sufficient to establish new synapses. Upregulation of MT dynamics is correlated with the onset of synapse remodeling, and increasing the number of dynamic MTs can rescue the block in remodeling in *tba-1(gf) dlk-1(0)*. We further identified novel kinesin-1 mutations that facilitate synaptic vesicle transport during remodeling in *tba-1(gf) dlk-1(0)*, likely through an increase in the MT binding affinity of the motor. Our findings demonstrate that dynamic MTs promote neural circuit remodeling, independent of neurite outgrowth.

Results

DD remodeling depends on the MT cytoskeleton and DLK-1

tba-1(ju89) (*tba-1(gf)*) is a gain-of-function mutation that converts a glycine residue to arginine (G414R) in the C-terminal H11-H12 loop of the α-tubulin TBA-1, causing a mild

disruption of synapse morphology and a reduction in synapse number (Baran et al., 2010). To test whether *tba-1(gf)* also affected DD remodeling, we examined the localization pattern of a DD neuron-specific synaptic marker (*juIs137*: P_{flp-13}-SNB-1::GFP). In wild type animals grown at 20°C, DD remodeling was completed by the end of the second larval (L2) stage (~28 hrs post hatching, hph), but in *tba-1(gf)* animals remodeling was not completed until adulthood (~56 hph) (Figure 2.S1A), suggesting that an altered MT cytoskeleton delayed synapse remodeling.

To understand how MTs regulate synapse remodeling, we searched for genetic interactors of *tba-1(gf)*. We found that loss of the MAPKKK DLK-1 (*dlk-1(0)*), together with *tba-1(gf),* resulted in a striking synergistic effect on DD remodeling. In L1 animals of wild type, *tba-1(gf), dlk-1(0)* single and *tba-1(gf) dlk-1(0)* double mutants, DD neurons formed synapses along the ventral nerve cord (VNC) (Figure 2.1A, C). By the adult stage, DD neurons in wild type, *tba-1(gf)* and *dlk-1(0)* single mutants remodeled their synapses and formed new synapses along the dorsal nerve cord (DNC) (Figure 2.1B, C). In contrast, *tba-1(gf) dlk-1(0)* adults showed a complete lack of synaptic puncta in the DNC, and retained synaptic puncta in the VNC (Figure 2.1B, C). In >80% of adult *tba-1(gf) dlk-1(0)* animals, synaptic puncta were also retained in the commissures of DD neurons (n> 50 animals) (Figure 2.1B), suggestive of a failure in synaptic vesicle transport. *tba-1(gf)* animals exhibit mild axon outgrowth defects (Baran et al., 2010), which were not enhanced by *dlk-1(0)* (Figure 2.S1C, D), indicating that the synapse remodeling defect of *tba-1(gf) dlk-1(0)* was not caused by defects in axon outgrowth. The failure in DD remodeling in *tba-1(gf) dlk-1(0)* was also observed using markers for other presynaptic components, including SAD-1 and RAB-3 (Figure 2.S1G). However, the gross clustering pattern of postsynaptic $GABA_A$ receptors (UNC-49) in the dorsal muscles was normal in *tba-1(gf) dlk-1(0)* (Figure 2.S1G), indicating that the failure in synapse remodeling was restricted to pre-synaptic terminals.

To further characterize the anatomical changes in DD neuron pre-synaptic terminals, we performed ultrastructural analyses of DD neuron processes in young L1 and adult animals,

identified by their stereotypic position within the nerve cords (White et al., 1986). We observed comparable numbers of *en passant* DD neuron synapses (defined as synaptic vesicles clustered around an electron dense region called active zone) in the VNC of L1 wild type and *tba-1(gf) dlk-1(0)* animals (~6 synaptic boutons/10 μm; n=2 animals per genotype). In contrast, while the DNC of two WT adults contained 5 and 7 DD synaptic boutons in the 8 μm serially reconstructed, we observed only one dorsal DD synaptic bouton each in both *tba-1(gf) dlk-1(0)* animals reconstructed, which also contained significantly fewer vesicles than wild type (Figure 2.1D, E). Neither WT nor *tba-1(gf) dlk-1(0)* animals contained any recognizable DD synaptic boutons in the VNC. These studies provide further evidence that DD remodeling is severely impaired in *tba-1(gf) dlk-1(0)* animals.

The block in DD remodeling caused a distinct behavioral deficit in adult *tba-1(gf) dlk-1(0)* animals. *tba-1(gf)* animals exhibit altered locomotion with reduced velocity and sinusoidal amplitude (Baran et al., 2010), compared to wild type or *dlk-1(0)* animals (Figure 2.1F, Figure 2.S1B). *tba-1(gf) dlk-1(0)* double mutant animals displayed a curved body shape during forward locomotion (Figure 2.1F) and coiled dorsally when prompted to move backwards. This synergistic interaction was specific to *dlk-1(0)* and *tba-1(gf)*, as *tba-1(0)* and *tba-1(0) dlk-1(0)* animals showed no detectable defects in locomotion and DD synapse organization (Figure 2.S1E, F). Moreover, expression of wild type *dlk-1* or *tba-1* in the D motor neurons rescued the dorsal coiling and synapse remodeling defects in *tba-1(gf) dlk-1(0)* (Figure 2.1G, H), consistent with previous conclusions that DLK-1 and TBA-1 act cell-autonomously (Baran et al., 2010; Nakata et al., 2005). Together, these data identify a previously unknown role for *dlk-1* and the MT cytoskeleton in promoting DD remodeling.

DLK-1 promotes new synapse formation during DD remodeling

We next addressed how the timing of DD remodeling was affected by *tba-1(gf)* and *dlk-1(0)* through developmental time-course studies. In wild type animals (grown at 20°C),

synapses of DD neurons initially formed with ventral body wall muscles, were eliminated starting in late L1, and new synapses were formed with dorsal body wall muscles by late L2 (Figure 2.2A; Hallam & Jin, 1998; Park et al., 2011; Zhou & Walthall, 1998). *dlk-1(0)* animals displayed a short delay in forming new synapses in the dorsal neurites of DD neurons, resembling the delay seen in *tba-1(gf)* animals (Figure 2.2A, 2.S1A). In *tba-1(gf) dlk-1(0)* animals, a few dorsal synaptic puncta of reduced intensity were present from the L2-L4 stage, but adult animals lacked detectable synapses in the dorsal DD processes (Figure 2.2A, B).

To test the temporal requirement for *dlk-1* activity during DD remodeling, we induced its expression at different developmental stages using a heat shock promoter driven *dlk-1* construct. Inducing *dlk-1* expression in larval or adult wild type animals did not cause remodeling defects (Figure 2.2C). When *dlk-1* was induced in *tba-1(gf) dlk-1(0)* during DD remodeling (22 hph), >70% of the animals eliminated synapses to the ventral body muscles and formed new synapses with dorsal body wall muscles, which were maintained to adulthood (Figure 2.2C, D). Moreover, *dlk-1* induction in any other developmental stage did not result in the retention of transient synapses observed in the dorsal DD neuron processes of L2-L4 *tba-1(gf) dlk-1(0)* animals (Figure 2.2A, B), indicating that *dlk-1* activity was primarily required for formation, not maintenance, of new synapses (Figure 2.2C, D).Thus, transient expression of *dlk-1* in the L2 stage is required for establishing new synapses during DD remodeling.

DLK-1 regulates DD remodeling through p38/PMK-3 and MT catastrophe factors

Previous studies have established that DLK-1 signals via the p38 MAP kinase PMK-3, the MAPK activated kinase MAK-2 and the transcription factor CEBP-1 to co-ordinate synapse formation (Nakata et al., 2005; Yan et al., 2009). To test if DLK-1 acts through the same downstream genes to promote DD remodeling, we constructed double mutants of *tba-1(gf)* with *pmk-3(0), mak-2(0)* and *cebp-1(0). tba-1(gf); pmk-3(0)* completely blocked DD remodeling, and retained synaptic puncta in the VNC, indistinguishable from *tba-1(gf) dlk-1(0)* animals (Figure

2.3A, D). *tba-1(gf); pmk-3(0)* animals also coiled dorsally during backward movement like *tba-1(gf) dlk-1(0)* animals (data not shown). However, in *tba-1(gf); mak-2(0)* and *tba-1(gf); cebp-1(0)* adult animals, we observed DD synaptic puncta in the DNC, and the number of synapses in the double mutant animals was similar to that of *tba-1(gf)* single mutants (Figure 2.S2A). Thus DD remodeling proceeded normally in *cebp-1* or *mak-2* mutant animals, suggesting that DLK-1 functions through other downstream genes.

The MT depolymerizing kinesin-13 (KLP-7) was previously found to act downstream of the DLK-1 pathway in axon regeneration (Ghosh-Roy et al., 2012). To test whether KLP-7 acted in synapse remodeling, we examined its interaction with *tba-1(gf)*. *tba-1(gf); klp-7(0)* double mutants displayed impaired DD remodeling, partially resembling *tba-1(gf) dlk-1(0)* (Figure 2.3B, D). The partial remodeling defects of the *tba-1(gf); klp-7(0)* animals also suggested that the DLK cascade might act via multiple MAPs in regulating synapse remodeling. We further tested several other MAPs and found that loss of the MT severing protein spastin (SPAS-1) (Roll-Mecak & McNally, 2010) also synergized with *tba-1(gf)* to impair DD remodeling (Figure 2.3C, D), whereas loss of MT stabilizing proteins like doublecortin (ZYG-8) (Moores et al., 2004) and EMAP (ELP-1) (Houtman et al., 2007) did not (data not shown). Taken together, these results suggest that DLK-1 acts through PMK-3 and MT catastrophe factors like KLP-7 and SPAS-1 to regulate DD remodeling.

Dynamic MTs are reduced in *tba-1(gf) dlk-1(0)*

To understand how the interaction between *tba-1(gf)* and *dlk-1(0)* affected the MT cytoskeleton, we first assessed gross changes in MT composition. Analyses of whole-mount immunostaining using antibodies against total tubulin and a variety of microtubule post-translational modifications (MT-PTMs) (Janke & Bulinski, 2011) showed no significant changes in the nerve cords of *tba-1(gf) dlk-1(0)* (Figure 2.S3A-E), although subtle changes in DD neurons could be masked by the presence of other neurites (White et al., 1986).

To directly visualize MTs in DD neurons, we next examined the ultrastructure of the MT cytoskeleton preserved using high pressure freeze fixation. We collected transverse sections of both nerve cords. In wild type and *dlk-1(0)* animals, MTs predominantly ran longitudinally along the axon, their cross-section appearing as concentric circles in transverse sections (Figure 2.S4A). In *tba-1(gf)* animals we observed an additional population of misoriented MTs, oriented parallel to transverse sections (Figure 2.S4A, 2.S4B). In *tba-1(gf) dlk-1(0)* there was an overall increase in the number of axonal MTs (Figure 2.4B), but significantly fewer misoriented MTs than in *tba-1(gf)* alone (Figure 2.S4B). There was also a two-fold increase in the number of synaptic MTs in *tba-1(gf), dlk-1(0)* and *tba-1(gf) dlk-1(0)* when compared to wild type (Figure 2.4B). We further analyzed MT length and continuity by serial reconstructions of 8 μm of the dorsal DD process (Figure 2.4A). MTs parallel to the axon were reconstructed as continuous tracks, while misoriented MTs were not continuous in adjacent sections and could not be reconstructed. Noticeably, *tba-1(gf) dlk-1(0)* showed a significant increase in the length of continuous MT tracks compared to wild type animals (Figure 2.4C, 2.S4A).

To test how the increase in MT length and number observed in fixed EM samples affected MT dynamics in *tba-1(gf) dlk-1(0)*, we imaged MT growth using fluorescently tagged EBP-2 (P_{unc-25}EBP-2::GFP). End Binding Proteins (EBPs) like EBP-2 transiently bind to the plus ends of growing (dynamic) MTs (Ghosh-Roy et al., 2012; Mimori-Kiyosue, Shiina & Tsukita, 2000), and EBP-2::GFP movement is recorded in movies and analyzed as tracks on kymographs (Figure 2.4E, F). We analyzed kymographs from both the proximal and distal DD neurites in the VNC of adult animals. As the *unc-25* promoter labels both DD and VD neurons, these kymographs also included information from the proximal VD neurites (Figure 2.4D). The EBP-2::GFP track velocity, run length, direction and number were equivalent in both proximal and distal neurites; so the data were pooled for further analysis. We observed a striking reduction in the number of EBP-2::GFP tracks in *tba-1(gf) dlk-1(0)* compared to wild type animals (Figure 2.4F, H), even as the steady state fluorescence intensity of EBP-2::GFP was indistinguishable

between wild type and *tba-1(gf) dlk-1(0)* (Figure 2.S4C, D). The reduction in dynamic MTs was not restricted to the VNC; the number of tracks in the commissures and DNC were also reduced in *tba-1(gf) dlk-1(0)* (Figure 2.S4E-H and data not shown). The run length of EBP-2::GFP tracks was increased in *tba-1(gf) dlk-1(0)* (Figure 4I) while MT growth velocity was reduced (Figure 2.4J), indicative of more persistent MT growth than wild type. The reduction in EBP-2::GFP tracks, together with the increased number and length of MTs in fixed EM samples, indicates a loss in balance in the number of stable and dynamic MTs in *tba-1(gf) dlk-1(0).*

An increase in dynamic MTs facilitates DD remodeling

To address whether changes in MT dynamics correlated with DD remodeling, we imaged EBP-2::GFP in L1 animals before and after the onset of DD remodeling (6-8 hph and 12-14 hph, respectively; Figure 2.5A-E). The VD neurons were not born at both time points, allowing us to assay changes in MT dynamics only in the DD neurites. Before DD remodeling, wild type and *tba-1(gf) dlk-1(0)* animals had similar numbers of EBP-2::GFP tracks (Figure 2.5B-D). At the onset of DD remodeling, wild type animals showed a significant increase in the number of growing MTs (Figure 2.5B, D). In contrast, we observed no significant difference in MT dynamics in *tba-1(gf) dlk-1(0)* before and after the onset of remodeling (Figure 2.5C, D). We also found that in the ventral DD processes of both larval (Figure 2.5E) and adult (Figure 2.4G) animals, >80% of the EBP-2::GFP tracks moved in the anterograde direction, indicating that MT polarity in DD neurons was unchanged during remodeling. These data suggest that changes in MT dynamics, but not polarity, are necessary for DD remodeling.

We then asked if altering MT dynamics could directly affect DD remodeling. Nocodazole is an MT destabilizing drug shown to be effective in *C. elegans* motor neurons (Chalfie & Thompson, 1982). We treated L1 animals with 10 μM nocodazole before DD remodeling, and then placed them on drug free plates until adulthood. The number of dynamic MTs was increased in adult animals following nocodazole treatment, while MT polarity was

unchanged compared to control animals (Figure 2.5H-J). Adult DD neurons in nocodazole treated wild type animals also formed synapses along the DNC (Figure 2.5F, G). Importantly, in *tba-1(gf) dlk-1(0)*, such acute nocodazole treatment significantly rescued the failure in DD remodeling, with fewer synaptic puncta retained along the VNC and increased synaptic puncta along the DNC, compared to control animals (Figure 2.5F, G). Together, these findings support a conclusion that an increase in the number of dynamic MTs in DD neurons promotes synapse remodeling.

Gain-of-function kinesin-1 mutations suppress the DD remodeling defects of *tba-1(gf) dlk-1(0)*

To gain further insight into how MT dynamics regulate DD remodeling, we screened for EMS-induced mutations that suppressed the synaptic and behavioral defects of *tba-1(gf) dlk-1(0)*. We identified two mutations (*ju972* and *ju977*) (Figure 2.6A-C) that affect the gene *unc-116*, the heavy chain of the anterograde motor KIF5/kinesin-1. *ju972* alters a conserved Gly274 to Arg in the motor domain, and *ju977* alters a conserved Glu432 to Lys in the coiled-coil Rod 1 domain, which acts as a flexible hinge affecting motor motility (Grummt et al., 1998; Figure 2. 6C, 2.S5A).

We rescued the suppression of the behavioral and synaptic defects of *tba-1(gf) dlk-1(0)* by *ju972* and *ju977* by overexpressing wild type UNC-116 (Figure 2.6D, E). Conversely, overexpression of UNC-116(G274R) and UNC-116(E432K) in *tba-1(gf) dlk-1(0)* suppressed both behavioral and synaptic defects (Figure 2.6D, E). These results demonstrate that *unc-116(ju972)* and *unc-116(ju977)* caused the behavioral and synaptic suppression of *tba-1(gf) dlk-1(0)*. The reduction in synapse number seen in *tba-1(gf)* alone was not suppressed by either *unc-116(ju972)* or *unc-116(ju977)* (Figure 2.6A, B), and neither mutation showed any effect in *dlk-1(0)* (Figure 2.6A, B). Together, these genetic data show that the *unc-116* mutations specifically suppress the synergistic remodeling defects of *tba-1(gf) dlk-1(0).*

Previously characterized *unc-116* alleles range from being mildly uncoordinated to almost paralyzed, with severe defects in synapse development and organelle trafficking (Byrd et al., 2001; Yan et al., 2013). In contrast, *unc-116(ju972)* and *unc-116(ju977)* showed wild type locomotion and normal GABAergic synapse development (Figure 2.6 A, B and data not shown). Both alleles also complemented other hypomorphic *unc-116* alleles in locomotion and synapse development (data not shown). Moreover, analysis of immunostaining for endogenous UNC-116 revealed no discernable changes in protein localization in these two mutants (Figure 2.S5B). These data indicate that both *ju972* and *ju977* are gain-of-function mutations of *unc-116* (designated as *unc-116(gf)).*

Several *unc-116* loss-of-function alleles, including *unc-116(e2310),* decrease MT transport and alter MT polarity in *C. elegans* bipolar DA motor neurons (Yan et al., 2013). However, we found that *unc-116(e2310)* did not suppress the behavioral or synaptic remodeling defects of *tba-1(gf) dlk-1(0)* animals (data not shown). Imaging of EBP-2::GFP in *unc-116(ju972)* revealed no effects on MT polarity in DD neurons (Figure 2.S5C, D), or increase the number of dynamic MTs in *tba-1(gf) dlk-1(0)* (Figure 2.S5C, E). Thus, these observations suggest that the *unc-116(gf)* mutations do not alter neuronal MTs in the DD neurons, and instead compensate for the DD remodeling defect in *tba-1(gf) dlk-1(0)* through a different mechanism.

To understand how the *unc-116(gf)* mutations might affect kinesin-1 function and suppress *tba-1(gf) dlk-1(0),* we modeled the motor domain of UNC-116. We found that G274 (mutated to arginine in *unc-116(ju972)*) was a conserved residue in the MT binding domain (L12/α5) of the motor (Woehlke et al., 1997) (Figure 2.7A), and could potentially affect MT-motor affinity. A previous alanine scan of the MT binding domain of human kinesin-1 found that mutating residue Glu270 (Glu273 in UNC-116) to alanine resulted in increased affinity of the motor domain to MTs (Woehlke et al., 1997). Since Glu273 is next to Gly274, we attempted to phenocopy the suppression of *tba-1(gf) dlk-1(0)* by *unc-116(gf)* using UNC-116(E273A).

tba-1(gf) dlk-1(0) animals that expressed UNC-116(E273A) remodeled their DD synapses to a similar extent as animals that transgenically expressed UNC-116(G274R) or contained *unc-116(ju972)* (Figure 2.7B). As a control, overexpressing wild type UNC-116 did not rescue the DD remodeling defect of *tba-1(gf) dlk-1(0)*. These observations suggest that the suppressing activity of the *unc-116(gf)* alleles on *tba-1(gf) dlk-1(0)* could be due to increased MT-motor affinity that compensated for the MT defects in *tba-1(gf) dlk-1(0)* animals.

Synaptic vesicle transport during remodeling requires dynamic MTs

Anterograde motors of the kinesin superfamily drive axonal transport of various membrane organelles, including synaptic vesicle precursors (Hirokawa et al., 2009). The kinesin motors of the kinesin-3 subfamily (UNC-104 in *C. elegans*) are generally thought to be the major motors involved in axonal synaptic vesicle precursor transport. Indeed, reducing *unc-104* function completely blocks synaptic vesicle precursor transport in *C. elegans* (Hall & Hedgecock, 1996). However, multiple studies also show that kinesin-1 motors regulate synaptic vesicle precursor transport (Bryd et al., 2001; Mimori-Kiyosue, Shiina & Tsukita, 2000). To test the interaction of *unc-116(gf)* with *unc-104* in synaptic vesicle transport, we constructed *unc-104(lf); unc-116(ju972)* and *unc-104(lf); unc-116(ju977)* double mutant animals. We observed that the synaptic vesicle transport defects of *unc-104(lf)* animals were partially suppressed by both *unc-116(gf)* alleles, indicated by the increase in synaptic puncta along the VNC (Figure 2.7C, D), suggesting that *unc-116(gf)* could play a direct role in synaptic vesicle transport. We then hypothesized that the *unc-116(gf)* alleles might compensate for the block in synaptic vesicle precursor transport resulting from the loss of dynamic MTs in *tba-1(gf) dlk-1(0)*. To test this idea, we assayed synaptic vesicle transport in DD neuron commissures during remodeling (14-18 hph). In wild type animals, we observed SNB-1::GFP labeled vesicles moving in anterograde (towards the DNC) and retrograde directions, with a strong anterograde bias (Figure 2.7F, G). The average velocity (~1.1 μm/s) and proportion of anterogradely moving

vesicles was unchanged in *tba-1(gf) dlk-1(0)* and *tba-1(gf) dlk-1(0); unc-116(ju977)* animals, compared to wild type (Figure 2.7G). Interestingly, there was a significant reduction in the number of mobile vesicles in *tba-1(gf) dlk-1(0)*, which was reversed in *tba-1(gf) dlk-1(0); unc-116(ju977)* (Figure 2.7H), indicating that *tba-1(gf) dlk-1(0)* altered kinesin-1 movement to affect synaptic vesicle transport during remodeling. Since the loss of dynamic MTs was responsible for defective synapse remodeling in *tba-1(gf) dlk-1(0)*, we conclude that dynamic microtubules promote kinesin-1 dependent synaptic vesicle transport during synapse remodeling.

Discussion

Synapse remodeling is an essential process in the development of mature neuronal circuits in many animals, including humans (Hensch, 2004). However, whether cytoskeletal changes underlie the coordinated elimination and formation of synapses has not been well addressed. Synapse remodeling in *C. elegans* DD neurons is a precisely timed process, with synaptic connectivity changes achieved in the complete absence of neurite remodeling (Hallam & Jin, 1998; White, Albertson & Anness, 1978). Using this model, we have discovered that dynamic MTs are required for coordinating motor movement and synaptic vesicle transport during circuit rewiring.

By imaging MT growth, we show that while the ventral process of the DD neuron switches from an axonal to a dendritic identity during remodeling, MT polarity remains plus end out, a typically axonal polarity for many organisms (Conde & Cáceres, 2009). Instead, our data reveal that changes in MT stability are critical for DD remodeling. An increase in dynamic MTs in wild type animals correlated with the onset of DD remodeling. In contrast, *tba-1(gf) dlk-1(0)* animals showed no change in the number of dynamic MTs in the same developmental time window, and were defective in DD remodeling. Ultrastructural analysis suggests that the loss of dynamic MTs in *tba-1(gf) dlk-1(0)* is likely due to increased MT stability. Supporting this idea, acute nocodazole treatment, which resulted in increased MT dynamics, could rescue defective

DD remodeling in *tba-1(gf) dlk-1(0).* Although MTs in mature axons are predominantly stable, it is being increasingly appreciated that dynamic MTs are important for a variety of neuronal processes, including axon regeneration (Cho & Cavalli, 2012; Ghosh-Roy et al., 2012), dendritic spine growth (Jaworski et al., 2009) and memory formation (Uchida et al., 2014). Our studies reveal a specific role for dynamic MTs in modulating plasticity of pre-synaptic terminals, independent of axon outgrowth.

The DLK family of kinases regulates many aspects of nervous system development and response to injury (Bounoutas et al., 2011; Ghosh-Roy et al., 2012; Klinedinst et al., 2013; Nakata et al., 2005; Valakh et al., 2013; Welsbie et al., 2013; Yan et al., 2009). The idea that DLK-1 is triggered by cytoskeletal instability has been documented in a variety of contexts (Bounoutas et al., 2011; Valakh et al., 2013). By genetically altering the MT cytoskeleton using *tba-1(gf)*, we find that *dlk-1* is necessary for DD remodeling. Transient activation of *dlk-1* at the onset of remodeling promotes the formation of new synapses during DD remodeling, which are maintained to adulthood. It is interesting to note that a few synaptic vesicles were transiently observed in the DNC of *tba-1(gf) dlk-1(0)* animals in the late larval stages. It is likely that the stabilization and maintenance of new synaptic sites is dependent on the transport of sufficient numbers of vesicles, consistent with similar findings in cultured mammalian neurons (Jin & Garner, 2008; McAllister, 2007). Moreover, induction of *dlk-1* expression in the late larval stages did not cause the stabilization of nascent dorsal synapses in *tba-1(gf) dlk-1(0),* implying that *dlk-1* is not involved in the maintenance of new synapses. We propose that transient activation of DLK-1, through its target p38/PMK-3, regulates the activity of MT catastrophe factors like KLP-7 and SPAS-1 in the upregulation of dynamic MTs to promote new synapse formation.

Synaptic plasticity relies on regulated axonal transport of synaptic components along MTs, and a key player in this process is kinesin-1 (Cai, Pan & Sheng, 2007; Puthanveettil et al., 2008). We identified novel kinesin-1 mutations that suppress the DD remodeling defects in

tba-1(gf) dlk-1(0) animals, without altering their MT composition. Our data suggest that these gain-of-function kinesin-1 alleles increase the MT binding affinity, and in turn, the processivity of the motor to compensate for reduced synaptic vesicle transport in *tba-1(gf) dlk-1(0)*. Modifications in MT-motor affinity have important consequences in disease pathology, as mutations in the mammalian kinesin Kif21A that alter MT-motor binding have been found to cause oculo-motor axon stalling (Cheng et al., 2014). A recent study also reported that an increase in the overall negative charge of the C-terminal H12 helix of another *C. elegans* α-tubulin, MEC-12, increased the MT binding affinity of the minus end directed motor dynein, resulting in synaptic vesicle mistargeting in mechanosensory neurons (Hsu et al., 2014). This result differs from our findings in that an increase in the positive charge of the kinesin-1 motor suppresses synaptic vesicle trafficking defects of *tba-1(gf) dlk-1(0)* double mutants, even though *tba-1(gf)* increases the net positive charge of the H12 helix. However, we note that neither G274R nor E432K mutations, located on the motor head and coiled-coil Rod 1 domain of kinesin-1, respectively, show any effect on *tba-1(gf)* single mutants, and both suppress *tba-1(gf) dlk-1(0)* to the same extent. Hsu *et al.*, also observed that simply increasing the overall positive charge of the H11-H12 loop, using a MEC-12(G416R) mutation, did not significantly change synaptic vesicle targeting in the mechanosensory neurons, consistent with our findings. We speculate that the loss of dynamic MTs in *tba-1(gf) dlk-1(0)* affects MT-motor interactions more profoundly than *tba-1(gf)* alone, and further investigation will be required to tease apart the various factors that affect MT-motor interactions in different cellular contexts *in vivo*.

Our observations also highlight the importance of MT dynamic instability in kinesin-1 mediated transport. MT-PTMs like tyrosination and acetylation have been associated with modulating kinesin-1 binding and velocity (Janke & Bulinski, 2011). Although we did not detect gross changes in MT-PTMs in *tba-1(gf) dlk-1(0)*, we find that modulation of MT dynamics using nocodazole could rescue defective DD remodeling, indicating that any changes in MT-PTMs were secondary to an increase in the dynamic MT population. In cultured hippocampal neurons,

kinesin-1 displays increased affinity to the axon initial segment, which is rich in dynamic MTs, to regulate polarized axonal transport (Nakata & Hirokawa, 2003). A recent study also found preferential binding of kinesin-1 to GTPγS MTs, which are believed to mimic the plus ends of growing MTs (Bechstedt & Brouhard, 2012; Maurer et al., 2011). These observations, together with this study, support the idea that growing MTs themselves promote kinesin-1 dependent axonal transport. Up-regulation of kinesin-1 is essential for learning induced synaptic changes (Puthanveettil et al., 2008). Our findings underscore the importance of dynamic MTs in coordinating motor and cargo interactions necessary for structural synaptic plasticity**.**

Experimental Procedures

C. elegans culture

Strains were maintained at 20°C on NGM plates unless noted otherwise. Information on alleles and genotypes of strains is summarized in Supplementary Experimental Procedures. To collect L1 animals, 20-30 gravid adults were placed on a seeded NGM plate to allow egg-laying for 2hrs. The hatched L1s were collected 10 hrs later. *tba-1(gf)* and *tba-1(gf)dlk-1(0)* animals showed a 10-12 hrs delay from egg lay to hatching, thus hatched L1s were collected 22 hrs later.

Fluorescent imaging of synapses and axons

L4 animals of the relevant genotypes were cultured at 20°C overnight, and day 1 adults were imaged using a Zeiss LSM 710 confocal microscope. Animals were anaesthetized in 0.6 mM levamisole on 2% agar pads for image acquisition. Z-stacks were generated from slices of 0.6 μm thickness. Images were processed using Zen lite software. Synaptic puncta and axon outgrowth defects were quantified manually using a Zeiss Axioplan 2 microscope equipped with Chroma HQ filters.

SNB-1::GFP trafficking

L2 stage animals (14-18 hrs post hatching at 20°C) were collected for analysis, and anesthetized using 30 mM muscimol on 10% agarose pads. 4-D imaging was performed using a Yokogawa CSU-X1 spinning disc confocal head placed on a Nikon Eclipse Ti confocal microscope equipped with a piezo Z stage for fast Z- acquisition and a Hamamatsu Lineage EMx2-IK camera (1,024X1,024 active pixels), controlled using μManager. The entire DD commissure was visualized in 5-6 slices (180 ms/slice), and images were collected for 20 frames with an interval of 300 ms between each frame. The resulting movies were analyzed using Metamorph (Molecular Devices) to generate kymographs for analysis of number, velocity and direction of movement of synaptic vesicles. Particles with a velocity <0.5 μm/s were removed from the analysis.

Nocodazole treatment

L1 animals were placed on seeded 10 μM nocodazole, or buffer control (M9 containing DMSO) plates and incubated for 9 hrs at 20°C. The animals were then transferred to unseeded plates for 10 minutes to remove bacteria containing the drugs and subsequently moved to fresh seeded NGM plates until day 1 adult stage. These animals were then used for imaging synaptic remodeling and microtubule dynamics.

Statistical Analysis

Statistical analysis was performed using GraphPad Prism 5. Normal distribution of samples was tested using D'Agostino & Pearson omnibus normality test. Significance was determined using unpaired t-tests for two samples, One way ANOVA followed by Tukey's multiple comparison tests and two way ANOVA followed by Bonferroni posttests for multiple samples.

Isolation of *unc-116(ju972)* and *unc-116(ju977)*

tba-1(gf) dlk-1(0) animals were mutagenized using Ethyl Methane Sulphonate (EMS) following standard procedures (Brenner, 1974). F2 animals with improved locomotion were selected as putative suppressors in a nonclonal screen. Several suppressors were determined to be intragenic loss of function mutations in *tba-1(gf)* and contained either stop codon changes or missense mutations (not shown). *ju972* and *ju977* were determined to be extragenic and mapped to the gene *unc-116* following whole genome sequence analysis by MAQGene (Bigelow et al., 2009).

Plasmid and transgene generation

Plasmids were generated using Gateway technology (Invitrogen). Genomic DNA for *unc-116* and *tba-1* were amplified from purified genomic DNA by PCR using Phusion HF DNA polymerase (Finnzyme), and subcloned into PCR8 entry vectors. Site-directed mutagenesis was performed using Pfu Ultra polymerase (Agilent Technologies) to generate mutations corresponding to UNC-116(G274R), UNC-116(E432K) and UNC-116(E273A) following manufacturer protocols. The *dlk-1* minigene contained cDNA from exon 1-6 and exon 8 onwards, and genomic DNA in exon 6-8, as previously described (Yan & Jin, 2012). Primer and sequence information is available on request for all the clones generated in this study. Transgenic animals were generated by microinjection, following standard procedures (Mello et al., 1991), using plasmids of interest at 1-5 ng/ul and Pgcy-8-GFP or Pttx-3-GFP (80-90 ng/ul) as co-injection markers. A minimum of 2-3 transgenes were generated for each construct described in this study. For rescue experiments using *unc-116*, *tba-1* and *dlk-1* constructs, the data from 3 transgenes was pooled in statistical analyses.

Antibodies and immunostaining

The primary antibodies used were mouse monoclonal DM1A for α-tubulin (Sigma) at 1:400 dilution, mouse monoclonal α-6B11-1 for acetylated tubulin (Sigma) at 1:500 dilution, rabbit polyclonal anti-Δ2-tubulin (Millipore AB3203) at 1:500 dilution, monoclonal rat anti-tyrosinated tubulin YL1/2 (Santa Cruz Biotechnology) at 1:100 dilution and polyclonal rabbit anti-UNC-116 antibody at 1:500 dilution (McNally et al., 2010). Alexa conjugated secondary antibodies were from Molecular Probes, and used at 1: 2,000 dilutions. Whole mount immunostaining was performed following the Finney and Ruvkun protocol (Finney & Ruvkun, 1990) with minor modification. Briefly, worms of mixed stages were fixed in 1% paraformaldehyde and repeated freeze-thaw cycles with liquid N2. Samples were then treated with 1% β-mercaptoethanol and DTT to break the disulfide links in the cuticle, after which they were incubated with primary and secondary antibodies. Confocal images of the VNC about 50 μm posterior to the vulva were quantified.

Heat shock induced expression of *dlk-1*

Transgenic animals expressing *oxEx1268* (*Phsp-16.2DLK-1-mCherry; Pmyo-2GFP*) (Hammarlund et al., 2009) in the wild type and *tba-1(gf) dlk-1(0)* backgrounds were selected by positive pharyngeal GFP expression. L1, L2, L3, L4 and young adult animals were heat shocked at 33°C for 2 hours in an incubator. Heat shocked animals were maintained at 20°C after heat shock until they reached day 1 adulthood, when they were imaged using a Zeiss LSM 710 confocal microscope.

EBP-2::GFP image acquisition and analysis

Animals were anaesthetized in 0.6 mM levamisole on 2% agar pads for image acquisition. Live imaging for monitoring EBP-2 dynamics was done using a Yokogawa CSU-X1 spinning disc confocal head with a Photometrics Cascade II EMCCD camera (1,024 X 1,024

active pixels) controlled by μManager (http://www.micro-manager.org). 100 single plane images were taken serially at an exposure time of 114ms with an interval of 230ms between each frame, and analyzed using Metamorph software (Molecular Devices) to generate kymographs for analysis.

Modeling the motor head of UNC-116

The UNC-116 motor head shares 80% sequence identity with residues 254-341 of rat kinesin-1(Kif5c Nkhc2) and 75% identity with residues 8-358 *Drosophila* kinesin-1 (Khc kin CG7765). Using the solved crystal structure of rat (PDB ID: 2kinB) and *Drosophila* (PDB ID: 2y65C) kinesin-1 (Kozielski et al., 1997; Yi et al., 2011), the structure of UNC-116 was modeled using SWISS-Model (http://swissmodel.expasy.org/) and viewed using PyMOL (The PyMOL Molecular Graphics System, Version 1.3.0.4 Schrödinger, LLC).

EM serial reconstruction

Animals of the desired developmental stage (L1 or one-day old adults) were immobilized using high pressure fixation with a high-pressure freezer (BAL-TEC HPM 010) at -176°C (Rostaing et al., 2004). The samples were freeze substituted in 2% osmium tetroxide and 0.1% uranyl acetate in acetone at -90°C (48 hrs) and then at -20°C (16 hrs) using a freeze-substitution apparatus (Leica EM AFS2). After infiltration and embedding in Durcupan ACM resin blocks, the samples were polymerized at 60°C for 48 hrs. Serial sections of 50 nm thickness were collected from the anterior part of the worm (after the posterior pharyngeal bulb) using Leica ULTRACUT UCT. Sections were collected onto pioloform coated slot grids and were stained for 5 minutes in 2.5% uranyl acetate in 70% methanol, followed by washing in Reynold's lead citrate for 3 minutes. Serial images from both the dorsal and ventral nerve cords were collected with a Gatan digital camera with 2,688 X 2,672 pixel resolution (using Gatan Digital Micrograph acquisition software) on a transmission electron microscope (JEOL-1200 EX,

80kv) at 10,000× magnification. Digital images from both nerve cords were then imported into Reconstruct 3D reconstruction software. Sections were realigned for accurate 3D measurements and visualization. Membranes, synaptic densities, vesicles and microtubules were manually traced on the serial image sections with Wacom Graphire3 Pen Tablet input hardware. The 3D scenes were rendered and saved as a 360° bitmap images.

Acknowledgements

This chapter is a reprint, in full, of Kurup, N., Yan, D., Goncharov, A., & Jin, Y. (2015). Dynamic microtubules drive circuit rewiring in the absence of neurite remodeling *Current Biology*, *25*(12), 1594-1605; with permission of all the authors. The dissertation author was the primary author.

N. K. designed, interpreted and performed experiments and wrote the paper, D. Y. designed and performed the *tba-1(gf) dlk-1(0)* suppressor screen, A. G. performed EM analyses and Y. J. designed and interpreted experiments and wrote the paper. We are grateful to A. Desai, S. Roy, Y. Zou, S. Halpain and members of our labs for advice and helpful discussions. We thank A. D. Chisholm, W. Knowlton, K.W. Kim, M. Chuang, M. Andrusiak, K. Noma, S. Takayanagi-Kiya and Z. Wang for comments on the manuscript. We thank F. McNally for anti-UNC-116 antibodies, G. Peeters for use of a spinning disk confocal microscope, E. Jorgensen for *oxEx1268* line, the Caenorhabditis Genetics Center and the Mitani lab (Tokyo Women's Medical College) for strains. Y.J. is an Investigator, and A. G. and D. Y. were research associates, of the Howard Hughes Medical Institute. N. K. was a recipient of the Latham & Watkins Graduate Fellowship. This work was supported by HHMI and an NIH grant (NINDS R01 035546 to Y. J.).

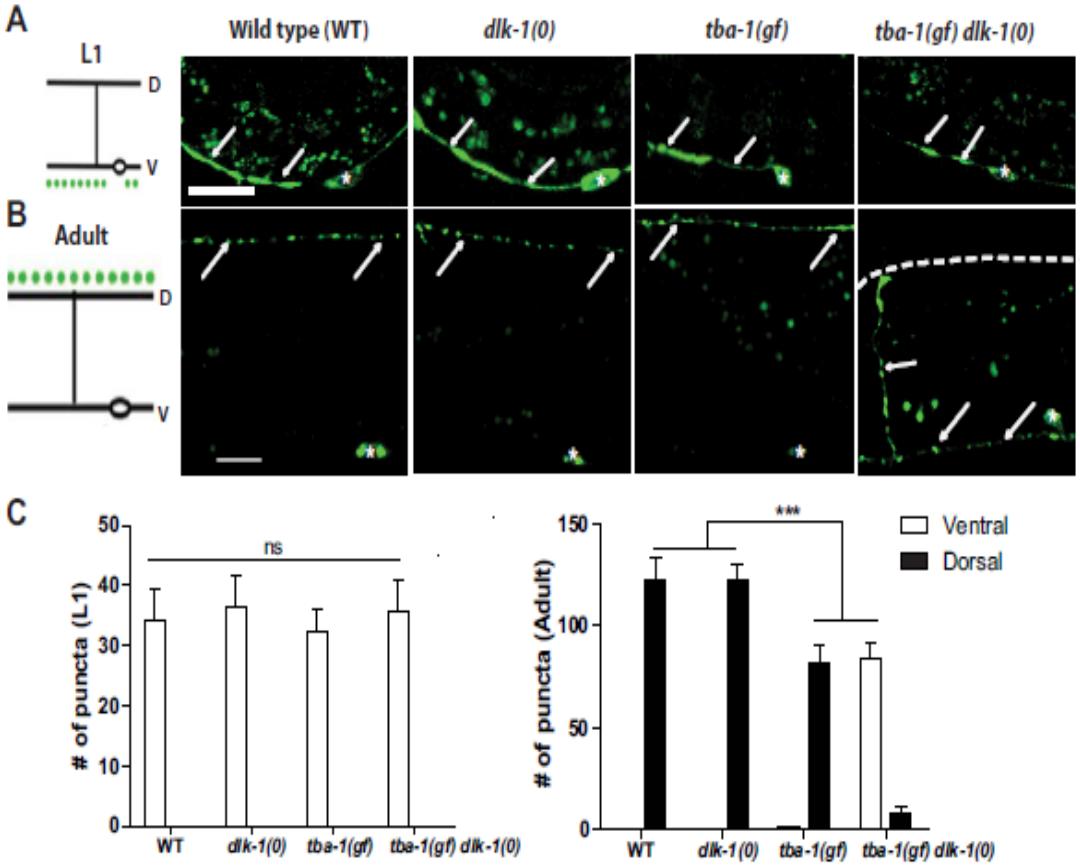

Figure 2.1 *tba-1(gf) dlk-1(0)* animals are defective in DD remodeling

(A, B) Representative images of DD synapses (P_{flp-13}-SNB-1::GFP (*juIs137*)) in L1 and adult animals. White arrows indicate synaptic vesicles; white asterisks, DD cell bodies in the VNC; and dashed white line, the location of DNC in *tba-1(gf) dlk-1(0).* Scale bars: 10 µm. (C) Quantification of synaptic puncta in the VNC and DNC of L1 (left) and adult (right) animals. Data are mean ± SEM; n=10 animals per genotype. Statistics: One-Way ANOVA followed by Tukey's posttest; ***p<0.001, ns- not significant. (D) Representative EM sections of DD neuron processes in the DNC, DD neuron is outlined in red. Scale bar: 100 nm. (E) Quantification of the number of synaptic vesicles in DD synapse boutons (sections containing an active zone). Data are mean ± SEM; n= synapse boutons (on graph). Statistics: unpaired t-test with Welch's correction; **p<0.01. (F) Bright field images of the typical body posture on food. White arrow represents bent tail in *tba-1(gf) dlk-1(0).* Scale bar: 200 µm. (G, H) Cell autonomous rescue of the behavioral (G) and synapse remodeling (H) defects of *tba-1(gf) dlk-1(0)*. Data are mean ± SEM; n=30 animals per genotype. Statistics: One-Way ANOVA followed by Tukey's posttest; **p<0.01, ***p<0.001. See also Figure 2.S1.

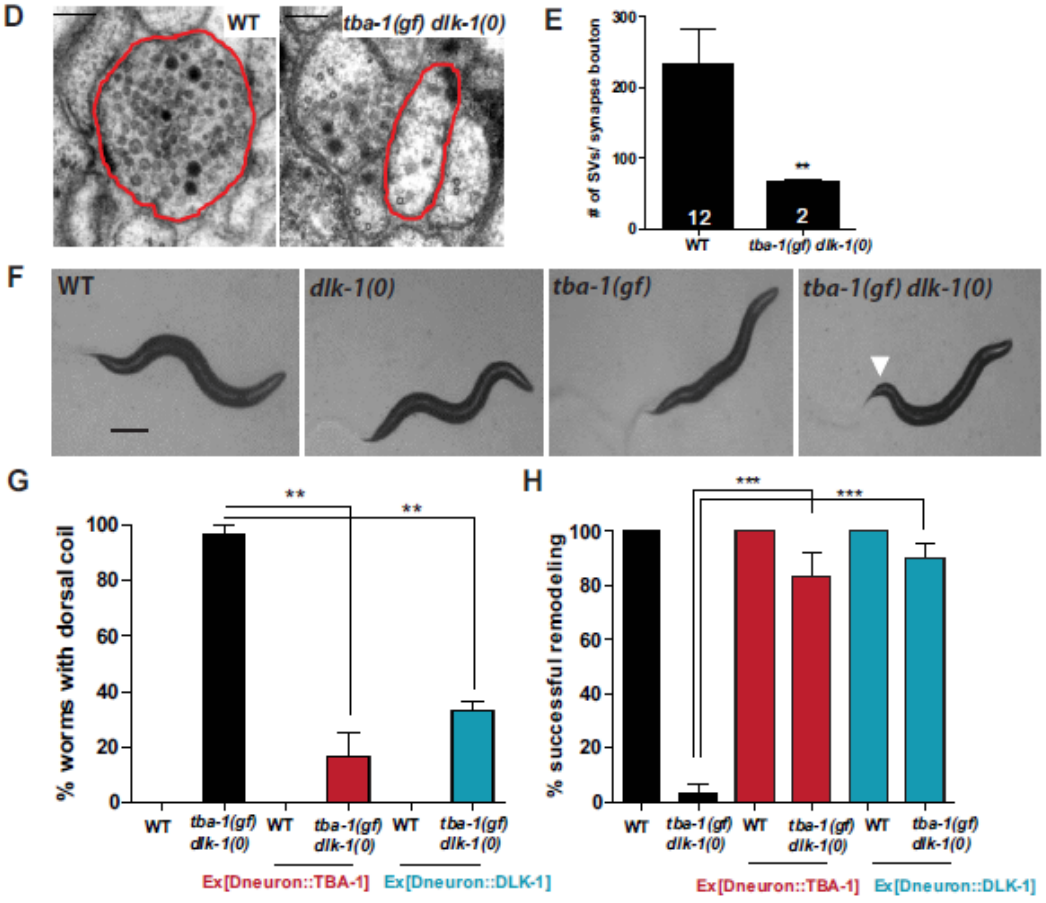

Figure 2.1 (continued) *tba-1(gf) dlk-1(0)* animals are defective in DD remodeling

(A, B) Representative images of DD synapses (P_{flp-13}-SNB-1::GFP (*juIs137*)) in L1 and adult animals. White arrows indicate synaptic vesicles; white asterisks, DD cell bodies in the VNC; and dashed white line, the location of DNC in *tba-1(gf) dlk-1(0).* Scale bars: 10 µm. (C) Quantification of synaptic puncta in the VNC and DNC of L1 (left) and adult (right) animals. Data are mean ± SEM; n=10 animals per genotype. Statistics: One-Way ANOVA followed by Tukey's posttest; ***p<0.001, ns- not significant. (D) Representative EM sections of DD neuron processes in the DNC, DD neuron is outlined in red. Scale bar: 100 nm. (E) Quantification of the number of synaptic vesicles in DD synapse boutons (sections containing an active zone). Data are mean ± SEM; n= synapse boutons (on graph). Statistics: unpaired t-test with Welch's correction; **p<0.01. (F) Bright field images of the typical body posture on food. White arrow represents bent tail in *tba-1(gf) dlk-1(0).* Scale bar: 200 µm. (G, H) Cell autonomous rescue of the behavioral (G) and synapse remodeling (H) defects of *tba-1(gf) dlk-1(0).* Data are mean ± SEM; n=30 animals per genotype. Statistics: One-Way ANOVA followed by Tukey's posttest; **p<0.01, ***p<0.001. See also Figure 2.S1.

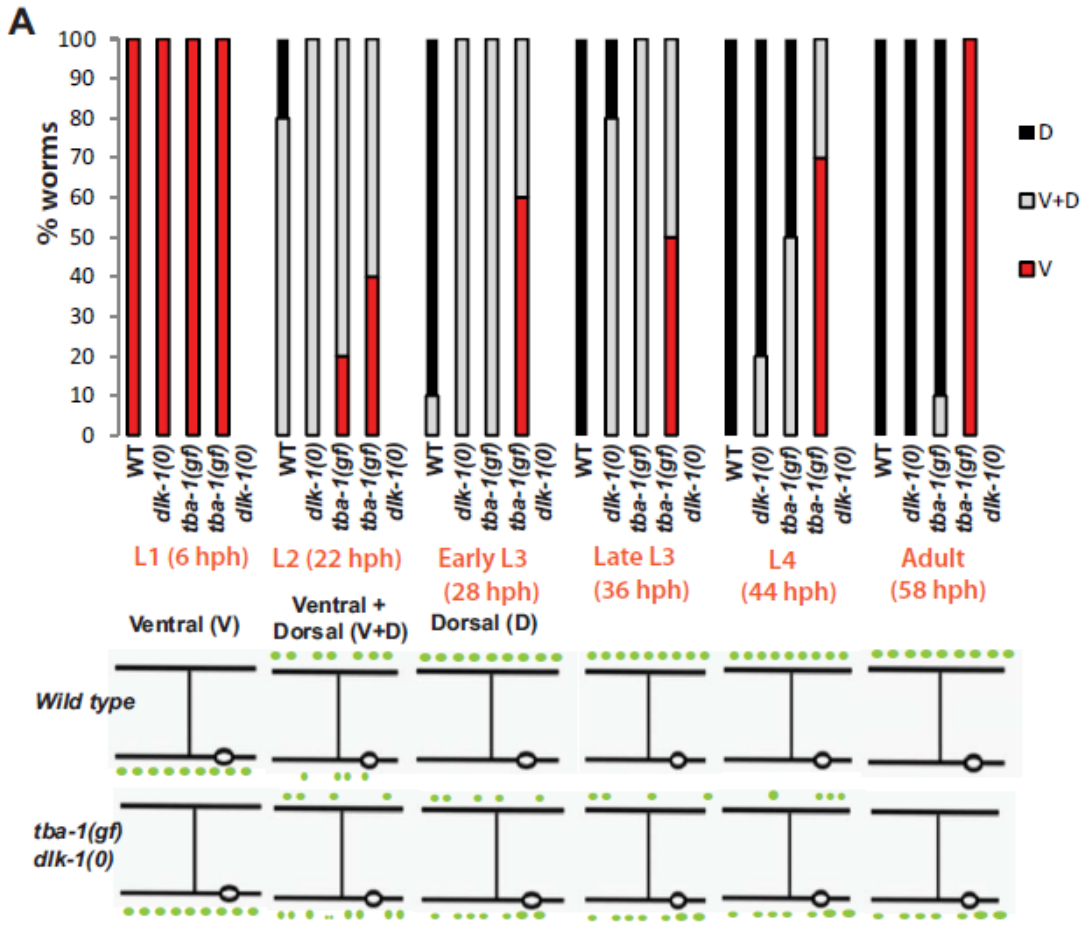

Figure 2.2 DLK-1 is required for establishing dorsal synapses during DD remodeling

(A) (Top) Progress of DD remodeling at 20°C from L1 (6 hph) to adult stages (56 hph) using *juIs137*. V: Synaptic puncta observed only along the VNC; V+D: synaptic puncta observed along both the VNC and DNC; D: synaptic puncta only along the DNC. n=10 animals per genotype for each time point. (Bottom) Schematic of DD remodeling. In WT, DD synapses are completely ventral (V) in the L1 stage, V+D in the L2 stage and then completely dorsal (D) after the L3 stage.(B) *juIs137* intensity in the DNC during remodeling in WT and *tba-1(gf) dlk-1(0)* animals. Data are mean ± SEM; n=6 animals for each genotype per time point. Statistics: 2-way ANOVA followed by Bonferroni posttests; *p<0.05, **p<0.01. (C) Rescue of DD remodeling defects in adult worms upon induction of DLK-1 at various larval stages in WT and *tba-1(gf) dlk-1(0)*; n=20 animals per genotype for each time point. (D) Representative images of synapse location in an adult *tba-1(gf) dlk-1(0)* animal with no DLK-1 induction, DLK-1 induction at L2 stage (22 hph) and early L3 stage (28 hph). White arrows indicate the location of synaptic vesicles; dashed white line, the DNC; and white asterisks, DD cell bodies. Scale bar: 10 μm.

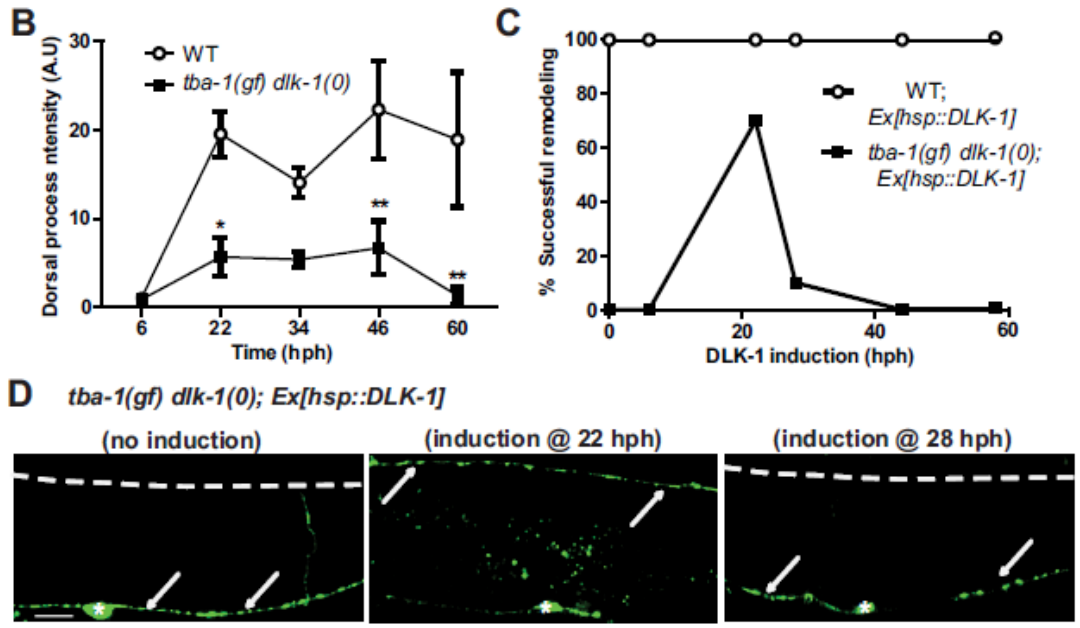

Figure 2.2 (continued) DLK-1 is required for establishing dorsal synapses during DD remodeling

(A) (Top) Progress of DD remodeling at 20°C from L1 (6 hph) to adult stages (56 hph) using *juIs137*. V: Synaptic puncta observed only along the VNC; V+D: synaptic puncta observed along both the VNC and DNC; D: synaptic puncta only along the DNC. n=10 animals per genotype for each time point. (Bottom) Schematic of DD remodeling. In WT, DD synapses are completely ventral (V) in the L1 stage, V+D in the L2 stage and then completely dorsal (D) after the L3 stage.(B) *juIs137* intensity in the DNC during remodeling in WT and *tba-1(gf) dlk-1(0)* animals. Data are mean ± SEM; n=6 animals for each genotype per time point. Statistics: 2-way ANOVA followed by Bonferroni posttests; *p<0.05, **p<0.01. (C) Rescue of DD remodeling defects in adult worms upon induction of DLK-1 at various larval stages in WT and *tba-1(gf) dlk-1(0)*; n=20 animals per genotype for each time point. (D) Representative images of synapse location in an adult *tba-1(gf) dlk-1(0)* animal with no DLK-1 induction, DLK-1 induction at L2 stage (22 hph) and early L3 stage (28 hph). White arrows indicate the location of synaptic vesicles; dashed white line, the DNC; and white asterisks, DD cell bodies. Scale bar: 10 μm.

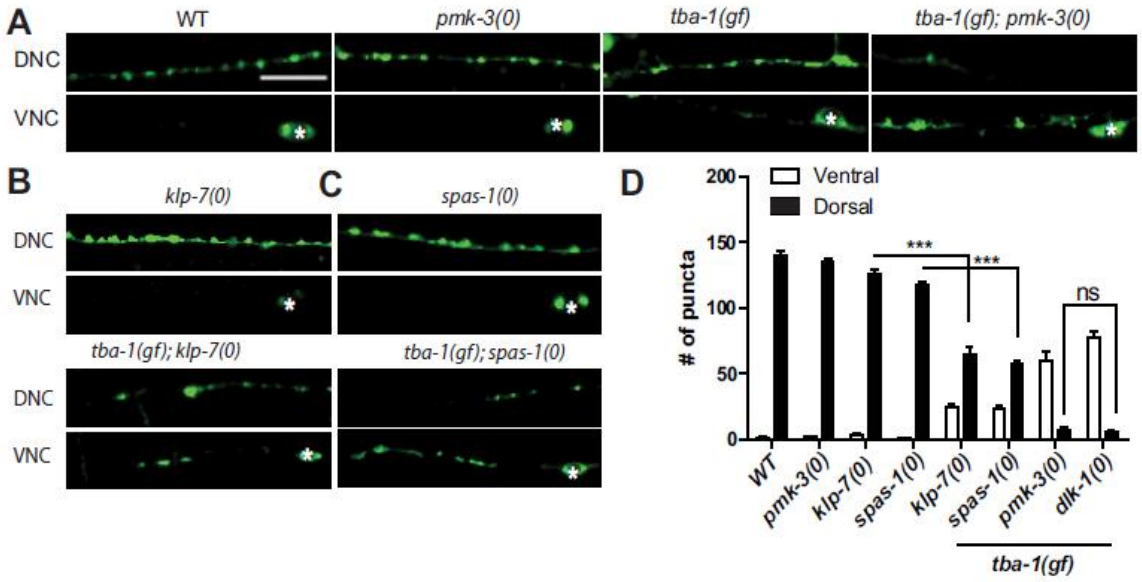

Figure 2.3 DLK-1 signals through PMK-3, and partly via KLP-7 and SPAS-1, in promoting DD remodeling

(A-C) Images of DD neuron synapses (*juIs137)* in genotype as indicated. White asterisk mark DD cell bodies on the VNC. Scale bars: 10 µm. (D) Quantification of ventral and dorsal DD synaptic puncta. Data are represented as mean ± SEM; n=10 animals per genotype. Statistics: One-Way ANOVA followed Tukey's posttest; ***p<0.001, ns- not significant. See also Figure 2.S2.

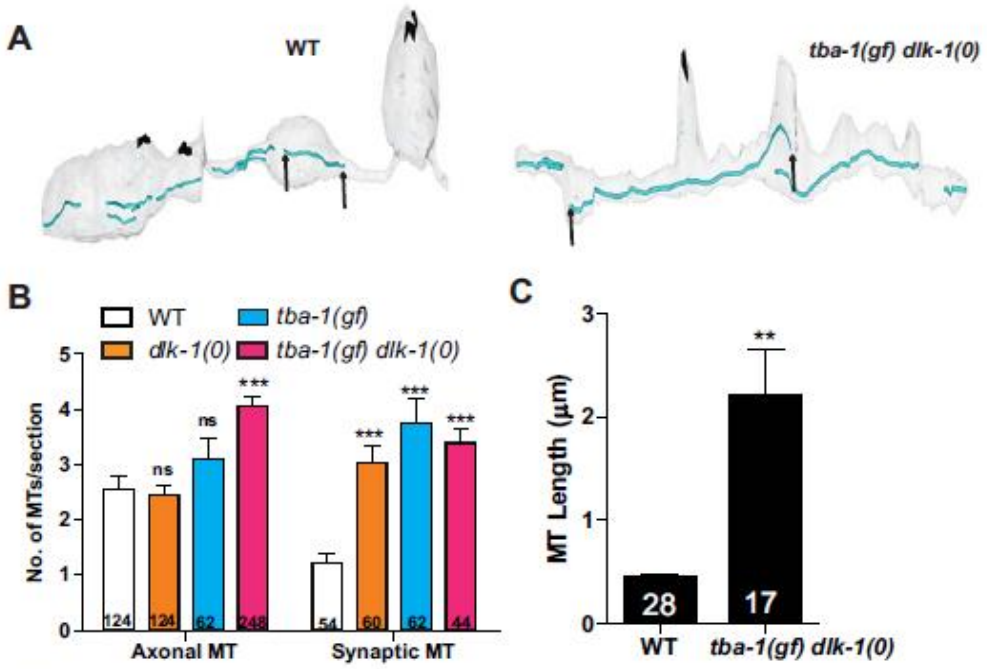

Figure 2.4 Dynamic MTs are reduced in *tba-1(gf) dlk-1(0)*

(A) Serial reconstruction of the dorsal processes of DD neurons in WT (~8 µm) and *tba-1(gf) dlk-1(0)* (~7.5 µm). Represented in blue are microtubules, and in black are active zones of pre-synaptic terminals. MT ends are indicated by black arrows.(B) MTs in DD neuron axonal (sections with no active zones) and synaptic (sections with active zones) sections. Data are mean ± SEM; n=# of sections for each genotype (graph). Statistics- 2-Way ANOVA followed by Bonferroni posttest; ***p<0.001, ns-not significant. (C) MT length in the DNC of WT and *tba-1(gf) dlk-1(0)* DD neurons. Data are mean ± SEM; n=# of MTs (graph). Statistics - unpaired t-test with Welch's correction; **p<0.01. (D) EBP-2::GFP tracks (red) in the VNC of adult DD (black) and VD (gray) neurons , with proximal (blue) and distal (yellow) neurites used for imaging. (E, F) MT dynamics from proximal (blue outline) and distal (yellow) DD neurites in (E) WT and (F) *tba-1(gf) dlk-1(0)* adults. Red line indicates a single EBP-2::GFP track moving in the anterograde direction. Vertical lines on the kymographs are caused by intensity differences of EBP-2::GFP along the VNC. (G-J) Quantification of (G) direction of movement, (H) number, (I) run length and (J) velocity of EBP-2::GFP tracks in the proximal and distal neurites. Data are mean ± SEM; n=# of animals in (G-H) and # of EBP-2::GFP tracks in (I-J). Statistics - unpaired t-test (with Welch's correction for (I)); ns-not significant, ***p<0.001, *p<0.05, **p<0.01. See also Figure 2.S3 and 2.S4.

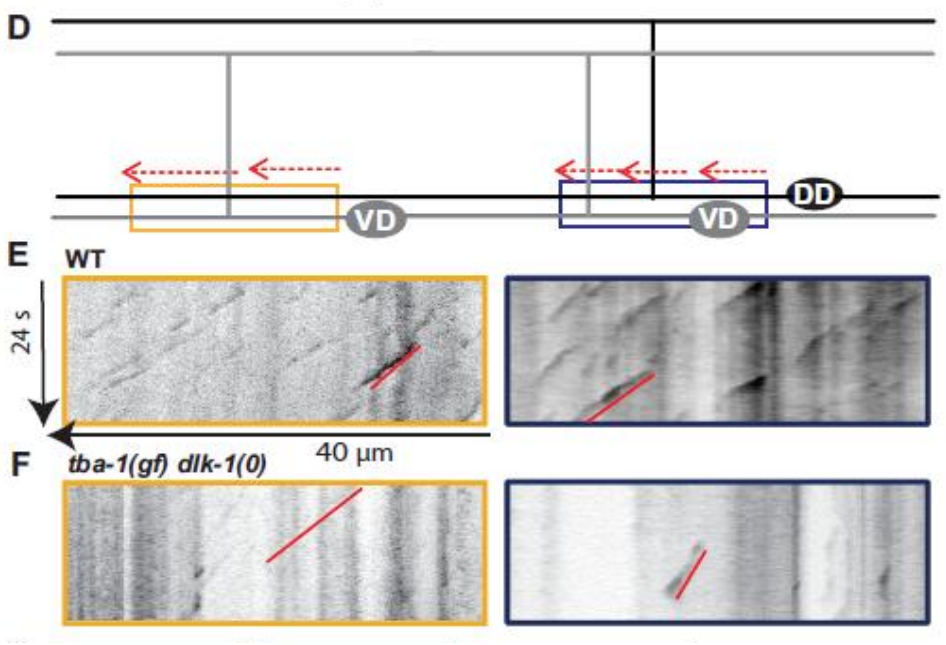

Figure 2.4 (continued) Dynamic MTs are reduced in *tba-1(gf) dlk-1(0)*

(A) Serial reconstruction of the dorsal processes of DD neurons in WT (~8 µm) and *tba-1(gf) dlk-1(0)* (~7.5 µm). Represented in blue are microtubules, and in black are active zones of pre-synaptic terminals. MT ends are indicated by black arrows.(B) MTs in DD neuron axonal (sections with no active zones) and synaptic (sections with active zones) sections. Data are mean ± SEM; n=# of sections for each genotype (graph). Statistics- 2-Way ANOVA followed by Bonferroni posttest; ***p<0.001, ns-not significant. (C) MT length in the DNC of WT and *tba-1(gf) dlk-1(0)* DD neurons. Data are mean ± SEM; n=# of MTs (graph). Statistics - unpaired t-test with Welch's correction; **p<0.01. (D) EBP-2::GFP tracks (red) in the VNC of adult DD (black) and VD (gray) neurons , with proximal (blue) and distal (yellow) neurites used for imaging. (E, F) MT dynamics from proximal (blue outline) and distal (yellow) DD neurites in (E) WT and (F) *tba-1(gf) dlk-1(0)* adults. Red line indicates a single EBP-2::GFP track moving in the anterograde direction. Vertical lines on the kymographs are caused by intensity differences of EBP-2::GFP along the VNC. (G-J) Quantification of (G) direction of movement, (H) number, (I) run length and (J) velocity of EBP-2::GFP tracks in the proximal and distal neurites. Data are mean ± SEM; n=# of animals in (G-H) and # of EBP-2::GFP tracks in (I-J). Statistics - unpaired t-test (with Welch's correction for (I)); ns-not significant, ***p<0.001, *p<0.05, **p<0.01. See also Figure 2.S3 and 2.S4.

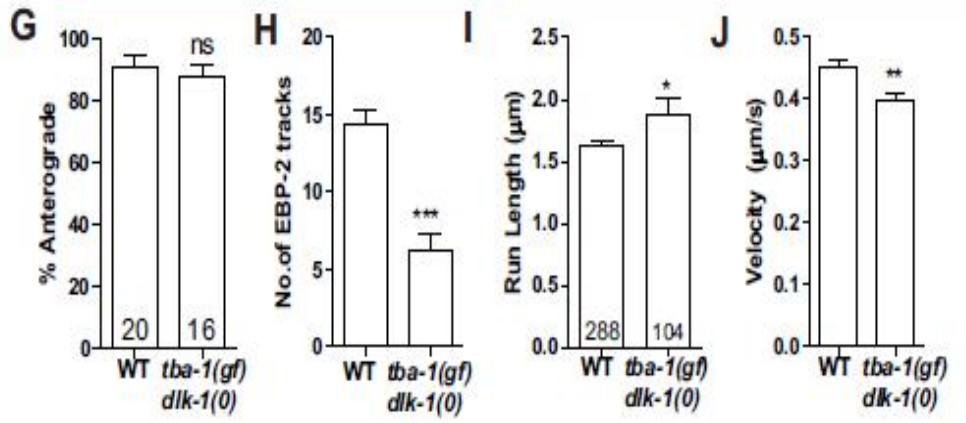

Figure 2.4 (continued) Dynamic MTs are reduced in *tba-1(gf) dlk-1(0)*

(A) Serial reconstruction of the dorsal processes of DD neurons in WT (~8 µm) and *tba-1(gf) dlk-1(0)* (~7.5 µm). Represented in blue are microtubules, and in black are active zones of pre-synaptic terminals. MT ends are indicated by black arrows.(B) MTs in DD neuron axonal (sections with no active zones) and synaptic (sections with active zones) sections. Data are mean ± SEM; n=# of sections for each genotype (graph). Statistics- 2-Way ANOVA followed by Bonferroni posttest; ***p<0.001, ns-not significant. (C) MT length in the DNC of WT and *tba-1(gf) dlk-1(0)* DD neurons. Data are mean ± SEM; n=# of MTs (graph). Statistics - unpaired t-test with Welch's correction; **p<0.01. (D) EBP-2::GFP tracks (red) in the VNC of adult DD (black) and VD (gray) neurons , with proximal (blue) and distal (yellow) neurites used for imaging. (E, F) MT dynamics from proximal (blue outline) and distal (yellow) DD neurites in (E) WT and (F) *tba-1(gf) dlk-1(0)* adults. Red line indicates a single EBP-2::GFP track moving in the anterograde direction. Vertical lines on the kymographs are caused by intensity differences of EBP-2::GFP along the VNC. (G-J) Quantification of (G) direction of movement, (H) number, (I) run length and (J) velocity of EBP-2::GFP tracks in the proximal and distal neurites. Data are mean ± SEM; n=# of animals in (G-H) and # of EBP-2::GFP tracks in (I-J). Statistics - unpaired t-test (with Welch's correction for (I)); ns-not significant, ***p<0.001, *p<0.05, **p<0.01. See also Figure 2.S3 and 2.S4.

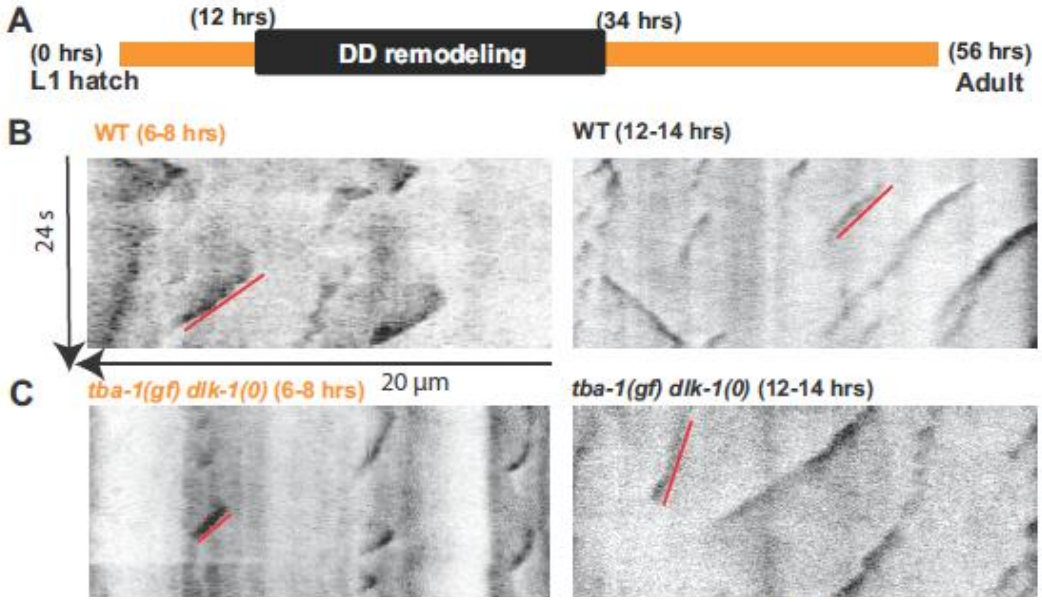

Figure 2.5 DD remodeling requires dynamic MTs

(A) Timeline of DD remodeling at 20°C. (B, C) Representative kymographs of MT dynamics in WT and *tba-1(gf) dlk-1(0)* before (6-8 hph) and after (12-14 hph) the onset of DD remodeling. Red line represents a single EBP-2::GFP track moving in the anterograde direction. Horizontal lines on the kymographs are caused by slight movement of the animal during imaging. (D, E) Quantification of the (D) number and (E) direction of movement of EBP-2::GFP tracks in WT and *tba-1(gf) dlk-1(0)* animals before and during DD remodeling. Data are mean ± SEM; n=# of animals, shown in (D). Statistics – One way ANOVA followed by Tukey's posttest; ***p<0.001, ns-not significant. (F) DD synapses (*juIs137)* in the VNC and DNC of WT and *tba-1(gf) dlk-1(0)* adults after acute 10 µM nocodazole treatment before DD remodeling. White asterisks represent DD cell bodies. Scale bar: 10 µm. (G) Quantification of dorsal and ventral DD synaptic puncta distribution after acute M9 (buffer control) and nocodazole treatment. Data are mean ± SEM; n=10 animals per genotype for each drug treatment. Statistics – One way ANOVA followed by Tukey's posttest; *p<0.05, **p<0.01. (H) Representative kymographs of EBP-2::GFP movement in the adult VNC of WT (buffer control) and WT (nocodazole treated) animals. Red line represents a single EBP-2::GFP track moving in the anterograde direction. (I, J) Quantification of (I) direction of movement and (J) number of EBP-2::GFP tracks. Data are mean ± SEM; n=# of animals, shown on (I). Statistics - unpaired t-test; **p<0.01; ns-not significant.

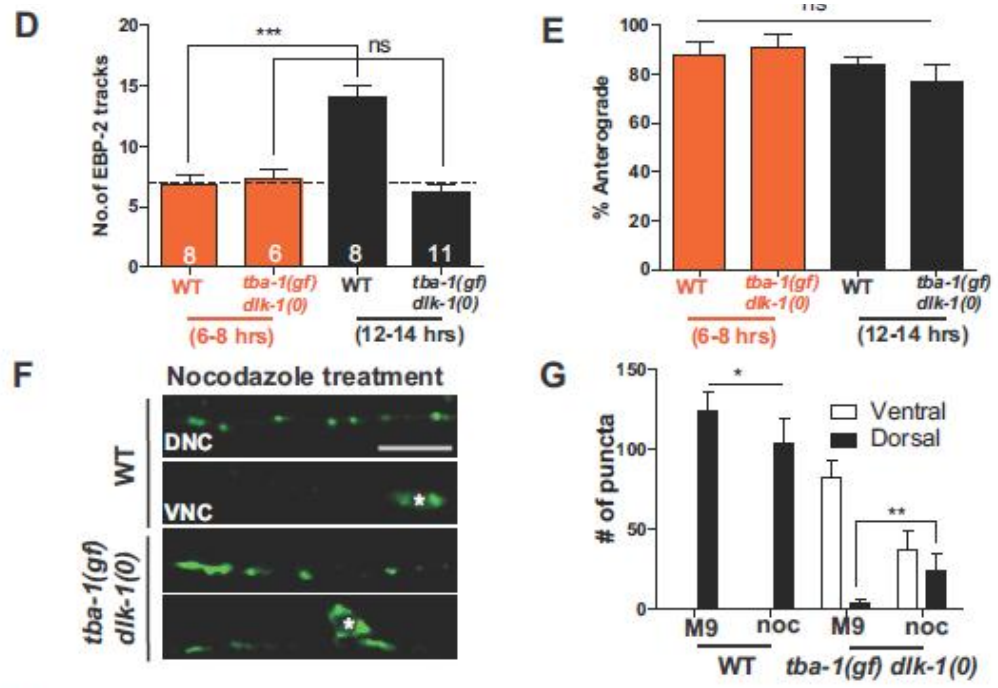

Figure 2.5 (continued) DD remodeling requires dynamic MTs

(A) Timeline of DD remodeling at 20°C. (B, C) Representative kymographs of MT dynamics in WT and *tba-1(gf) dlk-1(0)* before (6-8 hph) and after (12-14 hph) the onset of DD remodeling. Red line represents a single EBP-2::GFP track moving in the anterograde direction. Horizontal lines on the kymographs are caused by slight movement of the animal during imaging. (D, E) Quantification of the (D) number and (E) direction of movement of EBP-2::GFP tracks in WT and *tba-1(gf) dlk-1(0)* animals before and during DD remodeling. Data are mean ± SEM; n=# of animals, shown in (D). Statistics – One way ANOVA followed by Tukey's posttest; ***p<0.001, ns-not significant. (F) DD synapses (*juIs137)* in the VNC and DNC of WT and *tba-1(gf) dlk-1(0)* adults after acute 10 µM nocodazole treatment before DD remodeling. White asterisks represent DD cell bodies. Scale bar: 10 µm. (G) Quantification of dorsal and ventral DD synaptic puncta distribution after acute M9 (buffer control) and nocodazole treatment. Data are mean ± SEM; n=10 animals per genotype for each drug treatment. Statistics – One way ANOVA followed by Tukey's posttest; *p<0.05, **p<0.01. (H) Representative kymographs of EBP-2::GFP movement in the adult VNC of WT (buffer control) and WT (nocodazole treated) animals. Red line represents a single EBP-2::GFP track moving in the anterograde direction. (I, J) Quantification of (I) direction of movement and (J) number of EBP-2::GFP tracks. Data are mean ± SEM; n=# of animals, shown on (I). Statistics - unpaired t-test; **p<0.01; ns-not significant.

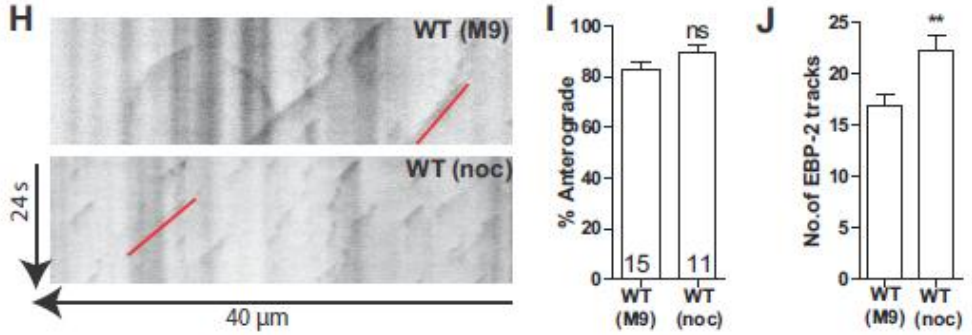

Figure 2.5 (continued) DD remodeling requires dynamic MTs

(A) Timeline of DD remodeling at 20°C. (B, C) Representative kymographs of MT dynamics in WT and *tba-1(gf) dlk-1(0)* before (6-8 hph) and after (12-14 hph) the onset of DD remodeling. Red line represents a single EBP-2::GFP track moving in the anterograde direction. Horizontal lines on the kymographs are caused by slight movement of the animal during imaging. (D, E) Quantification of the (D) number and (E) direction of movement of EBP-2::GFP tracks in WT and *tba-1(gf) dlk-1(0)* animals before and during DD remodeling. Data are mean ± SEM; n=# of animals, shown in (D). Statistics – One way ANOVA followed by Tukey's posttest; ***p<0.001, ns-not significant. (F) DD synapses (*juIs137)* in the VNC and DNC of WT and *tba-1(gf) dlk-1(0)* adults after acute 10 µM nocodazole treatment before DD remodeling. White asterisks represent DD cell bodies. Scale bar: 10 µm. (G) Quantification of dorsal and ventral DD synaptic puncta distribution after acute M9 (buffer control) and nocodazole treatment. Data are mean ± SEM; n=10 animals per genotype for each drug treatment. Statistics – One way ANOVA followed by Tukey's posttest; *p<0.05, **p<0.01. (H) Representative kymographs of EBP-2::GFP movement in the adult VNC of WT (buffer control) and WT (nocodazole treated) animals. Red line represents a single EBP-2::GFP track moving in the anterograde direction. (I, J) Quantification of (I) direction of movement and (J) number of EBP-2::GFP tracks. Data are mean ± SEM; n=# of animals, shown on (I). Statistics - unpaired t-test; **p<0.01; ns-not significant.

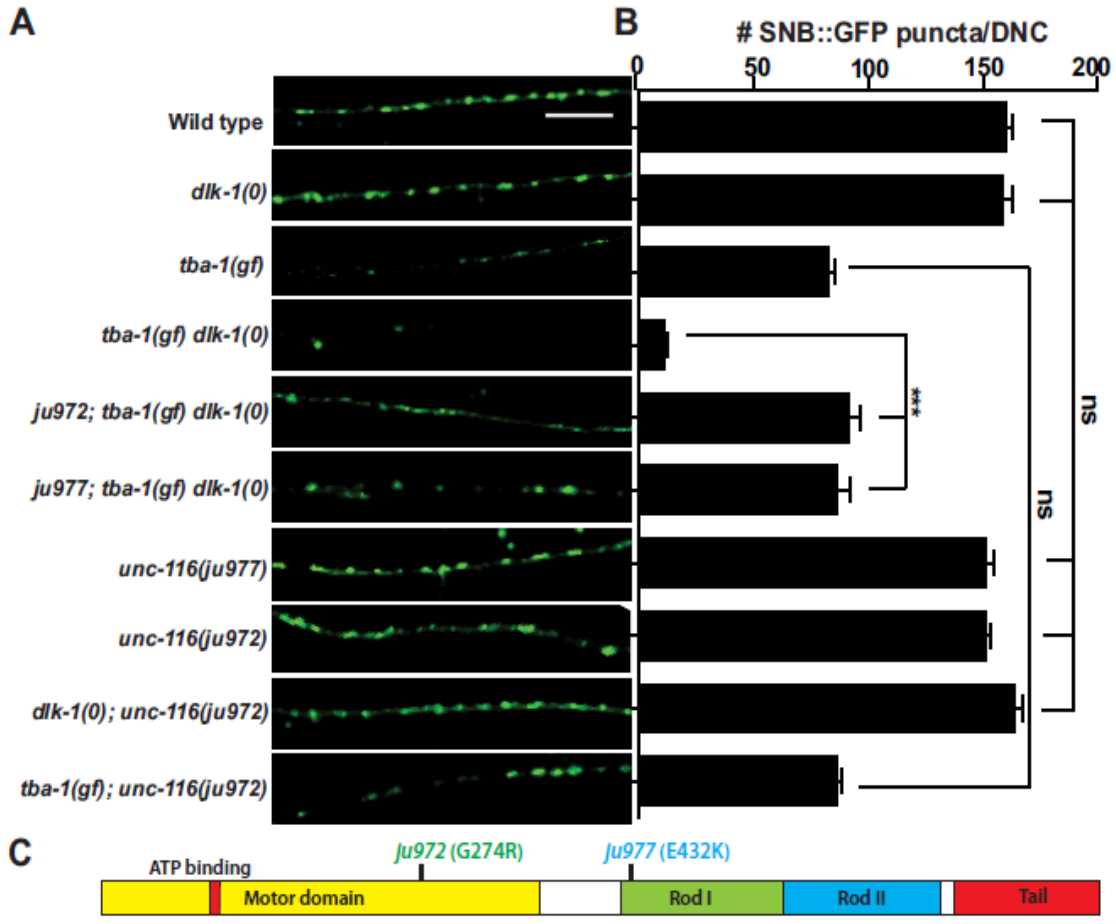

Figure 2.6 Gain-of-function kinesin-1 mutations suppress *tba-1(gf) dlk-1(0)*

(A) DD synapses in the adult DNC using P_{unc-25}-SNB-1::GFP (*juIs1*). Scale bar: 10 µm. (B) Quantification of DD synapses in the DNC. Data are mean ± SEM; n=10 animals per genotype. Statistics - One-way ANOVA followed by Tukey's posttest; ***p<0.001, ns-not significant. (C) UNC-116 protein domains; G274R (green) - *ju972*, E432K (blue) - *ju977*. (D, E) Rescue of (D) behavioral and (E) synaptic defects of *tba-1(gf) dlk-1(0)* by transgenes expressing *ju972* or *ju977*. Data are mean ± SEM; n=30 animals per genotype. Statistics- One way ANOVA followed by Tukey's posttest; ***p<0.001, ns-not significant. See also Figure 2.S5.

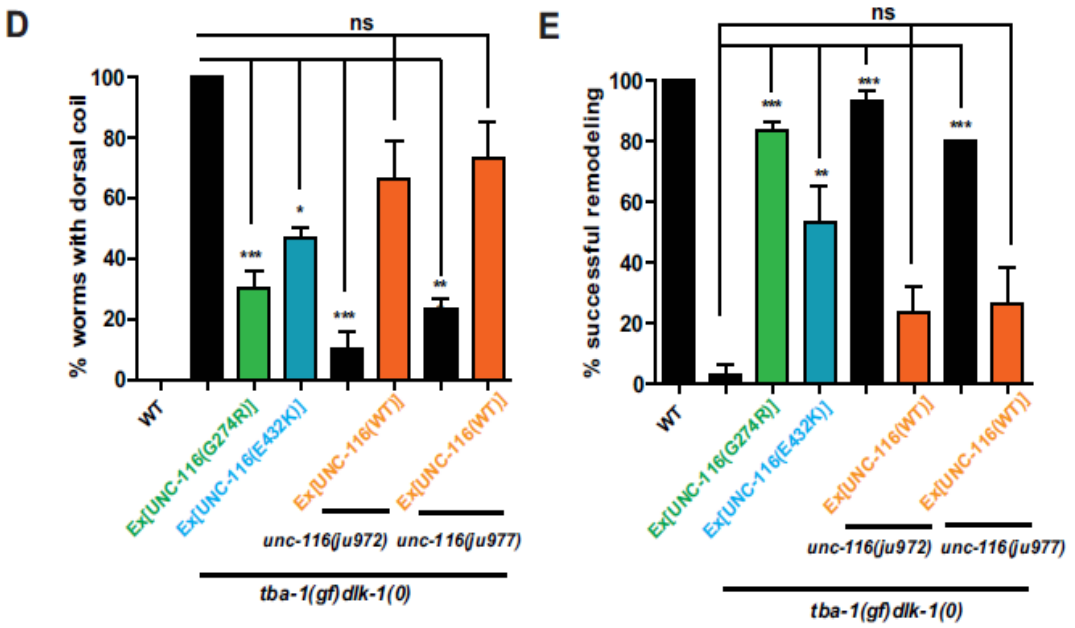

Figure 2.6 (continued) Gain-of-function kinesin-1 mutations suppress *tba-1(gf) dlk-1(0)*

(A) DD synapses in the adult DNC using P_{unc-25}-SNB-1::GFP (*juIs1*). Scale bar: 10 µm. (B) Quantification of DD synapses in the DNC. Data are mean ± SEM; n=10 animals per genotype. Statistics - One-way ANOVA followed by Tukey's posttest; ***p<0.001, ns-not significant. (C) UNC-116 protein domains; G274R (green) - *ju972*, E432K (blue) - *ju977*. (D, E) Rescue of (D) behavioral and (E) synaptic defects of *tba-1(gf) dlk-1(0)* by transgenes expressing *ju972* or *ju977*. Data are mean ± SEM; n=30 animals per genotype. Statistics- One way ANOVA followed by Tukey's posttest; ***p<0.001, ns-not significant. See also Figure 2.S5.

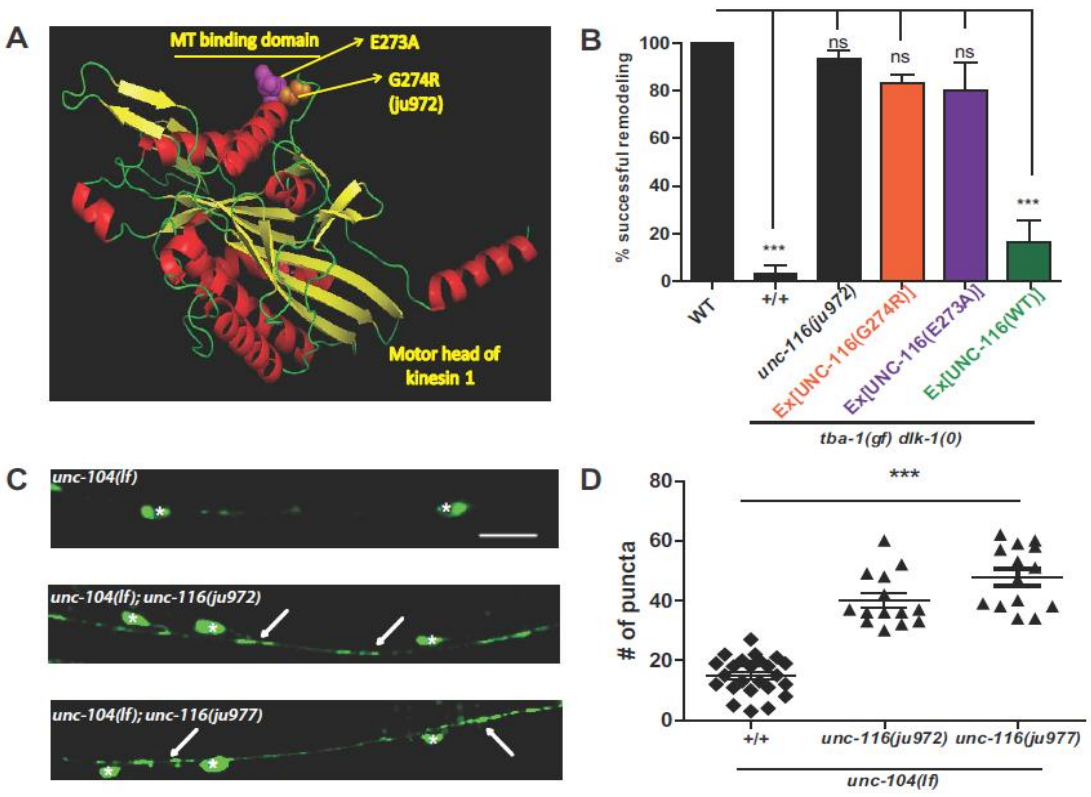

Figure 2.7 *unc-116(gf)* increases MT binding affinity to promote synaptic vesicle transport

(A) Prediction of the motor head of *C. elegans* UNC-116 (8-358aa) modeled on SWISS-MODEL and rendered using PyMOL.. (B) Rescue of DD remodeling defects of *tba-1(gf) dlk-1(0)* animals by transgenes expressing UNC-116(E273A). No rescue was observed with wild type kinesin-1 transgenes. Data are represented as mean ± SEM; n=30 animals per genotype. Statistics- One way ANOVA followed by Tukey's posttest; ***p<0.001; ns-not significant. (C-D) Images and quantification of D neuron synapses in the VNC of *unc-104(lf), unc-104(lf); unc-116(ju972)* and *unc-104(lf); unc-116(ju977)* animals expressing *juIs1* (P_{unc-25}-SNB-1::GFP). White asterisks represent DD and VD cell bodies, white arrows indicate synapses. Scale bar: 10 μm. Statistics - unpaired t-test; ***p<0.001. (E) Schematic of bidirectional synaptic vesicle transport along the commissure during DD remodeling. Solid arrow represents the anterograde direction, *i.e*, towards the DNC. (F) Representative kymographs of synaptic vesicle transport along the DD commissure. Solid arrowheads indicate vesicles moving in the anterograde direction, and open arrowheads indicate vesicles moving in the retrograde direction. Vertical lines on the kymographs represent stationary puncta and also indicate intensity differences of SNB-1::GFP along the commissure. (G, H) Quantification of (G) direction of movement and (H) number of mobile vesicles during DD remodeling.

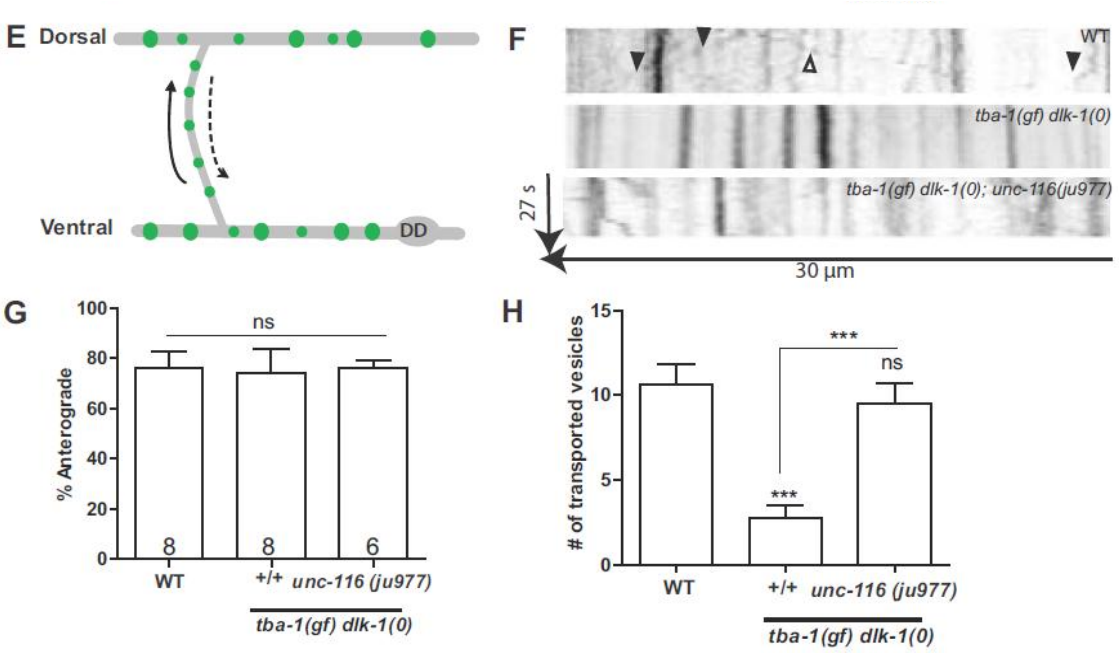

Figure 2.7 (continued) *unc-116(gf)* increases MT binding affinity to promote synaptic vesicle transport

(A) Prediction of the motor head of *C. elegans* UNC-116 (8-358aa) modeled on SWISS-MODEL and rendered using PyMOL.. (B) Rescue of DD remodeling defects of *tba-1(gf) dlk-1(0)* animals by transgenes expressing UNC-116(E273A). No rescue was observed with wild type kinesin-1 transgenes. Data are represented as mean ± SEM; n=30 animals per genotype. Statistics- One way ANOVA followed by Tukey's posttest; ***p<0.001; ns-not significant. (C-D) Images and quantification of D neuron synapses in the VNC of *unc-104(lf), unc-104(lf); unc-116(ju972)* and *unc-104(lf); unc-116(ju977)* animals expressing *juIs1* (P_{unc-25}-SNB-1::GFP). White asterisks represent DD and VD cell bodies, white arrows indicate synapses. Scale bar: 10 µm. Statistics - unpaired t-test; ***p<0.001. (E) Schematic of bidirectional synaptic vesicle transport along the commissure during DD remodeling. Solid arrow represents the anterograde direction, *i.e,* towards the DNC. (F) Representative kymographs of synaptic vesicle transport along the DD commissure. Solid arrowheads indicate vesicles moving in the anterograde direction, and open arrowheads indicate vesicles moving in the retrograde direction. Vertical lines on the kymographs represent stationary puncta and also indicate intensity differences of SNB-1::GFP along the commissure. (G, H) Quantification of (G) direction of movement and (H) number of mobile vesicles during DD remodeling.

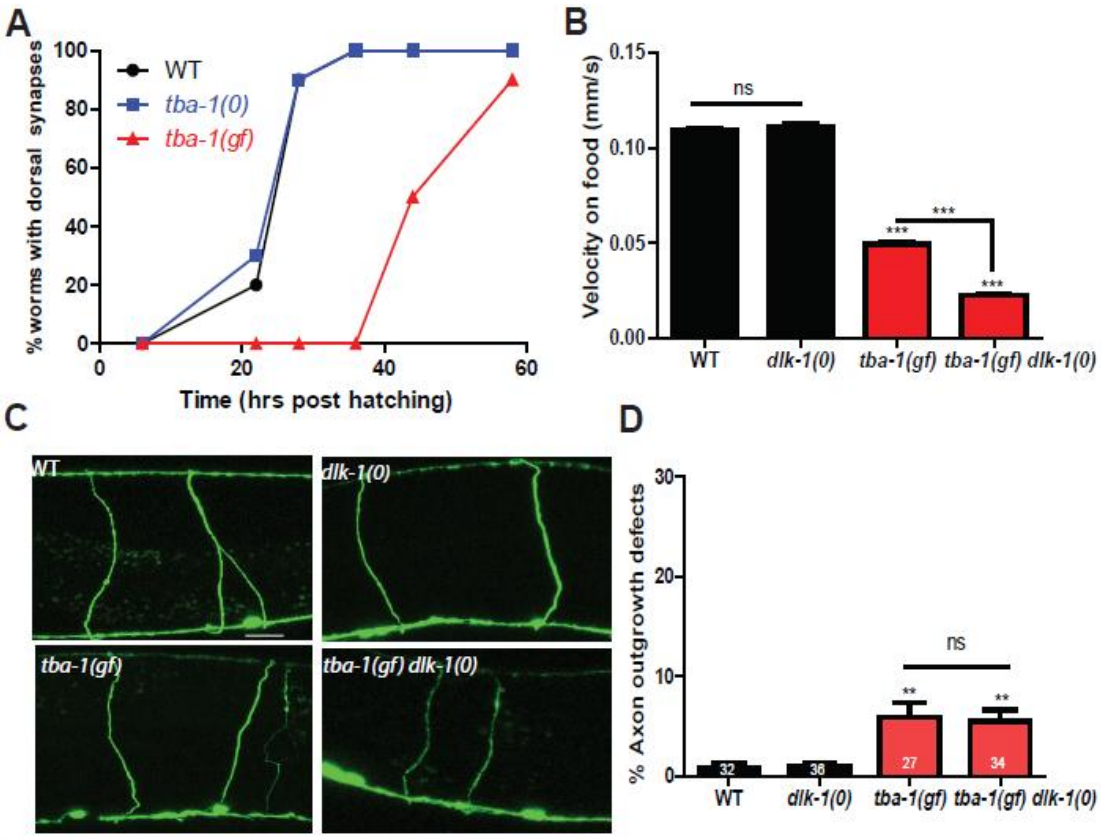

Figure 2.S1 Related to Figure 2.1

(A) Remodeling time in WT, *tba-1(0)* and *tba-1(gf)* animals; n=10 animals per genotype per time point. (B) Quantification of the locomotion velocity of WT, *dlk-1(0)*, *tba-1(gf)* and *tba-1(gf) dlk-1(0)* animals on food. Data are mean ± SEM; n=10 animals for each genotype. Statistics: One-way ANOVA followed by Tukey's posttest; ***p<0.001, ns-not significant. (C) Images of axon morphology in WT, *dlk-1(0)*, *tba-1(gf)* and *tba-1(gf) dlk-1(0)* animals using Punc-25-GFP (*juIs76*). Scale bar: 10 µm. (D)Quantification of axon outgrowth defects (gaps in the axons and commissure branching defects) in WT, *dlk-1(0)*, *tba-1(gf)* and *tba-1(gf) dlk-1(0)* animals. Data are represented as mean ± SEM; n>27 animals per genotype. Statistics – One-way ANOVA followed by Tukey's posttest; **p<0.01, ns-not significant. (E) Bright field image of a *tba-1(0)* animal, along with images of synapses in the dorsal cord of wild type and *tba-1(0)* using *juIs137* (Pflp-13-SNB-1::GFP). Scale bars- bright field: 200 µm and *juIs137*: 10 µm. (F) Bright field image of a *tba-1(0) dlk-1(0)* animal, along with images of synapses in the dorsal cord of wild type and *tba-1(0) dlk-1(0)* using *juIs1* (Punc-25-SNB-1::GFP). Scale bars- bright field: 200 µm and *juIs1*: 10 µm. (G) Images of the DNC and VNC of WT and *tba-1(gf)dlk-1(0)* animals expressing P*unc-25* -SAD-1::GFP and P*unc-25* -mCherry::RAB-3 in the GABAergic D neurons, and UNC-49::GFP in body wall muscles . Scale bar: 10 µm.

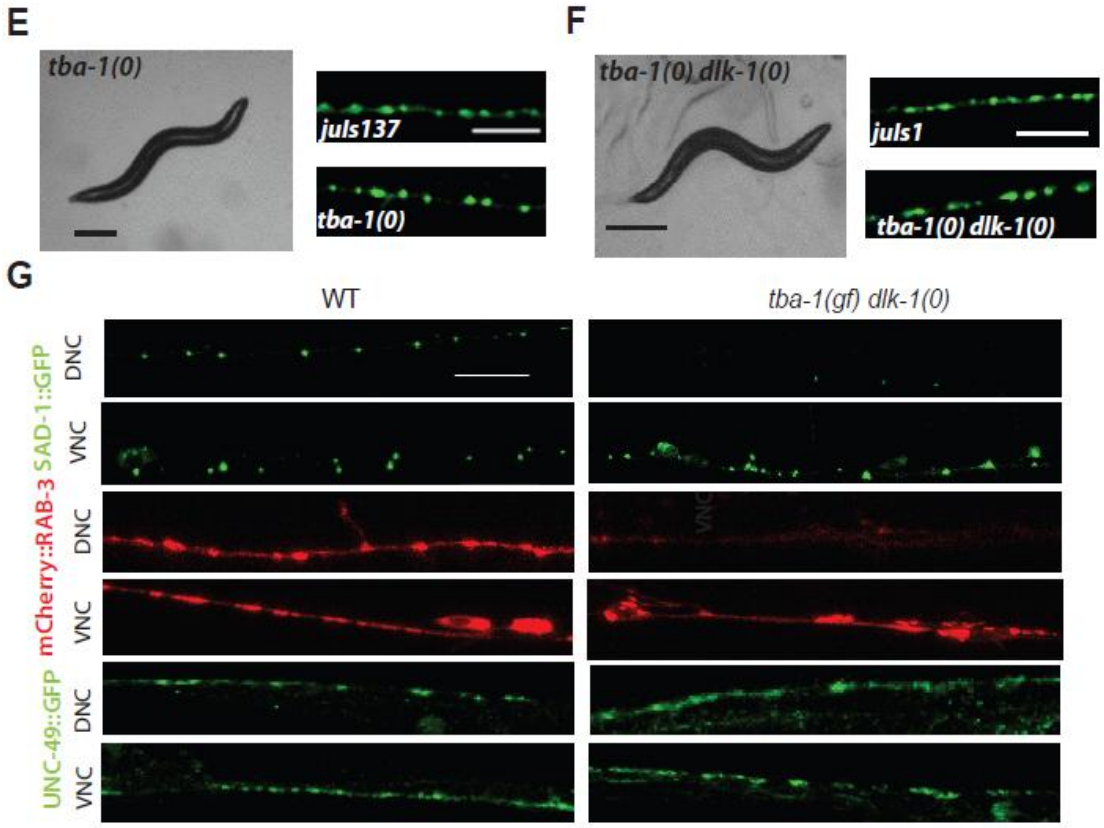

Figure 2.S1(continued) Related to Figure 2.1

(A) Remodeling time in WT, *tba-1(0)* and *tba-1(gf)* animals; n=10 animals per genotype per time point. (B) Quantification of the locomotion velocity of WT, *dlk-1(0)*, *tba-1(gf)* and *tba-1(gf) dlk-1(0)* animals on food. Data are mean ± SEM; n=10 animals for each genotype. Statistics: One-way ANOVA followed by Tukey's posttest; ***p<0.001, ns-not significant. (C) Images of axon morphology in WT, *dlk-1(0)*, *tba-1(gf)* and *tba-1(gf) dlk-1(0)* animals using Punc-25-GFP (*juIs76*). Scale bar: 10 µm. (D)Quantification of axon outgrowth defects (gaps in the axons and commissure branching defects) in WT, *dlk-1(0)*, *tba-1(gf)* and *tba-1(gf) dlk-1(0)* animals. Data are represented as mean ± SEM; n>27 animals per genotype. Statistics – One-way ANOVA followed by Tukey's posttest; **p<0.01, ns-not significant. (E) Bright field image of a *tba-1(0)* animal, along with images of synapses in the dorsal cord of wild type and *tba-1(0)* using *juIs137* (Pflp-13-SNB-1::GFP). Scale bars- bright field: 200 µm and *juIs137*: 10 µm. (F) Bright field image of a *tba-1(0) dlk-1(0)* animal, along with images of synapses in the dorsal cord of wild type and *tba-1(0) dlk-1(0)* using *juIs1* (Punc-25-SNB-1::GFP). Scale bars- bright field: 200 µm and *juIs1*: 10 µm. (G) Images of the DNC and VNC of WT and *tba-1(gf)dlk-1(0)* animals expressing P*unc-25* -SAD-1::GFP and P*unc-25* -mCherry::RAB-3 in the GABAergic D neurons, and UNC-49::GFP in body wall muscles . Scale bar: 10 µm.

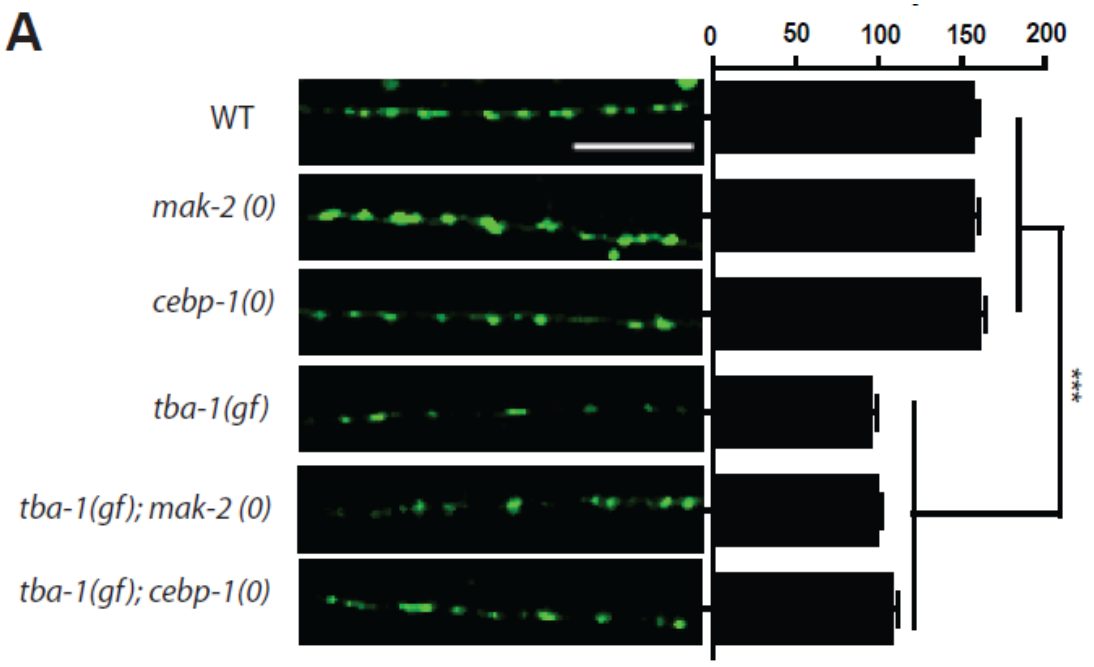

Figure 2.S2 Related to Figure 2.3

(A) (left) Images of DNC synapses of WT, *mak-2(0)*, *cebp-1(0)*, *tba-1(gf)*, *tba-1(gf); mak-2(0)* and *tba-1(gf); cebp-1(0)* adult animals using *juIs1* (Punc-25-SNB-1::GFP). Scale bar: 10 μm. (right) Quantification of DNC synapses. ***p<0.001.

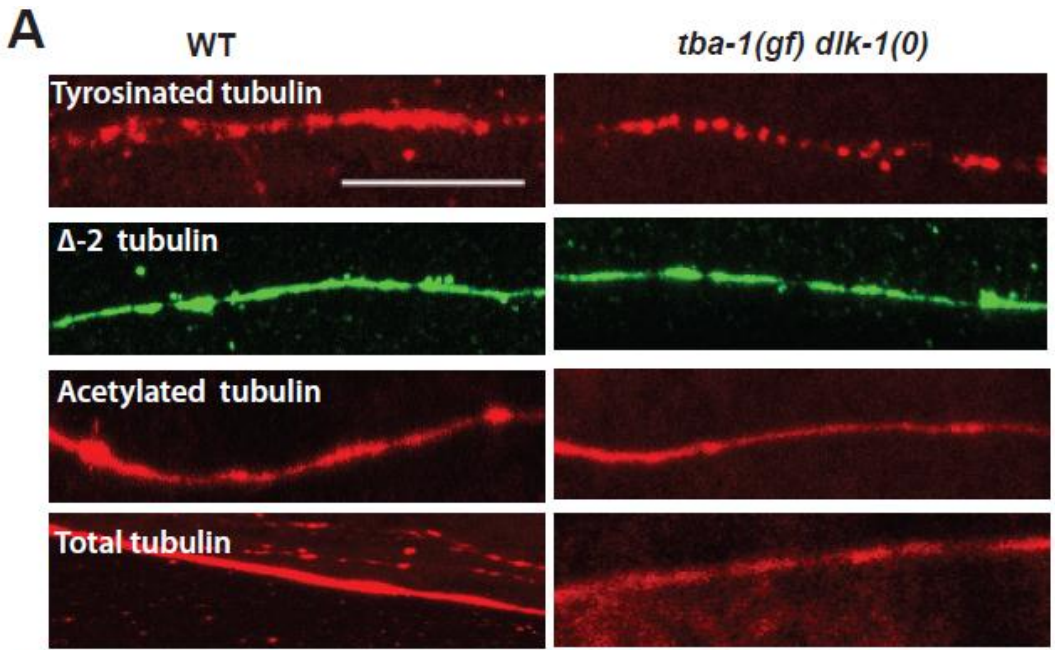

Figure 2.S3 Related to Figure 2.4

(A) Representative images of tyrosinated tubulin, Δ-2 tubulin, acetylated tubulin and total tubulin immunostaining in the VNC of WT and *tba-1(gf) dlk-1(0)* animals. Scale bar: 10 µm. (B-E) Quantification of (B) Tyrosinated, (C) Δ-2 tubulin, (D) Acetylated tubulin and (E) Total tubulin levels by immunostaining. Data are mean ± SEM; n=10 animals per genotype. Statistics: unpaired t-test; ns - not significant.

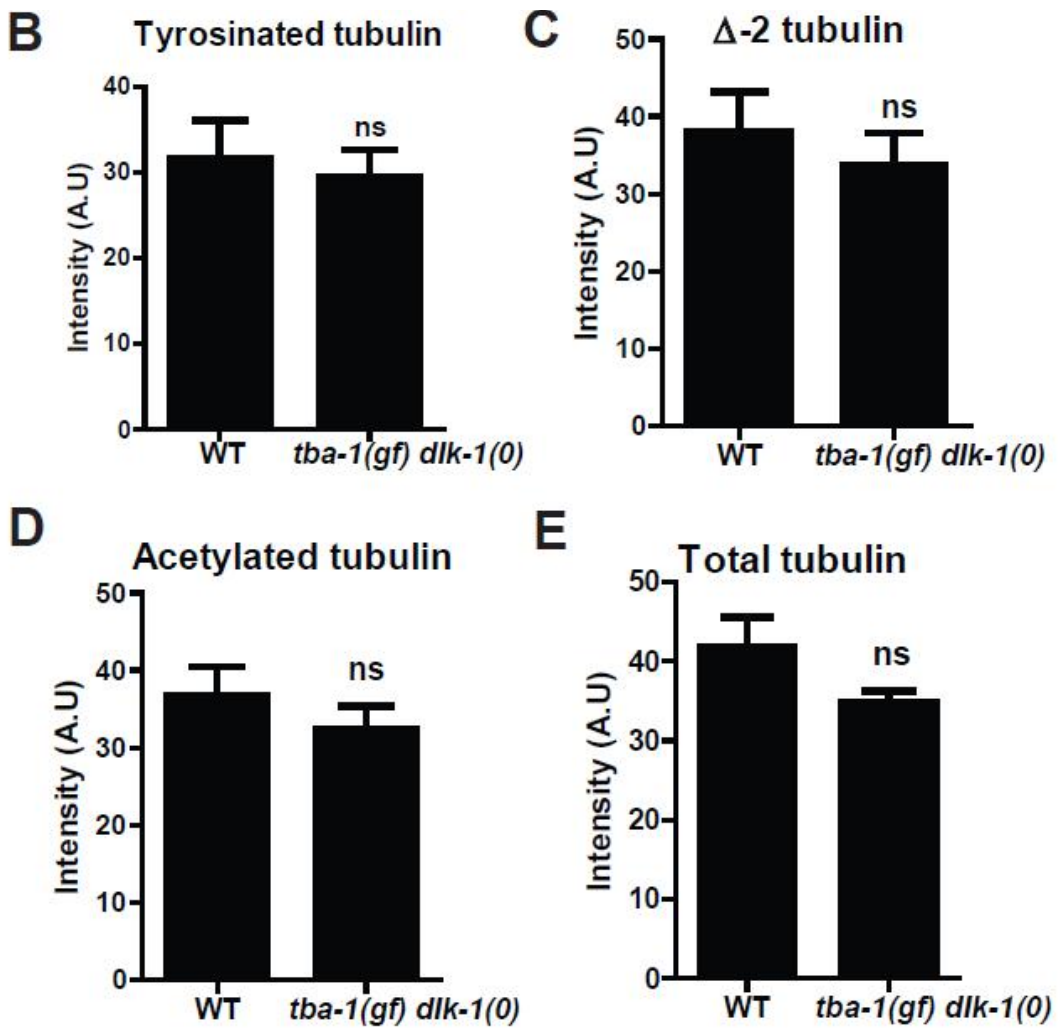

Figure 2.S3 (continued) Related to Figure 2.4

(A) Representative images of tyrosinated tubulin, Δ-2 tubulin, acetylated tubulin and total tubulin immunostaining in the VNC of WT and *tba-1(gf) dlk-1(0)* animals. Scale bar: 10 μm. (B-E) Quantification of (B) Tyrosinated, (C) Δ-2 tubulin, (D) Acetylated tubulin and (E) Total tubulin levels by immunostaining. Data are mean ± SEM; n=10 animals per genotype. Statistics: unpaired t-test; ns - not significant.

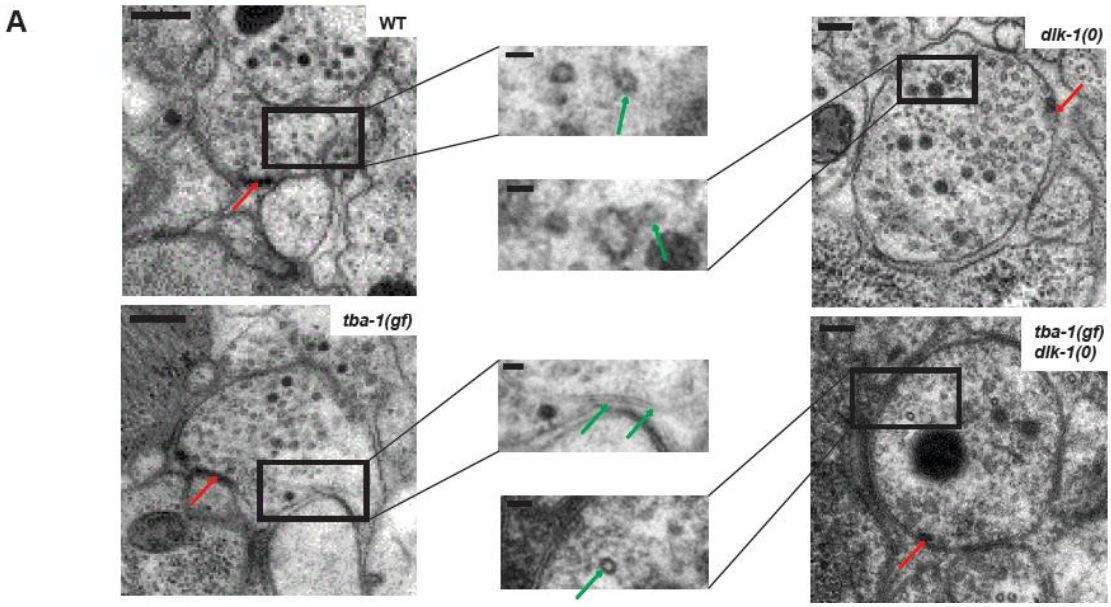

Figure 2.S4 Related to Figure 2.4

(A) EM sections of synaptic boutons of DD neurons. Red arrowheads indicate active zones and green arrowheads indicate MTs. Scale bar (top left): 200 nm (main), 50 nm (enlarged). (B, C) Quantification of the number of normal (perpendicular to the plane of the section) and misoriented (parallel to the plane of the section) MTs per section in the axonal (B) region and synaptic (C) region of the DD neuron. Data are represented as mean ± SEM; number of sections is indicated on each bar graph. Statistics- 2-Way ANOVA followed by Bonferroni posttest; ***p<0.001, when compared to WT. (D) Images of EBP-2-GFP expression in the VNC of WT and *tba-1(gf) dlk-1(0)* animals. White asterisks on DD and VD cell bodies. Scale bar: 10 μm. (E) Quantification of EBP-2::GFP intensity in the VNC of WT and *tba-1(gf) dlk-1(0)* animals. Statistics: unpaired t-test; data not significant. (F) Schematic representation of EBP-2 tracks in the commissures of adult D neurons. (G) Kymographs of adult WT and *tba-1(gf) dlk-1(0)* D neuron commissures. (H, I) Quantification of (H) direction of movement and (I) number of EBP-2 tracks. Data are represented as mean ± SEM; number of animals for each genotype is represented on (H). Statistics: One-Way ANOVA followed by Tukey's posttest; *p<0.05, ns- not significant.

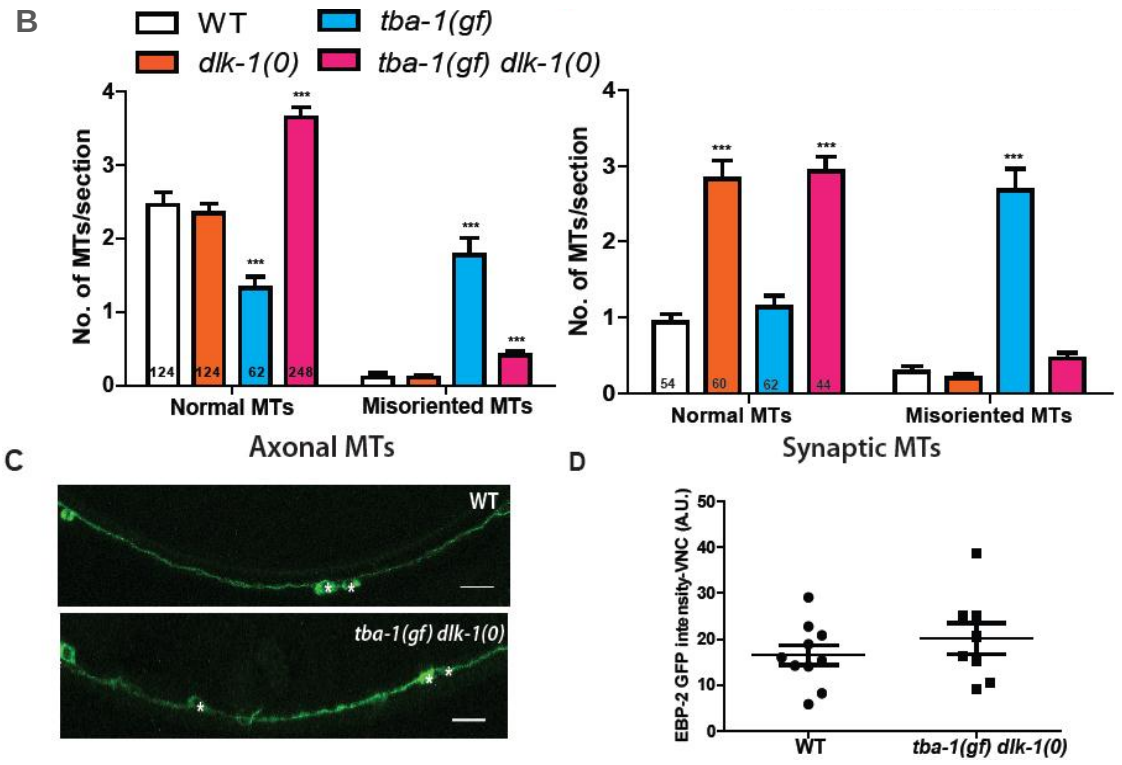

Figure 2.S4 (continued) Related to Figure 2.4

(A) EM sections of synaptic boutons of DD neurons. Red arrowheads indicate active zones and green arrowheads indicate MTs. Scale bar (top left): 200 nm (main), 50 nm (enlarged). (B, C) Quantification of the number of normal (perpendicular to the plane of the section) and misoriented (parallel to the plane of the section) MTs per section in the axonal (B) region and synaptic (C) region of the DD neuron. Data are represented as mean ± SEM; number of sections is indicated on each bar graph. Statistics- 2-Way ANOVA followed by Bonferroni posttest; ***p<0.001, when compared to WT. (D) Images of EBP-2-GFP expression in the VNC of WT and *tba-1(gf) dlk-1(0)* animals. White asterisks on DD and VD cell bodies. Scale bar: 10 μm. (E) Quantification of EBP-2::GFP intensity in the VNC of WT and *tba-1(gf) dlk-1(0)* animals. Statistics: unpaired t-test; data not significant. (F) Schematic representation of EBP-2 tracks in the commissures of adult D neurons. (G) Kymographs of adult WT and *tba-1(gf) dlk-1(0)* D neuron commissures. (H, I) Quantification of (H) direction of movement and (I) number of EBP-2 tracks. Data are represented as mean ± SEM; number of animals for each genotype is represented on (H). Statistics: One-Way ANOVA followed by Tukey's posttest; *p<0.05, ns- not significant.

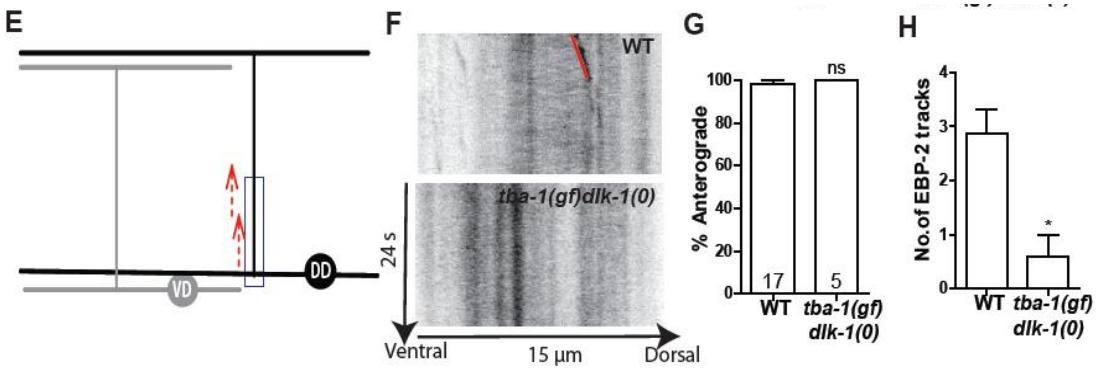

Figure 2.S4 (continued) Related to Figure 2.4

(A) EM sections of synaptic boutons of DD neurons. Red arrowheads indicate active zones and green arrowheads indicate MTs. Scale bar (top left): 200 nm (main), 50 nm (enlarged). (B, C) Quantification of the number of normal (perpendicular to the plane of the section) and misoriented (parallel to the plane of the section) MTs per section in the axonal (B) region and synaptic (C) region of the DD neuron. Data are represented as mean ± SEM; number of sections is indicated on each bar graph. Statistics- 2-Way ANOVA followed by Bonferroni posttest; ***p<0.001, when compared to WT. (D) Images of EBP-2-GFP expression in the VNC of WT and *tba-1(gf) dlk-1(0)* animals. White asterisks on DD and VD cell bodies. Scale bar: 10 µm. (E) Quantification of EBP-2::GFP intensity in the VNC of WT and *tba-1(gf) dlk-1(0)* animals. Statistics: unpaired t-test; data not significant. (F) Schematic representation of EBP-2 tracks in the commissures of adult D neurons. (G) Kymographs of adult WT and *tba-1(gf) dlk-1(0)* D neuron commissures. (H, I) Quantification of (H) direction of movement and (I) number of EBP-2 tracks. Data are represented as mean ± SEM; number of animals for each genotype is represented on (H). Statistics: One-Way ANOVA followed by Tukey's posttest; *p<0.05, ns- not significant.

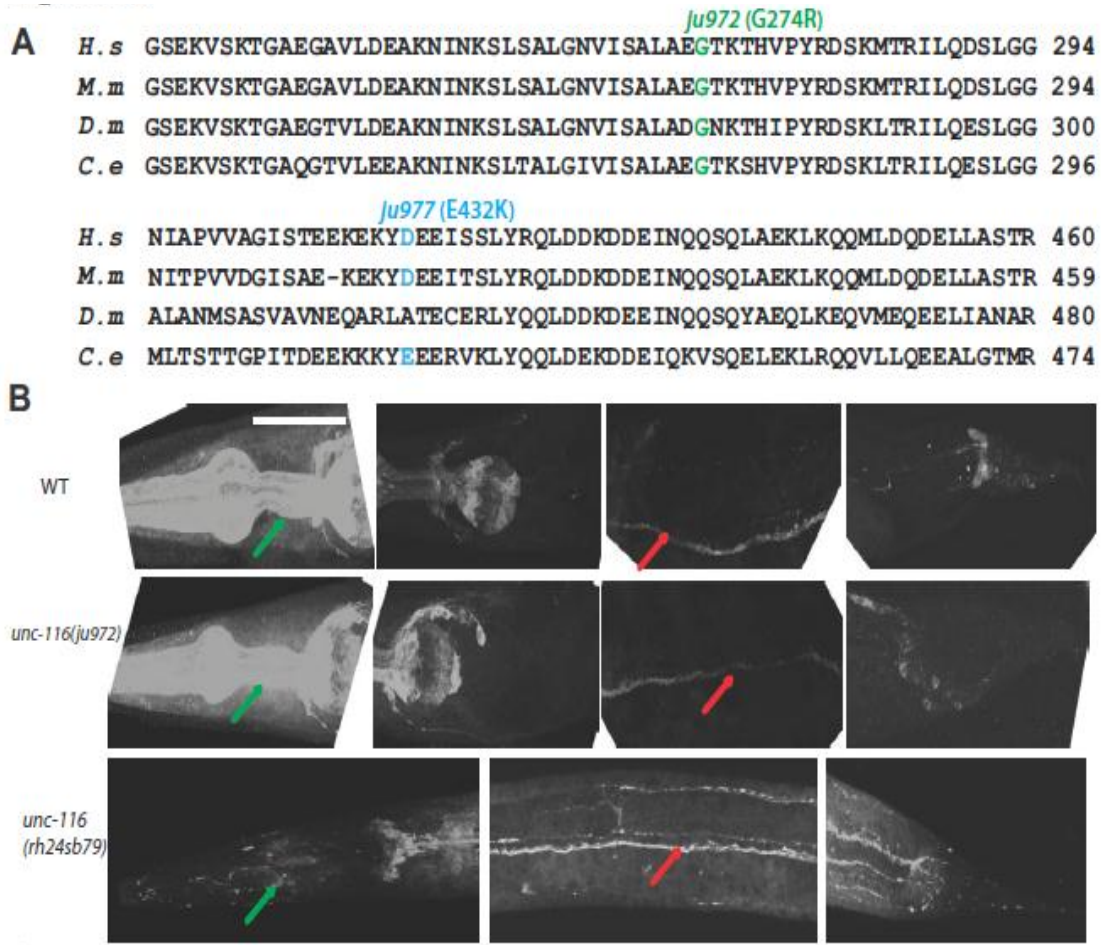

Figure 2.S5 Related to Figure 2.6

(A) Alignment of UNC-116 protein in *C. elegans (C.e)*, *Drosophila (D.m)*, mouse (*M.m*) and human (*H.s*) homologs; G274R (green) - *ju972*, E432K (blue) - *ju977*. (B) Images of wild type, *unc-116* animals (*ju972*, *rh24sb79*) stained using an antibody against the C-terminal of UNC-116. Green arrows point to pharyngeal staining and red arrows point to staining along the VNC. Scale bar: 50 µm (C) Representative kymographs of EBP-2 movement in the adult VNC of WT, *tba-1(gf) dlk-1(0)* and *tba-1(gf) dlk-1(0); unc-116(gf)* animals. Red line indicates a single EBP-2::GFP track moving in the anterograde direction. Vertical lines on the kymographs are caused by intensity differences of EBP-2::GFP along the VNC. (D, E) Quantification of (D) direction of movement and (E) number of EBP-2 tracks in WT, *tba-1(gf) dlk-1(0)* and *tba-1(gf) dlk-1(0); unc-116(ju972)* adults. Data are mean ± SEM; number of animals is depicted on (c). Statistics- One way ANOVA followed by Tukey's posttest; ***$p<0.001$, ns-not significant.

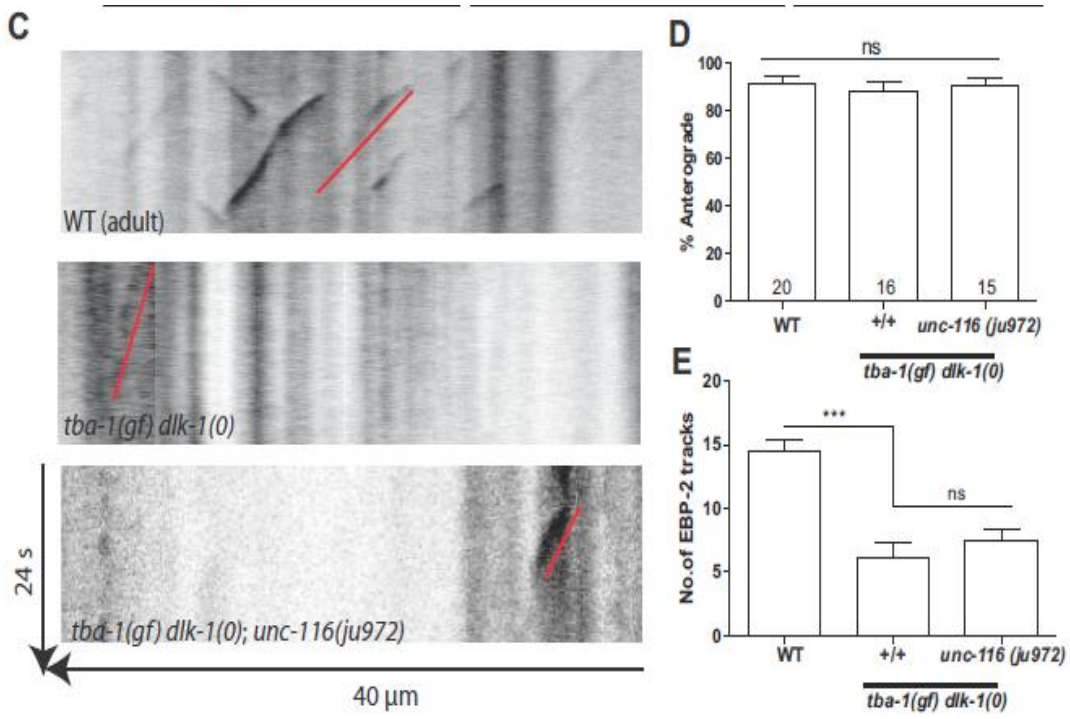

Figure 2.S5 (continued) Related to Figure 2.6

(A) Alignment of UNC-116 protein in *C. elegans (C.e)*, *Drosophila (D.m)*, mouse (*M.m*) and human (*H.s*) homologs; G274R (green) - *ju972*, E432K (blue) - *ju977*. (B) Images of wild type, *unc-116* animals (*ju972*, *rh24sb79*) stained using an antibody against the C-terminal of UNC-116. Green arrows point to pharyngeal staining and red arrows point to staining along the VNC. Scale bar: 50 µm (C) Representative kymographs of EBP-2 movement in the adult VNC of WT, *tba-1(gf) dlk-1(0)* and *tba-1(gf) dlk-1(0); unc-116(gf)* animals. Red line indicates a single EBP-2::GFP track moving in the anterograde direction. Vertical lines on the kymographs are caused by intensity differences of EBP-2::GFP along the VNC. (D, E) Quantification of (D) direction of movement and (E) number of EBP-2 tracks in WT, *tba-1(gf) dlk-1(0)* and *tba-1(gf) dlk-1(0); unc-116(ju972)* adults. Data are mean ± SEM; number of animals is depicted on (c). Statistics- One way ANOVA followed by Tukey's posttest; ***p<0.001, ns-not significant.

Table 2.1 List of strains used in this study

Strain	Genotype	Allele or Transgene
CZ333	*juIs1 IV*	*juIs1* [*Punc-25-SNB-1::GFP; lin-15(+)*] (Hallam & Jin, 1998)
CZ2569	*tba-1(ju89) I; juIs1 IV*	*ju89*: Gly414Arg (C1581T) (Baran et al., 2010)
CZ2060	*juIs137 II*	*juIs137* [*Pflp-13-$_{SNB}$-1::GFP; lin-15(+)*] (Sakaguchi-Nakashima et al., 2007)
CZ18652	*dlk-1(tm4024) I; juIs137 II*	
CZ2411	*tba-1(ju89) I; juIs137 II*	
CZ16989	*tba-1(ju89)dlk-1(tm4024) I; juIs137 II*	
CZ4152	*juIs76 II*	*juIs76* [*Punc-25-GFP; lin-15(+)*] (Huang et al., 2002)
CZ15941	*dlk-1(tm4024) I; juIs76 II*	
CZ14295	*tba-1(ju89) I; juIs76 II; juIs231*	*juIs231* [*Punc-25-mCherry::RAB-3; Pttx-3-RFP*] (Baran et al., 2010)
CZ16587	*tba-1(ju89)dlk-1(tm4024) I; juIs76 II*	
CZ20317	*tba-1(ok1135)I; juIs137 II*	*ok1135*: 1 kb deletion
CZ13936	*hpIs1 II; juIs231*	*hpIs1* [*Punc-25-SAD-1::GFP(L,S); lin-15(+)*] (Kim et al., 2010)
CZ14300	*tba-1(ju89)dlk-1(tm4024) I; hpIs1 II; juIs231*	
CZ21581	*juIs137 II; juEx6537*	*juEx6537* [*Punc-25-TBA-1; Pttx-3-GFP*]
CZ21584	*tba-1(ju89)dlk-1(tm4024) I; juIs137 II; juEx6537*	
CZ21587	*juIs137 II; juEx6540*	*juEx6540* [*Punc-25-DLK-1(minigene); Pttx-3-GFP*]

Table 2.1 (continued) List of strains used in this study

CZ21590	*tba-1(ju89)dlk-1(tm4024) I; juIs137 II; juEx6540*	
CZ3505	*juIs137 II; pmk-3(ok169) IV*	*ok169*: 1272bp deletion
CZ20316	*tba-1(ju89) I; juIs137 II; pmk-3(ok169) IV*	
CZ21574	*juIs1IV; cebp-1(tm2807)X*	*tm2807*: 479bp deletion
CZ15863	*tba-1(ju89)I; juIs1IV; cebp-1(tm2807)X*	
CZ8763	*mak-2(ok2394)juIs1IV*	*ok2394*: 878bp deletion
CZ19779	*tba-1(ju89)I; mak-2(ok2394)juIs1IV*	
CZ20219	*juIs137II; spas-1(ok1608)V*	*ok1608*:627bp deletion
CZ22154	*tba-1(ju89)I; juIs137II; spas-1(ok1608)V*	
CZ19774	*juIs137 II; oxEx1268*	*oxEx1268* [*Phsp-16.2-DLK-1::mCherry; Pmyo-2-GFP*] (Hammarlund et al., 2009)
CZ19775	*tba-1(ju89)dlk-1(tm4024) I; juIs137 II; oxEx1268*	
CZ20215	*tba-1(ju89) I*	
CZ15956	*dlk-1(tm4024) I*	
CZ16631	*tba-1(ju89)dlk-1(tm4024) I*	
CZ17824	*juEx5317*	*juEx5317* [*Punc-25-EBP-2::GFP; Pgcy-8-GFP*]
CZ20216	*dlk-1(tm4024) I; juEx5317*	
CZ20217	*tba-1(ju89) I; juEx5317*	
CZ20218	*tba-1(ju89)dlk-1(tm4024) I; juEx5317*	
CZ20615	*oxIs22*	*oxIs22* [*Punc-49::UNC-49-B::GFP; lin-15(+)*] (Bamber et al., 1999)
CZ18274	*tba-1(ju89)dlk-1(tm4024) I; oxIs22*	

Table 2.1 (continued) List of strains used in this study

CZ21928	*juIs137 II; klp-7(tm2143) III*	*tm2143*:875bp deletion
CZ21575	*tba-1(ju89) I; juIs137 II; klp-7(tm2143) III*	
CZ16994	*tba-1(ju89)dlk-1(tm4024) I;unc-116(ju972) III; juIs1 IV*	*ju972*: Gly274Arg (G1400A)
CZ16992	*tba-1(ju89)dlk-1(tm4024) I;unc-116(ju977) III; juIs1 IV*	*ju977*: Glu432Lys (G1921A)
CZ16634	*unc-116(ju977) III; juIs1 IV*	
CZ16629	*tba-1(ju89) I; unc-116(ju977) III; juIs1 IV*	
CZ16633	*unc-116(ju972) III; juIs1 IV*	
CZ16991	*tba-1(ju89) I; unc-116(ju972) III; juIs1 IV*	
CZ17360	*dlk-1(tm4024) I; unc-116(ju972) III; juIs1 IV*	
CZ4819	*unc-104(e1265) II; juIs1 IV*	*e1265*:Asp1541Asn (G4489A)
CZ21577	*unc-104(e1265) II; unc-116(ju972) III; juIs1 IV*	
CZ22740	*unc-104(e1265) II; unc-116(ju977) III; juIs1 IV*	
CZ21578	*tba-1(ju89)dlk-1(tm4024) I; unc-116(ju972) III; juEx5317*	
HR527	*unc-116(rh24sb79) III*	*rh24*: Ile302Met and Glu338Lys *sb79*: Gly45Glu (Yang, Mains & McNally, 2005)
CZ17826	*juIs1 IV; juEx5319*	*juEx5319* [*Punc-116-UNC-116(ju972); Pmyo-2-mCherry*]
CZ18277	*tba-1(ju89)dlk-1(tm4024) I; juIs1 IV; juEx5459*	*juEx5459* [*Punc-116-UNC-116(ju977); Pgcy-8-GFP*]

Table 2.1 (continued) List of strains used in this study

CZ18280	*tba-1(ju89)dlk-1(tm4024) I; juIs1 IV; juEx5462*	*juEx5462* [*Punc-116-UNC-116(ju972); Pgcy-8-GFP*]
CZ19771	*tba-1(ju89)dlk-1(tm4024) I; juIs1 IV; juEx5992*	*juEx5992* [*Prgef-1-UNC-116(E273A); Pgcy-8-GFP*]
CZ20319	*tba-1(ju89)dlk-1(tm4024) I; unc-116(ju972) III; juIs1 IV; juEx6179*	*juEx6179* [*Fosmid-WRM06276D08; Pgcy-8-GFP*]
CZ20322	*tba-1(ju89)dlk-1(tm4024) I; unc-116(ju977) III; juis1 IV; juEx6182*	*juEx6182* [*Fosmid-WRM06276D08; Pgcy-8-GFP*]
CZ21925	*tba-1(ju89)dlk-1(tm4024) I;unc-116(ju972) III; juIs1 IV; juEx6624*	*juEx6624* [*Prgef-UNC-116; Pgcy-8-GFP*]

Table 2.2: List of constructs used in this study

Plasmid	Description	Transgenes generated
pCZGY2332	Punc-25 (2kb promoter)-EBP-2 cDNA-mGFP-unc-54 3'UTR	*juEx5317, juEx5318*
pCZGY2626	Punc-116 (2kb promoter)-unc-116 genomic DNA with G274R-unc-54 3'UTR	*juEx5319, juEx5462-5464*
pCZGY2627	Punc-116 (2kb promoter)-unc-116 genomic DNA with E432K-unc-54 3'UTR	*juEx5640-5642*
pCZGY2628	Punc-25 (2kb promoter)-dlk-1 minigene-unc-54 3'UTR	*juEx6540-6542*
pCZGY2630	Punc-25 (2kb promoter)-tba-1 genomic DNA-unc-54 3'UTR	*juEx6537-6539*
pCZGY2633	Prgef-1 (3.5kb promoter)-unc-116 genomic DNA-unc-54 3'UTR	*juEx6624-6626*
pCZGY2634	Prgef-1 (3.5kb promoter)-unc-116 genomic DNA with E273A-unc-54 3'UTR	*juEx5992-5994*

References

Bamber, B. A., Beg, A. A., Twyman, R. E., & Jorgensen, E. M. (1999). The *Caenorhabditis elegans unc-49* locus encodes multiple subunits of a hetero-multimeric GABA Receptor. *J. Neurosci., 19,* 5348-5359.

Baran, R., Castelblanco, L., Tang, G., Shapiro, I., Goncharov, A., & Jin, Y. (2010). Motor neuron synapse and axon defects in a *C. elegans* alpha-tubulin mutant. *PloS one, 5*:e9655.

Bechstedt, S., & Brouhard, G. J. (2012). Doublecortin recognizes the 13-protofilament microtubule cooperatively and tracks microtubule ends. *Developmental cell, 23,* 181-92.

Bigelow, H., Doitsidou, M., Sarin, S., & Hobert, O. (2009). MAQGene: software to facilitate *C. elegans* mutant genome sequence analysis. *Nature methods, 6,* 549.

Bounoutas, A., Kratz, J., Emtage, L., Ma, C., Nguyen, K. C., & Chalfie, M. (2011). Microtubule depolymerization in *Caenorhabditis elegans* touch receptor neurons reduces gene expression through a p38 MAPK pathway. *Proceedings of the National Academy of Sceinces, 108,* 3982-3987.

Brenner, S. (1974). The genetics of *Caenorhabditis elegans. Genetics, 77,* 71–94.

Byrd, D. T., Kawasaki, M., Walcoff, M., Hisamoto, N., Matsumoto, K., & Jin, Y. (2001). UNC-16, a JNK-signaling scaffold protein, regulates vesicle transport in *C . elegans*. *Neuron, 32,* 787-800.

Cai, Q., Pan, P. Y., & Sheng, Z. H. (2007). Syntabulin-kinesin-1 family member 5B-mediated axonal transport contributes to activity-dependent presynaptic assembly. *J. Neurosci., 27,* 7284-96.

Chalfie, M., & Thomson, J. N. (1982). Structural and functional diversity in the neuronal microtubules of *Caenorhabditis elegans*. *The Journal of cell biology, 93,* 15-23.

Cheng, L., Desai, J., Miranda, C. J., Duncan, J. S., Qiu, W., Nugent, A. A., Kolpak, A. L., Wu, C. C., Drokhlyansky, E., Delisle, M. M., Chan, W-M., Wei, Y., Propst, F., Reck-Peterson, S. L., & Fritzsch, B. (2014). Human CFEOM1 mutations attenuate KIF21A autoinhibition and cause oculomotor axon stalling. *Neuron, 82,* 334-349.

Cho, Y., and Cavalli, V.(2012). HDAC5 is a novel injury-regulated tubulin deacetylase controlling axon regeneration. *EMBO Journal, 31,* 3063-78.

Conde, C., & Cáceres, A. (2009). Microtubule assembly, organization and dynamics in axons and dendrites. *Nature reviews Neuroscience, 10,* 319-32.

Destexhe, A., & Marder, E. (2004). Plasticity in single neuron and circuit computations. *Nature, 431,* 789-795.

Finney, M., & Ruvkun, G. (1990). The *unc-86* gene product couples cell lineage and cell identity in *C. elegans*. *Cell, 63,* 895-905.

Ghosh-Roy, A., Goncharov, A., Jin, Y., & Chisholm, A. D. (2012). Kinesin-13 and tubulin

posttranslational modifications regulate microtubule growth in axon regeneration. *Developmental cell*, *23*, 716-28.

Grummt, M., Henningsen, U., Fuchs, S., Schleicher, M., & Schliwa, M. (1998). Importance of a flexible hinge near the motor domain in kinesin-driven motility. *The EMBO Journal*, *17*, 5536-5542.

Hall, D. H., & Hedgecock, E. M. (1996). Kinesin-Related Gene unc-104 is required for axonal transport of synaptic vesicles in *C . elegans*. *Cell*, *65*, 837-847.

Hallam, S.J. & Jin, Y. (1998) *lin-14* regulates the timing of synaptic remodeling in *Caenorhabditis elegans*. *Nature, 395*, 644-647.

Hammarlund, M., Nix, P., Hauth, L., Jorgensen, E.M., & Bastiani, M. (2009). Axon regeneration requires a conserved MAP Kinase Pathway. *Science, 323*, 802-806.

Harris, K. M., & Weinberg, R. J. (2012). Ultrastructure of synapses in the mammalian brain. *Cold Spring Harbor Perspectives in Biology*, *4:a005587*.

Hensch, T. K. (2004). Critical period regulation. *Annual review of neuroscience*, *27*, 549-79.

Hirokawa, N., Noda, Y., Tanaka, Y., & Niwa, S. (2009). Kinesin superfamily motor proteins and intracellular transport. *Nature reviews. Molecular cell biology*, *10*, 682-696.

Hsu, J-M, Chen, C-H, Chen, Y-C, Mcdonald, K. L., Gurling, M., Lee, A., Garriga, G., & Pan, C-L. (2014). Genetic analysis of a novel Tubulin mutation that redirects synaptic vesicle targeting and causes neurite degeneration in *C . elegans*. *PLoS genetics*, *10*, e1004715.

Houtman, S. H., Rutteman, M., & Zeeuw, C. I. D. E. (2007). Echinoderm microtubule associated protein like protein 4, a member of the echinoderm microtubule associated protein family, stabilizes microtubules. *Neuroscience*, *144*, 1373-1382.

Huang, X., Cheng, H.J, Tessier-lavigne, M., & Jin, Y. (2002). MAX-1, a Novel PH / MyTH4 / FERM domain cytoplasmic protein implicated in netrin- mediated axon repulsion. *Neuron*, *34*, 563-576.

Hummel, T., Krukkert, K., Roos, J., Davis, G.W., & Klambt, C.(2000). *Drosophila* Futsch / 22C10 is a MAP1B-like protein required for dendritic and axonal development. *Neuron*, *26*, 357-370.

Janke, C., & Bulinski, J. C. (2011). Post-translational regulation of the microtubule cytoskeleton: mechanisms and functions. *Nature reviews. Molecular cell biology*, *12*, 773-86.

Jaworski, J., Kapitein, L. C., Gouveia, S. M., Dortland, B. R., Wulf, P. S., Grigoriev, I., Camera, P., Spangler, S.A., Stefano, P.D., Demmers, J. Krugers, H., Defilippi, P., Akhmanova, A., Hoogenraad, C. C. (2009). Dynamic microtubules regulate dendritic spine morphology and synaptic plasticity. *Neuron*, *61*, 85-100.

Jin, Y., & Garner, C. C. (2008). Molecular mechanisms of presynaptic differentiation. *Annu. Rev. Cell Dev. Biol.*, *24*: 237-62.

Kim, J. S. M., Hung, W., Narbonne, P., Roy, R., & Zhen, M. (2010).*C. elegans* STRAD α and

SAD cooperatively regulate neuronal polarity and synaptic organization. *Development*, *102*, 93-102.

Klinedinst, S., Wang, X., Xiong, X., Haenfler, J. M., & Collins, C. A. (2013). Independent pathways downstream of the Wnd/DLK MAPKKK regulate synaptic structure, axonal transport, and injury signaling. *J. Neurosci.*, *33*, 12764-78.

Kozielski, F., Sack, S., Marx, A., Thormahlen, M., Schonbrunn, E., Biou, V., Thompson, A.,Mandelkow, E.M. & Mandelkow, E. (1997). The crystal structure of dimeric kinesin and implications formicrotubule-dependent motility. *Cell*, *91*, 985-994.

Maurer, S. P., Bieling, P., Cope, J., Hoenger, A., & Surrey, T. (2011). GTPγS microtubules mimic the growing microtubule end structure recognized by end-binding proteins (EBs). *Proceedings of the National Academy of Sciences*, *108*, 3988–3993.

McNally, K.L., Martin, J.L., Ellefson, M., & McNally, F.J. (2010). Kinesin dependent transport results in polarized migration of the nucleus in oocytes and inward movement of yolk granules in meiotic embryos. *Dev. Biol.*, *339*,126–140.

McAllister A.K. (2007). Dynamic aspects of CNS synapse formation. *Annu. Rev. Neurosci. 30*: 425–50.

Mello, C. C., Kramer, J. M., Stinchcomb, D., & Ambros, V. (1991). Efficient gene transfer in *C. elegans*: extrachromosomal maintenance and integration of transforming sequences. *The EMBO Journal*, *10*, 3959-3970.

Mimori-Kiyosue, Y., Shiina, N., & Tsukita, S. (2000). The dynamic behavior of the APC-binding protein EB1 on the distal ends of microtubules. *Current biology*, *10*, 865-8.

Moores, C. A., Francis, F., Chelly, J., Houdusse, A., Milligan, R. A., Jolla, L., Mentaux, R., & Saint, F. (2004). Mechanism of microtubule stabilization by doublecortin. *Molecular Cell*, *14*, 833-839.

Nahm, M., Lee, M-J., Parkinson, W., Lee, M., Kim, H., Kim, Y-J., Kim, S., Cho, Y. S., Min, B-M., Bae, Y. C., Broadie, K., & Lee, S. (2013). Spartin regulates synaptic growth and neuronal survival by inhibiting BMP mediated microtubule stabilization. *Neuron*, *77*, 680-695.

Nakata, K., Abrams, B., Grill, B., Goncharov, A., Huang, X., Chisholm, A. D., & Jin, Y. (2005). Regulation of a DLK-1 and p38 MAP kinase pathway by the ubiquitin ligase RPM-1 is required for presynaptic development. *Cell*, *120*, 407-20.

Nakata, T., & Hirokawa, N. (2003). Microtubules provide directional cues for polarized axonal transport through interaction with kinesin motor head. *The Journal of cell biology*, *162*, 1045-55.

Park, M., Watanabe, S., Poon, V. Y. N., Ou, C.Y., Jorgensen, E. M., & Shen, K. (2011). CYY-1/cyclin Y and CDK-5 differentially regulate synapse elimination and formation for rewiring neural circuits. *Neuron*, *70*, 742-57.

Puthanveettil, S. V., Monje, F. J., Miniaci, M. C., Choi, Y.-beom, Karl, K. A., Khandros, E., Gawinowicz, M. A., Sheetz, M. P. & Kandel, E. R. (2008). A new component in synaptic

plasticity : upregulation of Kinesin in the neurons of the gill-withdrawal reflex. *Cell*, *135*, 960-973.

Roll-Mecak, A., & Mcnally, F. J. (2010). Microtubule-severing enzymes. *Current Opinion in Cell Biology*, *22*, 96-103.

Roos, J., Hummel, T., Ng, N., Klambt, C. & Davis, G. W. (2000). *Drosophila* Futsch regulates synaptic microtubule organization and is necessary for synaptic Growth. *Neuron*, *26*, 371-382.

Rostaing, P., Weimer, R. M., Jorgensen, E. M., & Triller, A. (2004). Preservation of immunoreactivity and fine structure of adult *C. elegans* tissues using high-pressure freezing. *Journal of Histochemistry & Cytochemistry*, *52*, 1-12.

Sakaguchi-Nakashima, A., Meir, J. Y., Jin, Y., Matsumoto, K., & Hisamoto, N. (2007). LRK-1, a *C. elegans* PARK8-related kinase, regulates axonal-dendritic polarity of SV proteins. *Current biology*, *17*, 592-8.

Uchida, S., Martel, G., Pavlowsky, A., Takizawa, S., Hevi, C., Watanabe, Y., Kandel, E. R., Alarcon, J.M. & Shumyatsky, G. P. (2014). Learning-induced and stathmin-dependent changes in microtubule stability are critical for memory and disrupted in ageing. *Nature Communications*, *5*, 1-13.

Valakh, V., Walker, L. J., Skeath, J. B., & DiAntonio, A. (2013). Loss of the spectraplakin short stop activates the DLK injury response pathway in *Drosophila*. *J. Neurosci.*, *33*, 17863-73.

Welsbie, D. S., Yang, Z., Ge, Y., Mitchell, K. L., Zhou, X., Martin, S. E., Berlinicke, C. A., Hackler Jr., L., Fuller, J., Fu J., Cao, L. H., Han, B., Auld, D., Xue, T., Hirai, S. I., Germain, L., Simard-Bisson, C., Blouin, R., Nguyen, J. V., Davis, C-H. O., Enke, R. A., Boye, S. L., Merbs, S. L., Marsh-Armstrong, N., Hauswirth, W. W., Diantonio, A., Nickells, R. W., Inglese, J., Hanes, J., Yau, K-W., Quigley, H. A., Zack, D. J. (2013). Functional genomic screening identifies dual leucine zipper kinase as a key mediator of retinal ganglion cell death. *Proceedings of the National Academy of Sciences*, *110*, 4045-4050.

White, J. G., Albertson, D.G. & Anness, M.A.R. (1978). Connectivity changes in a class of motorneurons during the development of a nematode. *Nature*, *271*, 764-766.

White, J. G., Southgate, E., Thomson, J. N., & Brenner, S. (1986). The Structure of the Nervous System of the Nematode *Caenorhabditis elegans*. *Philosophical Transactions of the Royal Society B: Biological Sciences*, *314*, 1-340.

Woehlke, G., Ruby, a K., Hart, C. L., Ly, B., Hom-Booher, N., & Vale, R. D. (1997). Microtubule interaction site of the kinesin motor. *Cell*, *90*, 207-16.

Yan, D., & Jin, Y. (2012). Regulation of DLK-1 kinase activity by calcium-mediated dissociation from an inhibitory isoform. *Neuron*, *76*, 534-48.

Yan, D., Wu, Z., Chisholm, A. D., & Jin, Y. (2009). The DLK-1 kinase promotes mRNA stability and local translation in C. elegans synapses and axon regeneration. *Cell*, *138*, 1005-18.

Yan, J., Chao, D. L., Toba, S., Koyasako, K., Yasunaga, T., Hirotsune, S., & Shen, K. (2013). Kinesin-1 regulates dendrite microtubule polarity in *Caenorhabditis elegans*. *eLife, 2*, e00133-e00133.

Yang, H.Y., Mains, P. E., & McNally, F. J. (2005). Kinesin-1 mediates translocation of the meiotic spindle to the oocyte cortex through KCA-1, a novel cargo adapter. *JCB, 169*, 447-57.

Yi, H., Kaan, K., Hackney, D. D., & Kozielski, F. (2011). The structure of the kinesin-1 motor-tail complex reveals the mechanism of autoinhibition. *Science, 333*, 883-5.

Zhou, H. M., & Walthall, W. W. (1998) UNC-55, an orphan nuclear hormone receptor, orchestrates synaptic specificity among two classes of motor neurons in *Caenorhabditis elegans*. *J. Neurosci., 18*, 10438-44.

Chapter 3

Differential regulation of polarized synaptic vesicle trafficking and synapse stability in neural circuit rewiring in *Caenorhadbitis elegans*

Abstract

Neural circuits are dynamic, with activity-dependent changes in synapse density and connectivity peaking during different phases of animal development. In *C. elegans*, young larvae form mature motor circuits through a dramatic switch in GABAergic neuron connectivity, by concomitant elimination of existing synapses and formation of new synapses that are maintained throughout adulthood. We have previously shown that an increase in microtubule dynamics during motor circuit rewiring facilitates new synapse formation. Here, we further investigate cellular control of circuit rewiring through the analysis of mutants obtained in a forward genetic screen. Using live imaging, we characterize novel mutations that alter cargo binding in the dynein motor complex and enhance anterograde synaptic vesicle movement during remodeling, providing *in vivo* evidence for the tug-of-war between kinesin and dynein in fast axonal transport. We also find that a casein kinase homolog, TTBK-3, inhibits stabilization of nascent synapses in their new locations, a previously unexplored facet of structural plasticity of synapses. Our study delineates temporally distinct signaling pathways that are required for effective neural circuit refinement.

Introduction

Neurons communicate through synapses, necessitating a system of checks and balances to achieve precise patterns of synaptic connectivity that execute neural circuit function. Large scale axonal growth and pruning mediate synapse formation with appropriate targets during

development, shaping neuronal circuits during critical periods of plasticity (Hensch, 2004). Hyper- and hypo- connectivity in different brain regions is a widely observed phenomenon in children with autism spectrum disorders (ASDs) and related comorbid conditions (Ecker, 2016). Brain development defects during critical postnatal periods of plasticity are also thought to contribute to schizophrenia, which has a varying age of onset (Lewis & Levitt, 2002). Structural synaptic plasticity is not purely a developmental phenomenon-synapse remodeling occurs in both normal and diseased adult brains in various contexts (Holtmaat & Svoboda, 2009; Marc et al., 2003). The mechanisms underlying synapse assembly and elimination have thus been the subject of intense study for several decades, although a majority of experimental models focused on synaptic plasticity that is coupled to neurite outgrowth and retraction (Luo & O' Leary, 2005; Sanes & Litchman, 1999). With recent advances in *in vivo* imaging techniques, instances of synaptic rewiring that are independent of large scale neurite rearrangement have been identified in the mammalian central nervous system (Holtmaat &Svoboda, 2009; Hong et al., 2014). Elucidating the mechanisms underlying the cellular dynamics of such refinement, particularly in pre-synaptic terminals, is of general significance.

In the *C. elegans* locomotor circuit, a subset of type-D GABAergic motor neurons exhibits critical period synapse plasticity. Upon birth and in young larvae, the Dorsal D (DD) neurons initially form synapses with ventral body wall muscles. During an early developmental molt, these early synapses are disassembled, and new synapses are formed with dorsal body wall muscles, without overt changes in neuronal morphology (White, Albertson & Anness, 1978; Figure 3.1A). DD synapse remodeling is developmentally stereotyped, activity dependent, and uncoupled from neurite outgrowth, providing a tractable genetic framework to study the molecular mechanisms underlying structural synaptic plasticity. Numerous studies have provided insights into the conserved transcriptional programs that regulate the initiation of DD synapse remodeling and that maintain the temporal precision of synapse remodeling (reviewed in Kurup & Jin, 2016).

Once circuit connectivity changes have been initiated in the DD neurons, the cellular execution of synapse assembly and disassembly takes place. Pre-synaptic terminals are eliminated from the DD ventral neurite, following which synaptic vesicles are transported to the DD dorsal neurite where they assemble to form new synapses that are stable for the lifetime of the animal. Previous work from our lab and others has found that dynamic microtubules (MTs) are required for synaptic vesicle transport to DD dorsal neurite during remodeling (Kurup et al., 2015) and the patterning of new pre-synaptic terminals is achieved by the sequential action of anterograde and retrograde motors Kinesin-3/UNC-104 and dynein, respectively (Park et al., 2011). Synapse elimination from the DD ventral neurite is mediated in part by the cyclin Y homolog CYY-1 and the apoptotic cell death pathway (Meng et al., 2016; Park et al., 2011).

In this study, we characterized multiple mutants isolated from a genetic screen for genes involved in DD synapse remodeling. We performed this screen on a mutant strain containing a gain-of-function (*gf)* mutation of alpha-tubulin *tba-1*, and a loss-of-function (*0)* mutation of the conserved MAPKKK.*dlk-1*. This *tba-1(gf) dlk-1(0)* double mutant combination results in defective DD synapse remodeling due to a reduction in MT dynamics (Kurup et al., 2015). We identified mutations in the *C. elegans* α- and β-tubulin genes *tba-1* and *tbb-2* that reversed defects in MT architecture. We also show that novel mutations in the minus end directed motor dynein and its adaptor protein dynactin ameliorate defects in kinesin-mediated synaptic vesicle transport to the DD dorsal neurite during remodeling, highlighting the interdependence of the two motors even in cases of polarized cargo movement. We further find that a member of the casein kinase superfamily, TTBK-3, specifically acts after remodeling is complete to modulate nascent synapse stability on the dorsal neurite, a previously uncharacterized aspect of synaptic plasticity. Our observations indicate that the dynein motor complex and TTBK-3 act at distinct temporal windows to differentially regulate synapse rewiring.

Results

A forward genetic screen to identify novel regulators of DD synapse remodeling

A missense mutation in *C. elegans* α-tubulin, *tba-1(ju89)* (henceforth *tba-1(gf)*) results in a mild reduction in the synapse number of GABAergic motor neurons and a dampening of the amplitude of sinusoidal locomotion (Baran et al., 2010; Kurup et al., 2015; Figure 3.1B). In animals carrying both *tba-1(gf)* and a loss of function of the conserved MAPKKK DLK-1 (*dlk-1(0)*), DD remodeling is completely blocked such that the dorsal neurites contain almost no synapses, when visualized by the synaptic marker *juIs1* (P_{unc-25}-SNB-1-GFP) (Kurup et al., 2015; Figure 3.1B). Consistent with a lack of GABAergic innervation, *tba-1(gf) dlk-1(0)* double mutant animals are uncoordinated and coil dorsally when touched in the head (Kurup et al., 2015; Figure 3.1C). We performed a suppressor screen on *tba-1(gf) dlk-1(0); juIs1* animals, first based on behavioral improvement, then by visual examination of synapses in DD neurons. We mapped the suppressor mutations to various genetic loci using whole genome sequencing and subsequent recombinant mapping (see methods). Below, we report the characterization of these mutations.

Intragenic mutations of *tba-1* and a novel mutation of *tbb-2* ameliorate the activity of *tba-1(gf)*

tba-1(gf) alters a conserved glycine residue to arginine (G414R) in the C-terminal H11-12 loop of α-tubulin (Baran et al., 2010; Figure 3.S1). This C-terminal domain of α-tubulin is implicated in microtubule associated protein (MAP) binding (Nogales, Wolf & Downing, 1998), and the G414R mutation resulted in MTs that are misoriented at both synaptic and asynaptic sites along the axonal processes of DD neurons (Kurup et al., 2015). *tba-1(0)* null mutants appeared wild-type, presumably due to functional redundancy among the nine α-tubulin

homologs in *C .elegans* (Baran et al., 2010; Kurup et al., 2015). Double mutant animals of *tba-1(0)* and *dlk-1(0)* are also superficially normal, indicating that *tba-1(gf)* acts synergistically with *dlk-1(0)* to produce defective synapse remodeling (Kurup et al., 2015). We found eight mutants that fully suppressed the uncoordinated behavior of *tba-1(gf) dlk-1(0)* and were completely normal with regards to synapse formation and DD synapse remodeling. DNA sequence analyses *of tba-1* revealed that these suppressors contained additional mutations besides the *ju89* nucleotide change, and therefore were classified as intragenic revertants of *tba-1(gf)* (Figure 3.1C). Three suppressors (*ju964*, *ju966* and *ju975)* caused nonsense mutations at different amino acids of *tba-1* (Figure 3.1D; Table 3.1). This suggests that truncated versions of TBA-1 produced in these mutants were likely not functional. One missense mutation at the start codon ATG (*ju980*) also behaved similar to *tba-1(0),* with synapse formation and locomotion restored to normal in *tba-1(ju980 ju89) dlk-1(0)* animals (Figure 3.1B, D). The other four suppressors caused missense mutations at highly conserved regions of α-tubulin (Figure 3.1D, 3.S1; Table 3.1). Two missense mutations (*ju973* (L426F) and *ju987* (A419T)) were in H12 of the C-terminal domain, and could possibly have reversed the MAP binding defects caused by *tba-1(gf)* (Fig 1D and S1 Fig). Another missense mutation, *ju965* (S138L), was close to the GTP binding pocket of α-tubulin (Nogales, Wolf & Downing, 1998; Figure 3.1D, 3.S1). The last missense mutation, *ju962* (S285F), was in the intermediate domain of α-tubulin, reported to be necessary for binding of the MT stabilizing drug, taxol (Nogales, Wolf & Downing, 1998; Figure 3.1D, 3.S1). Mutations in the intermediate domain or the GTP binding pocket possibly prevented the incorporation of *tba-1* into MT polymers. While we cannot exclude the possibility that these mutations might also reduce TBA-1 protein levels, these results highlight the *in vivo* importance of specific residues within functional domains of α-tubulin.

The *C. elegans* genome encodes six β-tubulin genes that function partially redundantly in various tissues of the organism and at different developmental stages (Baugh et al., 2003; Gogonea et al., 1999; Lockhead et al., 2016; Lu, Srayko & Mains, 2004). We mapped the

suppressor *ju1535* to β-tubulin *tbb-2*, causing a conserved Proline305 to Serine change (P305S) in the intermediate domain, which lies in the internal surface of the MT polymer (Figure 3.1E, 3.S1). *tbb-2 (ju1535)* partially suppressed the behavioral and synapse remodeling defects of *tba-1(gf) dlk-1(0)* (Figure 3.1G; Table 3.1), and such suppression was rescued by transgenic expression of wild type TBB-2 in *tba-1(gf) dlk-1(0); tbb-2(ju1535)* animals (Figure 3.1H). Interestingly, *tbb-2 (ju1535)* single mutant animals were smaller than wild type animals, and displayed a significant reduction in DD neuron synapse number, similar to *tba-1(gf)* animals (Figure 3.1F, G). Since *tba-1* and *tbb-2* form heterodimers in the *C. elegans* embryo, and have overlapping neuronal expression patterns (Baugh et al., 2003; Fukushige, Yasuda & Siddiqui, 1995; Lu, Srayko & Mains, 2004), we hypothesized that *tbb-2(ju1535)* might suppress *tba-1(gf)* alone. Indeed, *tba-1(gf); tbb-2(ju1535)* double mutant animals displayed increased DD neuron synapse numbers compared to either single mutant, albeit fewer than those seen in wild type animals (Figure 3.1F, G).

tbb-2(ju1535) behaved as a neomorphic allele, as *gk129, a* null *(0)* mutation of *tbb-2* did not cause overt defects in locomotion or synapse formation and also did not suppress the synapse remodeling defects of *tba-1(gf) dlk-1(0)* animals (Figure 3.1F, G). *tba-1(gf); tbb-2(0)* animals were viable and displayed similar synapse formation defects to *tba-1(gf)* single mutant animals, whereas *tba-1(0); tbb-2(0)* animals were lethal due to their requirement in early embryonic development (Baran et al., 2010). Taken together, these results suggest that while heterodimers of TBA-1 and TBB-2 were essential for embryonic development, in the absence of *tbb-2, tba-1(gf)* could form heterodimers with other β-tubulins that were incorporated into MTs. *tba-1(gf)* resulted in a change in MT architecture (Kurup et al., 2015) and is a mutation altering the external surface of MTs, separate from domains responsible for GTP binding and heterodimer formation (Nogales, Wolf & Downing, 1998; Figure 3.S1). Thus, the suppression of *tba-1(gf)* by *tbb-1(ju2535)* may likely be through either modifying or reducing the incorporation of *tba-1(gf); tbb-2(ju1535)* heterodimers in MTs, in turn reducing the number of abnormal MTs.

Dynein-dynactin complex function is important for synapse remodeling

We mapped one of the suppressors, *ju1279*, to the *C. elegans* cytoplasmic dynein heavy chain, *dhc-1*. Cytoplasmic dynein is a large multi-subunit molecular motor that comprises of two catalytic heavy chains, as well as numerous light and intermediate chains. Dynein moves towards MT minus ends and is the primary motor involved in retrograde axonal transport, with mutations in dynein and its adaptor proteins implicated in several neurodegenerative disorders (Millecamps & Julien, 2013). *ju1279* converts a conserved proline residue to leucine (P262L) in the N-terminal region 1 of the tail domain of *dhc-1* (Figure 3.2A, 3.S2), which is responsible for dynein homodimerization and acts as a scaffold for subunit assembly (Carter, Diamant & Urnavicius, 2016). *dhc-1(ju1279)* acted as a weak suppressor of *tba-1(gf) dlk-1(0)*, since synapse remodeling was only partially restored in *dhc-1(ju1279) tba-1(gf) dlk-1(0)* triple mutant animals, with a significant reduction in dorsal neurite synapse number compared to *tba-1(gf)* animals (Figure 3.2B, C). We confirmed that *dhc-1(ju1279)* was causative by rescuing the suppression of *tba-1(gf) dlk-1(0)* using extra-chromosomal copies of a fosmid containing the full genomic region of DHC-1 (Figure 3.2B, C).

To understand how the *ju1279* allele affects *dhc-1* function, we examined two well characterized alleles of *dhc-1*, *or195* (O' Rourke et al., 2007) and *js319* (Koushika et al., 2004). *or195* is a conserved serine to leucine change in the MT binding stalk region of *dhc-1* resulting in temperature sensitive lethality (Figure 3.2A) , while *js319* is a splice site mutation in the C-terminal conserved motor domain of *dhc-1* (Ou et al., 2010), producing viable but visibly dumpy animals at 25^{o}C (Figure 3.2A, 3.S2). In contrast, *dhc-1(ju1279)* animals appeared superficially wild type at 25^{0}C, as did *dhc-1(ju1279)/dhc-1(js319)* and *dhc-1(ju1279)/dhc-1(or195)* heterozygous animals (Figure 3.S2). *dhc-1(js319)* animals also had reduced DD synapse numbers (Figure 3.2D) while overexpression of wild type DHC-1 or

dhc-1(ju1279) did not alter synapse number in adult animals (Figure 3.2C, D). Additionally, triple mutants of *dhc-1(js319)* or *dhc-1(or195)* with *tba-1(gf) dlk-1(0)* were embryonic lethal even at temperatures lower than 25^0C. Taken together, these results suggest that *ju1279* is a novel allele of *dhc-1*, uniquely altering dynein function in the context of synapse remodeling.

Another suppressor, *ju993*, changed valine 229 to isoleucine in the *C. elegans* p62 subunit of dynactin *dnc-4* (Figure 3.2D). Dynactin is a large multi-subunit protein complex that is essential for most cellular functions of cytoplasmic dynein, including MT binding and linking dynein to its cargo during fast axonal transport (Kardon & Vale, 2009; Karki, Tokito & Holzbaur, 2000; Waterman-Storer et al., 1997; Yeh et al., 2012). *dnc-4*, together with p25 and p27 subunits, interacts with actin-related proteins Arp1 and Arp11 to form the pointed end of the dynactin complex, which is positioned diametrically opposite dynein motor domains to primarily influence cargo binding (Karki, Tokito & Holzbaur, 2000; Urnavicius et al., 2015; Yeh et al., 2012). In *dnc-4(ju993)* adult animals DD neurons formed synapses in the dorsal neurites, and the pattern and number of synapses were comparable to wild type. In *tba-1(gf) dlk-1(0)* animals, *dnc-4(ju993)* significantly increased the number of synapses in DD dorsal neurites (Figure 3.2E). Expression of wild type copies of DNC-4(+) rescued the suppression of *tba-1(gf) dlk-1(0)* by *dnc-4(ju933)* (Figure 3.2E). *dnc-4(ju933)* complemented the temperature-sensitive embryonic lethality of *dnc-4(or633)*, which altered a conserved glutamic acid to lysine in the N-terminal region (O'Rourke et al., 2011; Figure 3.S2). Additionally, *dnc-4(or633)* did not suppress the synapse remodeling defects of *tba-1(gf) dlk-1(0)* at the permissive temperature (20^oC), or when shifted to the restrictive temperature (25^oC) after embryonic development (Figure 3.2F), indicating that *ju993* is a novel mutation of *dnc-4*. In conjunction with the effects on SV transport seen in *dhc-1(ju1279)* animals, and the similar levels of suppression seen in both *dhc-1* and *dnc-4* alleles (Figure 3.2C, E), we propose that altering dynein-dynactin complex interactions has a profound effect synapse remodeling.

Altered dynein activity promotes anterograde vesicle transport during remodeling

We next sought to understand the mechanism by which *dhc-1(ju1279)* suppressed the synapse remodeling defects of *tba-1(gf) dlk-1(0)*. The remodeling defects in *tba-1(gf) dlk-1(0)* animals were primarily brought about by an increase in MT stability, resulting in reduced synaptic vesicle (SV) transport in the DD neurons during remodeling (Kurup et al. 2015). We first considered the possibility that *dhc-1(ju1279)* modifies MT dynamics in *tba-1(gf) dlk-1(0)*, since an established role of cytoplasmic dynein is to stabilize dynamic MT plus ends by tethering them to the cell cortex (Hendricks et al., 2012). However, *dhc-1(ju1279)* had no significant effect on the number of dynamic MTs or their direction of growth in both wild type and *tba-1(gf) dlk-1(0)* adults (Figure 3.S2), leading us to conclude that the suppression of synapse remodeling defects by *dhc-1(ju1279)* did not result from a change in MT dynamics.

Since the *ju1279* allele affects the tail domain of DHC-1, which is structurally adjacent to the cargo binding domain of the dynein motor complex (Urnavicius et al., 2015), we wondered whether SV transport was altered in the mutant animals. We assayed SV transport along the commissures of DD neurons during synapse remodeling in wild type and mutant animals using 4-dimensional (4-D) imaging (Figure 3.3A). In wild type animals, most SVs moved in the anterograde direction, i.e., away from the cell body and towards their new location in the dorsal neurite (Figure 3.3C). This proportion of anterogradely moving SVs was maintained in *tba-1(gf) dlk-1(0)* animals (Figure 3.3C), albeit with a strong reduction in the total number of mobile SVs (Kurup et al., 2015; Figure 3.3B). Addition of *dhc-1(ju1279)* did not change mobile SV numbers; instead we observed a significant increase in the proportion of SVs moving anterogradely in both *dhc-1(ju1279)* single and *dhc-1(ju1279) tba-1(gf) dlk-1(0)* triple mutant animals (Figure 3.3B, C). We also imaged SV transport in *dhc-1(js319)* animals during DD remodeling, and did not find any increase in anterogradely moving SVs. Together, these data indicate that an increase in anterogradely moving SVs in *dhc-1(ju1279) tba-1(gf) dlk-1(0)* triple

mutant animals ameliorates a reduction in the total number of SVs reaching the dorsal neurite to promote synapse formation during remodeling.

We previously reported two suppressors (*ju972* and *ju977*) to be novel alleles of the anterograde motor, Kinesin-1/UNC-116 (Kurup et al., 2015). *unc-116(ju972)* strongly suppressed defective remodeling in *tba-1(gf) dlk-1(0)* by increasing total SV transport during remodeling, without altering the proportion of anterogradely moving SVs (Kurup et al., 2015; Figure 3.3B-D). Kinesins and dynein are classically thought of being in a "tug-of-war" during bi-directional cargo transport, highlighting the interdependence of the two motors for axonal transport in either direction (Belyy et al., 2016; Hendricks et al., 2010; Martin et al., 1999; Figure 3.3D). We then wanted to see whether modifying dynein function using *dhc-1(ju1279)* would have any effect on SV transport in *unc-116(ju972)* animals. In both wild type and *tba-1(gf) dlk-1(0)* backgrounds, *dhc-1(ju1279); unc-116(ju972)* double mutant animals displayed a significant increase in both total number of mobile SVs and the proportion of anterogradely moving SVs, resulting in a strong anterograde bias in SV transport (Figure 3.3B, C). These observations led us to hypothesize that *dhc-1(ju1279)* likely weakens the interaction between the dynein complex and SVs, shifting the balance of bidirectional cargo transport in the anterograde direction (Figure 3.3D).

The kinase TTBK-3 acts cell autonomously in DD neuron remodeling

We mapped another suppressor mutation of *tba-1(gf) dlk-1(0)*, *ju978*, to the kinase *ttbk-3* (F32B6.10) (Figure 3.4A; Table 3.1). *ttbk-3(tm4006)*, a deletion allele that removes the N-terminus and part of the kinase domain, also suppressed the synapse remodeling defects of *tba-1(gf) dlk-1(0)* (Figure 3.S3). Single mutants of *ju978* or *tm4006* were superficially wild type with no synapse formation or remodeling defects (Figure 3.4A-C; 3.S3). We verified that *ttbk-3(ju978)* was causative for suppression of *tba-1(gf) dlk-1(0)* by overexpressing wild type

TTBK-3 in *tba-1(gf) dlk-1(0); ttbk-3(ju978)* animals, and observed a block in synapse remodeling in the transgenic animals (Figure 3.4B, C). These results indicate that loss of *ttbk-3* specifically restores synapse remodeling in *tba-1(gf) dlk-1(0)* animals.

TTBK-3 belongs to a large expansion of the Casein-kinase (CK1) superfamily in *C. elegans*, sharing 32% identity in the kinase domain to human tau-tubulin kinases (TTBK1 and TTBK2) (Manning, 2005). Tau-tubulin kinases were first identified by their ability to phosphorylate the MT-associated protein tau and tubulin; mammalian TTBK1 is highly enriched in the nervous system, while TTBK2 is more broadly expressed (Liao et al., 2015; Sato et al., 2006). *ju978* generated a STOP codon in the C-terminal end of *ttbk-3*, which could result in a truncated protein with an intact kinase domain that lacked a coiled-coil domain further downstream (Figure 3.4A, D). Since *ttbk-3(ju978)* suppressed *tba-1(gf) dlk-1(0)* to a similar extent as *ttbk-3(tm4006)*, we asked whether the catalytic activity of *ttbk-3* was required for synapse remodeling. Overexpressing kinase-dead versions of TTBK-3 (K115A or D209A) (Wanf & Madelkow, 2015) failed to rescue *tba-1(gf) dlk-1(0); ttbk-3(ju978)* (Figure 3.4D). We also obtained similar results using a mutant TTBK-3 lacking the C-terminal coiled-coil domain (Figure 3.4D). These results suggest that both the catalytic activity of the kinase domain and the coiled-coil domain are likely required for TTBK-3 function in synapse remodeling.

As reported by a recent study, expression of *ttbk-3* was weak and extremely variable (Bouskila et al., 2013) and we were not able to reliably examine its neuronal expression pattern using extrachromosomal arrays of GFP driven by the endogenous *ttbk-3* promoter. Expression of GFP tagged TTBK-3 in D motor neurons (P_{unc-25}-TTBK-3-GFP) showed both diffuse and punctate GFP accumulation in the cell body and neurites during the L3 and L4 developmental stages, with a more diffuse distribution of GFP observed in adult animals (Figure 3.S3). GFP expression was almost undetectable outside the cell body during the period of DD synapse remodeling in L1 and L2 animals. To test if TTBK-3 acted cell autonomously in the DD neurons to regulate remodeling, we overexpressed TTBK-3 under a DD neuron specific promoter (P_{flp-13}),

which rescued the suppression of defective remodeling by *ttbk-3(ju978)* to a similar degree as full-length *ttbk-3*. As a control, expression of TTBK-3 from a muscle specific promoter (*myo-3*) failed to do so (Figure 3.4B, C), supporting the conclusion that TTBK-3 is required in DD neurons.

TTBK-3 modulates nascent synapse stability after DD remodeling

Next, we focused on how *ttbk-3* could regulate synapse remodeling. Tau is a MAP that plays important roles in axonal transport, MT dynamics and neurite outgrowth during development, and is misregulated in neurodegenerative disease (Neal et al., 2016). We tested a null mutation of the *C. elegans* homolog of tau, *ptl-1* , and found that *ptl-1(0)* did not have any effect on synapse formation or remodeling in wild type animals, and also failed to suppress the synapse remodeling defects of *tba-1(gf) dlk-1(0)* animals (Figure 3.S3). We also tested a null allele of *ttbk-7* (R90.1), the closest homolog of mammalian TTBK1/2 (65% sequence identity), which also failed to suppress *tba-1(gf) dlk-1(0)* (Figure 3..S3). These observations suggest *ttbk-3* likely acts through mechanisms independent of regulation of Tau.

We next imaged MT dynamics and SV transport and found that neither changed in *tba-1(gf) dlk-1(0); ttbk-3(tm4006)* animals when compared to *tba-1(gf) dlk-1(0)* animals (S3 Fig). Taken together with the expression pattern in DD neurons, this data suggested that *ttbk-3* was not involved in the early stages of synapse formation during remodeling. We then assayed the temporal requirement of *ttbk-3* in synapse remodeling using GFP tagged TTBK-3 expressed under a heat-shock inducible promoter ($P_{hsp\text{-}16.2}$-TTBK-3-GFP). Following heat-shock in young adult animals TTBK-3-GFP formed punctate aggregates in neurons, the pharynx, the intestinal lumen and posterior intestinal cells (Figure 3.S3). To assay *ttbk-3* requirement, we induced TTBK-3 expression at various larval stages, and observed behavioral and synapse remodeling phenotypes in the induced animals at adulthood (Figure 3.5A). Heat-shock treated wild type

animals (with or without TTBK-3-GFP) did not coil dorsally and had normal dorsal neurite synapse formation (Figure 3.5B, C). On the other hand, heat shock treatment of L4 stage *tba-1(gf) dlk-1(0); ttbk-3(ju978)* animals expressing TTBK-3-GFP significantly reduced the suppression of both behavioral and synapse remodeling defects by *ttbk-3(ju978),* when compared to non-transgenic animals undergoing the same heat shock treatment (Figure 3.5D, E). We observed no difference in the extent of suppression between transgenic and non- transgenic animals that were heat-shocked at any other developmental stage, suggesting that *ttbk-3* specifically played a role in synapse remodeling at the L4 stage, and was not required for the induction of synapse remodeling at the L1-L2 stage. We previously reported the presence of transient dorsal neurite synaptic puncta in *tba-1(gf) dlk-1(0)* animals from the L2-L4 stage, which were then eliminated as the animal achieved adulthood (Kurup et al., 2015). Indeed, the intensity of SNB-1-GFP foci observed along the dorsal neurite at the L4 stage was higher in *ttbk-3(tm4006)* animals, both in the wild type and *tba-1(gf) dlk-1(0)* backgrounds (Figure 3.S4). This suggested the existence of a mechanism to regulate the stabilization and maintenance of new synaptic sites formed on the dorsal neurite during remodeling. Since adding back wild type TTBK-3 at the L4 stage removed dorsal neurite synapses in *tba-1(gf) dlk-1(0); ttbk-3(ju978)* animals, we concluded that TTBK-3 antagonizes the stability of nascent synapses that are formed during synapse remodeling.

Discussion

Modifications to synapse architecture occur throughout the lifetime of an animal, either dependent or independent of large scale neurite rewiring (Holtmaat & Svoboda, 2009; Hong et al., 2009; Luo & O' Leary, 2005; Marc et al., 2003; Sanes & Lichtman, 1999). In this study, we dissect the mechanisms underlying a *C. elegans* model of structural synaptic plasticity, where

synapses are eliminated and re-assembled along different neurites of the same neuron during a developmentally defined time scale (Kurup & Jin, 2016).

We had previously shown that *tba-1(gf) dlk-1(0)* animals failed to complete synapse remodeling because of enhanced MT stability in DD neurons (Kurup et al., 2015). To identify additional regulators of the remodeling process, we screened for mutants that reversed the synaptic and behavioral defects of *tba-1(gf) dlk-1(0)* animals following EMS mutagenesis. Since we performed a non-clonal screen for homozygous viable adult animals, we were not able to isolate suppressors that might cause either lethality or sterility. Of the viable suppressors that we characterized, more than half were missense or nonsense alleles of *tba-1* that either reverted *tba-1(gf)* function back to wild type or resulted in null mutation of *tba-1*. Multiple mutations in human α-tubulin have been implicated in neuronal disorders like lissencephaly and ALS, and their effects on MTs have only been studied using *in vitro* overexpression models (Keays et al., 2007; Kumar et al., 2010; Smith et al., 2014). All the missense *tba-1* alleles that we identified in this screen alter invariant residues adjacent to disease-linked mutations in the C-terminal H12, the GTP binding domain and the loop between H8 and S7 (Keays et al., 2007; Kumar et al., 2010; Smith et al., 2014; annotated in Figure 3.S1), highlighting the importance of these three regions for α-tubulin functionality *in vivo*.

The non-tubulin suppressor mutations displayed incomplete suppression of the synapse remodeling defects of *tba-1(gf) dlk-1(0).* On their own, none of these alleles had any effect on synapse formation or animal behavior. This might result from multiple factors. First, as was the case with motor proteins and their adaptors (*unc-116*, *dhc-1* and *dnc-4* alleles), the screen identified novel mutations that subtly altered protein function in such a way that embryonic development was completed and the animals were viable. Next, loss of function alleles in *ttbk-3(ju978)* behaved superficially wild type, likely because of the presence of other redundant kinases, which might also explain the incomplete suppression on *tba-1(gf) dlk-1(0)*. Finally, any suppressors with strong behavioral deficits were likely missed since the design of our screen

aimed to identify animals with wild type behavior first, and then assayed for restoration of DD synapse remodeling.

A key bottleneck to successful DD synapse remodeling is the motor dependent transport of SVs from the ventral to the dorsal neurite. Consistently, a majority of the suppressors altered either anterograde or retrograde motor function to compensate for a reduction in SV transport in *tba-1(gf) dlk-1(0)*. We previously identified kinesin-1 mutations that increased motor motility, and here, we characterized dynein-dynactin mutations that could alter cargo binding, with both strategies increasing anterograde SV transport along the DD neuron commissure during remodeling. However, while there was an overall increase in bidirectional SV transport in *unc-116(ju972)* animals, *dhc-1(ju1279)* selectively increased anterograde SV transport. This likely reflects the distinct motor domains targeted by *ju972* and *ju1279* on kinesin and dynein, respectively, with MT-motor interactions affecting bidirectional transport and variations in motor-cargo binding biasing transport in the direction with more engaged motors. Our results thus highlight both the interdependence and the competition between anterograde and retrograde motors during bidirectional cargo transport *in vivo*. The combination of *unc-116(ju972)* and *dhc-1(ju1279)* had an additive effect on SV transport, with an increase in both the total and anterogradely moving vesicle pools. Interestingly, *dhc-1(ju1279); unc-116(ju972)* did not enhance the number of dorsal neurite synapses in *tba-1(gf) dlk-1(0)* compared to *unc-116(ju972)* alone (Figure 3.S4), indicating that the synapse formation defects caused by *tba-1(gf)* alone (Baran et al., 2010) could not be suppressed simply by an increase in the number of available SVs.

Studies in cultured mammalian neurons indicate that nascent synapse stability is dependent on the transport of sufficient numbers of SVs to the site of new synapse formation (Jin & Garner, 2008; McAllister, 2007). In *tba-1(gf) dlk-1(0)* animals, the lack of sufficient SVs at sites of new synapse formation on the dorsal neurite resulted in their destabilization and subsequent elimination at the L4 stage (Kurup et al., 2015). Here, we found that TTBK-3, a *C.*

elegans member of the casein kinase superfamily, promotes synapse destabilization along the dorsal neurite, and loss of *ttbk-3* was sufficient to maintain newly formed synapses in *tba-1(gf) dlk-1(0)*. Synapse destabilization by TTBK-3 is likely phosphorylation dependent, and future studies will be required to identify potential substrates. The coiled-coil domain was also required for TTBK-3 function, leading us to speculate a possible regulatory role for the domain on kinase function. We previously showed that the initiation of dorsal neurite synapse formation was mediated by *dlk-1* at the L2 stage; however *ttbk-3* does not appear to play a role at this stage (Kurup et al., 2015). *ttbk-3* is also not involved in ventral neurite synapse elimination during DD neuron remodeling, which is complete by L3 stage (Kurup et al., 2015; Meng et al., 2016; Park et al., 2011). These results demonstrate that developmental synapse remodeling is marked by distinct phases of synapse formation, elimination and maintenance, each under tight spatio-temporal control to achieve precise neuronal connectivity.

Experimental Procedures

C. elegans culture

Strains were maintained at 20°C on NGM plates unless noted otherwise (Brenner, 1974). Information on alleles and genotypes of strains is summarized in S2 Table**.**

Plasmid and transgene generation

Plasmids were generated using Gateway technology (Invitrogen). DNA for *dnc-4* and *ttbk-3* constructs was amplified from purified genomic or cDNA by PCR using Phusion HF DNA polymerase (Finnzyme) (Table 3.4), and subcloned into PCR8 entry vectors. Transgenic animals were generated by microinjection, following standard procedures (Mello et al., 1991), using plasmids of interest at various concentrations (listed in Table 3.3) and Pgcy-8-GFP (80-90 ng/µl) or Pmyo-2-mCherry (2.5 ng/µl) as co-injection markers. A minimum of 2-3 transgenes were

generated for each construct described in this study. For rescue experiments using *dhc-1*, *dnc-4* and *ttbk-3* constructs, the data from 3 transgenes was pooled in statistical analyses. A list of the plasmids used in this study and the transgenic arrays generated from them is listed in Table 3.3. Primer information for the DNA clones generated in this study is listed in Table 3.4.

Fluorescent imaging of synapses

L4 animals were cultured at 20°C overnight, and day 1 adults were imaged using a Zeiss LSM 710 confocal microscope. Animals were anaesthetized in 0.6 mM levamisole on 2% agar pads for image acquisition. Z-stacks were generated from slices of 0.6 μm thickness. Images were processed using Zen lite software. Synaptic puncta number was quantified manually using a Zeiss Axioplan 2 microscope equipped with Chroma HQ filters.

SNB-1::GFP trafficking

L2 stage animals (14-18 hrs post hatching when maintained at 20°C) were collected for analysis, and anesthetized using 30 mM muscimol on 10% agarose pads. 4-D imaging was performed using a Yokogawa CSU-W1 spinning disc confocal head placed on a Leica DMi8 confocal microscope equipped with a piezo Z stage for fast Z- acquisition controlled using MetaMorph (Molecular Devices). The entire DD commissure was visualized in 5-6 slices and images were collected for a total of 20 frames. The resulting movies were analyzed using Metamorph to generate kymographs for analysis of number and direction of movement of synaptic vesicles.

EBP-2::GFP image acquisition and analysis

Animals were anaesthetized in 30mM muscimol on 10% agarose pads for image acquisition. Live imaging for monitoring EBP-2 dynamics was done using a Yokogawa CSU-W1 spinning disc confocal head placed on a Leica DMi8 confocal microscope controlled by MetaMorph. 200 single plane images were taken serially at an exposure time of 113ms with an interval of 230ms

between each frame, and analyzed using Metamorph software (Molecular Devices) to generate kymographs for analysis.

Analysis of mutants from *tba-1(gf) dlk-1(0)* suppressor screen

tba-1(gf) dlk-1(0) animals were mutagenized using Ethyl Methane Sulphonate (EMS) following standard procedures (Brenner, 1974). F2 animals with improved locomotion were selected as putative suppressors in a non-clonal screen. Several suppressors were determined to be intragenic loss of function mutations in *tba-1(gf)* by sequencing the genic region of *tba-1* for any additional mutations. Two of the extragenic suppressors, *ju972* and ju977, were determined to be extragenic and mapped to the gene *unc-116* following whole genome sequence analysis by MAQGene (Bigelow et al., 2009). The results of whole genome sequencing of the remaining suppressors were analyzed using a Galaxy (https://usegalaxy.org/) workflow, and the causative mutations were identified by linkage analysis of the suppression to the SNPs identified in the whole sequence analysis.

Heat shock induced expression of *ttbk-3*

Transgenic animals expressing $P_{hsp\text{-}16.2}$TTBK-3-GFP; $P_{myo\text{-}2}$ mCherry in the wild type and *tba-1(gf) dlk-1(0); ttbk-3(0)* backgrounds were selected by positive pharyngeal mCherry expression. L1, L2, L3, L4 and young adult animals were heat shocked at 34^{o}C for 2 hours in an incubator. Heat shocked animals were maintained at 20^{o}C after heat shock until they reached day 1 adulthood, when they were imaged using a Zeiss LSM 710 confocal microscope.

Statistical Analysis

Statistical analysis was performed using GraphPad Prism 5. Normal distribution of samples was tested using D'Agostino & Pearson omnibus normality test. Significance was determined using One way ANOVA followed by Tukey’s multiple comparison tests and two way ANOVA followed by Bonferroni posttests for multiple samples.

Acknowledgements

This chapter is a reprint, in full, of Kurup, N., Yan, D., Kono, K., & Jin, Y. (2017) Differential regulation of polarized synaptic vesicle trafficking and synapse stability in neural circuit rewiring in *Caenorhabditis elegans*. *PLOS Genetics*, *13*(6): e1006844, with permission of all the authors. The dissertation author was the primary author.

N. K. designed, interpreted and performed most experiments and wrote the paper, D. Y. designed and performed the *tba-1(gf) dlk-1(0)* suppressor screen, K.K. mapped *tbb-2(ju1535)* and performed experiments, and Y. J. designed experiments and interpreted data, and co-wrote the paper. We thank S. Cherra for customizing the Galaxy workflow and sharing software analysis for SNP-mapping. We thank K.W. Kim, N.H. Tang. K. Noma, M. Andrusiak and S. Park for critical reading of the manuscript. We are grateful to members of the Jin and Chisholm labs for advice and helpful discussions. We thank the Caenorhabditis Genetics Center, supported by the National Institutes of Health (P40 OD010440), and the Mitani lab (Tokyo Women's Medical College) for providing strains used in this study.

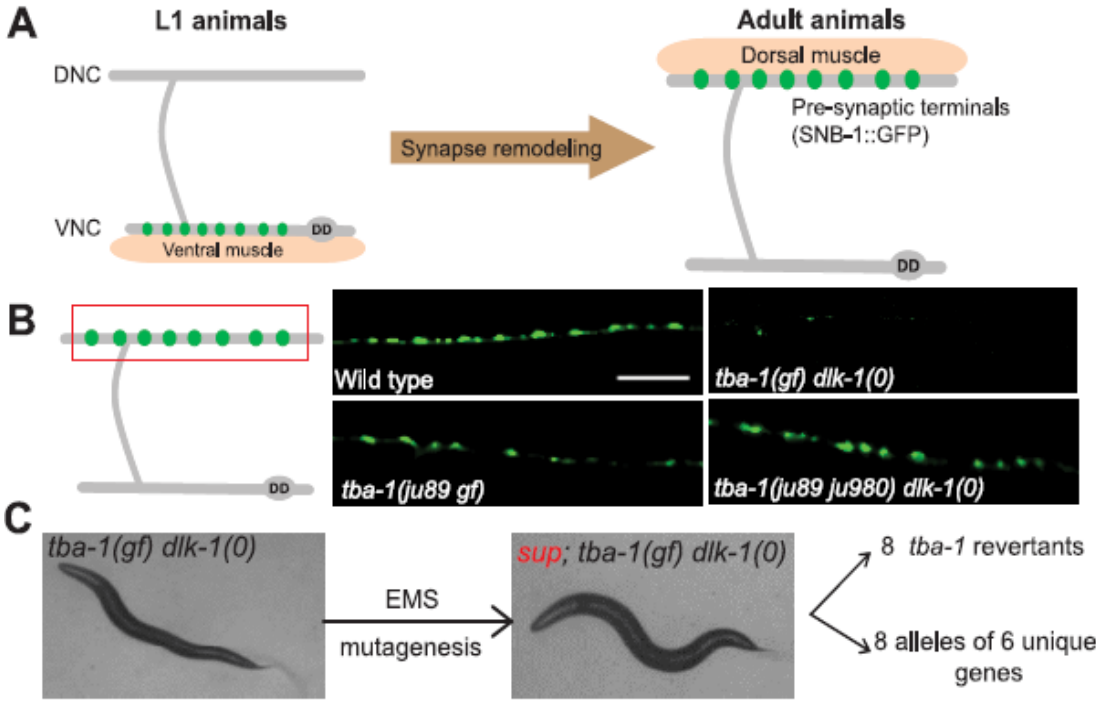

Figure 3.1 Intragenic mutations in *tba-1* and a novel *tbb-2* mutation suppress synapse remodeling defects in *tba-1(gf) dlk-1(0)*

(A) Schematic of remodeling of DD neuron synapses. In young larvae, pre-synaptic terminals are visualized along the ventral nerve cord (VNC) using GFP- tagged synaptobrevin (SNB-1::GFP). These synapses are completely eliminated in wild type animals, to form new synapses along the dorsal nerve cord (DNC). (B) Schematic of an adult DD neuron, with the red box representing the region of interest. Representative images of DD synapses in the adult DNC of various genotypes, visualized using P_{unc-25}-SNB-1::GFP (*juIs1*). Scale bar: 10 µm. (C) Bright field images of a *tba-1(gf) dlk-1(0)* animal and an animal isolated following EMS mutagenesis of *tba-1(gf) dlk-1(0)*. (D) Gene structure of *tba-1*, with *tba-1(gf) (ju89)* and all the intragenic suppressors listed. (E) Gene structure of *tbb-2*, with *ju1535* and reference allele *gk129* marked. (F) Representative images of DD synapses in the adult DNC of various genotypes, visualized using P_{unc-25}-SNB-1::GFP (*juIs1*). Scale bar: 10 µm. (G) Quantification of synaptic puncta in the DNC of adult animals. Data are mean ± SEM; n>10 animals per genotype. Statistics: One-Way ANOVA followed by Tukey's posttest; ***p<0.001, ns- not significant. (H) DNC synapses in *tba-1(gf) dlk-1(0); tbb-2(ju1535); juIs1* animals that either lack or contain a rescuing transgene expressing wild type TBB-2 (Ex-TBB-2(+)).

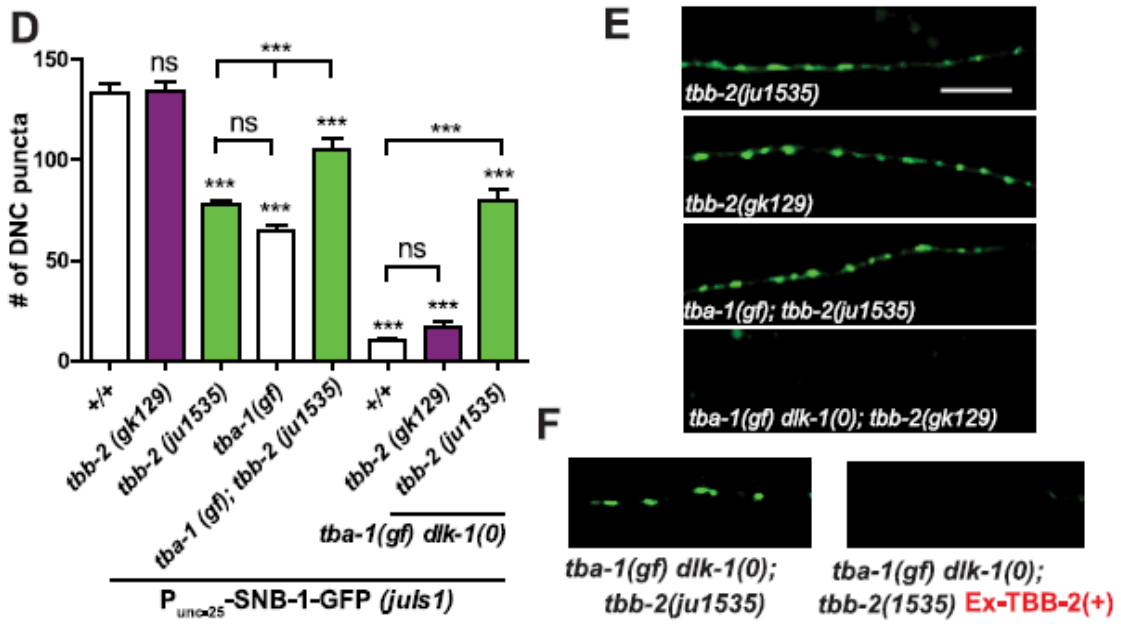

Figure 3.1 (continued) Intragenic mutations in *tba-1* and a novel *tbb-2* mutation suppress synapse remodeling defects in *tba-1(gf) dlk-1(0)*

(A) Schematic of remodeling of DD neuron synapses. In young larvae, pre-synaptic terminals are visualized along the ventral nerve cord (VNC) using GFP- tagged synaptobrevin (SNB-1::GFP). These synapses are completely eliminated in wild type animals, to form new synapses along the dorsal nerve cord (DNC). (B) Schematic of an adult DD neuron, with the red box representing the region of interest. Representative images of DD synapses in the adult DNC of various genotypes, visualized using $P_{unc\text{-}25}$-SNB-1::GFP (*juIs1*). Scale bar: 10 μm. (C) Bright field images of a *tba-1(gf) dlk-1(0)* animal and an animal isolated following EMS mutagenesis of *tba-1(gf) dlk-1(0)*. (D) Gene structure of *tba-1*, with *tba-1(gf) (ju89)* and all the intragenic suppressors listed. (E) Gene structure of *tbb-2*, with *ju1535* and reference allele *gk129* marked. (F) Representative images of DD synapses in the adult DNC of various genotypes, visualized using $P_{unc\text{-}25}$-SNB-1::GFP (*juIs1*). Scale bar: 10 μm. (G) Quantification of synaptic puncta in the DNC of adult animals. Data are mean ± SEM; n>10 animals per genotype. Statistics: One-Way ANOVA followed by Tukey's posttest; ***p<0.001, ns- not significant. (H) DNC synapses in *tba-1(gf) dlk-1(0); tbb-2(ju1535); juIs1* animals that either lack or contain a rescuing transgene expressing wild type TBB-2 (Ex-TBB-2(+)).

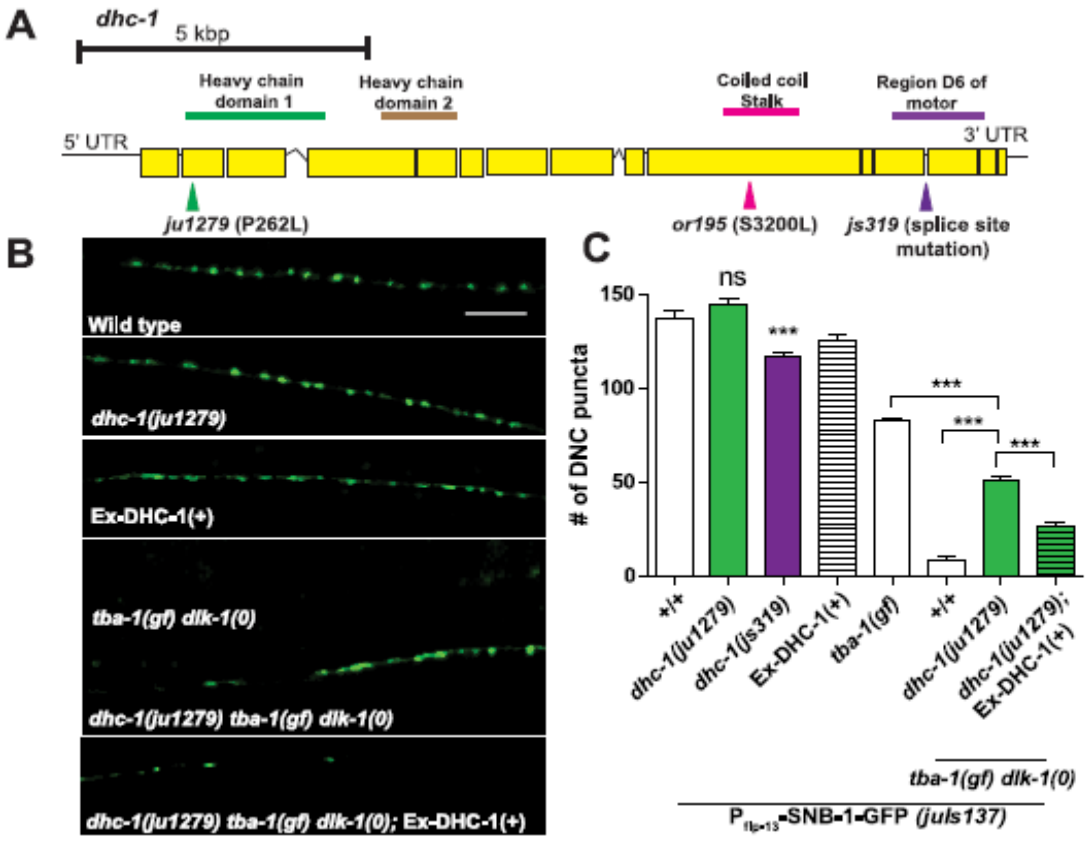

Figure 3.2 *ju1279* and *ju993* are novel alleles of *dhc-1* and *dnc-4*, respectively

(A) Gene structure of *dhc-1*, with *ju1279* and reference alleles *or195* and *js319* marked. *ju1279* alters the N-terminal Heavy chain domain 1, *or195* alters the coiled coil stalk and *js319* alters region D6 of the motor. (B) Representative images of DD synapses along the DNC (P_{flp-13}-SNB-1::GFP (*juIs137*)) in adult animals. Ex-DHC-1 denotes extrachromosomal copies of wild type DHC-1. Scale bar: 10 µm. (C) Quantification of synaptic puncta in the DNC of adult animals. Data are mean ± SEM; n>10 animals per genotype. Statistics: One-Way ANOVA followed by Tukey's posttest; ***p<0.001, ns- not significant. (D) Gene structure of *dnc-4*, with *ju933* and the reference allele *or633* also marked. (E) Quantification of synaptic puncta in the DNC (P_{unc-25}-SNB-1::GFP (*juIs1*)) of adult animals. Ex-DNC-4(+) denotes extrachromosomal copies of wild type DNC-4. Data are mean ± SEM; n>8 animals per genotype. Statistics: One-Way ANOVA followed by Tukey's posttest; ***p<0.001, ns- not significant. (F) Quantification of synaptic puncta in the DNC (P_{flp-13}-SNB-1::GFP (*juIs137*)) of adult animals. Animals were cultured at two different temperatures, the permissive (20^{o}C) and restrictive (25^{o}C) temperatures for *or633*, starting from late L1. Data are mean ± SEM; n>8 animals per genotype. Statistics: One-Way ANOVA followed by Tukey's posttest; ns- not significant.

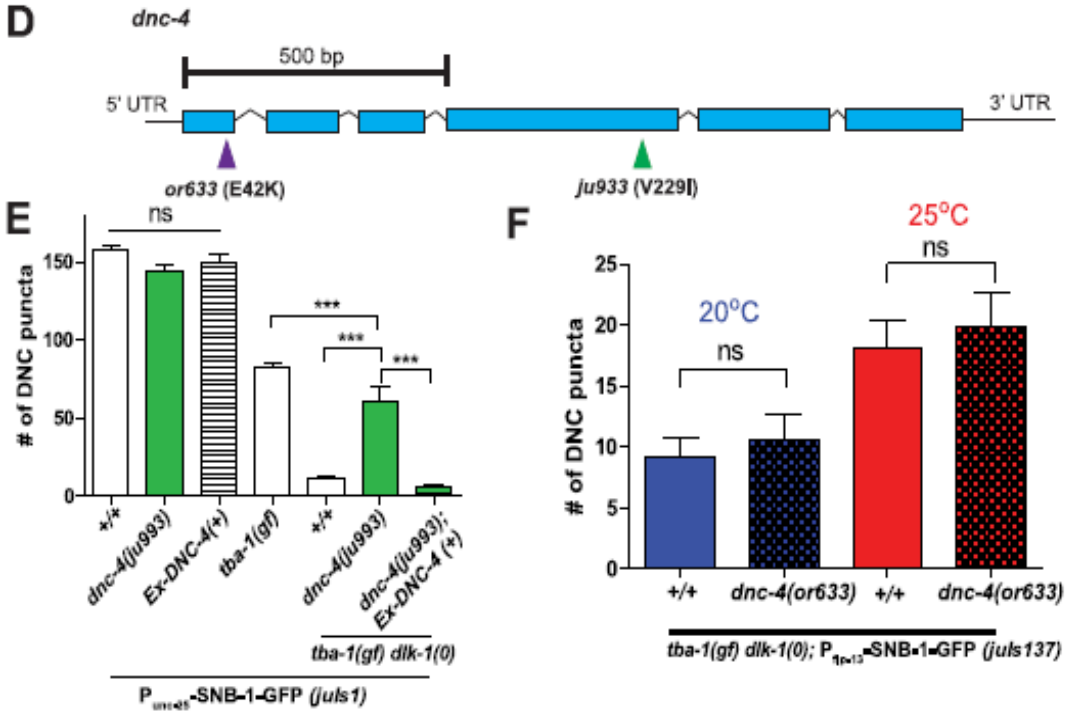

Figure 3.2 (continued) *ju1279* and *ju993* are novel alleles of *dhc-1* and *dnc-4*, respectively

(A) Gene structure of *dhc-1*, with *ju1279* and reference alleles *or195* and *js319* marked. *ju1279* alters the N-terminal Heavy chain domain 1, *or195* alters the coiled coil stalk and *js319* alters region D6 of the motor. (B) Representative images of DD synapses along the DNC (P_{flp-13}-SNB-1::GFP (*juIs137*)) in adult animals. Ex-DHC-1 denotes extrachromosomal copies of wild type DHC-1. Scale bar: 10 µm. (C) Quantification of synaptic puncta in the DNC of adult animals. Data are mean ± SEM; n>10 animals per genotype. Statistics: One-Way ANOVA followed by Tukey's posttest; ***p<0.001, ns- not significant. (D) Gene structure of *dnc-4*, with *ju933* and the reference allele *or633* also marked. (E) Quantification of synaptic puncta in the DNC (P_{unc-25}-SNB-1::GFP (*juIs1*)) of adult animals. Ex-DNC-4(+) denotes extrachromosomal copies of wild type DNC-4. Data are mean ± SEM; n>8 animals per genotype. Statistics: One-Way ANOVA followed by Tukey's posttest; ***p<0.001, ns- not significant. (F) Quantification of synaptic puncta in the DNC (P_{flp-13}-SNB-1::GFP (*juIs137*)) of adult animals. Animals were cultured at two different temperatures, the permissive (20°C) and restrictive (25°C) temperatures for *or633*, starting from late L1. Data are mean ± SEM; n>8 animals per genotype. Statistics: One-Way ANOVA followed by Tukey's posttest; ns- not significant.

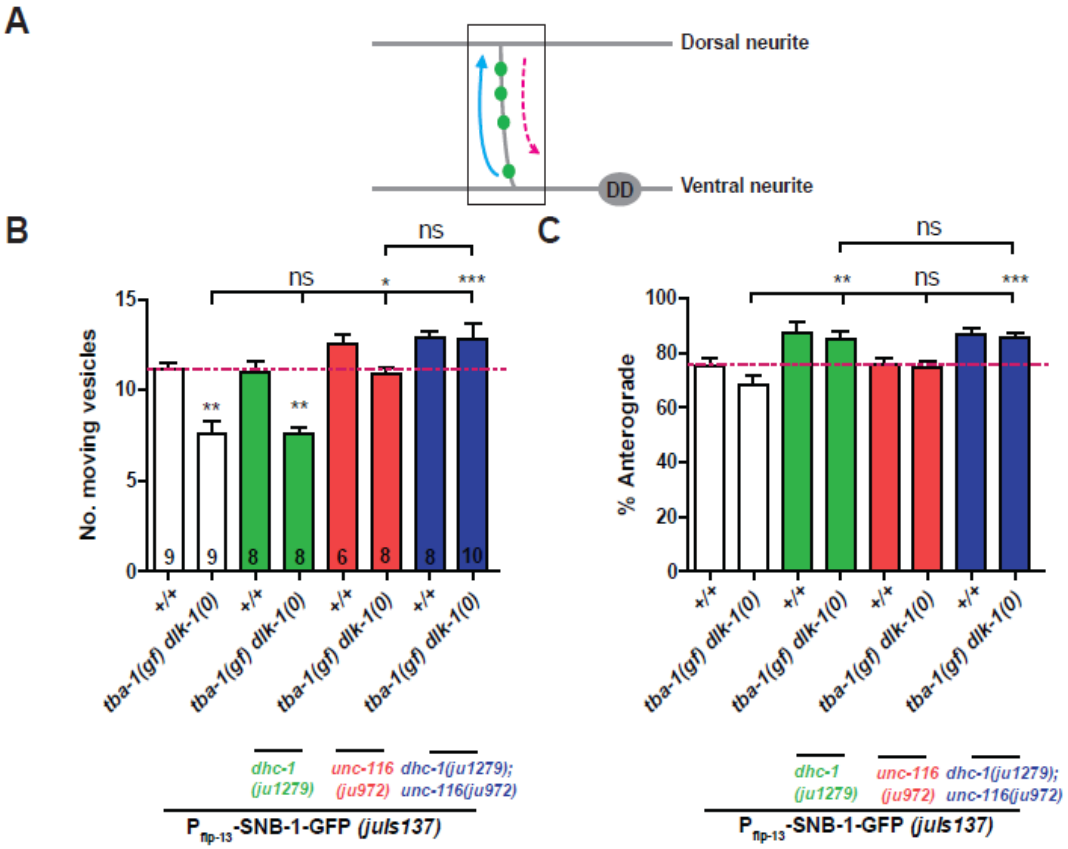

Figure 3.3 *dhc-1(ju1279)* enhances anterograde transport during synapse remodeling

(A) Schematic of imaging region (black box) in the DD neuron. SVs move in both the anterograde (blue solid arrow) and retrograde directions (pink dotted arrow) during remodeling. (B, C) Quantification of: (B) number of mobile vesicles, (C) their direction of movement during remodeling for various genotypes. Data are mean ± SEM; n= no. of animals (shown on (B)). Statistics: One-way ANOVA followed by Tukey's posttest;*p<0.05, ***p<0.001, **p<0.01, n.s.-not significant. (D) Model of bidirectional cargo transport during DD neuron synapse remodeling. a) In wild type animals, kinesin (red) and the dynein (blue)-dynactin (yellow) complex transport SVs in both the anterograde and retrograde directions, with more SVs moving towards the dorsal neurite (anterograde). b) *unc-116(ju972)* (black stars) modifies the MT binding domain of kinesin to enhance both anterograde and retrograde SV transport. c) Almost all SVs move in the anterograde direction in *dhc-1(ju1279)* (green star) and *dnc-4(ju993)* (red star) animals, possibly due to a disruption in the interaction between the dynein-dynactin complex and SVs.

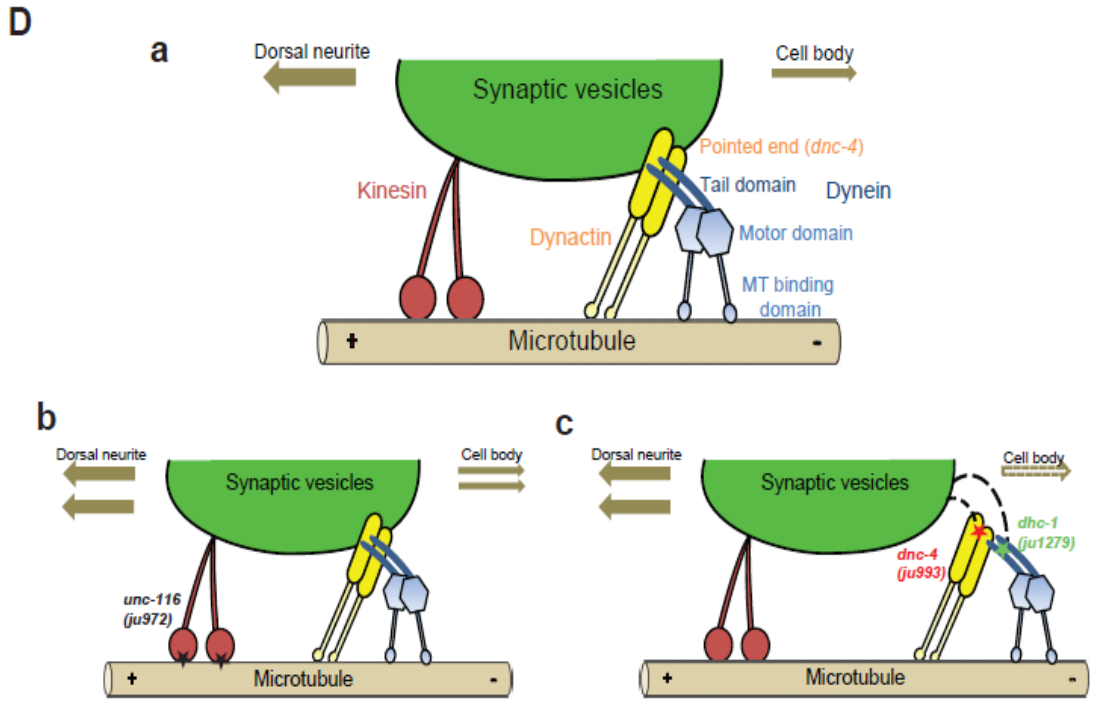

Figure 3.3 (continued) *dhc-1(ju1279)* enhances anterograde transport during synapse remodeling

(A) Schematic of imaging region (black box) in the DD neuron. SVs move in both the anterograde (blue solid arrow) and retrograde directions (pink dotted arrow) during remodeling. (B, C) Quantification of: (B) number of mobile vesicles, (C) their direction of movement during remodeling for various genotypes. Data are mean ± SEM; n= no. of animals (shown on (B)). Statistics: One-way ANOVA followed by Tukey's posttest;*p<0.05, ***p<0.001, **p<0.01, n.s.-not significant. (D) Model of bidirectional cargo transport during DD neuron synapse remodeling. a) In wild type animals, kinesin (red) and the dynein (blue)-dynactin (yellow) complex transport SVs in both the anterograde and retrograde directions, with more SVs moving towards the dorsal neurite (anterograde). b) *unc-116(ju972)* (black stars) modifies the MT binding domain of kinesin to enhance both anterograde and retrograde SV transport. c) Almost all SVs move in the anterograde direction in *dhc-1(ju1279)* (green star) and *dnc-4(ju993)* (red star) animals, possibly due to a disruption in the interaction between the dynein-dynactin complex and SVs.

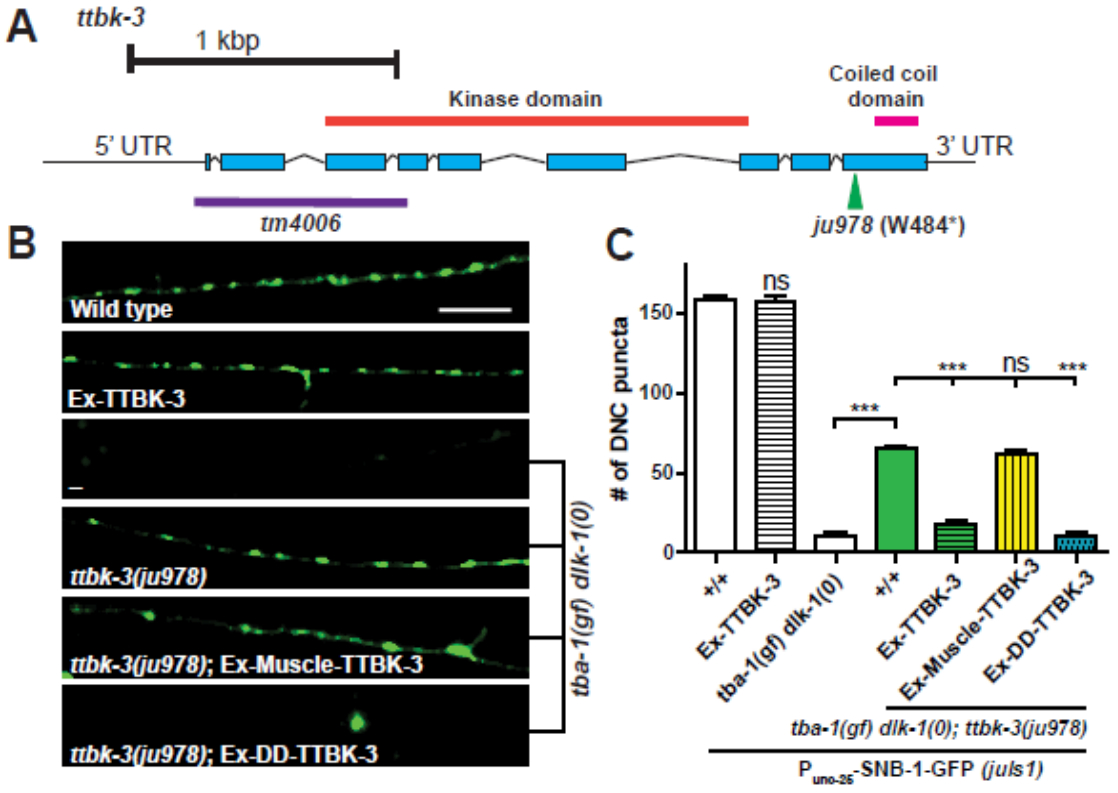

Figure 3.4 Kinase activity of *ttbk-3* is required for suppressing *tba-1(gf) dlk-1(0)*

(A) Gene structure of *ttbk-3*, with *ju978* and the deletion allele *tm4006* marked. (B) Representative images of DD neuron synapses along the DNC in adult animals imaged using P_{unc-25}-SNB-1-GFP (*juIs1*). Ex-Muscle-TTBK-3 and Ex-DDneuron-TTBK-3 denotes extrachromosomal copies of wild type TTBK-3 expressed under *myo-3* (muscle) and *flp-13* (DD neuron) promoters, respectively. Scale bar: 10 μm. (C) Quantification of synaptic puncta in the DNC (P_{unc-25}-SNB-1::GFP (*juIs1*)) of adult animals. Ex-TTBK-3 denotes extrachromosomal copies of wild type TTBK-3 expressed under its own promoter. Data are mean ± SEM; n>10 animals per genotype. Statistics: One-Way ANOVA followed by Tukey's posttest; ***p<0.001, ns- not significant. (D) Quantification of synaptic puncta in the DNC (P_{unc-25}-SNB-1::GFP (*juIs1*)) of adult animals. TTBK-3 contains a kinase domain and a C-terminal coiled-coil domain. Loss of either kinase domain activity (using kinase dead K115A and D209A mutants), or the coiled-coil domain in extrachromosomal copies of TTBK-3 (P_{flp-13}-TTBK-3), result in a failure to rescue *tba-1(gf) dlk-1(0); ttbk-3(ju978) juIs1* animals. Data are mean ± SEM; n>8 animals per genotype. Statistics: One-Way ANOVA followed by Tukey's posttest;*p<0.05, ***p<0.001, ns-not significant.

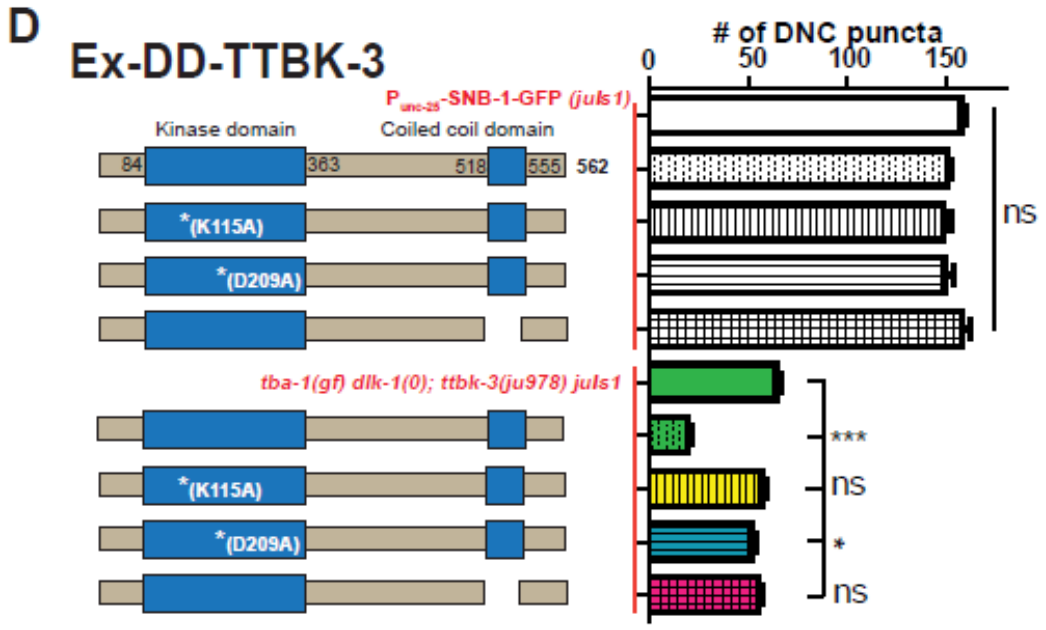

Figure 3.4 (continued) Kinase activity of *ttbk-3* is required for suppressing *tba-1(gf) dlk-1(0)*

(A) Gene structure of *ttbk-3*, with *ju978* and the deletion allele *tm4006* marked. (B) Representative images of DD neuron synapses along the DNC in adult animals imaged using P_{unc-25}-SNB-1-GFP (*juIs1*). Ex-Muscle-TTBK-3 and Ex-DDneuron-TTBK-3 denotes extrachromosomal copies of wild type TTBK-3 expressed under *myo-3* (muscle) and *flp-13* (DD neuron) promoters, respectively. Scale bar: 10 µm. (C) Quantification of synaptic puncta in the DNC (P_{unc-25}-SNB-1::GFP (*juIs1*)) of adult animals. Ex-TTBK-3 denotes extrachromosomal copies of wild type TTBK-3 expressed under its own promoter. Data are mean ± SEM; n>10 animals per genotype. Statistics: One-Way ANOVA followed by Tukey's posttest; ***p<0.001, ns- not significant. (D) Quantification of synaptic puncta in the DNC (P_{unc-25}-SNB-1::GFP (*juIs1*)) of adult animals. TTBK-3 contains a kinase domain and a C-terminal coiled-coil domain. Loss of either kinase domain activity (using kinase dead K115A and D209A mutants), or the coiled-coil domain in extrachromosomal copies of TTBK-3 (P_{flp-13}-TTBK-3), result in a failure to rescue *tba-1(gf) dlk-1(0); ttbk-3(ju978) juIs1* animals. Data are mean ± SEM; n>8 animals per genotype. Statistics: One-Way ANOVA followed by Tukey's posttest;*p<0.05, ***p<0.001, ns-not significant.

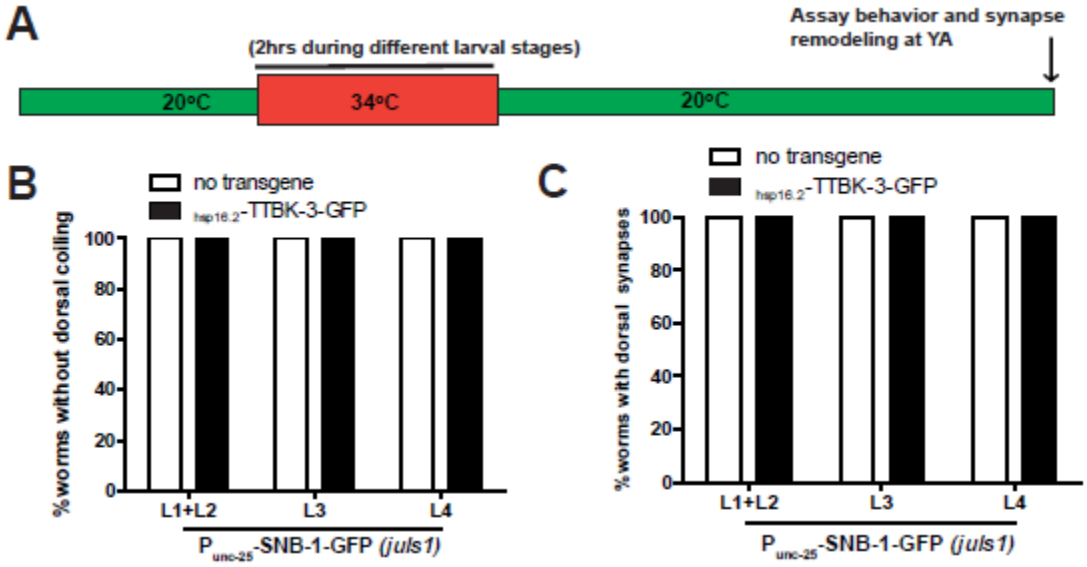

Figure 3.5 TTBK-3 is required for synapse maintenance during remodeling

(A) Schematic of heat shock assay, where animals are maintained at 20°C, undergo a 2hr heat shock during the developmental stage being tested, after which they are returned to 20°C and assayed at young adult stage. (B-E) Quantification of % animals with normal behavior (B, D) and synapse remodeling (C, E) following heat shock at L1-L4 stages. Data collected from 3 independent biological replicates, with n>10 animals each, and presented as mean ± SEM. Statistics- 2-Way ANOVA followed by Bonferroni posttest; ***p<0.001. (F) Representative images of DD neuron synapses along the DNC in adult animals imaged using P_{unc-25}-SNB-1-GFP (*juIs1*). Scale bar: 10 μm.

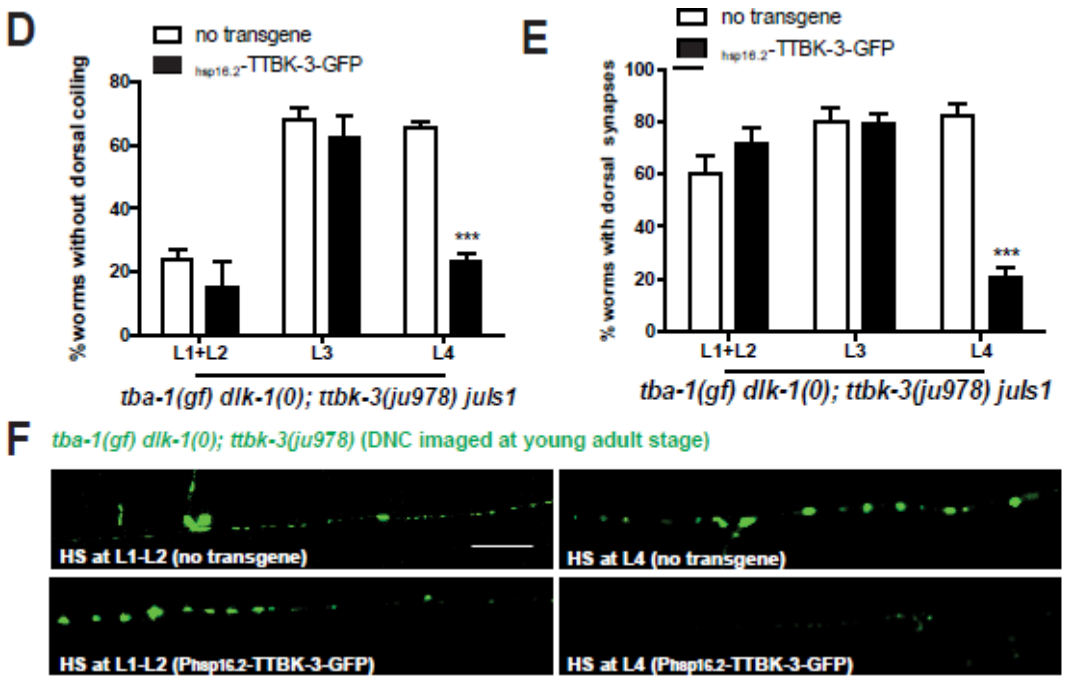

Figure 3.5 (continued) TTBK-3 is required for synapse maintenance during remodeling

(A) Schematic of heat shock assay, where animals are maintained at 20°C, undergo a 2hr heat shock during the developmental stage being tested, after which they are returned to 20°C and assayed at young adult stage. (B-E) Quantification of % animals with normal behavior (B, D) and synapse remodeling (C, E) following heat shock at L1-L4 stages. Data collected from 3 independent biological replicates, with n>10 animals each, and presented as mean ± SEM. Statistics- 2-Way ANOVA followed by Bonferroni posttest; ***p<0.001. (F) Representative images of DD neuron synapses along the DNC in adult animals imaged using P_{unc-25}-SNB-1-GFP (*juIs1*). Scale bar: 10 μm.

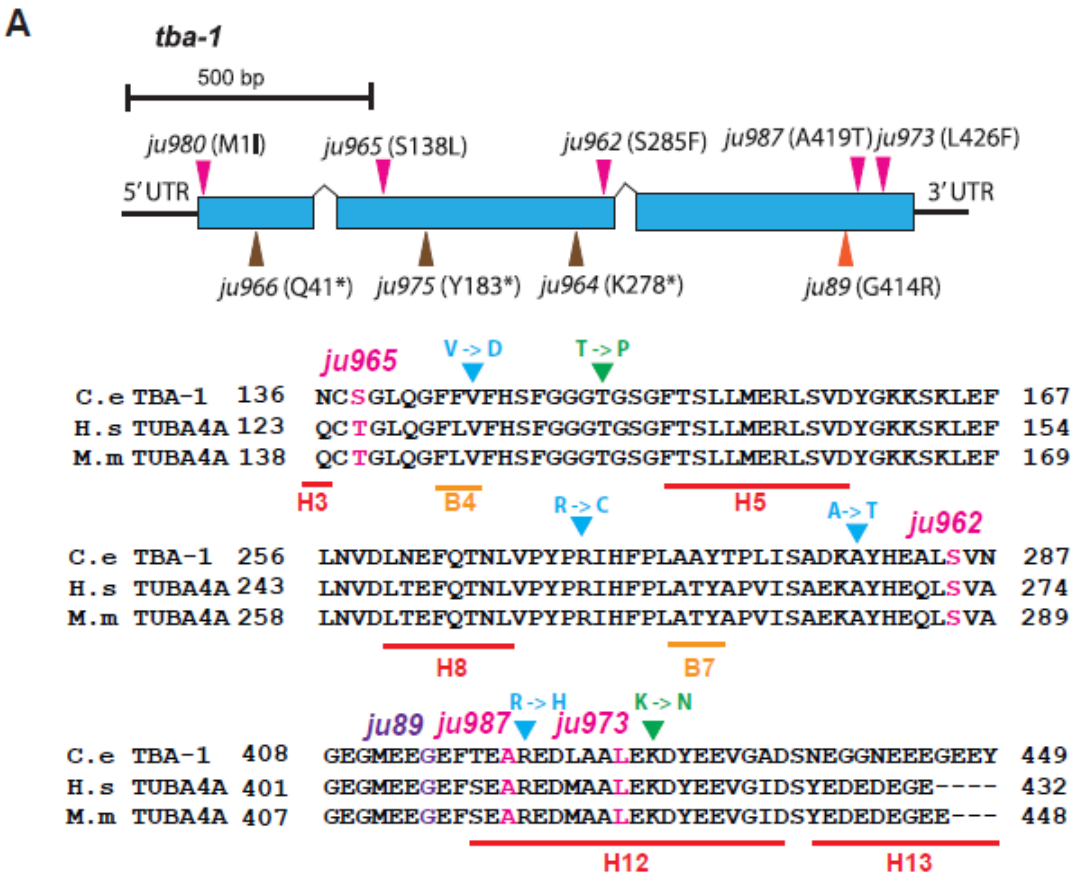

Figure 3.S1 Related to Figure 3.1

(A) Sequence alignment of parts of *C.elegans*, *H. sapiens* and *M. musculus* homologs of TBA-1. Sequence conservation of *ju89*, *ju962*, *ju965*, *ju973* and *ju987* is shown, as well as the location of various helices (H) and beta sheets (B). Also annotated are mutations linked to ALS (in green) and lissencephaly (in blue) disease phenotypes in patient samples. (B) Sequence alignment of parts of *C.elegans*, *H. sapiens* and *M. musculus* homologs of TBB-2, highlighting the conserved Proline that is altered in *ju1535*, which lies between H9 and H10 helices of *tbb-2*. (C) Structure prediction of *C. elegans* TBA-1 (based on PDB#4i4tc) modeled on SWISS-MODEL and rendered using PyMOL, with *ju89* (G414R) and the various missense mutations identified during the suppressor screen are also marked. (D) Structure prediction of *C. elegans* TBA-1 and TBB-2 (based on PDB# 1JFF) modeled on SWISS-MODEL and rendered using PyMOL, with the position of the internal and external MT surface, and the positions of *ju89* and *ju1535* highlighted.

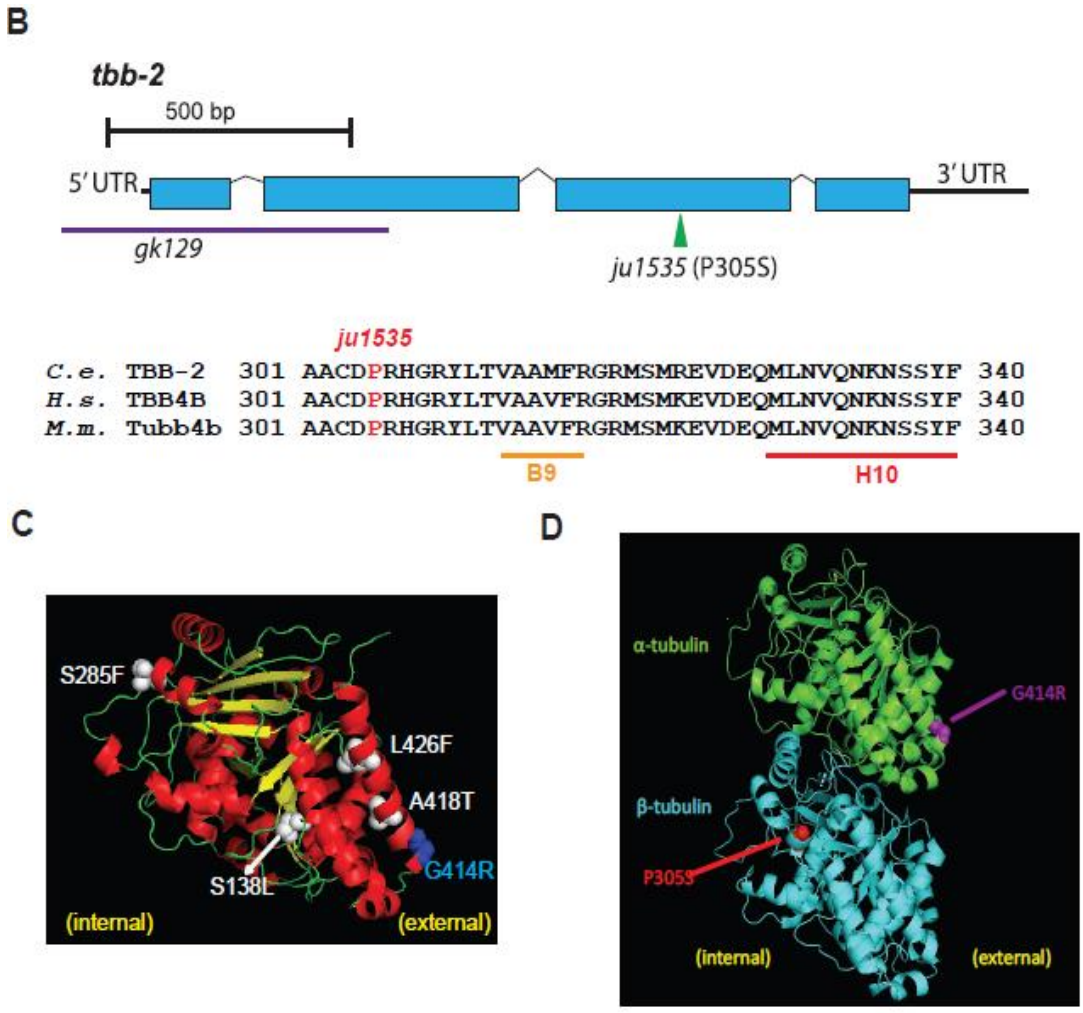

Figure 3.S1 (continued) Related to Figure 3.1

(A) Sequence alignment of parts of *C.elegans*, *H. sapiens* and *M. musculus* homologs of TBA-1. Sequence conservation of *ju89*, *ju962*, *ju965*, *ju973* and *ju987* is shown, as well as the location of various helices (H) and beta sheets (B). Also annotated are mutations linked to ALS (in green) and lissencephaly (in blue) disease phenotypes in patient samples. (B) Sequence alignment of parts of *C.elegans*, *H. sapiens* and *M. musculus* homologs of TBB-2, highlighting the conserved Proline that is altered in *ju1535*, which lies between H9 and H10 helices of *tbb-2*. (C) Structure prediction of *C. elegans* TBA-1 (based on PDB#4i4tc) modeled on SWISS-MODEL and rendered using PyMOL, with *ju89* (G414R) and the various missense mutations identified during the suppressor screen are also marked. (D) Structure prediction of *C. elegans* TBA-1 and TBB-2 (based on PDB# 1JFF) modeled on SWISS-MODEL and rendered using PyMOL, with the position of the internal and external MT surface, and the positions of *ju89* and *ju1535* highlighted.

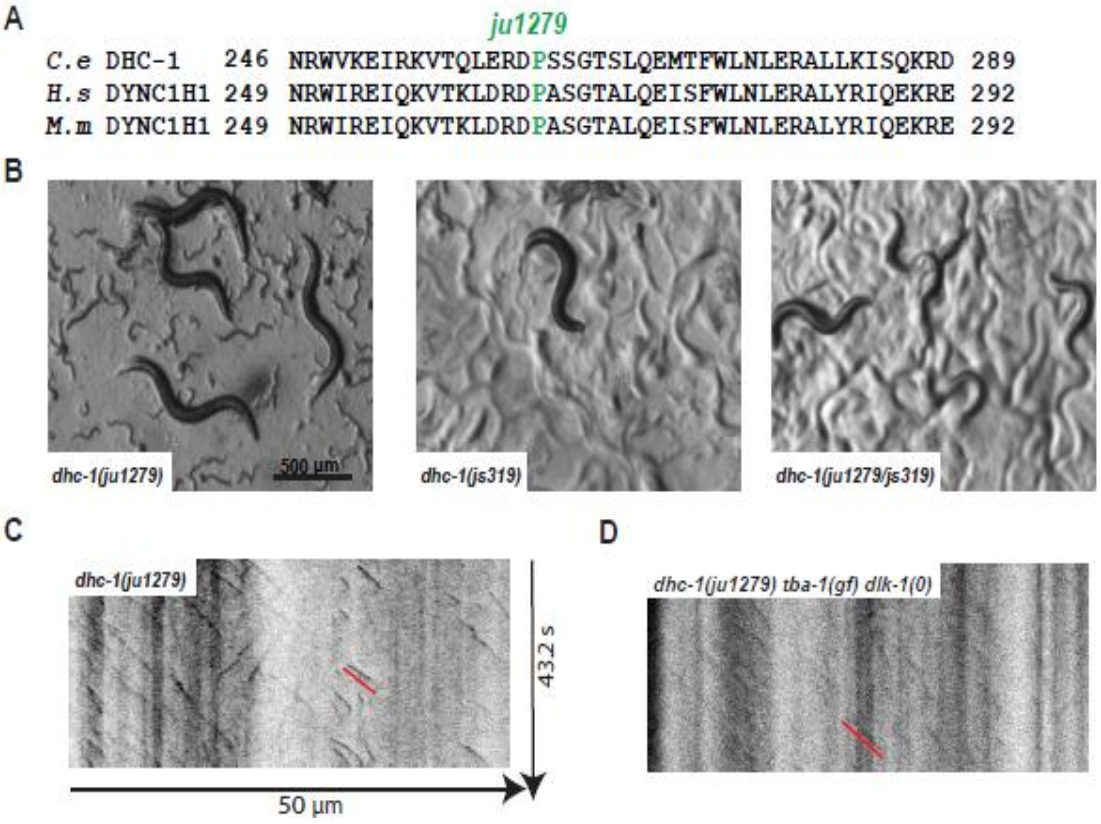

Figure 3.S2 Related to Figure 3.2

(A) Alignment of sequences of dynein heavy chains from *C.elegans*, *H. sapiens* and *M. musculus*, surrounding the conserved Proline residue that is mutated in *ju1279*. (B) Bright field images of various *dhc-1* alleles (homozygous *ju1279* and *js319*, and heterozygous *ju1279/js319*) cultured at 25^{o}C. (C, D) Representative kymographs of EBP-2 movement in the adult VNC of the respective genotypes. Red lines indicate EBP-2 comets moving in the anterograde direction. (E, F) Quantification of number of EBP-2 comets (D) and their direction of movement (E) for various genotypes. Data are mean ± SEM; n= number of animals (shown on (E)). Statistics: One-way ANOVA followed by Tukey's posttest; ***p<0.001, n.s.-not significant. (G) Bright field images of various *dnc-4* alleles (homozygous *ju933* and *or633*, and heterozygous *ju933/or633*) cultured at 25^{o}C.

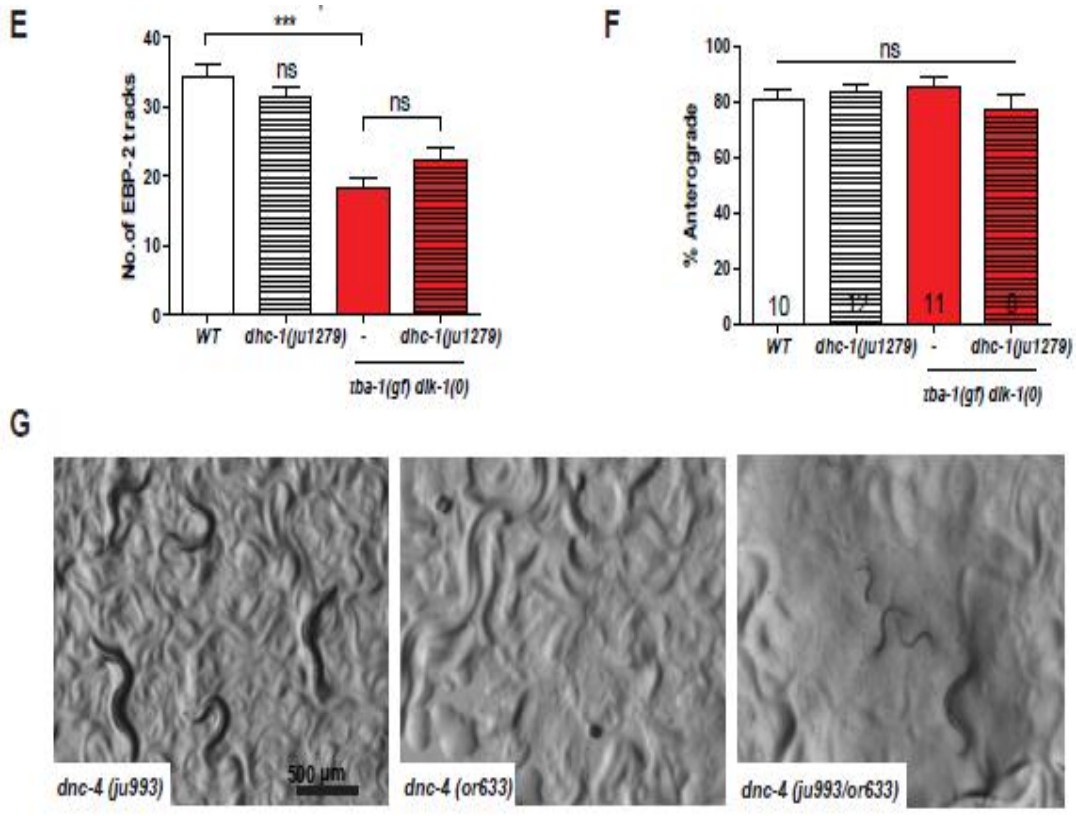

Figure 3.S2 (continued) Related to Figure 3.2

(A) Alignment of sequences of dynein heavy chains from *C.elegans*, *H. sapiens* and *M. musculus*, surrounding the conserved Proline residue that is mutated in *ju1279*. (B) Bright field images of various *dhc-1* alleles (homozygous *ju1279* and *js319*, and heterozygous *ju1279/js319*) cultured at 25°C. (C, D) Representative kymographs of EBP-2 movement in the adult VNC of the respective genotypes. Red lines indicate EBP-2 comets moving in the anterograde direction. (E, F) Quantification of number of EBP-2 comets (D) and their direction of movement (E) for various genotypes. Data are mean ± SEM; n= number of animals (shown on (E)). Statistics: One-way ANOVA followed by Tukey's posttest; ***p<0.001, n.s.-not significant. (G) Bright field images of various *dnc-4* alleles (homozygous *ju933* and *or633*, and heterozygous *ju933/or633*) cultured at 25°C.

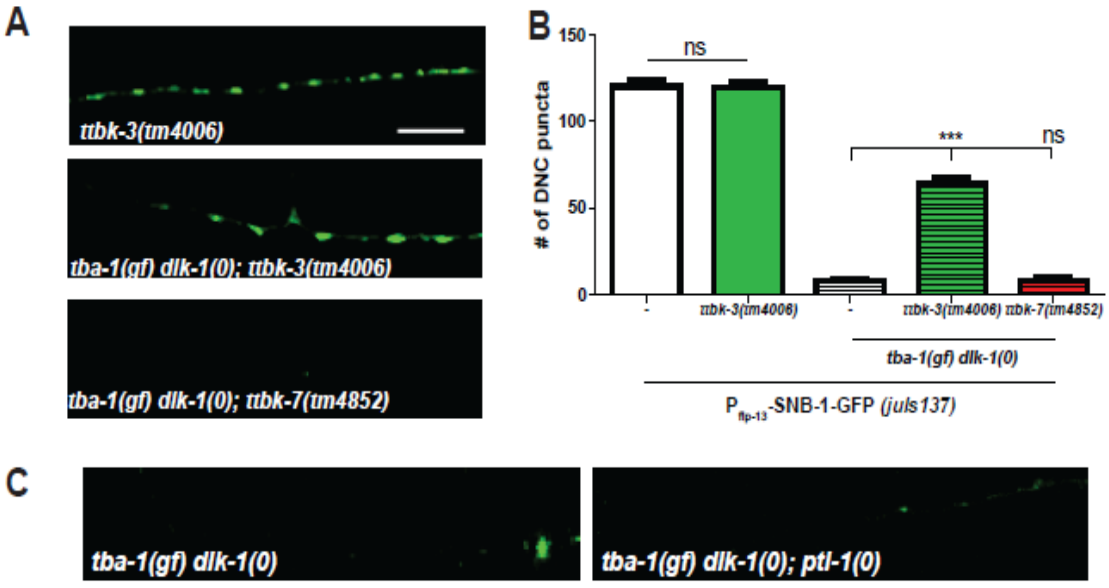

Figure 3.S3 Related to Figure 3.4 and 3.5

(A) Representative images of DD synapses along the DNC in adult animals using P_{flp-13}-SNB-1-GFP (*juIs137*). Scale bar: 10 µm. (B) Quantification of synaptic puncta in the DNC of adult animals. Data are mean ± SEM; n>10 animals per genotype. Statistics: One-Way ANOVA followed by Tukey's posttest; ***p<0.001, ns- not significant. (C) Representative images of synaptic puncta along the DNC imaged using P_{unc-25}-SNB-1-GFP (*juIs1*). Scale bar: 10 µm. (D) Representative images of TTBK-3-GFP expression in the GABAergic D motor neurons (driven by the *unc-25* promoter) in L3, L4 and adult animals. (E) Quantification of number of EBP-2 comets for various genotypes. Data are mean ± SEM; Statistics: One-way ANOVA followed by Tukey's posttest; ***p<0.001, n.s.-not significant. (F) Representative images of young adult wild type animals carrying the $P_{hsp-16.2}$-TTBK-3-GFP transgene, 4 hours after a 2hr heat shock period. Punctate structures are seen in the pharynx, some head neurons, the intestinal lumen, CAN neuron and a posterior intestinal cell. Scale bar: 10 µm.

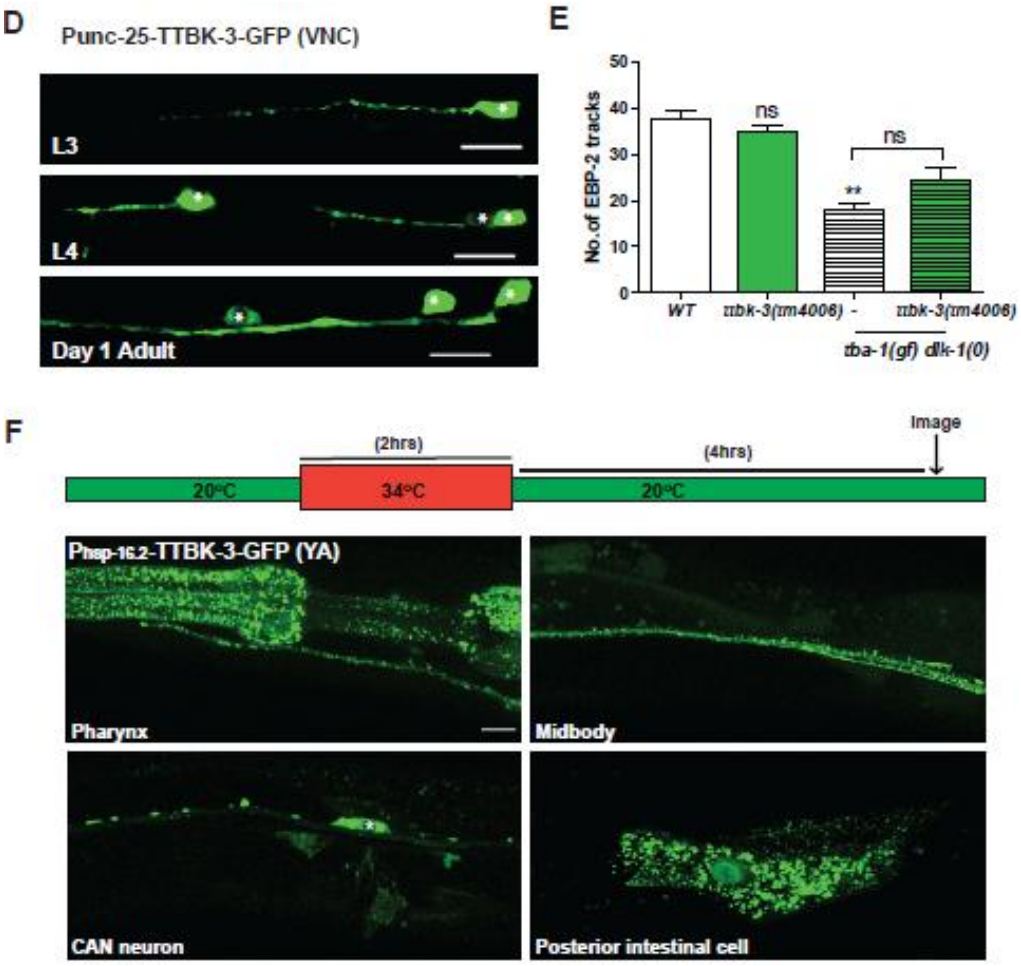

Figure 3.S3 (continued) Related to Figure 3.4 and 3.5

(A) Representative images of DD synapses along the DNC in adult animals using P_{flp-13}-SNB-1-GFP (*juIs137*). Scale bar: 10 µm. (B) Quantification of synaptic puncta in the DNC of adult animals. Data are mean ± SEM; n>10 animals per genotype. Statistics: One-Way ANOVA followed by Tukey's posttest; ***p<0.001, ns- not significant. (C) Representative images of synaptic puncta along the DNC imaged using P_{unc-25}-SNB-1-GFP (*juIs1*). Scale bar: 10 µm. (D) Representative images of TTBK-3-GFP expression in the GABAergic D motor neurons (driven by the *unc-25* promoter) in L3, L4 and adult animals. (E) Quantification of number of EBP-2 comets for various genotypes. Data are mean ± SEM; Statistics: One-way ANOVA followed by Tukey's posttest; ***p<0.001, n.s.-not significant. (F) Representative images of young adult wild type animals carrying the $P_{hsp-16.2}$-TTBK-3-GFP transgene, 4 hours after a 2hr heat shock period. Punctate structures are seen in the pharynx, some head neurons, the intestinal lumen, CAN neuron and a posterior intestinal cell. Scale bar: 10 µm.

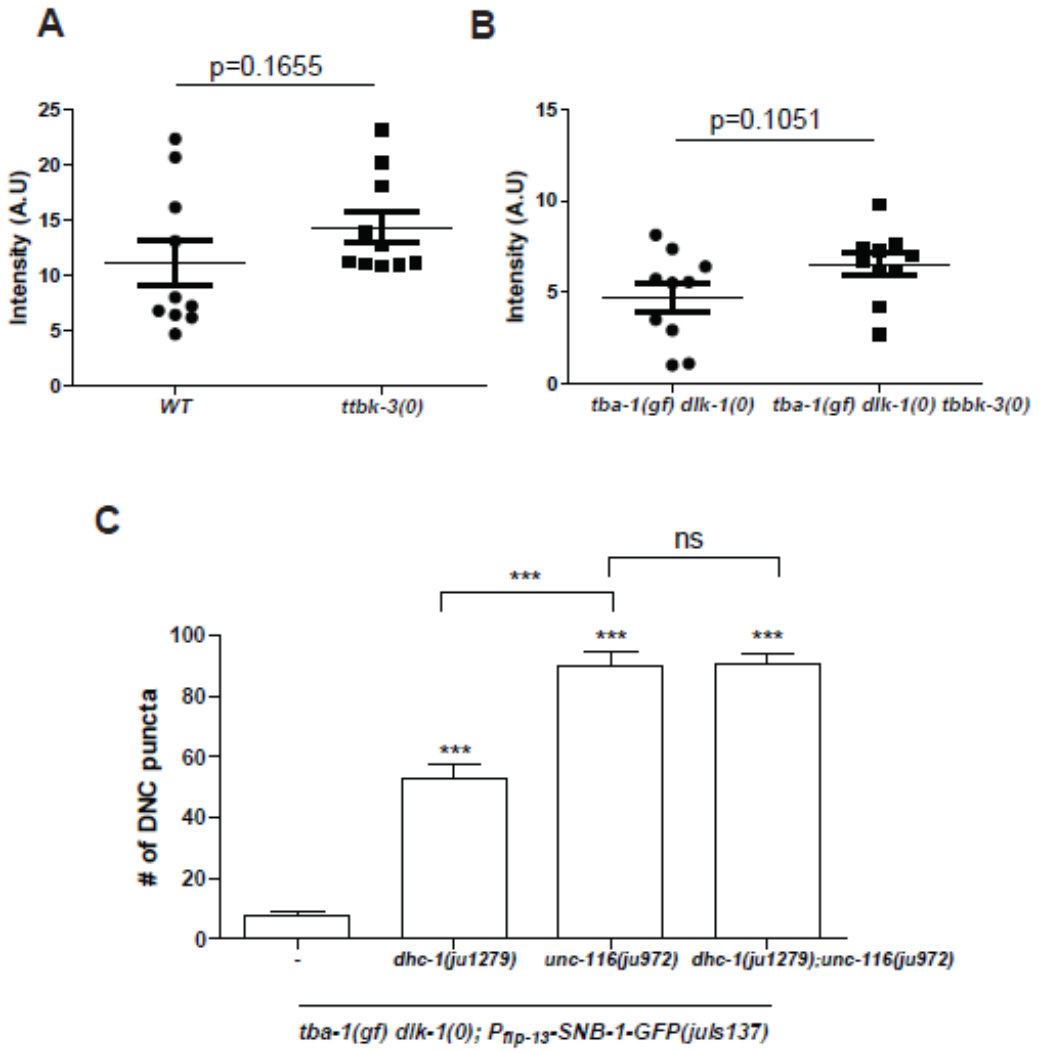

Figure 3.S4 Related to Discussion and Figure 3.5

(A, B) Quantification of SNB-1::GFP intensity (P_{flp-13}-SNB-1-GFP (*juIs137*)) in the DNC of L4 animals, anaesthetized using 30mM muscimol. Data are mean ± SEM; n=10 animals per genotype. Statistics: Mann-Whitney test, p-values are displayed on graph. (C) Quantification of synaptic puncta in the DNC of adult animals. Data are mean ± SEM; n>10 animals per genotype. Statistics: One-Way ANOVA followed by Tukey's posttest; ***p<0.001, ns- not significant.

Table 3.1 Suppressors of *tba-1(gf) dlk-1(0)*

Allele	**Gene**	**Mutation** **Amino acid (nu)**	**Function**
ju962	*tba-1*	S285F (C854T)	MT architecture
ju964	*tba-1*	K278*(A837T)	MT architecture
ju965	*tba-1*	S138L(C413T)	MT architecture
ju966	*tba-1*	Q41*(C121T)	MT architecture
ju973	*tba-1*	L426F(C1371T)	MT architecture
ju975	*tba-1*	Y183*(C599A)	MT architecture
ju980	*tba-1*	M1I(G3A)	MT architecture
ju987	*tba-1*	A419T(G1350A)	MT architecture
ju1535	*tbb-2*	P305S(C1062T)	MT architecture
ju972	*unc-116*	G274R(G1400A)	Transport
ju977	*unc-116*	E432K(G1921A)	Transport
ju1279	*dhc-1*	P262L(C832T)	Transport
ju993	*dnc-4*	S368F(G841A)	Transport
ju978	*ttbk-3*	W484*(G2440A)	Kinase
ju982	*ifp-1*	L363F(C1087T)	Cytoskeleton
ju963	*ifp-1*	P443S(C1327T)	Cytoskeleton

Table 3.2 List of strains used in this study

Strain	Genotype	Allele or Transgene
CZ333	*juIs1 IV*	*juIs1* [*Punc-25-SNB-1::GFP; lin-15(+)*]
CZ2569	*tba-1(ju89) I; juIs1 IV*	*ju89*: Gly414Arg
CZ15940	*dlk-1(tm4024) I; juIs1 IV*	*tm4024*: 460 bp deletion
CZ12121	*tba-1(ju89)dlk-1(tm4024) I; juIs1 IV*	
CZ2060	*juIs137 II*	*juIs137* [*Pflp-13-$_{SNB}$-1::GFP; lin-15(+)*]
CZ18652	*dlk-1(tm4024) I; juIs137 II*	
CZ2411	*tba-1(ju89) I; juIs137 II*	
CZ12177	*sem-4(n1378) tba-1(ju89) tba-1(ju962) dlk-1(tm4024) I; juIs1 IV*	*ju962*: Ser285Phe
CZ12179	*sem-4(n1378) tba-1(ju89) tba-1(ju964) dlk-1(tm4024) I; juIs1 IV*	*ju964*: Lys278*
CZ12180	*sem-4(n1378) tba-1(ju89) tba-1(ju965) dlk-1(tm4024) I; juIs1 IV*	*ju965*: Ser138Leu
CZ12181	*sem-4(n1378) tba-1(ju89) tba-1(ju966) dlk-1(tm4024) I; juIs1 IV*	*ju966*: Gln41*
CZ12345	*tba-1(ju89) tba-1(ju973) dlk-1(tm4024) I; juIs1 IV*	*ju973*: Leu426Phe
CZ12363	*tba-1(ju89) tba-1(ju975) dlk-1(tm4024) I; juIs1 IV*	*ju975*: Tyr183*
CZ12368	*tba-1(ju89) tba-1(ju980) dlk-1(tm4024) I; juIs1 IV*	*ju980*: Met1Iso
CZ12375	*tba-1(ju89) tba-1(ju987) dlk-1(tm4024) I; juIs1 IV*	*ju987*: Ala419Thr
C21593	*tba-1(ju89) dlk-1(tm4024) I; juIs1 IV; ifp-1(ju982) X*	*ju982*: Leu363Phe

Table 3.2 (continued) List of strains used in this study

CZ21594	*tba-1(ju89) dlk-1(tm4024) I; juIs137 II; ifp-1(ju982) X*	
CZ21596	*dlk-1(tm4024) I; juIs137 II; ifp-1(ju982) X*	
CZ21595	*tba-1(ju89) I; juIs137 II; ifp-1(ju982) X*	
CZ21597	*juIs137 II; ifp-1(ju982) X*	
CZ25360	*tbb-2(ju1535) III; juIs1 IV*	*ju1535*: Pro305Ser
CZ25355	*tba-1(ju89) I; tbb-2(ju1535) III; juIs1 IV*	
CZ25359	*tba-1(ju89) dlk-1(tm4024) I; tbb-2(ju1535) III; juIs1 IV*	
CZ25565	*tba-1(ju89) dlk-1(tm4024) I; tbb-2(gk129) III; juIs1 IV*	*gk129*: 766 bp deletion
CZ25564	*tbb-2(gk129) III; juIs1 IV*	
CZ25571	*juIs1 IV; juEx*	*juEx7692* [Ptbb-2-TBB-2; gcy-8-GFP]
CZ25574	*tba-1(ju89) dlk-1(tm4024) I; tbb-2(ju1535) III; juIs1 IV; juEx*	*juEx7695* [Ptbb-2-TBB-2; gcy-8-GFP]
CZ21346	*dhc-1(ju1279) tba-1(ju89) dlk-1(tm4024) I; juIs1 IV; ifp-1(ju963) X*	*ju963*: Pro443Ser *ju1279*: Pro262Leu
CZ21819	*tba-1(ju89) dlk-1(tm4024) I; juIs1 IV; ifp-1(ju963) X*	
CZ15115	*tba-1(ju89) dlk-1(tm4024) I; unc-116(ju977) III; juIs1 IV*	*ju977*: Glu432Lys
CZ23620	*tba-1(ju89) dlk-1(tm4024) I; dnc-4(ju993) juIs1 IV*	*ju993*: Val229Iso
CZ22433	*tba-1(ju89) dlk-1(tm4024) I; ttbk-3(ju978) juIs1 IV*	*ju978*: Trp484*
CZ22439	*dhc-1(ju1279) I; juIs137 II*	
CZ24719	*dhc-1(js319) I; juIs137 II*	*js319*: Splice site mutation
CZ16989	*tba-1(ju89)dlk-1(tm4024) I; juIs137 II*	
CZ22440	*dhc-1(ju1279) tba-1(ju89) dlk-1(tm4024) I; juIs137 II*	

Table 3.2 (continued) List of strains used in this study

CZ16994	*tba-1(ju89) dlk-1(tm4024) I;unc-116(ju972) III; juIs1 IV*	*ju972*: Gly274Arg
CZ16633	*unc-116(ju972) III; juIs1 IV*	
CZ16991	*tba-1(ju89) I; unc-116(ju972) III; juIs1 IV*	
CZ17360	*dlk-1(tm4024) I; unc-116(ju972) III; juIs1 IV*	
CZ16631	*tba-1(ju89)dlk-1(tm4024) I*	
CZ17824	*juEx5317*	*juEx5317* [*Punc-25-EBP-2::GFP; Pgcy-8-GFP*]
CZ20218	*tba-1(ju89)dlk-1(tm4024) I; juEx5317*	
CZ23623	*dhc-1(ju1279) I; juEx5317*	
CZ23624	*dhc-1(ju1279) tba-1(ju89)dlk-1(tm4024) I; juEx5317*	
CZ23625	*ttbk-3(tm4006) IV; juEx5317*	*tm4006*: 786 bp deletion + 21 bp insertion
CZ23626	*tba-1(ju89) dlk-1(tm4024) I; ttbk-3(tm4006) IV; juEx5317*	
CZ24382	*juIs137 II; juEx7441*	*juEx7441* [*Fosmid-WRM0639aB10; Pgcy-8-GFP*]
CZ24385	*dhc-1(ju1279) tba-1(ju89) dlk-1(tm4024) I; juIs137 II; juEx7444*	*juEx7444* [*Fosmid- WRM0639aB10; Pgcy-8-GFP*]
CZ17362	*juIs137 II; unc-116(ju972) III*	
	tba-1(ju89) dlk-1(tm4024) I; juIs137 II; unc-116(ju972) III	
CZ24580	*dhc-1(ju1279) I; juIs137 II; unc-116(ju972) III*	
CZ24581	*dhc-1(ju1279) I; tba-1(ju89) dlk-1(tm4024) I; juIs137 II; unc-116(ju972) III*	
CZ22741	*dnc-4(ju993) juIs1 IV*	

Table 3.2 (continued) List of strains used in this study

CZ23893	*dnc-4(ju993) juIs1 IV; juEx7288*	*juEx7288* [*Pdnc-4-DNC-4; Pgcy-8-GFP*]
CZ23896	*tba-1(ju89) dlk-1(tm4024) I; dnc-4(ju993) juIs1 IV; juEx7291*	*juEx7291* [*Pdnc-4-DNC-4; Pgcy-8-GFP*]
EU1506	*dnc-4(or633) IV*	*or633*: Glu42Lys
CZ23901	*tba-1(ju89) dlk-1(tm4024) I; juIs137 II; dnc-4(or633) IV*	
CZ22866	*juIs1 IV; juEx6991*	*juEx6991* [*Pttbk-3-TTBK-3; Pgcy-8-GFP*]
CZ22869	*tba-1(ju89) dlk-1(tm4024) I; ttbk-3(ju978) juIs1 IV; juEx6994*	*juEx6994* [*Pttbk-3-TTBK-3; Pgcy-8-GFP*]
CZ23362	*tba-1(ju89) dlk-1(tm4024) I; ttbk-3(ju978) juIs1 IV; juEx*	*juEx7141* [*Pmyo-3-TTBK-3; Pgcy-8-GFP*]
CZ23356	*tba-1(ju89) dlk-1(tm4024) I; ttbk-3(ju978) juIs1 IV; juEx*	*juEx7135* [*Pflp-13-TTBK-3; Pgcy-8-GFP*]
CZ24387	*juIs1 IV; juEx7447*	*juEx7447* [*Pflp-13-TTBK-3(cDNA full length); Pgcy-8-GFP*]
CZ24394	*juIs1 IV; juEx7453*	*juEx7453* [*Pflp-13-TTBK-3(cDNA (ΔCC)); Pgcy-8-GFP*]
CZ23627	*juIs1 IV; juEx7235*	*juEx7235* [*Pflp-13-TTBK-3(cDNA (K115A)); Pgcy-8-GFP*]

Table 3.2 (continued) List of strains used in this study

CZ23628	*juIs1 IV; juEx7236*	*juEx7236* [*Pflp-13-TTBK-3(cDNA (D209A); Pgcy-8-GFP*]
CZ24391	*tba-1(ju89) dlk-1(tm4024) I; ttbk-3(ju978) juIs1 IV; juEx7450*	*juEx7450* [*Pflp-13-TTBK-3(cDNA full length); Pgcy-8-GFP*]
CZ24397	*tba-1(ju89) dlk-1(tm4024) I; ttbk-3(ju978) juIs1 IV; juEx7456*	*juEx7456* [*Pflp-13-TTBK-3(cDNA (ΔCC)); Pgcy-8-GFP*]
CZ23629	*tba-1(ju89) dlk-1(tm4024) I; ttbk-3(ju978) juIs1 IV; juEx7237*	*juEx7237* [*Pflp-13-TTBK-3(cDNA (K115A)); Pgcy-8-GFP*]
CZ23632	*tba-1(ju89) dlk-1(tm4024) I; ttbk-3(ju978) juIs1 IV; juEx7241*	*juEx7241* [*Pflp-13-TTBK-3(cDNA (D209A)); Pgcy-8-GFP*]
CZ22965	*juIs137 II; ttbk-3(tm4006) IV*	
CZ23149	*tba-1(ju89) dlk-1(tm4024); juIs137 II; ttbk-3(tm4006) IV*	
CZ24720	*tba-1(ju89) dlk-1(tm4024); juIs137 II; ttbk-7(tm4852) V*	*tm4852*: 1051 bp deletion + 9 bp insertion
CZ22962	*tba-1(ju89) dlk-1(tm4024); ptl-1(ok621) III; juIs1 IV*	*ok621*: 1933 bp deletion
CZ24570	*juIs1 IV; juEx7537*	*juEx7537* [*Phsp16.2-TTBK-3-GFP; Pmyo-2-mCherry*]
CZ24574	*tba-1(ju89) dlk-1(tm4024) I; ttbk-3(ju978) juIs1 IV; juEx7541*	*juEx7541* [*Phsp16.2-TTBK-3-GFP; Pmyo-2-mCherry*]
CZ25487	*juEx7680*	*juEx7680* [*Punc-25-TTBK-3-GFP; Pgcy-8-GFP*]

Table 3.3 List of constructs used in this study

Plasmid	Description	Transgenes generated
pCZGY3197	tbb-2(2.4 kb promoter)-tbb-2 genomic DNA–tbb-2 3'UTR (156 bp)	*juEx7692-97* (Injected at 5 ng/µl)
pCZGY2332	unc-25(2 kb promoter)-EBP-2 cDNA-mGFP-unc-54 3'UTR	*juEx5317, juEx5318* (Injected at 5 ng/µl)
pCZGY3198	dnc-4(1.5 kb promoter)-dnc-4 genomic DNA–dnc-4 3'UTR (200 bp)	*juEx7288-93* (Injected at 20 ng/ µl)
pCZGY3199	ttbk-3(600 bp promoter)-ttbk-3 genomic DNA –ttbk-3 3'UTR (97 bp)	*juEx6991-96* (Injected at 10 ng/ µl)
pCZGY3201	flp-13(2.1 kb promoter)- ttbk-3 genomic DNA -unc-54 3'UTR	*juEx7132-37* (Injected at 20 ng/ µl)
pCZGY3202	myo-3(2.4 kb promoter)- ttbk-3 genomic DNA -unc-54 3'UTR	*juEx7138-43* (Injected at 20 ng/ µl)
pCZGY3207	flp-13(2.1 kb promoter)-ttbk-3 cDNA(full length)-unc-54 3'UTR	*juEx7447-52* (Injected at 1 ng/ µl)
pCZGY3208	flp-13(2.1 kb promoter)-ttbk-3 cDNA(ΔCC)-unc-54 3'UTR	*juEx7453-58* (Injected at 1 ng/ µl)
pCZGY3209	flp-13(2.1 kb promoter)-ttbk-3 cDNA(K115A)-unc-54 3'UTR	*juEx7235; juEx7237-39* (Injected at 20 ng/ µl)
pCZGY3210	flp-13(2.1 kb promoter)-ttbk-3 cDNA(D209A)-unc-54 3'UTR	*juEx7236; juEx7240-42* (Injected at 20 ng/ µl)
pCZGY3211	hsp16.2(436 bp promoter)-ttbk-3genomic DNA-GFP-unc-54 3'UTR	*juEx7537-7542* (Injected at 50 ng/ µl)
pCZGY3212	unc-25(1.2 kb promoter)-ttbk-3genomic DNA-GFP-unc-54 3'UTR	*juEx7680-7681*(Injected at 50 ng/µl)

Table 3.4 List of cloning primers used in this study

Primer	Sequence	Description
YJ12226	CGCAATAATGCACATTTGTGTG	Forward primer for amplifying TBB-2 genomic sequence to generate pCZGY3197
YJ12227	GATAGCATTCACTTCACTCAGATGC	Reverse primer for amplifying TBB-2 genomic sequence to generate pCZGY3197
YJ12228	GCACGAATTTGGAAAACTCG	Forward primer for amplifying DNC-4 genomic sequence to generate pCZGY3198
YJ12229	TACTCCATCTTGCCAGAATATTG	Reverse primer for amplifying DNC-4 genomic sequence to generate pCZGY3198
YJ12230	GATGTAATGTTGAAGTGAGAGTAGCC	Forward primer for amplifying TTBK-3 genomic sequence to generate pCZGY3199
YJ12231	GCAGCTCAGATATTTTTTATGTGCC	Reverse primer for amplifying TTBK-3 genomic sequence to generate pCZGY3199
YJ12232	ATGGTTGATGTAAGTGACAATGTTTTC	Forward primer for amplifying TTBK-3 genomic sequence (without promoter) to generate pCZGY3201-3202 and pCZGY3211-3212

Table 3.4 (continued) List of cloning primers used in this study

YJ12233	ATGGTTGATAAAAACAAAAAGAATCTTCC	Forward primer for amplifying TTBK-3 cDNA sequence to generate pCZGY3207-3210
YJ12234	TTATTTTGGAGATGAATTGAAAGTTCC	Reverse primer for amplifying TTBK-3 cDNA sequence to generate pCZGY3207-3210
YJ12235	GTCGCTCTGAAGTATTTGACGACTTTCAATTCATCTCCAA	Forward primer for site directed mutagenesis to generate pCZGY3208 from pCZGY3207
YJ12236	TTGGAGATGAATTGAAAGTCGTCAAATACTTCAGAGCGAC	Reverse primer for site directed mutagenesis to generate pCZGY3208 from pCZGY3207
YJ12237	GATCAGTATTACGCTGTAGCAATAGAAGTTCGCCTTACCTC	Forward primer for site directed mutagenesis to generate pCZGY3209 from pCZGY3207
YJ12238	GAGGTAAGGCGAACTTCTATTGCTACAGCGTAATACTGATC	Reverse primer for site directed mutagenesis to generate pCZGY3209 from pCZGY3207
YJ12239	AAGGTTTCATTCATCGAGCTATAAAACCGGAAAACCTATTGA	Forward primer for site directed mutagenesis to generate pCZGY3210 from pCZGY3207
YJ12240	TCAATAGGTTTTCCGGTTTTATAGCTCGATGAATGAAACCTT	Reverse primer for site directed mutagenesis to generate pCZGY3210 from pCZGY3207

References

Baran, R., Castelblanco, L., Tang, G., Shapiro, I., Goncharov, A., & Jin, Y. (2010). Motor neuron synapse and axon defects in a *C. elegans* alpha-tubulin mutant. *PloS one*, *5*:e9655.

Baugh, L. R., Hill, A. A., Slonim, D. K., Brown, E. L., & Hunter, C. (2003) Composition and dynamics of the Caenorhabditis elegans early embryonic transcriptome. *Development, 30,* 889–900.

Brenner, S. (1974) The genetics of *Caenorhabditis elegans. Genetics*, *77*, 71–94.

Belyy, V., Schlager, M. A., Foster, H., Reimer, A. E., Carter, A. P., & Yildiz, A. (2016). The mammalian dynein – dynactin complex is a strong opponent to kinesin in a tug-of-war competition. *Nature cell biology*, *18*(9), 1016-1024.

Bigelow, H., Doitsidou, M., Sarin, S., & Hobert, O. (2009) MAQGene: software to facilitate *C. elegans* mutant genome sequence analysis. *Nature methods, 6,* 549.

Bouskila, M., Esoof, N., Gay, L., Fang, E. H., Deak, M., Begley, M. J., Cantley, L. C., Prescott, A., Storey, K. G., & Alessi, D. R. (2013). TTBK2 kinase substrate specificity and the impact of spinocerebellar-ataxia-causing mutations on expression, activity, localization and development. *Biochem J.*, *437*(1), 157-167.

Bulat, V., Rast, M., & Pielage, J. (2014). Presynaptic CK2 promotes synapse organization and stability by targeting Ankyrin2. *JCB, 204*(1), 77-94.

Carter, A. P., Diamant, A. G., & Urnavicius, L. (2016). How dynein and dynactin transport cargos : a structural perspective. *Current opinion in structural biology*, *37*, 62-70.

Ecker, C. (2016). The neuroanatomy of autism spectrum disorder : An overview of structural neuroimaging findings and their translatability to the clinical setting. *Autism*, doi: 10.1177/1362361315627136.

Fukushige, T., Yasuda, H., & Siddiqui, S. S. (1995) Selective expression of the tba-1 alpha tubulin gene in a set of mechanosensory and motor neurons during the development of Caenorhabditis elegans. *Biochimica et Biophysica Acta, 1261,* 401–406.

Gogonea, C. B., Gogonea, V., Ali, Y. M. Jr, & Siddiqui, S. S. (1999) Computational prediction of the three-dimensional structures for the Caenorhabditis elegans tubulin family. *Journal of Molecular Graphics and Modelling*, *17*, 90-100.

Hallam, S.J. & Jin, Y. (1998) *lin-14* regulates the timing of synaptic remodeling in *Caenorhabditis elegans*. *Nature, 395,* 644-647.

Hendricks, A. G., Lazarus, J. E., Perlson, E., Gardner, M. K., Odde, D. J., Goldman, Y. E., & Holzbaur, E. L. F. (2012). Dynein tethers and stabilizes dynamic microtubule plus ends. *Current Biology*, *22*(7), 632-637.

Hendricks, A. G., Perlson, E., Ross, J. L., Schroeder III. H. W., Tokito, M., & Holzbaur, E. L. F. (2010). Motor coordination via a tug-of-war mechanism drives bidirectional vesicle transport. *Current Biology*, *20*(8), 697-702.

Hensch, T. K. (2004). Critical period regulation. *Annual review of neuroscience*, *27*, 549-79.

Holtmaat, A., & Svoboda, K. (2009). Experience-dependent structural synaptic plasticity in the mammalian brain. *Nature reviews. Neuroscience*, *10*, 647-658.

Hong, Y. K., Park, S., Litvina, E. Y., Morales, J., Sanes, J. R., & Chen, C. (2014). Refinement of the retinogeniculate synapse by bouton clustering. *Neuron*, *84*(2), 332-339.

Jorgensen, E. M., & Mango, S. E. (2002). The art and design of genetic screens: Caenorhabditis elegans. *Nature reviews Genetics*, *3*, 356-369.

Jin, Y., & Garner, C. C. (2008). Molecular mechanisms of presynaptic differentiation. *Annu. Rev. Cell Dev. Biol.*, *24*: 237-62.

Kardon, J. R., & Vale, R. D. (2009). Regulators of the cytoplasmic dynein motor. *Nature reviews. Molecular cell biology*, *10*(12), 854-865.

Karki, S., Tokito, M. K., & Holzbaur, E. L. F. (2000). A dynactin subunit with a highly conserved cysteine-rich motif interacts directly with Arp1. *The Journal of biological chemistry*, *275*(7), 4834-4839.

Keays, D.A., Tian, G., Poirier, K., Huang, G.J., Siebold, C., Cleak, J., Oliver, P.L., Fray, M., Harvey, R.J., Molnar, Z., Piñon, M. C., Dear, N., Valdar, W., Brown, S. D. M., Davies, K. E., Rawlins, J. N. P., Cowan, N. J., Nolan, P., Chelly, J., & Flint, J. (2007) Mutations in alpha-tubulin cause abnormal neuronal migration in mice and lissencephaly in humans. *Cell*, 128, 45–57.

Koushika, S. P., Schaefer, A. M., Vincent, R., Willis, J. H., Bowerman, B., & Nonet, M. L. (2004). Mutations in Caenorhabditis elegans cytoplasmic dynein components reveal specificity of neuronal retrograde cargo. *Journal of Neuroscience*, *24*(16), 3907-3916.

Kumar, R. A, Pilz, D. T., Babatz, T. D., Cushion, T. D., Harvey, K., Topf, M., Yates, L., Robb, S., Uyanik, G., Mancini, G. M. S., Rees, M. I., Harvey, R. J., & Dobyns, W. B. (2010). TUBA1A mutations cause wide spectrum lissencephaly (smooth brain) and suggest that multiple neuronal migration pathways converge on alpha tubulins. *Human molecular genetics*, *19*(14), 2817-27.

Kurup, N., & Jin, Y. (2016). Neural circuit rewiring : insights from DD synapse remodeling. *Worm*, *5*(1), e1129486. doi:10.1080/21624054.2015.1129486.

Kurup, N., Yan, D., Goncharov, A., & Jin, Y. (2015). Dynamic microtubules drive circuit rewiring in the absence of neurite remodeling. *Current Biology*, *25*(12), 1594-1605.

Lewis, D. A., & Levitt, P. (2002). Schizophrenia as a disorder of neurodevelopment. *Annu. Rev. Neurosci.*, *25*, 409-32.

Liao, J.-chi, Yang, T. T., Weng, R. R., Kuo, C.-te, & Chang, C.-wei. (2015). TTBK2 : A tau protein kinase beyond tau phosphorylation. *BioMed Research International*, doi.org/10.1155/2015/575170.

Lockhead, D., Schwarz, E. M., Hagan, R. O., Bellotti, S., Krieg, M., Barr, M. M., Dunn, A. R.,

Sternberg, P. W. & Goodman, M. B. (2016) The tubulin repertoire of C. elegans sensory neurons and its context-dependent role in process outgrowth. *Mol. Biol. Cell* doi: 10.1091/mbc.E16-06-0473.

Luo, L., & Leary, D. D. M. O. (2005). Axon retraction and degeneration in development and disease. *Annu. Rev. Neurosci.*, *28*, 127-156.

Lu, C., Srayko, M., & Mains, P. E. (2004) The Caenorhabditis elegans microtubule-severing complex MEI-1/MEI-2 katanin interacts differently with two superficially redundant beta-tubulin isotypes. *Mol. Biol. Cell.*, *15*, 142-50.

Marc, R. E., Jones, B. W., Watt, C. B., & Strettoi, E. (2003). Neural remodeling in retinal degeneration. *Progress in Retinal and Eye Research*, *22*, 607-655.

Manning, G., 2005 Genomic overview of protein kinases. WormBook**:** 1-19.

Martin, M., Iyadurai, S. J., Gassman, A., Gindhart, J. G., Hays, T. S., & Saxton, W. M. (1999). Cytoplasmic dynein, the dynactin complex, and kinesin are interdependent and essential for fast axonal transport. *Molecular biology of the cell*, *10*, 3717-3728.

McAllister, A. K. (2007). Dynamic aspects of CNS synapse formation. *Annu. Rev. Neurosci. 30*: 425–50.

Mello, C. C., Kramer, J. M., Stinchcomb, D., & Ambros, V. (1991) Efficient gene transfer in *C. elegans*: extrachromosomal maintenance and integration of transforming sequences. *EMBO J.*, *10*, 3959-3970.

Meng, L., Mulcahy, B., Cook, S.J., Neubauer, M., Wan, A., Jin, Y., & Yan, D. (2015). The cell death pathway regulates synapse elimination through cleavage of gelsolin in Caenorhabditis elegans neurons. *Cell Reports*, 11(11):1737-1748.

Millecamps, S., & Julien, J.-P. (2013). Axonal transport deficits and neurodegenerative diseases. *Nature reviews. Neuroscience*, *14*, 161-176.

Neal, S. J., Park, J., DiTiroo, D., Yoon, J., Shibuya, M., Choi, W., Schroeder, F. C., Butcher, R. A., Kim, K., & Sengupta, P. (2016). A forward genetic screen for molecules involved in pheromone-induced dauer formation in C. elegans. *G3*, doi:10.1534/g3.115.026450.

Nogales, E., Wolf, S. G., & Downing, K. H. (1998). Structure of the αβ tubulin dimer by electron crystallography. *Nature*, *391*, 199-204.

O' Rourke, S. M., Carter, C., Carter, L., Christensen, S. N., Jones, M. P., Nash, B., Price, M. H., Turnbull, D. W., Garner, A. R., Hamill, D. R., Osterberg, V. R., Lyczak, R., Madison, E. E., Nguyen, M. H., Sandberg, N. A., Sedghi, N., John, H., Yochem, J., Johnson, E. A., & Bowerman, B. (2011). A survey of new temperature-sensitive, embryonic-lethal mutations in *C. elegans* : 24 alleles of thirteen genes. *PloS one*, *6*(3), e16644.

O' Rourke, S. M.., Dorfman, M. D., Carter, J. C., & Bowerman, B. (2007). Dynein modifiers in *C. elegans* : light chains suppress conditional heavy chain mutants. *PLoS genetics*, *3*(8), e128.

Ou, C.-Y., Poon, V. Y., Maeder, C. I., Watanabe, S., Lehrman, E. K., Fu, A. K. Y., Park, M., Fu,

W-Y., Jorgensen, E.M., Ip, N. Y., & Shen, K.(2010). Two cyclin-dependent kinase pathways are essential for polarized trafficking of presynaptic components. *Cell*, *141*(5), 846-58.

Park, M., Watanabe, S., Poon, V.Y.N., Ou, C-Y, Jorgensen, E.M. & Shen, K. (2011). CYY-1/cyclin Y and CDK-5 differentially regulate synapse elimination and formation for rewiring neural circuits. *Neuron*, 70(4):742-57.

Urnavicius, L., Zhang, K., Diamant, A. G., Motz, C., Schlager, M. A., Yu, M., Patel, N. A., Robinson, C. V., Carter, A. P., Sapp, P. C., Leblond, C. S., Mckenna-yasek, D., Gkazi, A., Al-chalabi, A., & Berg, L. H. V. D. (2015). The structure of the dynactin complex and its interaction with dynein. *Science*, *347*(6229), 1441-1446.

Sakaguchi-Nakashima, A., Meir, J. Y., Jin, Y., Matsumoto, K., & Hisamoto, N. (2007). LRK-1, a *C. elegans* PARK8-related kinase, regulates axonal-dendritic polarity of SV proteins. *Current biology*, *17*, 592-8.

Sanes, J. R. & Lichtman, J. W. (1999). Development of the vertebrate neuromuscular junction. *Annu. Rev. Neurosci.* 22,389–442.

Sato, S., Cerny, R. L., Buescher, J. L., & Ikezu, T. (2006). Tau-tubulin kinase 1 (TTBK1), a neuron-specific tau kinase candidate, is involved in tau phosphorylation and aggregation. *J. Neurochem.*, (98), 1573-1584.

Smith, B. N., Ticozzi, N., Fallini, C., Gkazi, A. S., Topp, S., Kenna, K. P., Scotter, E. L., Kost, J., Keagle, P., Miller, J. W., Calini, D., Vance, C., Danielson, E. W., Troakes, C., Tiloca, C., Al-sarraj, S., Lewis, E. A., King, A., Colombrita, C., Pensato, V., Castellotti, B., Belleroche, J. D., Baas, F., Lma, A., Sapp, P. C., Mckenna-yasek, D., Mclaughlin, R. L., Polak, M., Asress, S., Mun, L., Dion, P. A., Leblond, C. S., Rouleau, G. A., Hardiman, O., Veldink, J. H., Berg, L. H. V. D., Al-chalabi, A., Pall, H., Shaw, P. J., Turner, M. R., Talbot, K., Taroni, F., Wu, Z., Glass, J. D., Gellera, C., Ratti, A., Brown, R. H. & Garcı, A. (2014). Exome-wide rare variant analysis identifies TUBA4A mutations associated with familial ALS. *Neuron*, *84*, 324-331.

Wang, Y., & Mandelkow, E. (2015). Tau in physiology and pathology. *Nature reviews. Neuroscience*, *17*(1), 5-21.

Waterman-Storer, C. M., Karki, S. B., Kuznetsov, S. A., Tabb, J. S., Weiss, D. G., Langford, G. M., & Holzbaur, E. L. F. (1997). The interaction between cytoplasmic dynein and dynactin is required for fast axonal transport. *PNAS*, *94*(October), 12180-12185.

White, J.G., Albertson, D.G., & Anness, M.A.R. (1978). Connectivity changes in a class of motor neurons during the development of a nematode. *Nature*, 271:764-766.

Yeh, T., Quintyne, N. J., Scipioni, B. R., Eckley, D. M., & Schroer, T. A. (2012). Dynactin's pointed-end complex is a cargo-targeting module. *Molecular biology of the cell*, *23*, 3827-3837.

Chapter 4

Intermediate filaments modulate microtubule dynamics to facilitate synapse rewiring

Abstract

Connectivity changes in developing neural circuits utilize a coordinated cellular machinery to form and eliminate synaptic connections. During larval development of *C. elegans* motor neurons, synapses are stereotypically rewired through a process facilitated by dynamic microtubules (MTs). Here, we identify a novel regulatory role for intermediate filaments (IFs) during synapse formation in neural circuit refinement. Through a combination of live imaging and ultrastructural analysis, we show that motor neurons with an increase in IFs displayed increased MT stability and a failure to rewire synapses. Conversely, either knocking out IF subunits or pharmacologically disrupting IF networks promotes MT dynamics and synaptic vesicle transport during synapse rewiring. Our data suggest that an elevation in IF levels inhibits MT dynamics *in vivo*. Several human motor neuron diseases are characterized by IF accumulation in axonal swellings; and our work sheds light on the impact of IFs on MT dynamics and axonal transport.

Introduction

A robust cytoskeletal network is essential to many aspects of neuronal function, including axon outgrowth, guidance and maintenance; as well as synapse formation and plasticity (Conde & Caceres, 2009; Dillon & Goda, 2005; Yuan, Rao & Nixon, 2017). Intermediate filaments (IFs) are one such cytoskeletal polymer, which comprise of different

classes that are expressed in a variety of tissues. Neurofilaments (NFs) are a specific IF class expressed in neurons that provide structural support for the establishment of axon caliber in large diameter myelinated axons (Lee & Cleveland, 1996; Yuan, Rao &Nixon, 2017). Overexpression of NFs in some mouse models has linked NF accumulation to motor neuron death, with impairment of axonal transport thought to be a precursor to neuron degeneration (Beaulieu, Nguyen, & Julien, 1999; Lee, Marszalek & Cleveland, 1994; Xu et. al., 1993). Changes in NF levels have also been associated with neuropsychiatric disorders such as bipolar disorder and schizophrenia, although whether NFs alter circuit activity remains unknown (Yuan & Nixon, 2016). The complexity in subunit composition and the variety of posttranslational modifications associated with NFs suggest potential roles for these filaments in neuronal functions outside of the maintenance of axon caliber (Snider & Omary, 2014). For example, several studies have shown a requirement for microtubule (MT) motors in mediating IF motility and report a close association between IFs and MTs during MT assembly (Bocquet et al., 2009; Chang & Goldman, 2004; Gan et al., 2016), supporting a mechanistic interaction between the two cytoskeletal networks.

In this study, we describe a novel role for IF assembly in promoting MT stabilization during synapse rewiring using *C. elegans*, a genetically tractable animal model extensively used to examine neuronal cytoskeletal architecture (Chalfie & Thomson, 1982; Chisholm et al., 2016). A comprehensive map of the *C. elegans* connectome in larvae and adults revealed a striking switch in motor neuron connectivity during larval development, independent of axon outgrowth or retraction (Hallam & Jin, 1998; White, Albertson & Anness, 1978; White et al., 1986). We previously found that an upregulation in the number of dynamic MTs was required for synaptic vesicle transport during motor neuron synapse rewiring (Kurup et al., 2015). Here, we show that IFs prevent synapse rewiring by hyper stabilizing neuronal MTs. Loss of IF subunits or pharmacological disruption of IF networks promotes MT dynamics and facilitates synapse rewiring. Our results reveal an unexpected role for IFs in maintaining MT stability during the

establishment of synaptic connections in functional neuronal circuits.

Results

Intermediate filament genes regulate synapse rewiring in *C. elegans*

At the end of larval stage 1 (L1), the Dorsal-D (DD) type motor neurons rewire their pre-synaptic connections from the ventral nerve cord (VNC) to the dorsal nerve cord (DNC), concurrent with the birth of Ventral-D (VD) type motor neurons, which then form synapses along the VNC (Kurup & Jin, 2016). We visualized DD-neuron pre-synaptic terminals using a GFP tagged synaptobrevin (SNB-1::GFP) reporter (*juIs137*: $P_{flp\text{-}13}$ SNB-1::GFP). In L1 animals, discrete synaptic puncta were present along the ventral neurites (Kurup et al., 2015), but in late larvae and adults, synaptic puncta were only seen along the dorsal neurites (Figure 4.1 A, C). We had previously shown that DD synapse remodeling depends on synergistic interactions between the MT cytoskeleton and the conserved MAPKKK DLK-1 using double mutant animals of a missense α-tubulin mutation (*tba-1(gf)*) and loss of function in *dlk-1(0)* that were defective in DD synapse rewiring (Kurup et al., 2015). Adult *tba-1(gf) dlk-1(0)* animals retained synaptic puncta along the VNC with little to no synapses along the DNC (Figure 4.1 A, C), resulting from a loss of dynamic MTs that impaired synaptic vesicle transport during rewiring (Kurup et al., 2015).

To identify regulators of MT dynamics during synapse rewiring, we screened for mutants that suppressed synapse rewiring defects in *tba-1(gf) dlk-1(0)* animals (Kurup et al., 2015, 2017). We identified two independent alleles (*ju982* and *ju963*) of a *C. elegans* IF homologue, *ifp-1* (Figure 4.1B). IFP-1 contains a conserved rod domain and a C-terminal Lamin Tail Domain, and shares 31% sequence identity with human NF α-internexin (Kaplan et al., 1990; Yuan et al., 2006; Figure 4.1B). *ju982* caused a conserved Leucine 363 to Phenylalanine change in the rod domain, while *ju963* changed Proline 443 to Serine adjacent to the rod domain (Figure 4.1B). Both alleles restored synapses to the dorsal neurite in *tba-1(gf) dlk-1(0)*. A null

mutation, *ifp-1(ok1609)* (hereafter denoted *ifp-1(0)*), that removes most of the rod domain and causes a premature stop showed stronger suppression of the synaptic defects of *tba-1(gf) dlk-1(0)* than either *ju983* or *ju963*, suggesting that they were hypomorphic alleles of *ifp-1* (Figure 4.1 A-C). Transgenic overexpression of wild-type IFP-1 specifically in the DD neurons of *tba-1(gf) dlk-1(0); ifp-1(ju982)* and *tba-1(gf) dlk-1(0); ifp-1(ju963)* animals restored the synapse rewiring defects seen in *tba-1(gf) dlk-1(0)* alone (Figure 4.1C). These results indicated that loss of function in *ifp-1* suppresses *tba-1(gf) dlk-1(0)* phenotypes, and that *ifp-1* acts cell autonomously to regulate DD synapse rewiring. *ifp-1* loss of function mutants alone displayed normal synapses, and overexpression of IFP-1 in wild-type animals also did not an effect on the number of synapses of DD neurons (Figure 4.1 A, C), suggesting that the effect of *ifp-1* on synapse formation was dependent on *tba-1(gf) dlk-1(0)*.

We next characterized IF expression in wild-type and *tba-1(gf) dlk-1(0)* animals. Using a transcriptional GFP reporter (driven by 1 kb upstream of the transcription start site of *ifp-1*), we found that IFP-1 was strongly expressed in the intestine and pharynx, as previously reported (Karabinos, Schunemann & Weber, 2006; Figure 4.S1A). Low levels of neuronal expression might be obscured by robust non-neuronal expression. To test this, we used RNAi to reduce the GFP signal in non-neuronal cells, since neurons in *C. elegans* are refractory to systemic RNAi (Winston, Molodowitch & Hunter, 2002). In P*ifp-1-GFP* transgenic animals with dampened intestinal and pharyngeal GFP expression, we observed weak GFP expression in the VNC and some head neurons (Figure 4.1D). We then examined IFP-1 protein expression by generating extrachromosomal transgenic animals expressing GFP fused to the C-terminal end of genomic IFP-1. In wild-type animals, IFP-1::GFP localized to filaments and puncta in the head, pharynx, and intestine (Figure 4.1E). In contrast, expression of IFP-1(L363F)::GFP, mimicking *ifp-1(ju982)*, showed a near complete loss of filamentous expression (Figure 4.S1C). In *tba-1(gf) dlk-1(0)* animals we observed an increase in IFP-1::GFP filament length and bundling in the intestine, while the number of IFP-1::GFP puncta in the head was reduced (Figure 4.S1B).

The *C. elegans* genome encodes 11 cytoplasmic IF homologs, at least 5 of which are essential for development as null mutants exhibit embryonic or larval lethality (Carberry et al., 2009; Karabinos et al., 2001; Winston, Molodowitch & Hunter, 2002; Woo et al., 2004; Zuela & Gruenbaum, 2001; Figure 4.S2A). To test whether other IFs besides *ifp-1* played a role in DD synapse rewiring, we crossed mutants of the non-essential IFs to *tba-1(gf) dlk-1(0)* double mutant animals. We quantitated the number of DNC synapses in *tba-1(gf) dlk-1(0)* adult animals, and found that loss of IFA-4 (*ifa-4(0)*) also restored DNC synapses, although to a lesser extent than *ifp-1(0)* (Figure 4.2A, B). These results suggest that *ifp-1* may act in concert with other cytoplasmic IFs to modulate DD synapse rewiring.

To examine endogenous IFA-4 expression, we inserted GFP at the C-terminal end of IFA-4 using CRISPR-Cas9 mediated genome engineering (Dickinson et al., 2013; Figure 4.2C). We observed strong expression of IFA-4::GFP (*ju1576)* predominantly in the excretory cells and rectum of young larvae (Figure 4.2D). In gravid adults, IFA-4::GFP was expressed at the pharynx-intestinal valve and formed a network within the uterus (Figure 4.S2B, C). The expression pattern of IFA-4::GFP was largely unaffected by *tba-1(gf) dlk-1(0)*, and we could not detect neuronal expression of IFA-4 protein in either wild-type or *tba-1(gf) dlk-1(0)* animals by live imaging (Figure 4.2D, 4.S2B, C). However, IFA-4 transcripts were detected in GABAergic D neurons in previous microarray analyses (Spencer et al., 2011). To test that even low expression levels of IFs in D neurons of *tba-1(gf) dlk-1(0)* resulted in defective synapse rewiring, we next took advantage of a recently developed GFP-degron system, which enabled the targeted depletion of GFP tagged proteins in a cell-type specific manner (Armenti et al., 2014; Wang et al., 2017). We expressed a transgene containing a nanobody against GFP fused to ZIF-1 specifically in the GABAergic D neurons. Since ZIF-1 targets proteins for cullin dependent degradation, any GFP-tagged protein in the D neurons would be degraded in animals expressing the transgene, while remaining intact in the rest of the animal (Armenti et al., 2014; Wang et al., 2017; Figure 4.2E). We confirmed the efficacy of this strategy by visibly knocking down of

SNB-1::GFP from *juIs137* animals, while a co-injection marker expressing GFP in the AFD neurons was unaffected (Figure 4.S2D and data not shown). We did not find any synaptic puncta in the dorsal neurites of adult *tba-1(gf) dlk-1(0)* animals expressing mCherry::RAB-3 in the D neurons, both when IFA-4 was tagged with GFP or was untagged (Kurup et al., 2015; Figure 4.2F). Depletion of IFA-4::GFP in the D neurons of *tba-1(gf) dlk-1(0)* animals led to the appearance of mCherry::RAB-3 puncta along the DNC, consistent with the suppression of synapse remodeling defects in *tba-1(gf) dlk-1(0)* by *ifa-4(0)* (Figure 4.2F). Taken together with the loss of synapses along the DNC in *tba-1(gf) dlk-1(0); ifp-1(0)* animals by the over-expression of IFP-1 specifically in the DD neurons (Figure 4.1C), we conclude that an increase in neuronal expression of IFs suppressed synapse rewiring.

IFs stabilize MTs in DD motor neurons

To understand how IF assembly was altered in the DD neurons of *tba-1(gf) dlk-1(0)* animals, we made reconstructions of serial section electron micrographs (EM) of the ventral DD neurite (~8 μm, Figure 4.3A-D, 4.S3A-D). We defined IFs as ~10 nm diameter continuous filaments along the reconstructed neurites. While we did not detect IFs in the ventral neurite of wild-type DD neurons, we found numerous long IFs in *tba-1(gf) dlk-1(0)* animals (Figure 4.3A, B). As a control, we also analyzed reconstructed DD neurites in *tba-1(gf) dlk-1(0); unc-116(ju972)* animals, which carried an additional Kinesin-1 mutation that suppressed the synapse rewiring defects of *tba-1(gf) dlk-1(0)* without altering MT dynamics (Kurup et al., 2015). *tba-1(gf) dlk-1(0); unc-116(ju972)* animals retained the long IFs seen in *tba-1(gf) dlk-1(0)* animals (Figure 4.3D, E). In contrast, *tba-1(gf) dlk-1(0); ifp-1(0)* triple mutant animals had a few fragmented IFs that were significantly shorter than *tba-1(gf) dlk-1(0)* animals (Figure 4.3C, E). Additionally, compared to wild-type animals, *tba-1(gf) dlk-1(0)* animals had an additional population of MTs >4 μm in length (Figure 4.3A, B, F). This population of long MTs was observed in *tba-1(gf) dlk-1(0); unc-116(ju972)* animals, but not in *tba-1(gf) dlk-1(0); ifp-1(0)*

triple mutants (Figure 4.3C, D, F). Additionally, micrographs from *tba-1(gf) dlk-1(0); ifp-1(0)* animals also contained more MTs/section on average than both wild-type and *tba-1(gf) dlk-1(0)* animals (Figure 4.3G). Taken together, these observations suggested that loss of IFs in *tba-1(gf) dlk-1(0)* resulted in a shift from prolonged MT growth to shorter more numerous MTs.

As the presence of IFs correlated with the presence of longer MTs, we hypothesized that IFs could play a role in modulating MT dynamics. To test this hypothesis, we assayed MT plus end dynamics in wild-type and *tba-1(gf) dlk-1(0)* animals, as well as *ifp-1(0)* and *ifa-4(0)* animals in the wild-type and *tba-1(gf) dlk-1(0)* backgrounds. We imaged the MT plus end-binding protein EBP-2 tagged to GFP expressed in the D motor neurons of adult animals, and analyzed growing MTs depicted by the appearance of tracks on kymographs (Kurup et al., 2015; Figure 4.4A). Most MT growth was in the anterograde direction in both wild-type and mutant animals, with differences arising in the number of growing MTs (Figure 4.4A-C). *tba-1(gf) dlk-1(0)* animals had a severe reduction in the number of dynamic MTs, compared to wild-type animals, as previously reported (Kurup et al., 2015; Figure 4.4A-C). *ifp-1(0)* and *ifa-4(0)* single mutants displayed normal MT dynamics, consistent with the lack of IFs in wild-type DD neurons (Figure 4.4A, C). Strikingly, both *ifp-1 (0)* and *ifa-4 (0)* reversed the impairment in MT dynamics in *tba-1(gf) dlk-1(0)* animals (Figure 4.4A, C), supporting a role for IFs in stabilizing MTs in DD neurons.

Pharmacological destabilization of IFs restores MT dynamics and synapse rewiring

Since we found that loss of IFs in *tba-1(gf) dlk-1(0)* animals could restore MT dynamics and promote synapse rewiring, we next wanted to test if pharmacologically manipulating IF assembly would result in a similar phenotype. 2, 5 Hexanedione (2, 5HD) is a metabolite of the industrial solvent hexane that causes IF disruption upon application to cultured mammalian cells (Durham, 1987), as well as chemical modifications of NFs in mammalian axons that possibly disrupt NF interaction with MTs, although the precise mechanism of 2, 5HD action is unclear

(Llorens, 2013; Xue, Shtylla & Brown, 2015). We first characterized the effects of 2, 5 HD exposure on *C. elegans* IF assembly using IFP-1::GFP. Chronic exposure of wild-type *C. elegans* to 2, 5 HD at concentrations greater than 1mM resulted in a reduction in brood size and significant developmental delays or even embryonic lethality, presumably because of the disruption of essential IF networks in the intestine and epidermis (Karabinos et al., 2001; Woo et al., 2004; Figure 4.S4A). Animals grown on 1mM 2, 5 HD were superficially wild-type in development and brood size (Figure 4.S4A). Under this condition, 2, 5 HD caused a strong reduction of IFP-1::GFP expression in the head, but IFP-1::GFP in the intestine appeared to aggregate (Figure 4.5A, 4.S4B).

We then tested whether this change in IF assembly could alter MT dynamics, by treating wild-type and *tba-1(gf) dlk-1(0)* L1 animals with 1mM 2, 5HD, acutely for ~9 hrs before the onset of synapse rewiring (Figure 4.5B). We found that there was no change in the number or direction of growth of dynamic MTs in wild-type animals after the acute 2, 5HD treatment, consistent with wild-type DD neurons lacking detectable IFs (Figure 4.5C-E). Interestingly, in *tba-1(gf) dlk-1(0)* acute 2, 5HD treatment caused a significant increase in MT dynamics, while the overall direction of MT growth was unchanged (Figure 4.5C-E). We also monitored synapse rewiring after acute treatment of L1 larvae with 1mM 2, 5 HD (Fig. 5f, g). Acute 2, 5 HD treatment did not alter synapse rewiring in wild-type or *tba-1(gf) dlk-1(0); ifp-1(0)* animals (Figure 4.5F, G). However, there was a significant increase in the number of synaptic puncta successfully reaching the dorsal neurite of adult *tba-1(gf) dlk-1(0)* animals following acute 2, 5HD treatment, accompanied by a reduction in the number of synaptic puncta retained along the ventral neurite (Figure 4.5F, G). Taken together, these results suggest that the presence of IFs was sufficient to shift the balance from dynamic to stable MTs to antagonize synapse rewiring in *C. elegans*.

Discussion

Actin, MTs and IFs constitute the three major cytoskeletal elements in most eukaryotic cells, and their co-ordinated interactions have been the subject of intense study for decades. The importance of IF-MT interactions in maintaining the cellular IF network was first demonstrated several years ago, when treatment of BHK-21 cells with colchicine to remove MTs resulted in IF aggregation as a juxtanuclear cap (Goldman, 1971). Here we focus on IF-MT interactions in neuronal development, using *C. elegans* as a model. The synapse rewiring defects in *tba-1(gf) dlk-1(0)* double mutants are a result of hyperstable MTs, and loss of function in IF genes *ifp-1* and *ifa-4* restored normal synapse rewiring in this background. We further characterized IF-MT interactions in living animals, revealing an underappreciated regulatory function for neuronal IFs in modulating MT dynamics *in vivo*. Our data suggest that the absence of IFs in wild-type DD motor neurons permits the MT destabilization required to facilitate synaptic vesicle transport to new sites during neural circuit rewiring. The functional significance of a bidirectional interaction between IF and MT networks is particularly relevant in neurodegenerative disease conditions like giant axonal neuropathy (GAN) , amyotrophic lateral sclerosis (ALS) and Charcot–Marie–Tooth disease, where toxic assemblies of IFs in neurons correlate with a fatal loss of motor and sensory function (Ashbury et al., 1972; . Lariviere & Julien, 2004).

Several observations are conducive to the idea that axonal MT stability is directly linked to IF levels. IFs are down- regulated following axonal injury in both the central and peripheral nervous systems (Hoffman & Cleveland, 1988; Hoffman, Pollock & Striph, 1993), which correlates with increased MT destabilization immediately after lesion in a variety of models (Bradke, Fawcett & Spira, 2012; Chisholm et al., 2016). IF upregulation is a hallmark of activated astrocytes, and both IF and MT depolymerisation can alter the directional motility of vesicles in rat astrocytes (Potokar et al., 2007). Recently, vimentin IFs have also been shown to act as a template for MT stabilization during cell migration in wounded retinal epithelial cells (Gan et al., 2016). Together with our findings during *C.elegans* synapse rewiring, these results

point to a universal role for IF-MT interactions in modulating both IF and MT stability.

The interaction between IF and MT networks have long been thought to occur through a variety of cross bridging molecules that contain both MT and IF binding domains. During astrocyte migration, the MT dependent rearrangements of IFs require the tumor suppressor adenomatous polyposis coli (APC) as a cross-bridging molecule to mediate IF-MT interaction (Sakamoto, Boeda & Etienne-Manneville, 2013). RNAi knockdown of the *C. elegans* homolog of APC (*apr-1*) specifically in DD neurons failed to restore synapse rewiring in *tba-1(gf) dlk-1(0)* animals, suggesting *apr-1* may not connect IFs and MTs during synapse rewiring (Figure 4.S5A-C). Plectin (Svitkina, Verkhovsky & Borisy, 1996) and MAP2/tau (Miyata et al., 1986) have also been implicated as potential IF-MT cross-bridging molecules, but as was the case with APC, DD-neuron specific RNAi knockdown of *C. elegans* plectin (*vab-10*) or mutant *C. elegans* tau (*ptl-1(0)*) (Kurup et al., 2017) could not phenocopy IF subunit loss in *tba-1(gf) dlk-1(0)* animals. IFs have also been thought to interact with MTs through MT motors like kinesin and dynein (Chang & Goldman, 2004), however the kinesin and dynein mutations identified in our suppressor screen had no effect on MT dynamics or composition in *tba-1(gf) dlk-1(0)* animals (Kurup et al., 2015, 2017; Figure 4.3D, E). Another possible mechanism for IF regulation of MTs is changes in IF post-translational modifications like phosphorylation, which control IF interaction with microtubule associated proteins (Chang & Goldman, 2004; Snider & Omary, 2014). However, both *ifp-1* and *ifa-4* lack the KSP repeat motif that is typically phosphorylated in mammalian NFs (Chang & Goldman, 2004; Snider & Omary, 2014). Further studies are required to understand how IFs and MTs interact during synapse rewiring, and *C.elegans* provides a useful genetic model to dissect the pathways involved in mediating this interaction.

Author Contributions

Conceptualization: N.K. and Y.J.; Methodology: N.K. and A.G., Investigation: N.K.

and A.G., Writing – Original Draft: N. K.; Writing – Review & Editing: N.K. and Y. J.; Funding Acquisition: Y. J..; Supervision: Y. J.

Experimental Procedures

C. elegans culture

C. elegans strains were maintained at 20-22°C on NGM plates following standard practices. Information on alleles and genotypes of strains is summarized in Supplementary Experimental Procedures. To collect L1 animals, 20-30 gravid adults were placed on a seeded NGM plate to allow egg-laying for 2hrs. The hatched L1s were collected 10 hrs later. *tba-1(gf)dlk-1(0)* animals showed a 10-12 hrs delay from egg lay to hatching; for these genotypes, hatched L1s were collected 22 hrs later.

Fluorescent imaging of GFP reporters

Appropriately staged animals were imaged using a Zeiss LSM 710 confocal microscope following anaesthetization in 0.6 mM levamisole on 2% agar pads for image acquisition. Z-stacks were generated from slices of 0.6 μm thickness and images were processed using Zen lite software. L4 animals of the relevant genotypes were cultured at 20°C overnight, and synaptic puncta of day 1 adults were quantified manually using a Zeiss Axioplan 2 microscope equipped with Chroma HQ filters.

EBP-2::GFP image acquisition and analysis

Animals were anaesthetized in 30mM muscimol on 10% agarose pads for image acquisition. Live imaging for experiments described in Figure 4 was done using a Yokogawa CSU-W1 spinning disc confocal head placed on a Leica DMi8 confocal microscope controlled by MetaMorph software (Molecular Devices). Live imaging for experiments described in Figure 5

was done using a Yokogawa CSU-X1 spinning disc confocal head with a Photometrics Cascade II EMCCD camera (1,024 X 1,024 active pixels) controlled by μManager (http://www.micro-manager.org). 100 (Fig 5) or 200 (Fig 4) single plane images were taken serially at an exposure time of 114ms with an interval of 230ms between each frame, and analyzed using Metamorph to generate kymographs for analysis.

Acute 2, 5 Hexanedione treatments

L1 animals were placed on seeded 1mM 2, 5 HD, or buffer (M9) control plates and incubated for 9 hrs at 20°C. The animals were then transferred to unseeded plates for 10 minutes to remove bacteria containing the drugs and subsequently moved to fresh seeded NGM plates until day 1 adult stage. These animals were then used for imaging synapse rewiring and MT dynamics.

Systemic GFP RNAi treatment

3-4 L4 transgenic animals carrying an IFP-1 transcriptional reporter were placed on NGM plates containing 5 mM IPTG and 25 μg/ml carbenicillin (Sigma), seeded with RNAi expressing HT115 bacteria. The transgenic progeny of these L4 animals were then imaged 3 days later using a Zeiss LSM 710 confocal microscope following anaesthetization in 0.6 mM levamisole on 2% agar pads.

EM serial reconstruction

One day adults were immobilized using high pressure fixation with a high-pressure freezer (BAL-TEC HPM 010) at -176°C. The samples were freeze substituted in 2% osmium tetroxide and 0.1% uranyl acetate in acetone at -90°C (48 hrs) and then at -20°C (16 hrs) using a freeze-substitution apparatus (Leica EM AFS2). After infiltration and embedding in Durcupan ACM resin blocks, the samples were polymerized at 60°C for 48 hrs. Serial sections of 50 nm thickness were collected from the anterior part of the worm (after the posterior pharyngeal bulb)

using Leica ULTRACUT. Sections were collected onto pioloform coated slot grids and were stained for 5 minutes in 2.5% uranyl acetate in 70% methanol, followed by washing in Reynold's lead citrate for 3 minutes. Serial images from both the dorsal and ventral nerve cords were collected with a Gatan digital camera with 2,688 X 2,672 pixel resolution (using Gatan Digital Micrograph acquisition software) on a transmission electron microscope (JEOL-1200 EX, 80kv) at 10,000× magnification. Digital images from both nerve cords were then imported into Reconstruct 3D reconstruction software. Sections were realigned for accurate 3D measurements and visualization. Membranes, intermediate filaments and microtubules were manually traced on the serial image sections with Wacom Graphire3 Pen Tablet input hardware. MTs were identified by their ~24nm diameter, and persistence in at least 4 serial sections, and IFs were identified by their ~10nm diameter, and persistence in at least 4 serial sections. The 3D scenes were rendered and saved as 360° bitmap images.

Statistical Analysis

Statistical analysis was performed using GraphPad Prism 5. Normal distribution of samples was tested using the D'Agostino & Pearson omnibus normality test. Details of the statistical analyses performed for each graph are presented in the corresponding figure legends.

Acknowledgments

This chapter, in full, is a reprint of Kurup, N., Goncharov, A., & Jin, Y. (submitted), Intermediate filaments modulate microtubule dynamics to facilitate synapse rewiring, with permission of all authors. The dissertation author was the primary author.

We are grateful to A. D. Chisholm, K. McCulloch, N. H. Tang, C. Piggott, K.W. Kim, S. Park and M. Andrusiak for comments on the manuscript, and other members of the Jin lab for useful discussions during the course of the study. We thank the Caenorhabditis Genetics Center, which is supported by the National Institutes of Health (P40 OD010440), and the Mitani lab

(Tokyo Women's Medical College) for strains used in this study. Y.J. was an Investigator, and A. G. was a research associate of the Howard Hughes Medical Institute. N. K. was a recipient of the Latham & Watkins Graduate Fellowship. This work was supported by HHMI and an NIH grant (NINDS R01 035546) to Y. J.

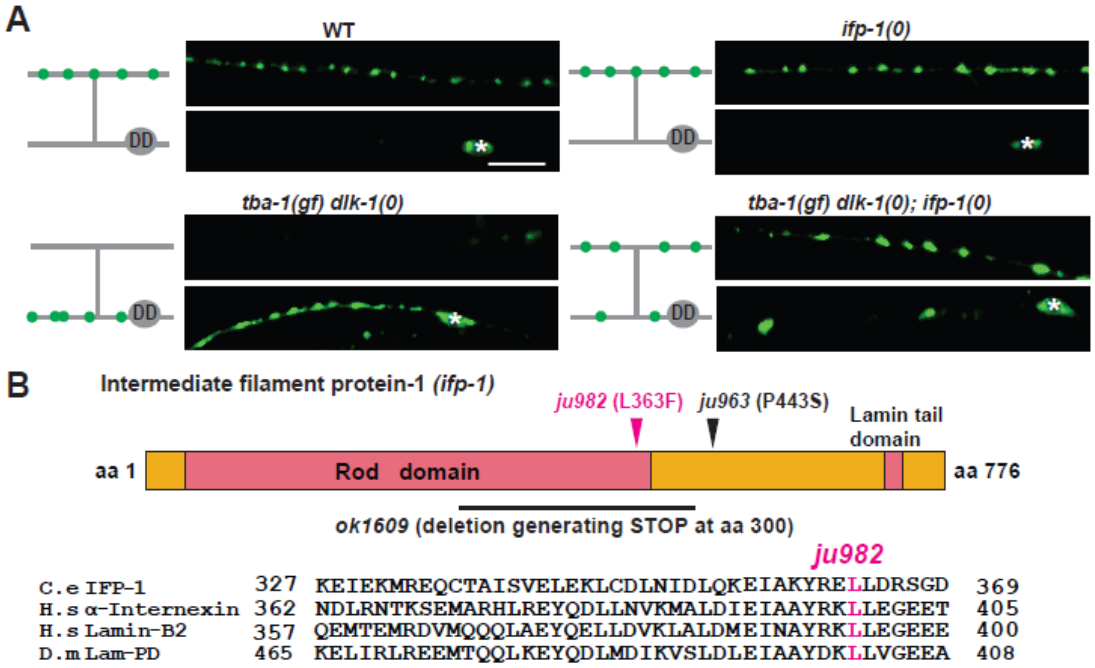

Figure 4.1 Loss of intermediate filament protein *ifp-1* suppresses synapse remodeling defects in *tba-1(gf) dlk-1(0)*

(A) Representative images of DD synapses along the VNC and DNC using P_{flp-13}-SNB-1::GFP (*juIs137*) in adult animals. Schematic of DD neuron (gray) with location of pre-synaptic vesicles (green) on left of each fluorescent image. White asterisk denotes DD neuron cell bodies. Scale bar: 10 µm. (B) Protein domains of IFP-1, depicting the positions of *ju982*, *ju963* and *ok1609* mutations, the conserved rod domain (13-365aa) and lamin tail domain (653-763aa) in the C-terminal. (C) Quantification of synaptic puncta in the DNC of adult animals. Data are mean ± SEM; n>10 animals per genotype. DD-IFP-1 denotes extrachromosomal copies of IFP-1(cDNA) expressed in DD neurons under the *flp-13* promoter. Statistics: One-Way ANOVA followed by Tukey's posttest; ***p<0.001 and ns- not significant. (D) GFP-RNAi treatment of worms expressing IFP-1-promoter fused to GFP (P*ifp-1*-GFP) revealed expression in head neurons and the VNC. Scale bar: 50 µm. (E) Expression pattern of IFP-1 protein in the head and intestine of WT worms using a C-terminal GFP tagged IFP-1 expressed under its own promoter. Scale bar: 50 µm. See also Suppl Fig 4.S1.

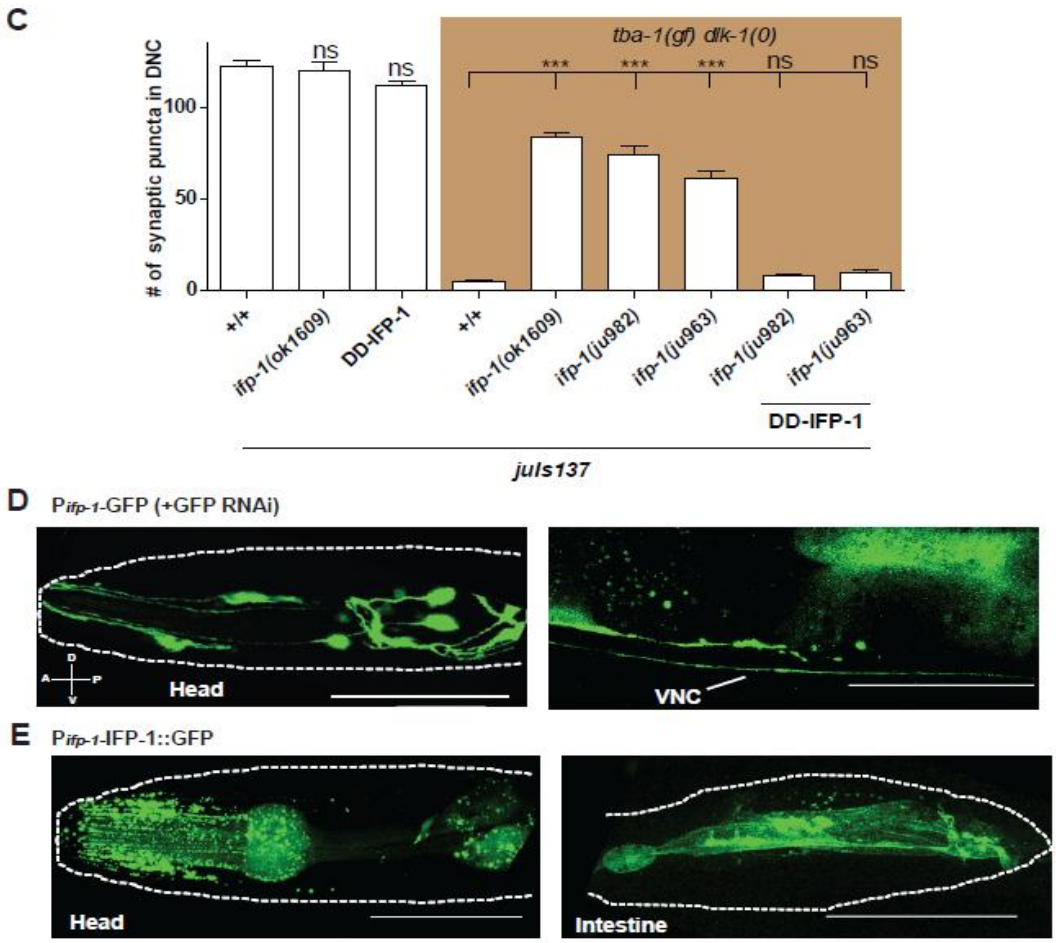

Figure 4.1(continued) Loss of intermediate filament protein *ifp-1* suppresses synapse remodeling defects in *tba-1(gf) dlk-1(0)*

(A) Representative images of DD synapses along the VNC and DNC using P_{flp-13}-SNB-1::GFP (*juIs137*) in adult animals. Schematic of DD neuron (gray) with location of pre-synaptic vesicles (green) on left of each fluorescent image. White asterisk denotes DD neuron cell bodies. Scale bar: 10 µm. (B) Protein domains of IFP-1, depicting the positions of *ju982*, *ju963* and *ok1609* mutations, the conserved rod domain (13-365aa) and lamin tail domain (653-763aa) in the C-terminal. (C) Quantification of synaptic puncta in the DNC of adult animals. Data are mean ± SEM; n>10 animals per genotype. DD-IFP-1 denotes extrachromosomal copies of IFP-1(cDNA) expressed in DD neurons under the *flp-13* promoter. Statistics: One-Way ANOVA followed by Tukey's posttest; ***p<0.001 and ns- not significant. (D) GFP-RNAi treatment of worms expressing IFP-1-promoter fused to GFP (P*ifp-1*-GFP) revealed expression in head neurons and the VNC. Scale bar: 50 µm. (E) Expression pattern of IFP-1 protein in the head and intestine of WT worms using a C-terminal GFP tagged IFP-1 expressed under its own promoter. Scale bar: 50 µm. See also Suppl Fig 4.S1.

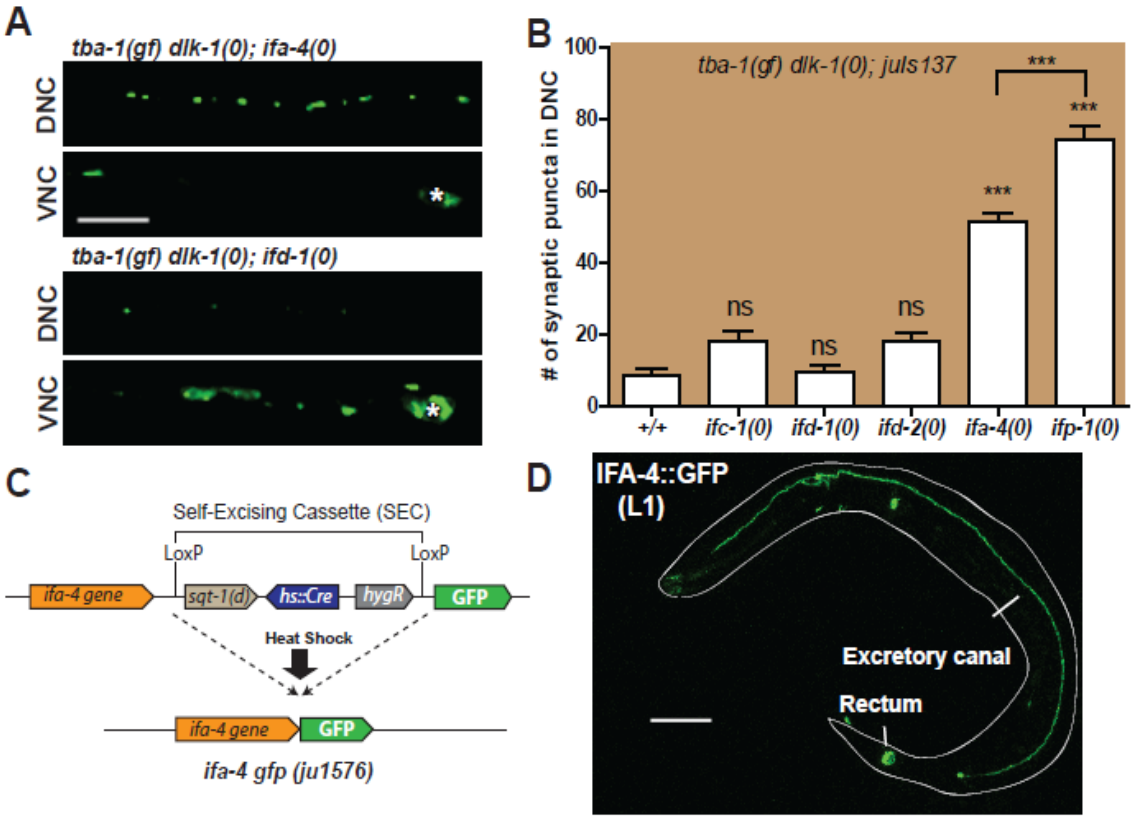

Figure 4.2 *ifa-4(0)* also suppresses DD synapse remodeling defects in *tba-1(gf) dlk-1(0)*

(A) Representative images of DD synapses in adult animals (*juIs137*). White asterisk denotes DD neuron cell bodies. Scale bar: 10 µm. (B) Quantification of synaptic puncta in the DNC of adult animals. Data are mean ± SEM; n>10 animals per genotype. Statistics: One-Way ANOVA followed by Tukey's posttest; ***p<0.001 and ns- not significant. (C) Schematic of CRISPR-Cas9 mediated knockin of GFP at 3' end of *ifa-4* gene. After homologous recombination of the repair plasmid into the genomic locus, the SEC is excised following heat shock at 37°C for 1 hr to drive the expression of Cre recombinase. (D) Representative image of a wild type L1 animal expressing endogenous GFP tagged IFA-4 in the excretory canal and rectum. Scale bar: 10 µm. (E) Schematic of GFP-degron system targeting IFA-4-GFP in D neurons for cullin mediated degradation. (F) Representative images of the dorsal neurites of adult animals expressing P_{unc-25}-mCherry-RAB-3. Scale bar: 10 µm. See also Suppl Fig 4.S2.

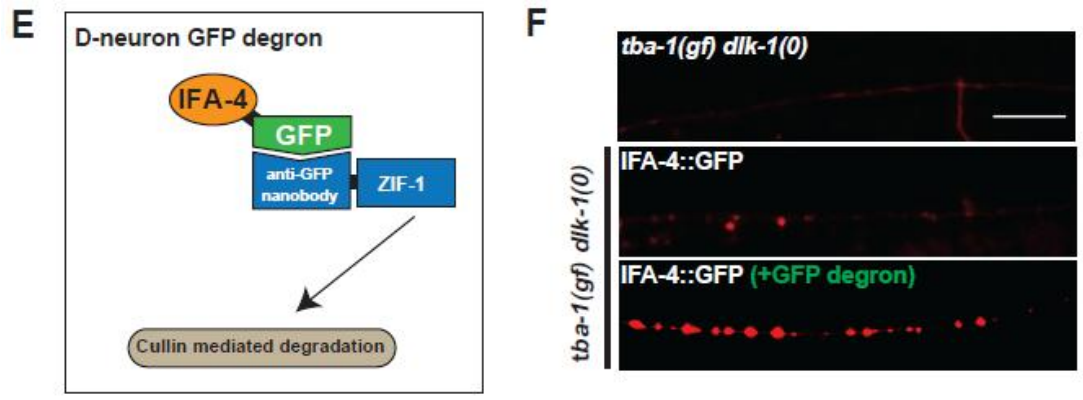

Figure 4.2 (continued) *ifa-4(0)* also suppresses DD synapse remodeling defects in *tba-1(gf) dlk-1(0)*

(A) Representative images of DD synapses in adult animals (*juIs137*). White asterisk denotes DD neuron cell bodies. Scale bar: 10 µm. (B) Quantification of synaptic puncta in the DNC of adult animals. Data are mean ± SEM; n>10 animals per genotype. Statistics: One-Way ANOVA followed by Tukey's posttest; ***p<0.001 and ns- not significant. (C) Schematic of CRISPR-Cas9 mediated knockin of GFP at 3' end of *ifa-4* gene. After homologous recombination of the repair plasmid into the genomic locus, the SEC is excised following heat shock at 37^{o}C for 1 hr to drive the expression of Cre recombinase. (D) Representative image of a wild type L1 animal expressing endogenous GFP tagged IFA-4 in the excretory canal and rectum. Scale bar: 10 µm. (E) Schematic of GFP-degron system targeting IFA-4-GFP in D neurons for cullin mediated degradation. (F) Representative images of the dorsal neurites of adult animals expressing P_{unc-25}-mCherry-RAB-3. Scale bar: 10 µm. See also Suppl Fig 4.S2.

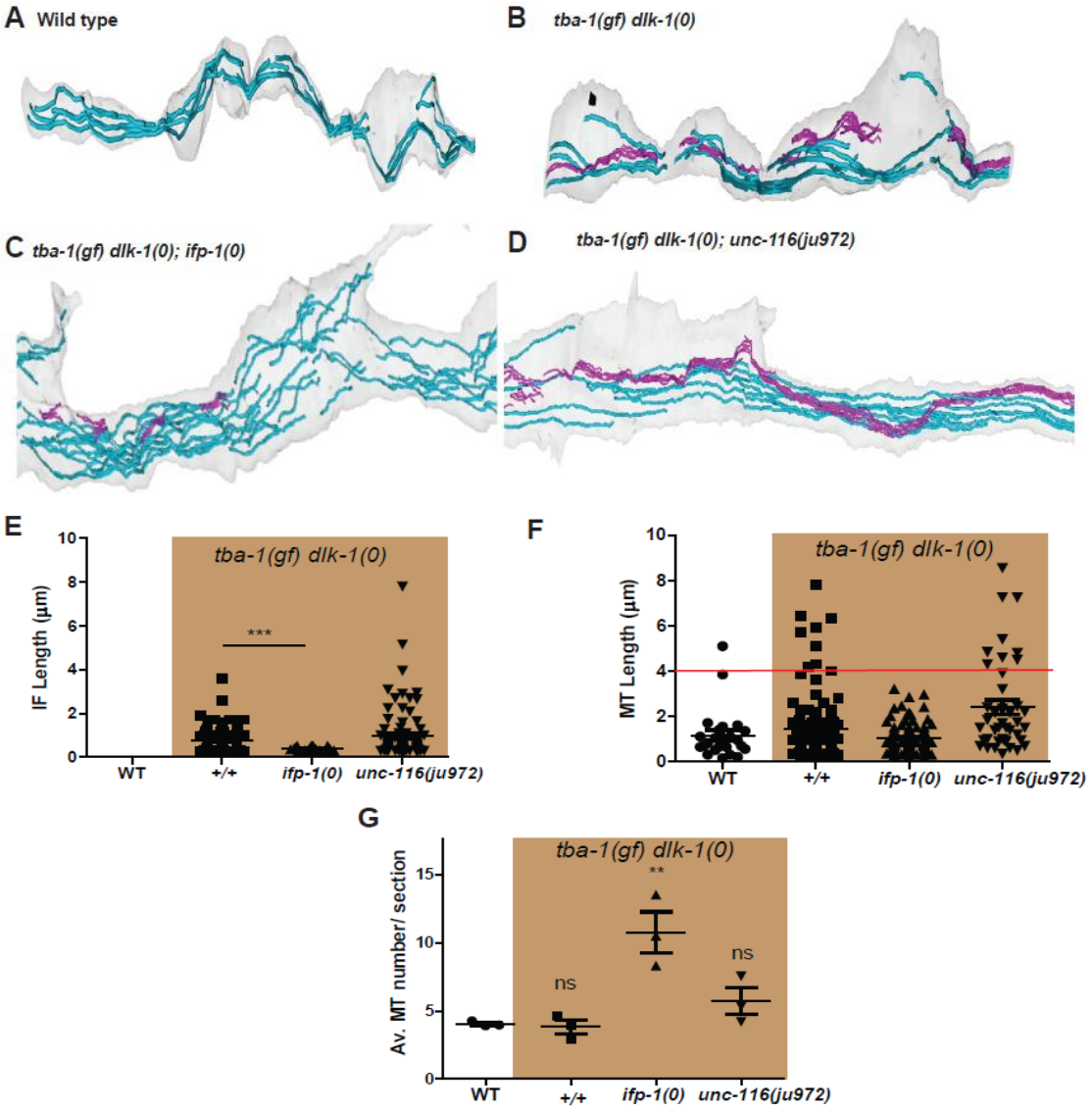

Figure 4.3 IFs are present in DD neurons of *tba-1(gf) dlk-1(0)* animals

(A-D) Serial reconstruction of EM images from ~8 µm of the ventral processes of DD neurons in WT (A), *tba-1(gf) dlk-1(0)* (B), *tba-1(gf) dlk-1(0); ifp-1(0)* (C) and *tba-1(gf) dlk-1(0); unc-116(ju972)* (D) animals. Represented in purple are intermediate filaments and blue are microtubules, and the black spot in (B) represents an active zone. (E) IF length in the ventral neurite of DD neurons. Data are mean ± SEM. Statistics- Mann Whitney test; ***p<0.0001. (F) MT length in the ventral neurite of DD neurons. Data are mean ± SEM. Red line delineates MTs >4 µm in length. (G) MT numbers/section in the ventral neurite of various genotypes. Statistics-One-way ANOVA; ***p<0.0001, ns-not significant. See also Suppl Fig 4.S3.

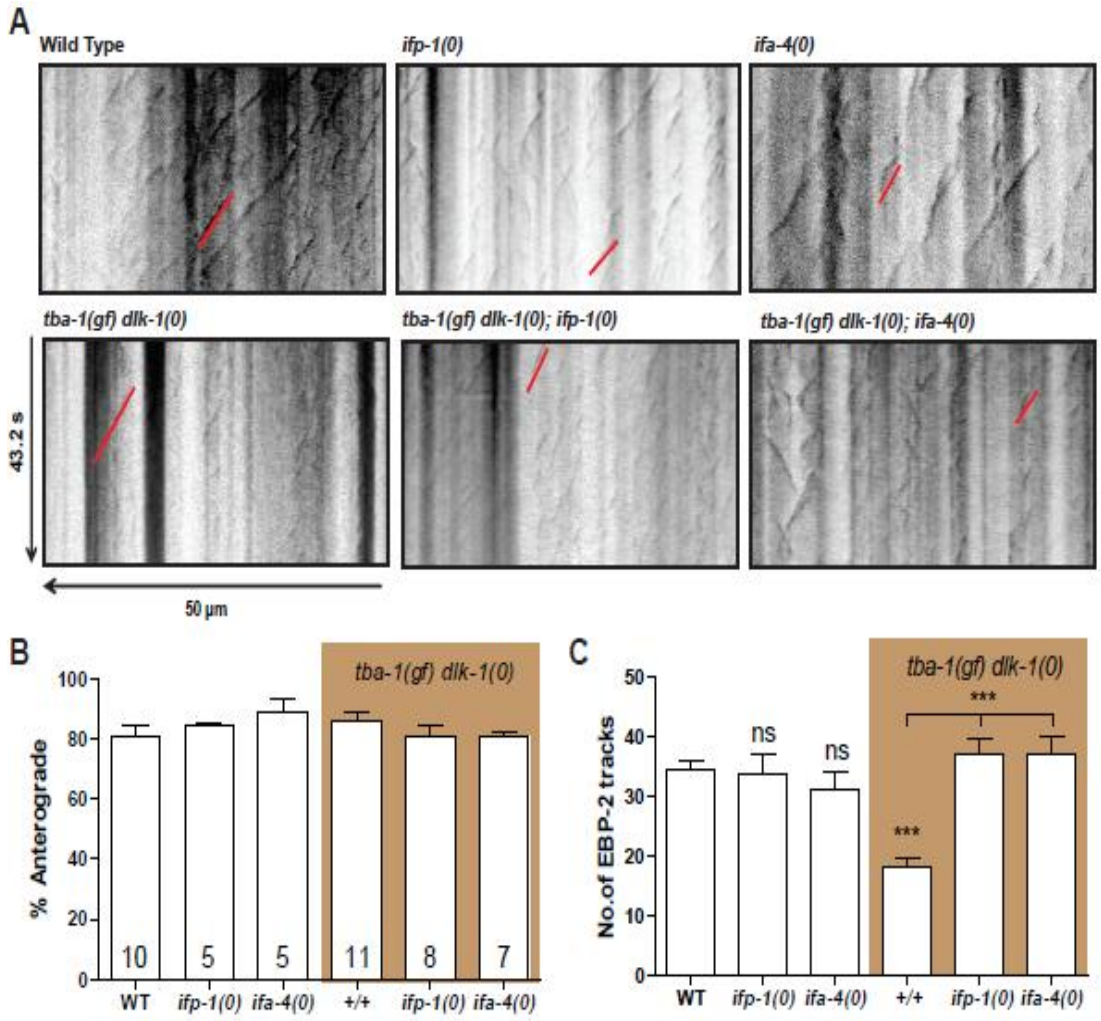

Figure 4.4 Loss of IFs promotes MT dynamics in *tba-1(gf) dlk-1(0)* animals

(A) Representative kymographs of MT dynamics in adult animals. X-axis is the distance imaged to generate the kymograph (measured from the cell body) and Y-axis is duration of imaging. Red line indicates a single EBP-2::GFP track moving in the anterograde direction. (B, C) Quantification of (B) direction of and (C) number of EBP-2::GFP tracks. Data are mean ± SEM; n=number of animals (shown on B). Statistics: One-Way ANOVA followed by Tukey's posttest; ns-not significant, ***p<0.001.

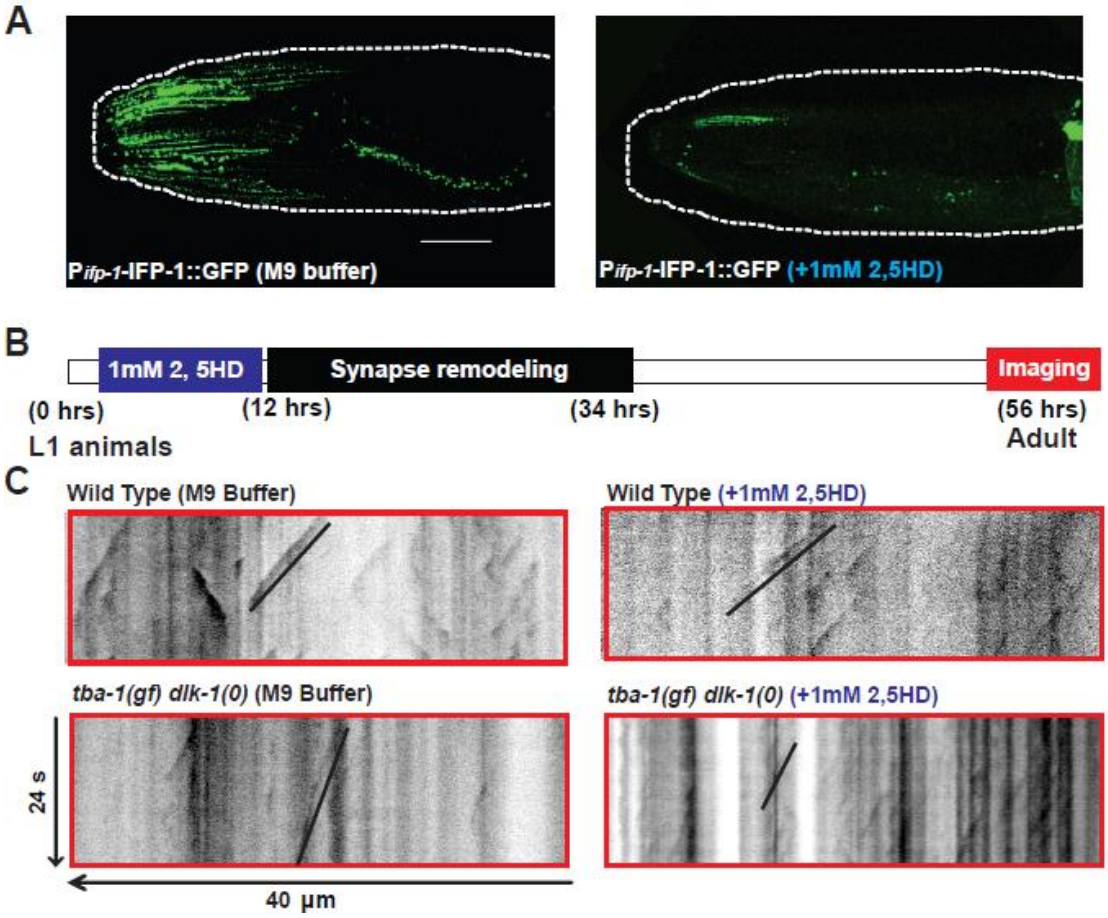

Figure 4.5 Acute treatment with 2, 5 Hexanedione restores MT dynamics and synapse rewiring in *tba-1(gf) dlk-1(0)* animals

(A) Expression levels of IFP-1 protein fused to GFP, after chronic treatment with 1mM 2,5HD or buffer control (M9). Animals were grown in drug containing plates from embryo to adulthood and imaged at day 1 adult stage. Scale bar: 20 µm. (B) Representation of acute drug treatment and imaging protocol for MT dynamics and synapse rewiring. (C) Representative kymographs of MT dynamics in drug treated and buffer control adult animals. Red line indicates a single EBP-2::GFP track. (D, E) Quantification of (D) direction of movement and (E) number of EBP-2::GFP tracks. Data are mean ± SEM; n=number of animals. (shown on d). Statistics: One-Way ANOVA followed by Tukey's posttest; ns-not significant, ***p<0.001. (F) Representative images of DD synapses along the DNC (P_{flp-13}-SNB-1::GFP (*juIs137*)) in adult animals. Scale bar: 10 µm. (G) Quantification of synaptic puncta in the VNC and DNC of adult animals. Data are mean ± SEM; n>10 animals per genotype. Statistics: One-Way ANOVA followed by Tukey's posttest; ***p<0.001, ns- not significant. See also Suppl Fig 4.S4.

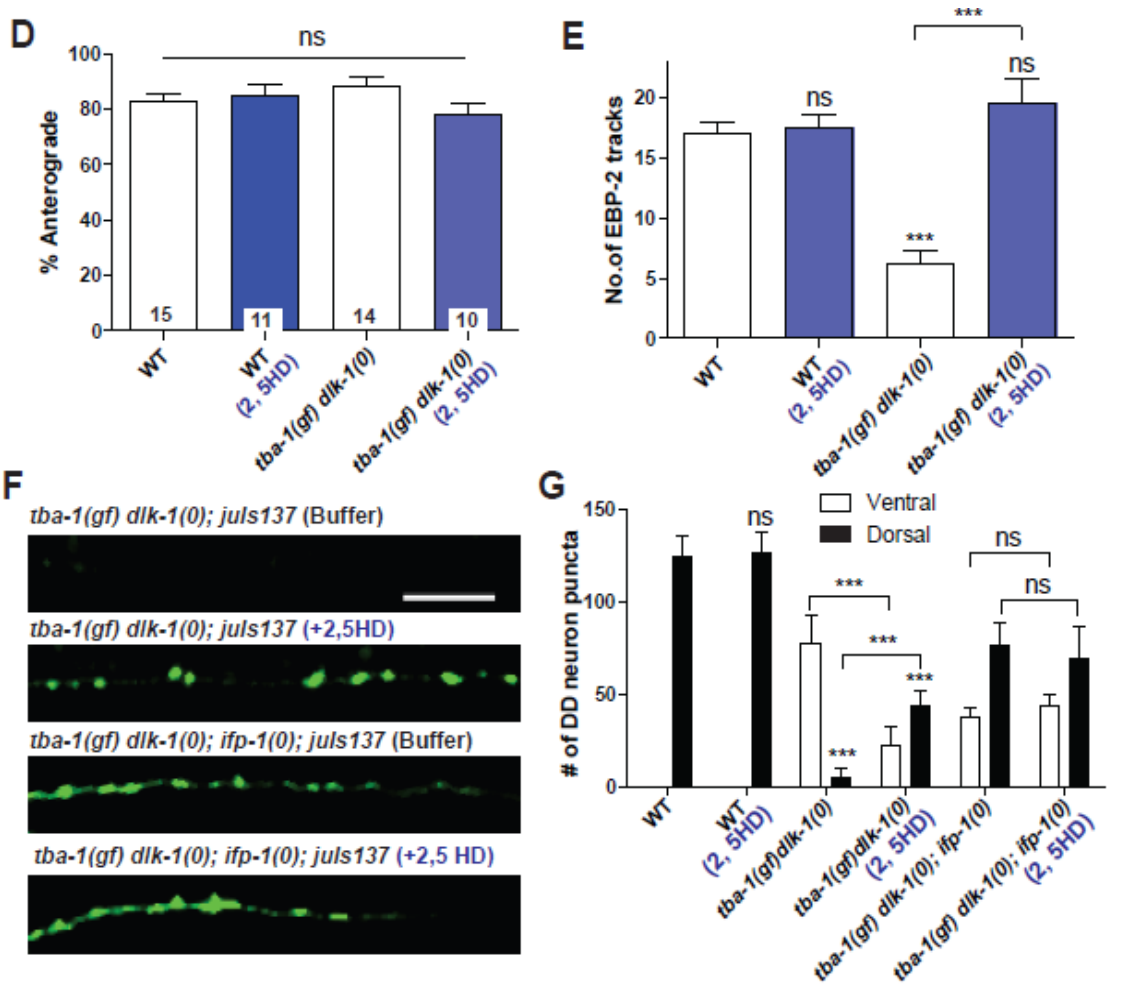

Figure 4.5 (continued) Acute treatment with 2, 5 Hexanedione restores MT dynamics and synapse rewiring in *tba-1(gf) dlk-1(0)* animals

(A) Expression levels of IFP-1 protein fused to GFP, after chronic treatment with 1mM 2,5HD or buffer control (M9). Animals were grown in drug containing plates from embryo to adulthood and imaged at day 1 adult stage. Scale bar: 20 µm. (B) Representation of acute drug treatment and imaging protocol for MT dynamics and synapse rewiring. (C) Representative kymographs of MT dynamics in drug treated and buffer control adult animals. Red line indicates a single EBP-2::GFP track. (D, E) Quantification of (D) direction of movement and (E) number of EBP-2::GFP tracks. Data are mean ± SEM; n=number of animals. (shown on d). Statistics: One-Way ANOVA followed by Tukey's posttest; ns-not significant, ***p<0.001. (F) Representative images of DD synapses along the DNC (P_{flp-13}-SNB-1::GFP (*juIs137*)) in adult animals. Scale bar: 10 µm. (G) Quantification of synaptic puncta in the VNC and DNC of adult animals. Data are mean ± SEM; n>10 animals per genotype. Statistics: One-Way ANOVA followed by Tukey's posttest; ***p<0.001, ns- not significant. See also Suppl Fig 4.S4.

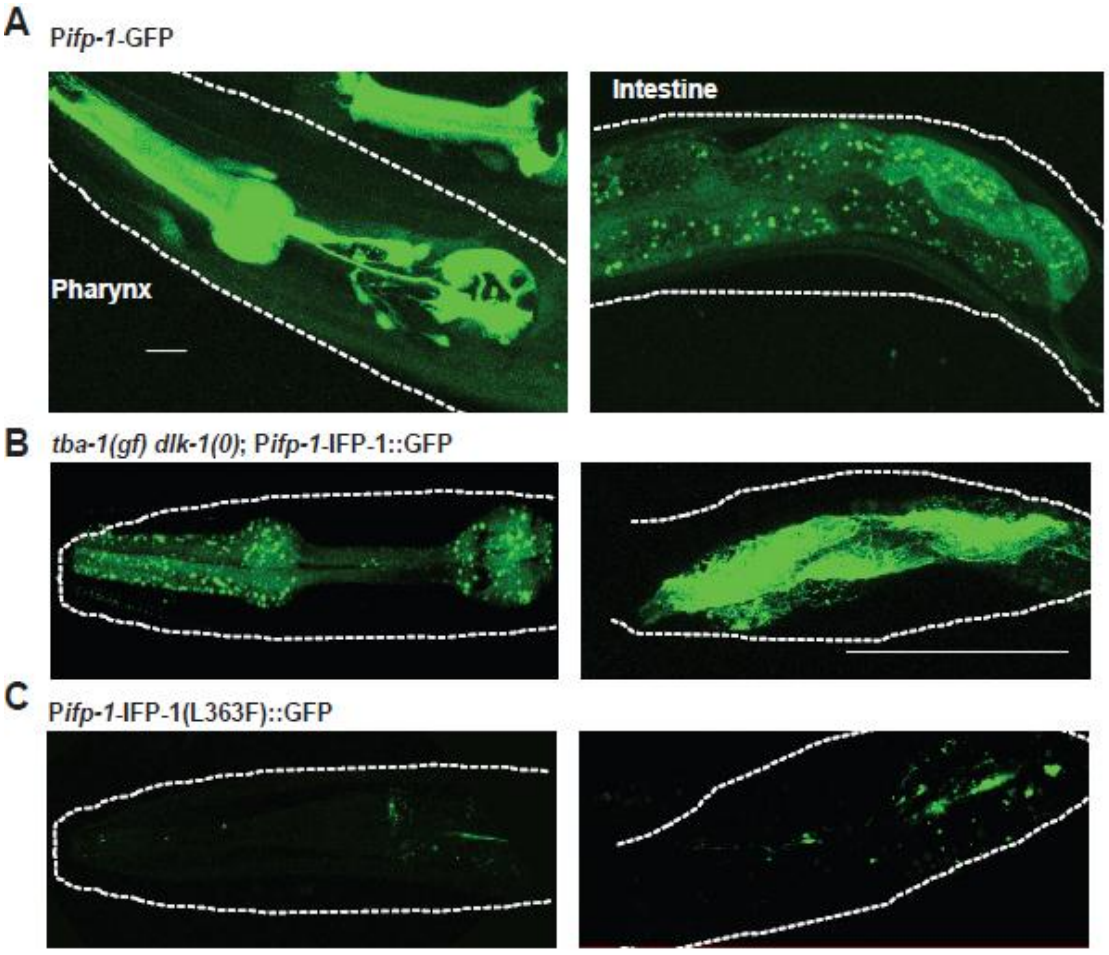

Figure 4.S1 Related to Figure 4.1

(A) Expression pattern of IFP-1-promoter fused to GFP, with strong expression observed in the pharynx and the intestine. Scale bar: 10 μm. (B) Expression pattern of wild type IFP-1::GFP fusion protein driven under its own promoter in the head and intestine of *tba-1(gf) dlk-1(0)* worms. (C) IFP-1(L363F)::GFP proteins show altered subcellular pattern in WT worms. Scale bar: 50 μm.

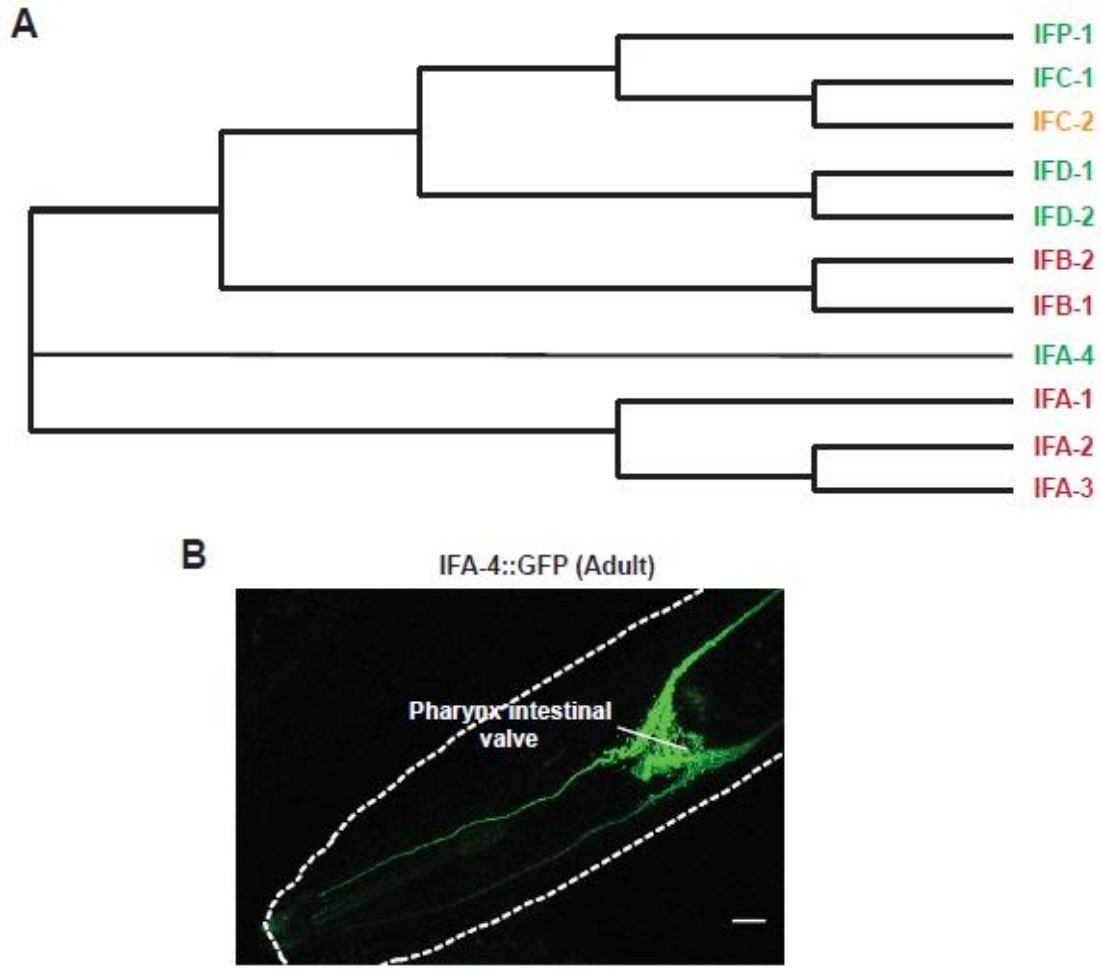

Figure 4.S2 Related to Figure 4.2

(A) Cladogram of the 11 intermediate filament homologs expressed in *C. elegans*. Loss of five of the homologs results in viable and superficially wild type animals (green), five are lethal (red) and one (IFC-2) is dumpy. The cladogram was generated using Clustal W (Neighbour joining method) using multiple sequence alignments generated using Clustal Omega. (B, C) Expression pattern of endogenous IFA-4::GFP (knockin allele *ju1576)* in WT animals at the adult stage. Scale bar: 10 μm. (D) *juIs137* expression levels in animals with a transgene expressing GFP-degron in the D motor neurons are reduced, compared to *juIs137* alone.

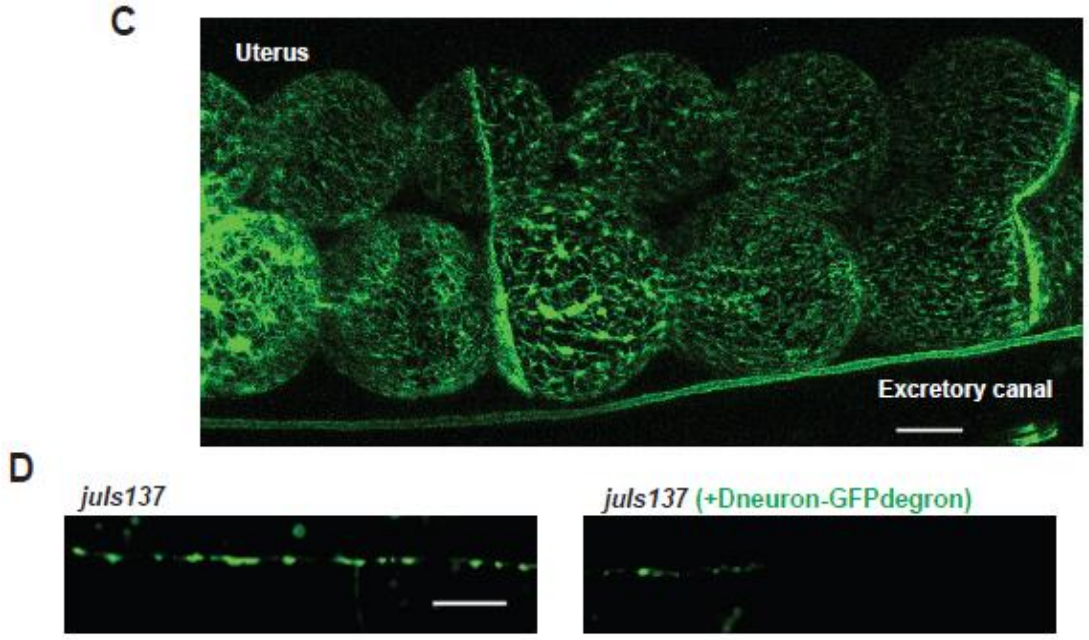

Figure 4.S2 (continued) Related to Figure 4.2

(A) Cladogram of the 11 intermediate filament homologs expressed in *C. elegans*. Loss of five of the homologs results in viable and superficially wild type animals (green), five are lethal (red) and one (IFC-2) is dumpy. The cladogram was generated using Clustal W (Neighbour joining method) using multiple sequence alignments generated using Clustal Omega. (B, C) Expression pattern of endogenous IFA-4::GFP (knockin allele *ju1576)* in WT animals at the adult stage. Scale bar: 10 μm. (D) *juIs137* expression levels in animals with a transgene expressing GFP-degron in the D motor neurons are reduced, compared to *juIs137* alone.

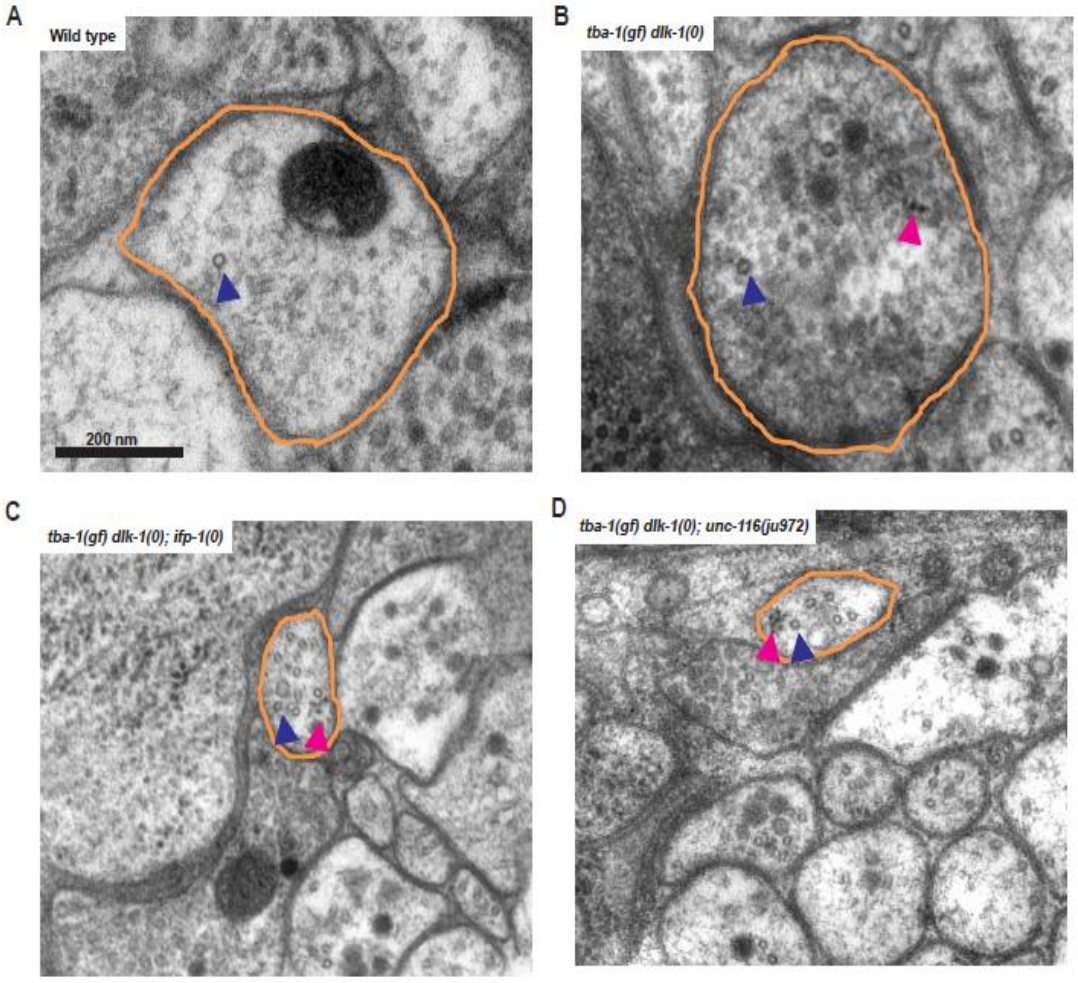

Figure 4.S3 Related to Figure 4.3

(A-D) Representative EM images of DD neurites along the VNC of various genotypes as indicated. Outlined in orange is a DD neurite, blue arrows point to MTs and red arrows point to IFs.

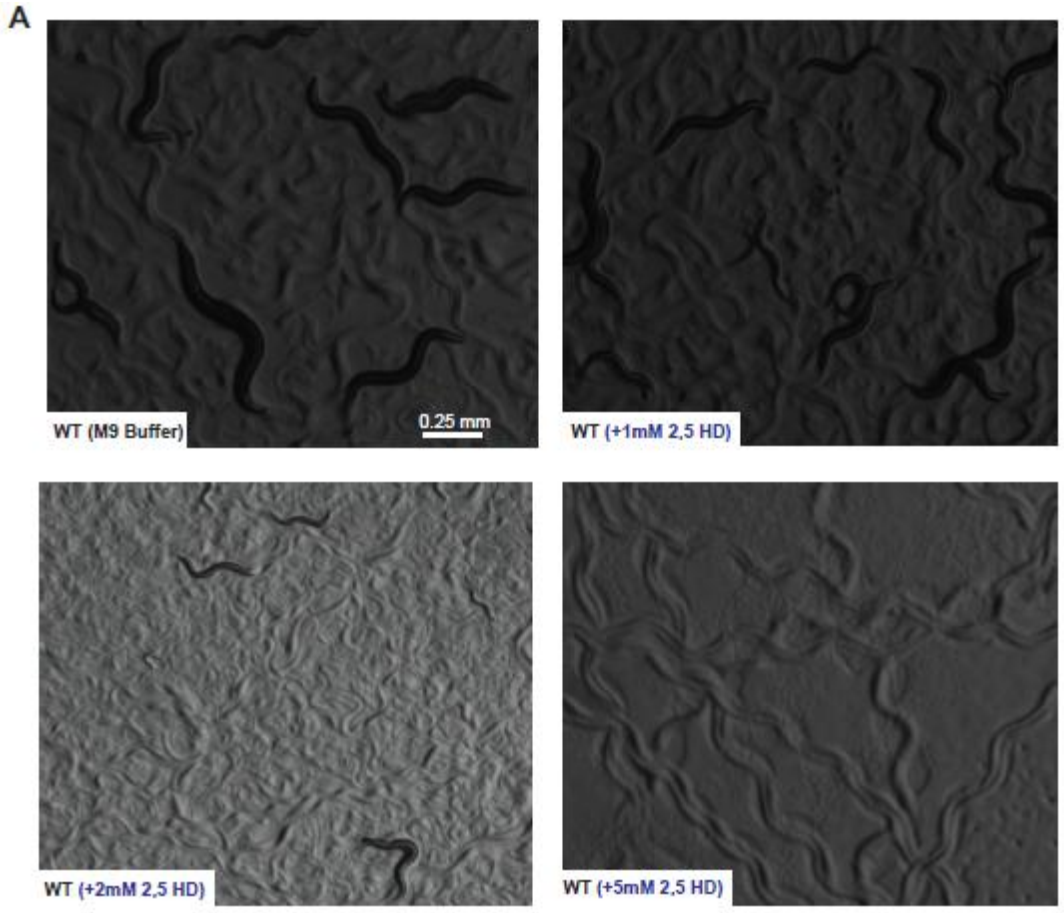

Figure 4.S4 Related to Figure 4.5

(A) Bright field images of wild type animals after treatment with various concentrations of 2, 5 HD. Three gravid adults were placed on plates containing either the buffer control (M9) or 2, 5 HD at 22^{o}C, and their progeny were imaged 3 days later. (B) Representative confocal images of IFP-1::GFP expression in the intestine of worms treated with M9 or various concentrations of 2, 5 HD. Scale bar: 50 μm.

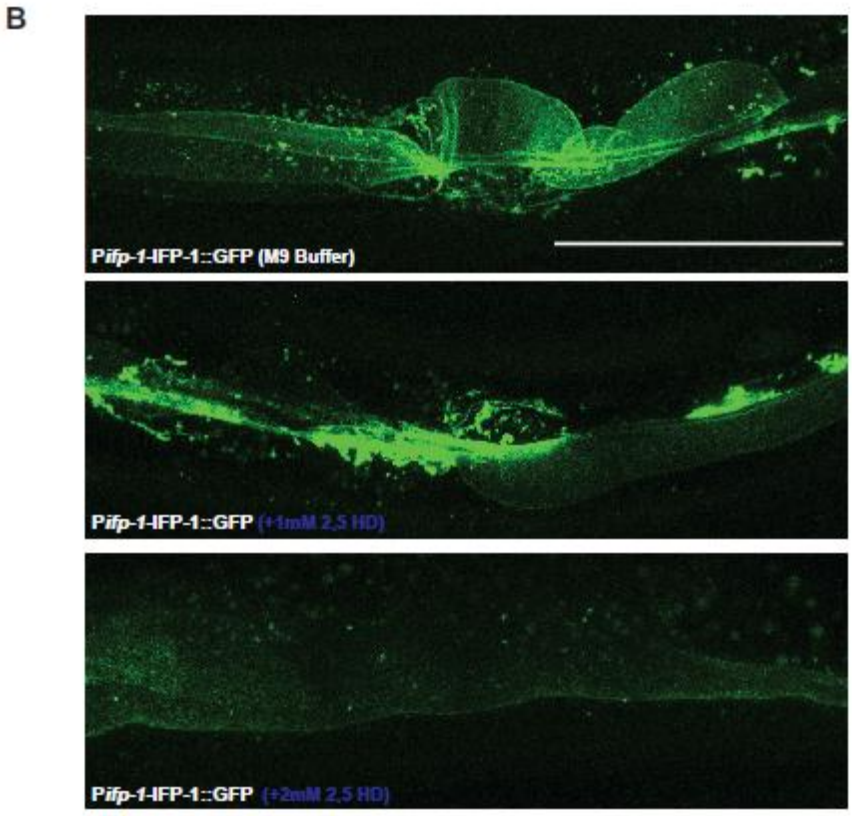

Figure 4.S4 (continued) Related to Figure 4.5

(A) Bright field images of wild type animals after treatment with various concentrations of 2, 5 HD. Three gravid adults were placed on plates containing either the buffer control (M9) or 2, 5 HD at 22^{o}C, and their progeny were imaged 3 days later. (B) Representative confocal images of IFP-1::GFP expression in the intestine of worms treated with M9 or various concentrations of 2, 5 HD. Scale bar: 50 μm.

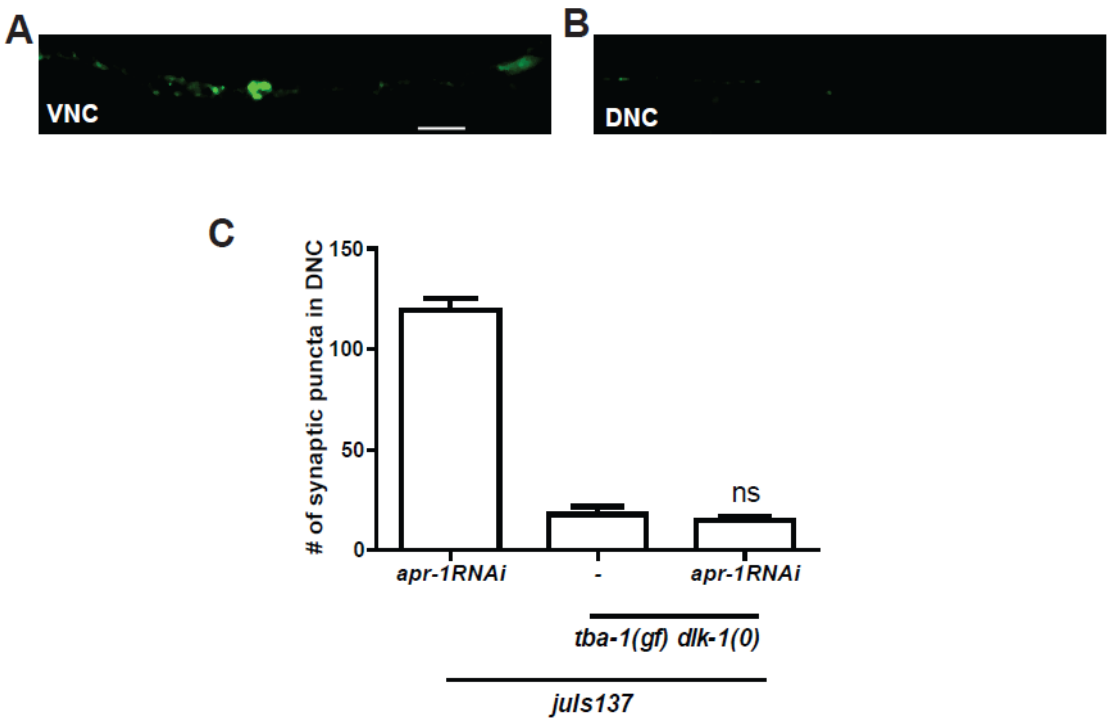

Figure 4.S5 Related to discussion

(A, B) Representative image of VNC (A) and DNC (B) of a *tba-1(gf) dlk-1(0)* animal expressing *apr-1* RNAi in the D motor neurons. Scale bar: 10 µm. (C) Quantification of number of SNB-1::GFP puncta along the DNC of various genotypes using *juIs137*. Statistics: One-way ANOVA with Tukey's posttest.

Table 4.1 List of strains used in this study

Strain	Genotype	Allele or Transgene
CZ2060	*juIs137 II*	*juIs137* [P_{flp-13}*SNB-1::GFP; lin-15(+)*]
CZ16989	*tba-1(ju89) dlk-1(tm4024) I; juIs137 II*	*ju89*: Gly414Arg *tm4024*: 460 bp deletion
CZ23387	*juIs137 II; ifp-1(ok1609) X*	*ok1609*: 1135 bp deletion
CZ19778	*tba-1(ju89) dlk-1(tm4024) I; juIs137 II; ifp-1(ok1609) X*	
CZ21594	*tba-1(ju89) dlk-1(tm4024) I; juIs137 II; ifp-1(ju982) X*	*ju982*: Leu363Phe
CZ22442	*tba-1(ju89) dlk-1(tm4024) I; juIs137 II; ifp-1(ju963) X*	*ju963*: Pro443Ser
CZ23344	*juIs137 II; juEx7123*	*juEx7123* [P_{flp-13}*IFP-1(cDNA); Pgcy-8-GFP*]
CZ23347	*tba-1(ju89) dlk-1(tm4024) I; juIs137 II; ifp-1(ju982) X; juEx7126*	*juEx7126* [P_{flp-13}*IFP-1(cDNA); Pgcy-8-GFP*]
CZ23350	*tba-1(ju89) dlk-1(tm4024) I; juIs137 II; ifp-1(ju963) X; juEx7129*	*juEx7129* [P_{flp-13}*IFP-1(cDNA); Pgcy-8-GFP*]
CZ16631	*tba-1(ju89) dlk-1(tm4024) I*	
CZ23899	*tba-1(ju89) dlk-1(tm4024) I; ifp-1(ok1609) X*	
CZ24128	*ifp-1(ok1609) X*	
CZ24400	*juEx7459*	*juEx7459* [P_{ifp-1} *IFP-1-GFP; Pmyo-3-mCherry*]
CZ22969	*tba-1(ju89) dlk-1(tm4024) I ; juEx7000*	

Table 4.1 (continued) List of strains used in this study

CZ24402	*juEx7461*	*juEx7461* [*Pifp-1-IFP-1(L363F)-GFP; myo-2-mCherry*]
CZ17824	*juEx5317*	*juEx5317* [*Punc-25-EBP-2::GFP; Pgcy-8-GFP*]
CZ20218	*tba-1(ju89)dlk-1(tm4024) I; juEx5317*	
CZ22966	*ifp-1(ok1609) X; juEx5317*	
CZ22967	*tba-1(ju89)dlk-1(tm4024) I; ifp-1(ok1609) X; juEx5317*	
CZ25483	*ifa-4(ok1734) X; juEx5317*	*ok1734*: 711 bp deletion
CZ25484	*tba-1(ju89)dlk-1(tm4024) I; ifa-4(ok1734) X; juEx5317*	
CZ24721	*tba-1(ju89) dlk-1(tm4024) I; juIs137 II; ifa-4(ok1734) X*	
CZ24723	*tba-1(ju89) dlk-1(tm4024) I; juIs137 II; ifc-1(ok2173) V*	*ok2173*: 2036 bp deletion, removes all of *ifc-1* except part of exon1
CZ24724	*tba-1(ju89) dlk-1(tm4024) I; juIs137 II; ifd-1(ok2404) X*	*ok2404*: 1863 bp deletion, out of frame
CZ24725	*tba-1(ju89) dlk-1(tm4024) I; juIs137 II; ifd-2(gk546849) X*	*gk546849*: Y69*
CZ25802	*ju1576 X*	*ju1576*: GFP insertion to C-terminal of IFA-4
CZ25805	*tba-1(ju89) dlk-1(tm4024) I; ju1576 X*	
CZ25856	*juEx7762*	*juEx7762*: [*Pifp-1-GFP; myo-2-mCherry*]
CZ13797	*tba-1(ju89) dlk-1(tm4024) I; ju1576 X; juIs234*	*juIs234*: [*Punc-25-mCherry::RAB-3; ttx-3::RFP*]

Table 4.1 (continued) List of strains used in this study

CZ25982	*tba-1(ju89) dlk-1(tm4024) I; ju1576 X; juIs234 ; juEx7790*	*juEx7790:* [*Punc-25-GFP-degron; myo-2::mcherry*]
CZ25808	*juIs137 II; juEx7745*	*juEx7745:* [*Punc-25-GFP-degron; gcy8::GFP*]
CZ25984	*juIs137 II; ifa-4(ok1734) ifp-1(ok1609) X*	
CZ25985	*tba-1(ju89) dlk-1(tm4024) I; juIs137 II; ifa-4(ok1734) ifp-1(ok1609) X*	

Table 4.2 List of constructs used in this study

Plasmid	**Description**	**Transgenes generated**
pCZGY3264	Pflp-13(2.1 kb)-IFP-1(cDNA)-unc 54 3'UTR	*juEx7123-7131*
pCZGY2332	Punc-25 (2 kb)-EBP-2 cDNA-mGFP-unc-54 3'UTR	*juEx5317*
pCZGY3265	Pifp-1(1 kb)-GFP-let 858 3'UTR	*juEx7762-63*
pCZGY3266	Pifp-1(1 kb)-IFP-1-unc 54 3'UTR	*juEx7000, juEx7459, juEx7460*
pCZGY3267	Pifp-1(4 kb)-IFP-1(L363F)-unc 54 3'UTR	*juEx7461, juEx7462*
pCZGY3268	pDD162 with IFA-4sgRNA	*ju1576*
pCZGY3269	pDD282 with 1kb IFA-4 homology arms	*ju1576*
pCZGY3272	Punc-25 (2 kb)-vhhGFP4-ZIF1 (GFP-degron)-unc 54 3'UTR	*juEx7790-7791, juEx7745-46*

Table 4.3 List of cloning primers used in this study

Primer	Sequence (5' to 3')	Description
YJ12255	CGCATGGATTCCGCTAACGC	Forward primer for amplifying IFP-1cDNA sequence to generate pCZGY3264
YJ12256	TTGTACAAGAAAGCTGGGTCGAATTCG	Reverse primer for amplifying IFP-1 cDNA sequence to generate pCZGY3264
YJ12257	GTGGTACGCATCATTCTTCG	Forward primer for amplifying IFP-1 promoter sequence to generate pCZGY3265
YJ12258	GCGCTGAAACAGTAACCATAAG	Reverse primer for amplifying IFP-1 promoter sequence to generate pCZGY3265
YJ12259	GTGGTACGCATCATTCTTCGTTG	Forward primer for IFP-1 genomic sequence for pCZGY3266
YJ12260	ATGATGATGATGGTCTGCATCTCC	Reverse primer for IFP-1 genomic sequence for pCZGY3266
YJ12261	ATTAGGTGTGTGAAGCACGTGTTTTAGAGCTAGAAATAGCAAGTTAAAATAAG	Forward primer for generating IFA-4 sgRNA for pCZGY3268
YJ12262	ACGTGCTTCACACACCTAATCaagacatctcgcaataggag	Reverse primer for generating IFA-4 sgRNA fo pCZGY3268
YJ12263	GGAAATCGCAAAATATCGGGAATTTCTCGACAGATCTGGAGATCC	Forward primer for site directed mutagenesis of IFP-1(L363F) for pCZGY3267
YJ12264	GGATCTCCAGATCTGTCGAGAAATTCCCGATATTTTGCGATTTCC	Reverse primer for site directed mutagenesis of IFP-1(L363F) for pCZGY3267

Table 4.3 (continued) List of cloning primers used in this study

YJ12265	CATGCGGTCACCAAACTGTG	Forward primer for 5' homology arm of IFA-4 for pCZGY3269
YJ12266	GGTGTGTGAAGCACGTTGACTG	Reverse primer for 5'homology arm of IFA-4 for pCZGY3269
YJ12267	TAATTGCATCAACCAATTAAATCC	Forward primer for 3' homology arm of IFA-4 for pCZGY3269
YJ12268	GTCATCCGACCATGTCTTCT	Reverse primer for 3'homology arm of IFA-4 for pCZGY3269

References

Asbury, A.K., Gale, M.K., Cox, S.C., Baringer, J.R., & Berg, B.O. (1972). Giant axonal neuropathy—a unique case with segmental neurofilamentous masses. *Acta neuropathologica, 20(3)*, 237–47.

Armenti, S. T., Lohmer, L. L., Sherwood, D. R., & Nance, J. (2014). Repurposing an endogenous degradation system for rapid and targeted depletion of C . elegans proteins. *Development*, *141*, 4640-4647.

Baran, R., Castelblanco, L., Tang, G., Shapiro, I., Goncharov, A., & Jin, Y. (2010). Motor neuron synapse and axon defects in a C. elegans alpha-tubulin mutant. *PloS one*, *5*(3), e9655.

Beaulieu, J. M., Nguyen, M.D., & Julien, J.P. (1999). Late onset death of motor neurons in mice overexpressing wild-type peripherin. *J Cell Biol.*,147: 531–544.

Bocquet, A., Berges, R., Frank, R., Robert, P., & Peterson, A. C. (2009). Neurofilaments bind tubulin and modulate its polymerization. *J. Neurosci.*, *29*(35), 11043-11054.

Bradke, F., Fawcett, J.W., Spira, M. E. (2012). Assembly of a new growth cone after axotomy: The precursor to axon regeneration. *Nat. Rev. Neurosci.*, *13*, 183–193.

Carberry, K., Wiesenfahrt, T., Windoffer, R., Bossinger, O., & Leube, R. E. (2009). Intermediate Filaments in Caenorhabditis elegans. *Cell Motility and the Cytoskeleton*, *864*, 852-864.

Chalfie, M., & Thomson, J. N. (1982). Structural and functional diversity in the neuronal microtubules of Caenorhabditis elegans. *The Journal of cell biology*, *93*(1), 15-23.

Chang, L., & Goldman, R. D. (2004). Intermediate filaments mediate cytoskeletal crosstalk. *Nat. Rev. Mol. Cell Biol.*, *5*, 601-613.

Chisholm, A. D., Hutter, H., Jin, Y., & Wadsworth, W. G. (2016). The genetics of axon guidance and axon regeneration in Caenorhabditis elegans. *Genetics*, *204*, 849-882.

Conde, C., & Cáceres, A. (2009). Microtubule assembly, organization and dynamics in axons and dendrites. *Nature reviews. Neuroscience*, *10*(5), 319-32.

Dickinson, D. J., Ward, J. D., Reiner, D. J., & Goldstein, B. (2013). Engineering the Caenorhabditis elegans genome using Cas9-triggered homologous recombination. *Nature methods*, *10*(10), 1028-34.

Dillon, C., & Goda, Y. (2005). The actin cytoskeleton : integrating form and function at the synapse. *Annu. Rev. Neurosci.*, *28*, 25-55.

Durham, H. D. (1987). 2,5-hexanedione aggregates vimentin-, but not keratin-, intermediate filaments. *Cell Biology International Reports*, *11*(4), 307-317.

Gan, Z., Ding, L., Burckhardt, C. J., Lowery, J., Zaritsky, A., Sitterly, K., Mota, A., Costigliola, N., Starker, C.G., Voltas, D.F., Tytell, J., Goldman, R.D. & Danuser, G. (2016). Vimentin intermediate filaments template microtubule networks to enhance persistence in cell polarity and directed migration. *Cell Systems*, *3*, 252-263.

Goldman, R.D. (1971). The role of three cytoplasmic fibers in BHK-21 cell motility. I. Microtubules and the effects of colchicine. *J. Cell Biol. 51*, 752–762.

Hallam, S.J. & Jin, Y. (1998) *lin-14* regulates the timing of synaptic remodeling in *Caenorhabditis elegans*. *Nature, 395*, 644-647.

Hoffman, P. N., & Cleveland, D. W. (1988). Neurofilament and tubulin expression recapitulates the developmental program during axonal regeneration : Induction of a specific 8-tubulin isotype. *PNAS, 85*, 4530-4533.

Hoffman, P. N., Pollock, S. C., & Striph, G. G. (1993). Altered gene expression after optic nerve transection: Reduced neurofilament expression as a general expression as a general response to axonal injury. *Exp. Neurol., 119*, 32-36.

Kaplan, M. P., Chin, S. S., Fliegner, K. H., Liem, R. K. (1990) α-Internexin, a novel neuronal intermediate filament protein, precedes the low molecular weight neurofilament protein (NF-L) in the developing rat brain. *J. Neuroscience, 10,* 2735–2748.

Karabinos, A., Schmidt, H., Harborth, J., Schnabel, R., & Weber, K. (2001). Essential roles for four cytoplasmic intermediate filament proteins in Caenorhabditis elegans development. *Proceedings of the National Academy of Sciences*, *98*(14), 7863-7868.

Karabinos, A., Schulze, E., Parry, D. A. D., & Weber, K. (2003). In Vivo and in Vitro evidence that the four essential Intermediate Filament (IF) proteins A1 , A2 , A3 and B1 of the nematode Caenorhabditis elegans form an obligate heteropolymeric IF system. *Journal of Molecular Biology, 333*, 307-319.

Karabinos, A., Schünemann, J., & Weber, K. (2004). Most genes encoding cytoplasmic intermediate filament (IF) proteins of the nematode Caenorhabditis elegans are required in late embryogenesis. *Eur. J. Cell Biol., 83*, 457-468.

Kurup, N., & Jin, Y. (2016). Neural circuit rewiring : insights from DD synapse remodeling. *Worm*, *5*(1), e1129486.

Kurup, N., Yan, D., Goncharov, A., & Jin, Y. (2015). Dynamic microtubules drive circuit rewiring in the absence of neurite remodeling. *Current Biology*, *25*(12), 1594-1605.

Kurup, N., Yan, D., Kono, K., & Jin, Y. (2017) Differential regulation of polarized synaptic vesicle trafficking and synapse stability in neural circuit rewiring in *Caenorhabditis elegans*. *PLOS Genetics, 13*(6): e1006844.

Lariviere R.C., & Julien J.P. (2004). Functions of intermediate filaments in neuronal development and disease. *J. Neurobiol., 58*,131–148.

Lee, M. K., & Cleveland, D. W. (1996). Neuronal intermediate filaments. *Annu. Rev. Neurosci., 19*, 187-217.

Lee, M. K., Marszalek, J. R., & Cleveland, D. W. (1994). A mutant neurofilament subunit causes massive, selective motor neuron death: Implications for the pathogenesis of human motor neuron disease. *Neuron* 13: 975–988.

Llorens, J. (2013). Toxic neurofilamentous axonopathies – accumulation of neurofilaments and axonal degeneration. *Journal of Internal Medicine*, *273*, 478-489.

Mimori-Kiyosue, Y., Shiina, N., & Tsukita, S. (2000). The dynamic behavior of the APC-binding protein EB1 on the distal ends of microtubules. *Current biology*, *10*, 865-8.

Miyata, Y., Hoshi, M., Nishidas, E., Minamis, Y., & Sakai, H. (1986). Binding of Microtubule-associated protein 2 and Tau to the intermediate filament reassembled from neurofilament 70-kDa subunit protein. *J. Biol. Chem.*, *286*(28), 13026-13030.

Potokar, M., Kreft, M., Li, L., Andersson, D. J., Pangrsˇicˇ, T., Chowdhury, H. H., Pekny, M., & Zorec, R. (2007). Cytoskeleton and vesicle mobility in astrocytes. *Traffic*, *8*, 12-20.

Sakaguchi-Nakashima, A., Meir, J. Y., Jin, Y., Matsumoto, K., & Hisamoto, N. (2007). LRK-1, a *C. elegans* PARK8-related kinase, regulates axonal-dendritic polarity of SV proteins. *Current biology*, *17*, 592-8.

Sakamoto, Y., Boeda, B., & Etienne-Manneville, S. (2013). APC binds intermediate filaments and is required for their reorganization during cell migration. *J. Cell Biol. 200,* 249–258.

Snider, N. T., & Omary, M. B. (2014). Post-translational modifications of intermediate filament proteins: mechanisms and functions. *Nat. Rev. Mol. Cell Biol.*, *15*(3), 163-177.

Spencer, W. C., Zeller, G., Watson, J. D., Henz, S. R., Watkins, K. L., Mcwhirter, R. D., Petersen, S., Sreedharan, V.T., Widmer, C., Jo, J., Reinke, V., Petrella, L., Strome, S., Von Stetina, S.E., Katz, M., Shaham, S., Ratsch, G., & Miller III, D.M. (2011). A spatial and temporal map of C. elegans gene expression. *Genome Research*, *21*, 325-341.

Svitkina, T. M., Verkhovsky, A. B. & Borisy, G. G. (1996). Plectin sidearms mediate interaction of intermediate filaments with microtubules and other components of the cytoskeleton. *J. Cell Biol.*, *135*, 991-1007.

Wang, S., Tang, N. H., Lara-gonzalez, P., Zhao, Z., & Dhanya, K. (2017). A toolkit for GFP-mediated tissue-specific protein degradation in C. elegans. *Development*, doi:10.1242/dev.150094

White, J. G., Albertson, D.G. & Anness, M.A.R. (1978). Connectivity changes in a class of motorneurons during the development of a nematode. *Nature*, *271*, 764-766.

White, J. G., Southgate, E., Thomson, J. N., & Brenner, S. (1986). The Structure of the Nervous System of the Nematode *Caenorhabditis elegans*. *Philosophical Transactions of the Royal Society B: Biological Sciences*, *314*, 1-340.

Winston, W. M., Molodowitch, C., & Hunter, C. P. (2002). Systemic RNAi in C . elegans Requires the Putative Transmembrane Protein SID-1. *Science*, *295*(March), 2456-2460.

Woo, W.-meng, Goncharov, A., Jin, Y., & Chisholm, A. D. (2004). Intermediate filaments are required for C . elegans epidermal elongation. *Developmental biology*, *267*, 216-229.

Xu, Z., Cork, L. C., Griffin, J.W., & Cleveland, D. W. (1993). Increased expression of neurofilament subunit NF-L produces morphological alterations that resemble the pathology of human motor neuron disease. *Cell*, *73*, 23–33.

Xue, C., Shtylla, B., & Brown, A. (2015). A stochastic multiscale model that explains the segregation of axonal microtubules and neurofilaments in neurological diseases. *PLoS Comput. Biol.*, *11*(8), e1004406. doi:10.1371/journal.pcbi.1004406.

Yuan, A., & Nixon, R. A. (2016). Specialized roles of neurofilament proteins in synapses : Relevance to neuropsychiatric disorders. *Brain Research Bulletin*, *126*, 334-346.

Yuan, A., Rao, M. V., & Nixon, R. A. (2017). Neurofilaments and neurofilament proteins in health and disease. *Cold Spring Harb Perspect Biol*, *9:a018309*.

Yuan, A., Rao, M. V., Sasaki, T., Chen, Y., Kumar, A., Liem, R. K. H., Eyer, J., Peterson, A. C., Julien, J-P., & Nixon, R. A. (2006). α -Internexin is structurally and functionally associated with the neurofilament triplet proteins in the mature CNS. *J. Neurosci.*, *26*(39), 10006-10019.

Zuela, N., & Gruenbaum, Y. (2016). Intermediate Filaments in Caenorhabditis elegans. *Methods in Enzymology*, 1st ed., Vol. 568, pp. 661-679.

Chapter 5

The role of MT stability in long distance synaptic vesicle transport and axon regeneration

Abstract

The presynaptic terminal of a chemical synapse contains a complex network of cytoskeletal elements that are essential for its formation and maintenance. Microtubules (MTs), which are polymers of α- and β-tubulin heterodimers, are an important component of this framework. Tubulin and MT-posttranslational modifications (PTMs) have been implicated in a variety of neuronal processes, including axon outgrowth, stability and cargo transport. There is some debate in the field as to whether acetylation, an MT-PTM that stabilizes MTs, affects polarized transport of neuronal cargo. In this chapter, I will address how MT acetylation affects synaptic vesicle trafficking and axon regeneration *in vivo*, as well as present some findings on the consequences of a missense mutation in α-tubulin on the formation of terminal synapses.

Introduction

The distinct architecture of neurons, which typically comprise of a long thin axon, and multiple shorter dendrites emerging from a single cell body, results in an unusual cytoskeletal framework. Principle components of this cytoskeleton are actin filaments and microtubules, and their dynamic interplay in the formation of the neurite growth cone has been well characterized (Conde & Cáceres, 2009). The role of actin at the synapse has been well elucidated, where synapse regulation through actin has been shown to take place both at the morphological level as well as in the modulation of synapse efficacy (Cingolani & Goda, 2008). Microtubules are predominantly thought to act as "highways" for cargo transport along the axon, but there is growing evidence that MTs play an integral role in synapse formation and maintenance. Studies

in cultured hippocampal neurons have shown that dendritic spines are sensitive to changes in MT dynamics, indicating that MTs play an active role in synaptic architecture (Hu et. al., 2008). Varying degrees of MT stabilization and destabilization also regulate structural plasticity of pre-synaptic terminals in a wide range of neuronal models (Brill et al., 2016; Mclaughlin et al., 2016; Nahm et al., 2013; Stephan et al., 2015).

Post-translational modifications like acetylation, polyglutamylation, tyrosination and detyrosination of α- and β- tubulin result in functionally distinct classes of MTs, with an enrichment of acetylated and detyrosinated tubulin in stable MT populations (Fukushima et al., 2009; Janke and Bulinski, 2011). While most MT-PTMs target the C-terminal tail of tubulin on the MT external surface, acetylation of Lys40 of α-tubulin modifies the internal MT lumen (Fukushima et al., 2009; Janke and Bulinski, 2011). MT acetylation has been implicated in promoting kinesin-1 binding and anterograde transport in cultured neurons, although it is not clear whether acetylation alone is sufficient for enhanced kinesin-1 binding and motility (Cai et al., 2009; Hammond et al., 2010; Reed et al., 2006). Direct *in vitro* multi-motor gliding assays also failed to show any kinesin-1 preference for acetylated over deacetylated MTs (Fischermeier, Diez, & Walter, 2012). We thus sought to examine whether a loss in MT acetylation altered anterograde synaptic vesicle transport *in vivo*, using *C. elegans* mechanosensory neurons as a model.

The mechanosensory neurons in *C.elegans* have a unique 15-protofilament MT structure that is largely composed of heterodimers of α-tubulin MEC-12 and β-tubulin MEC-7, with MEC-12 being the only α-tubulin that is acetylated at K40 (Chalfie & Thompson, 1982; Fukushige et al., 1999). MEC-17 and ATAT-2 are tubulin acetyltransferases that act redundantly in *C. elegans*, and loss of both results in the loss of K40 acetylation and 15 protofilament MTs in mechanosensory neurons, MT instability and axonal degeneration (Akella et al., 2010; Cueva et al., 2012; Neumann & Hilliard, 2014; Shida et al., 2010; Topalidou et al., 2012). We confirmed some of these findings as well as characterized the role of MEC-17 and ATAT-2 in synaptic

vesicle transport and axon regeneration after femtosecond laser injury. Since a majority of the neuronal defects seen in *mec-17* and *atat-2* null mutants were attributed to an increase in MT instability or dynamics (Neumann & Hilliard, 2014), we compared synaptic vesicle transport in double mutants of *mec-17* and *atat-2* to a missense mutation of α-tubulin TBA-1 (Gly414 to Arg in the C-terminal microtubule associated protein domain) that altered MT architecture and increased MT dynamics in *C. elegans* motor neurons (Baran et al., 2010; Kurup et al., 2015).

Results and Discussion

Loss of *mec-17* and *atat-2* alters neurite polarity, morphology and recovery from injury

The *C. elegans* genome encodes two α-tubulin N-acetyltransferase (α-TAT) genes, *mec-17* and *atat-2*, both of which contain catalytic Gcn5-related N-acetyltransferase (GNAT) domains. *mec-17* and *atat-2* share ~68% protein sequence homology, and while *mec-17* is predominantly expressed in the touch neurons, *atat-2* is more widely expressed (Akella et al., 2010; Shida et al., 2010). *ok2109* and *ok2415*, null alleles of *mec-17* and *atat-2* respectively, were used throughout this study and will be referred to henceforth as *mec-17(0)* and *atat-2(0)*. We performed a quantitative analysis of the neuronal outgrowth and polarity defects of *mec-17(0)* and *atat-2(0)* in the mechanosensory neurons using a *mec-7* promoter driven GFP transgene (*muIs32*).

The Anterior Lateral Mechanosensory neuron (ALM) and the Posterior Lateral Mechanosensory neuron (PLM) are two pairs of unipolar neurons that extend their axons anteriorly, and make terminal synapses on a distal axonal branch that either enters the nerve ring in the head of the animal (ALM) or the ventral nerve cord (PLM) (White et al., 1986) (Figure 5.1 A). Mechanosensory neuron polarity, as is the case with several mammalian neurons, is regulated by a variety of guidance cues, including Netrin, Slit/Robo and Wnt signaling pathways, and downstream of these guidance cues are effector molecules that modulate the actin and microtubule cytoskeleton (Hilliard & Bargmann, 2006; Prasad & Clark, 2006; Yu &

Bargmann, 2001). Wild type ALM neurons also extend a very short posterior process from the cell body that does not form any chemical synapses (Figure 5.1B). The ALM posterior processes of ATAT mutants were significantly longer than wild type animals and in some cases resulted in an almost bipolar neuron (Figure 5.1C, D). Functionality of the mechanosensory neuron circuit relies on the non-overlapping nature of anterior and posterior sensory fields, resulting in tiling of the anterior processes of ALM and PLM neurons so that they do not overlap (Chalfie et al., 1985; Gallegos & Bargmann, 2004). α-TAT mutant animals also displayed mild tiling defects, which along with the defects in neuronal polarity were more penetrant in *mec-17(0)* single and *mec-17(0); atat-2(0)* double mutants than *atat-2(0)* single mutant animals (Figure 5.1D). ALM and PLM processes of α-TAT mutants also displayed signs of early axonal degeneration, like blebbing and extraneous branching in young adult animals (Figure 5.1E, Pan et al., 2011). Interestingly, the penetrance of the blebbing phenotype was comparable in both single mutant animals and *mec-17(0); atat-2(0)* doubles (Figure 5.1F), which suggested that the neurite outgrowth and degeneration phenotypes had distinct causes. Indeed, there are several lines of evidence which indicate that α-TATs can alter MT stability in both an enzymatic and nonenzymatic manner, with defects in neurite extension taking place independent of MT acetylation (Kalebic et al., 2013; Neumann & Hilliard, 2014; Topalidou et al., 2012).

Since neurite extension and morphology were both impaired in α-TAT mutant animals, we next wondered if axon regeneration following injury was dependent on MT acetylation. Wild type *C.elegans* mechanosensory neurons consistently regenerate following femtosecond laser axotomy, with a rapid upregulation of dynamic MTs immediately following injury, followed by a more persistent growth phase where MT stability increases (Ghosh-Roy et al., 2012). MT-PTMs play an important role in modulating MT stability, with increased tubulin deacetylation and tyrosination during regrowth in mouse models of PNS injury and carboxypeptidases, which catalyze the formation of the stable Δ2 modification of tubulin promoting regrowth in *C.elegans* mechanosensory neurons (reviewed in Kurup, Sharifnia & Jin, 2013). On imaging total regrowth

length 24 hrs following laser injury (Figure 5.2A), we found that like in the case of neurite extension during development, *mec-17(0)* single and *mec-17(0); atat-2(0)* double mutants significantly reduced neurite outgrowth compared to wild type animals, while loss of *atat-2* had no effect on axon regeneration (Figure 5.2 B). This led us to conclude that MT acetylation by itself was unlikely to play a role in modulating MT dynamics following axotomy in *C. elegans*. Recent work has shown that αTATs enter the MT lumen through breaks in the MT lattice or at MT ends (Coombes et al., 2016), which could also be a mechanism by which *mec-17* can regulate MT stability during the various phases of axon regeneration.

Changes in MT architecture and stability modulate have distinct effects on synapse formation and vesicle transport

TBA-1 encodes a *C. elegans* α-tubulin expressed in neurons; however, loss of *tba-1* does not affect neuronal MT architecture because of redundancy among nine *C. elegans* α-tubulin homologs. Mutation of a C-terminal glycine residue to arginine (G414R) in TBA-1 resulted in altered MT architecture, neurite outgrowth and synapse formation defects in *C. elegans* motor neurons (Baran et al., 2010; Kurup et al., 2015). Since the C-terminal domain of α-tubulin undergoes several post-translational modifications (Janke & Bulinski, 2011), we tested whether TBA-1(G414R) (henceforth referred to as *tba-1(gf)*) changed the levels of MT-PTM in the mutant animals. Upon immunostaining fixed animals using antibodies directed against various MT-PTMs, we found no difference in the levels of acetylated tubulin, tyrosinated tubulin, Δ2 modified tubulin or total tubulin between WT and *tba-1(gf)* animals (Figure 5S1 A-E). As a control, *mec-17(0); atat-2(0)* double mutant animals had almost undetectable levels of acetylated tubulin (Figure 5S1A, B). We then decided to compare the effects *tba-1(gf)* and *mec-17(0); atat-2(0),* both of which modified neuronal MTs in different ways, on synapse formation and vesicle transport.

PLM neurons form a terminal synapse with the ventral nerve cord along a distal axonal

branch, and the pre-synaptic terminal can be visualized as an accumulation of GFP tagged RAB-3 vesicles termed the synaptic patch (White et al., 1986; Figure 5.3A). Comparing the synaptic patches of wild type, *tba-1(gf)* and *mec-17(0); atat-2(0)* animals, we found that while synapse morphology appeared normal in *mec-17(0); atat-2(0)* double mutants, the synaptic patch was wider and more disorganized in *tba-1(gf)* animals (Figure 5.3B). Additionally, while a majority of the synaptic patches in wild type and *mec-17(0); atat-2(0)* animals were stereotypically located posterior to the vulva, we observed significant mislocalization defects in *tba-1(gf)* animals, with the location of the patch moving anterior to or on either side of the vulva (Figure 5.3C). Interestingly, although synapse formation was normal in *mec-17(0); atat-2(0)* animals, synaptic vesicles accumulated along the anterior PLM process (Figure 5.3D), which could be caused by a change in either the velocity or directionality of synaptic vesicle transport.

To test this hypothesis, we performed time lapse imaging of synaptic vesicle transport in young adult animals, and observed vesicle movement in both the anterograde (towards the axon tip) and retrograde (towards the cell body) directions (Figure 5.4A). We analyzed vesicle movement as a function of distance and time using kymographs generated from time lapse videos for wild type, *tba-1(gf)* and *mec-17(0); atat-2(0)* animals (Figure 5.4B). Vesicles moved bidirectionally in all three cases, with no difference in the proportion of anterograde versus retrograde puncta (Figure 5.4C). As expected, there was a significant increase in the number of stationary synaptic vesicles in *mec-17(0); atat-2(0)* animals compared to either wild type or *tba-1(gf)* animals (Figure 5.4D). Vesicles moved at significantly faster velocities in *tba-1(gf)* animals, while there was no change in either anterograde or retrograde velocities in *mec-17(0); atat-2(0)* animals (Figure 5.4E). Taken together, our results suggest that MT acetylation was dispensable for polarized vesicle transport in *C. elegans* mechanosensory neurons, unlike previous observations in cultured cells (Reed et al., 2006). It is likely that synaptic vesicle stalling that was seen in *mec-17(0); atat-2(0)* animals were a result of MT instability, as with the case of neurite extension and axon regeneration deficits, although the exact nature of this

instability is unclear. Further studies are also required to analyze the mechanism by which cargo velocity is increased in the *tba-1(gf)* background, independent of any change in the levels of individual MT-PTMs. Since the C-terminal domain of α-tubulin also affects the binding of microtubule associated proteins (MAPs), one possibility is the modulation of MAP binding in *tba-1(gf)* animals. *tba-1(gf)* animals also have behavioral defects resulting from synapse formation defects in the *en passant* GABAergic and cholinergic motor neurons that regulate the sinusoidal locomotion of *C.elegans* (Baran et al., 2010; Kurup et al., 2015). Thus, using this phenotype, we were able to perform a suppressor screen to isolate animals with wild type behavior, and ongoing work aims to elucidate the identity of these suppressors, to gain further insight into the interactions between MT and their MAPs that are relevant to the formation and maintenance of both *en passant* and terminal synapses.

Acknowledgements

I would like to thank Y. Jin for mentorship through the work presented in this chapter, and Zilu Wu for assistance with live imaging assays and axotomy experiments.

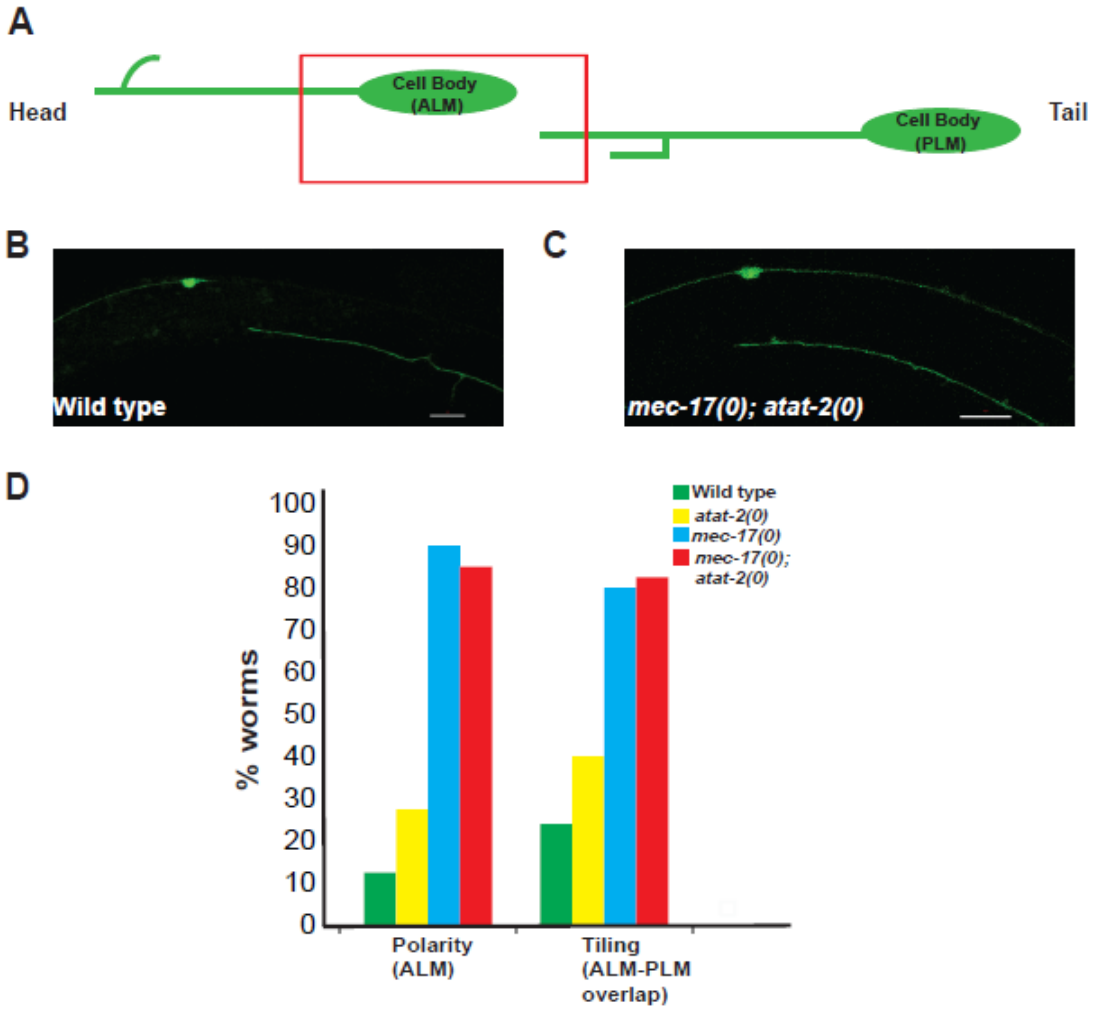

Figure 5.1 αTAT mutants exhibit a variety of neurite outgrowth defects

(A) Schematic diagram of a single wild type (WT) ALM neuron that extends an anterior process towards the head of the animal, and a single wild type PLM neuron that has a cell body close to the tail of the animal and extends an anterior process toward the midbody. The red box indicates the area imaged for analysis of neurite extension. (B) Wild type ALM neurons have a very short posterior process, and no overlap between the anterior processes of the ALM and PLM. Scale bar: 10 µm. (C) *mec-17(0); atat-2(0)* double mutant animals have long posterior ALM processes and significant ALM-PLM overlap. Scale bar: 10 µm. (D) Quantification of the percentage of animals exhibiting polarity and tiling defects in WT and mutant animals, n=40 animals for each genotype. (E) Examples of extraneous neurite branching (red box) and neurite blebbing (blue box) in *mec-17(0)* single and *mec-17(0); atat-2(0)* double mutant animals. (F) Quantification of blebbing phenotypes in the ALM and PLM of WT and mutant animals, n=25 animals for each genotype.

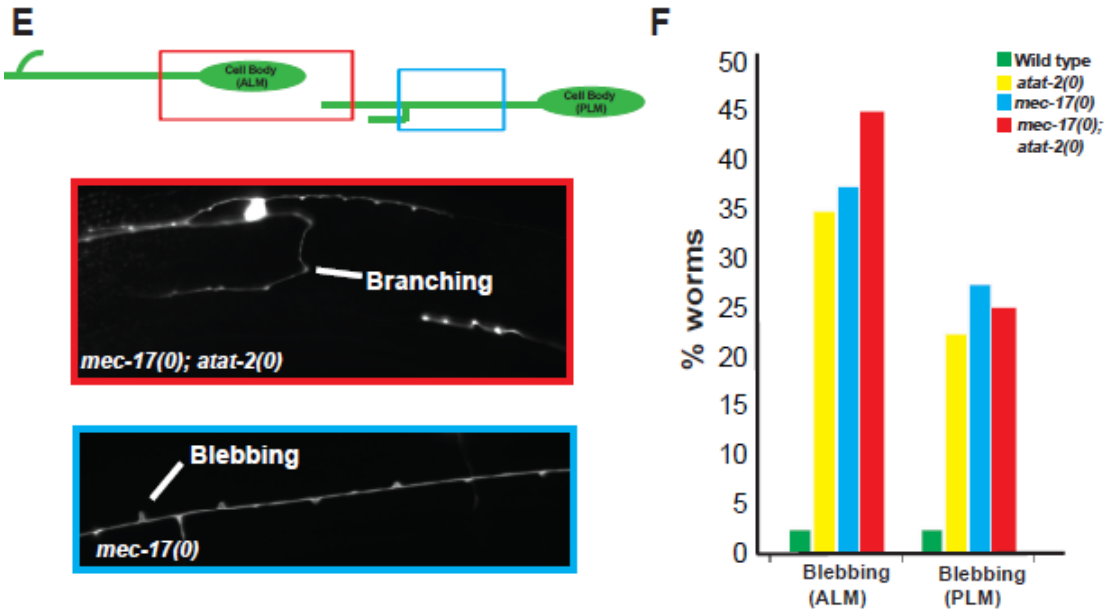

Figure 5.1 (continued) αTAT mutants exhibit a variety of neurite outgrowth defects

(A) Schematic diagram of a single wild type (WT) ALM neuron that extends an anterior process towards the head of the animal, and a single wild type PLM neuron that has a cell body close to the tail of the animal and extends an anterior process toward the midbody. The red box indicates the area imaged for analysis of neurite extension. (B) Wild type ALM neurons have a very short posterior process, and no overlap between the anterior processes of the ALM and PLM. Scale bar: 10 µm. (C) *mec-17(0); atat-2(0)* double mutant animals have long posterior ALM processes and significant ALM-PLM overlap. Scale bar: 10 µm. (D) Quantification of the percentage of animals exhibiting polarity and tiling defects in WT and mutant animals, n=40 animals for each genotype. (E) Examples of extraneous neurite branching (red box) and neurite blebbing (blue box) in *mec-17(0)* single and *mec-17(0); atat-2(0)* double mutant animals. (F) Quantification of blebbing phenotypes in the ALM and PLM of WT and mutant animals, n=25 animals for each genotype.

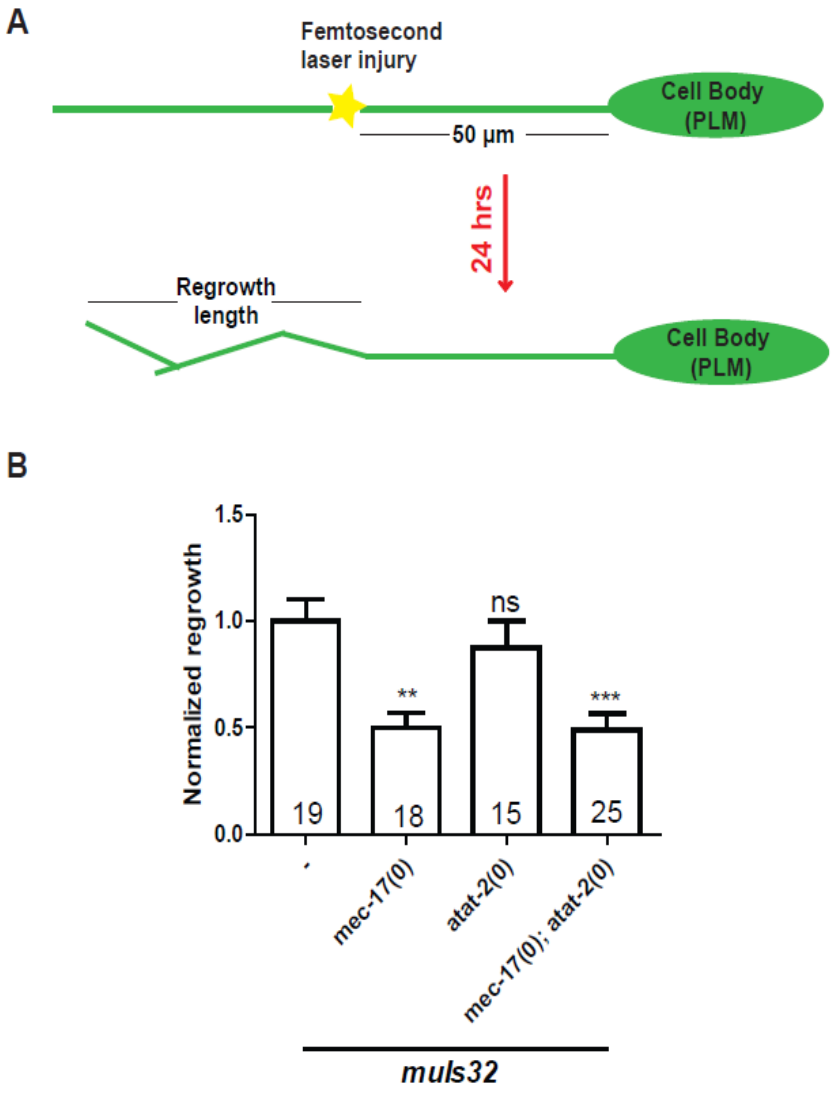

Figure 5.2 Axon regeneration is inhibited in *mec-17(0)* animals

(A) Schematic diagram of axotomy protocol in *C. elegans* mechanosensory neurons. Briefly, PLM neurons of young L4 animals expressing GFP under the *mec-7* promoter (*muIs32*) are injured using a femtosecond laser at a distance of 50 µm from the cell body. The animals are then recovered, and 24 hours later, the regrowth length is measured from the site of injury. (B) Quantification of normalized regrowth length 24 hours post injury; number of animals for each genotype is listed on the bar graph. Statistics: One-way ANOVA followed by Tukey's posttest; ***p<0.0001, ns-not significant.

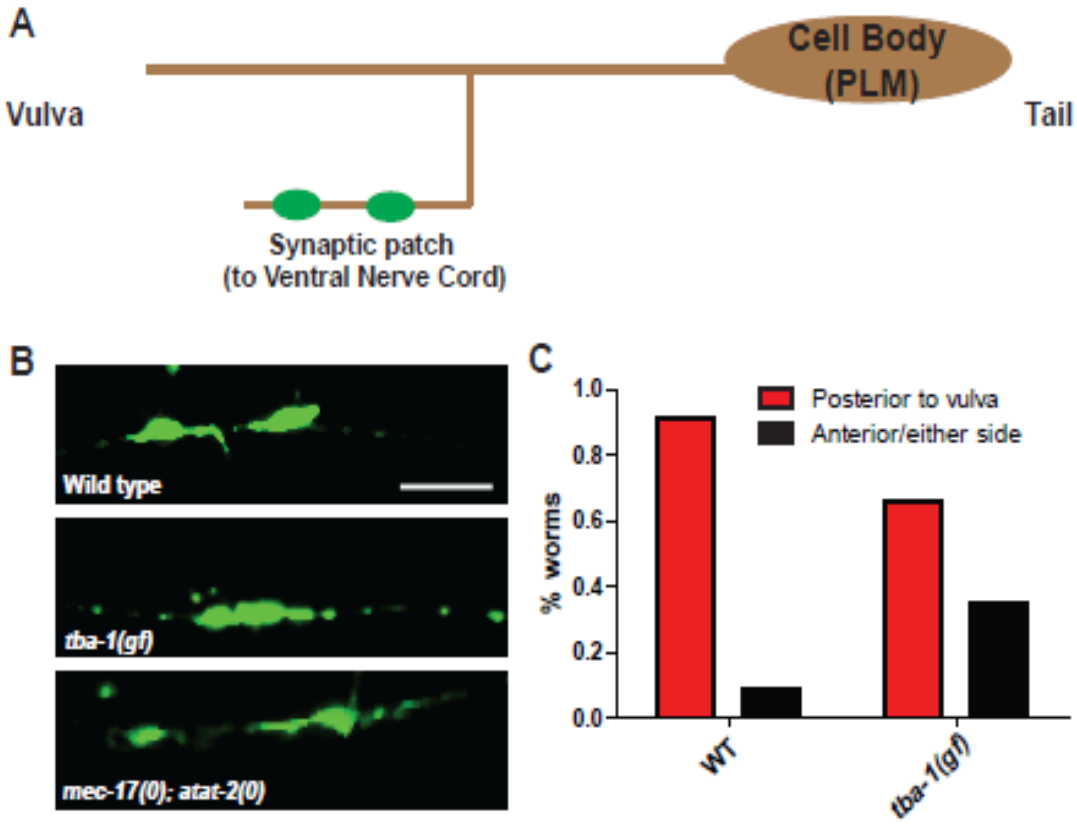

Figure 5.3 Synapse formation and localization is defective in *tba-1(gf)* animals

(A) Schematic diagram of the terminal synapse formed by a single *C. elegans* PLM neuron with the ventral nerve cord, visualized using synaptic vesicle protein RAB-3 tagged to GFP. (B) The synaptic patch formed by a PLM neuron in a wild type, *tba-1(gf)* and *mec-17(0); atat-2(0)* animal. Scale bar: 10 µm. (C) Quantification of synaptic mislocalization in tba-1(gf) animals anterior to or one either side of the vulva. (D) Synaptic vesicles accumulate along the anterior process of the PLM in *mec-17(0); atat-2(0)* animals, a phenotype that is not observed in WT and tba-1(gf) animals. Scale bar: 10 µm. See also: Figure 5S.1.

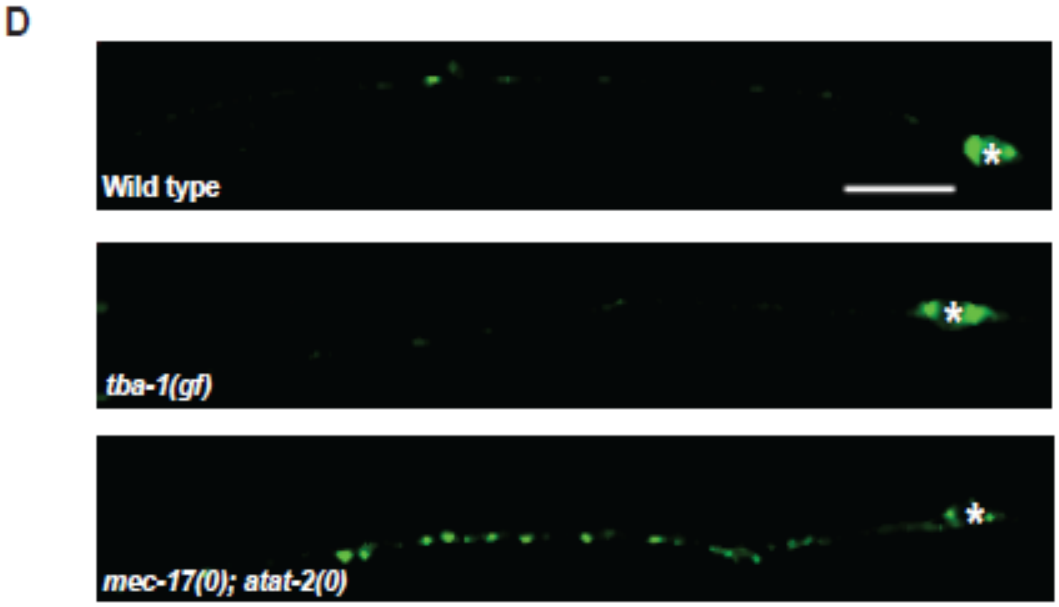

Figure 5.3 (continued) Synapse formation and localization is defective in *tba-1(gf)* animals
(A) Schematic diagram of the terminal synapse formed by a single *C. elegans* PLM neuron with the ventral nerve cord, visualized using synaptic vesicle protein RAB-3 tagged to GFP. (B) The synaptic patch formed by a PLM neuron in a wild type, *tba-1(gf)* and *mec-17(0); atat-2(0)* animal. Scale bar: 10 μm. (C) Quantification of synaptic mislocalization in tba-1(gf) animals anterior to or one either side of the vulva. (D) Synaptic vesicles accumulate along the anterior process of the PLM in *mec-17(0); atat-2(0)* animals, a phenotype that is not observed in WT and tba-1(gf) animals. Scale bar: 10 μm. See also: Figure 5S.1.

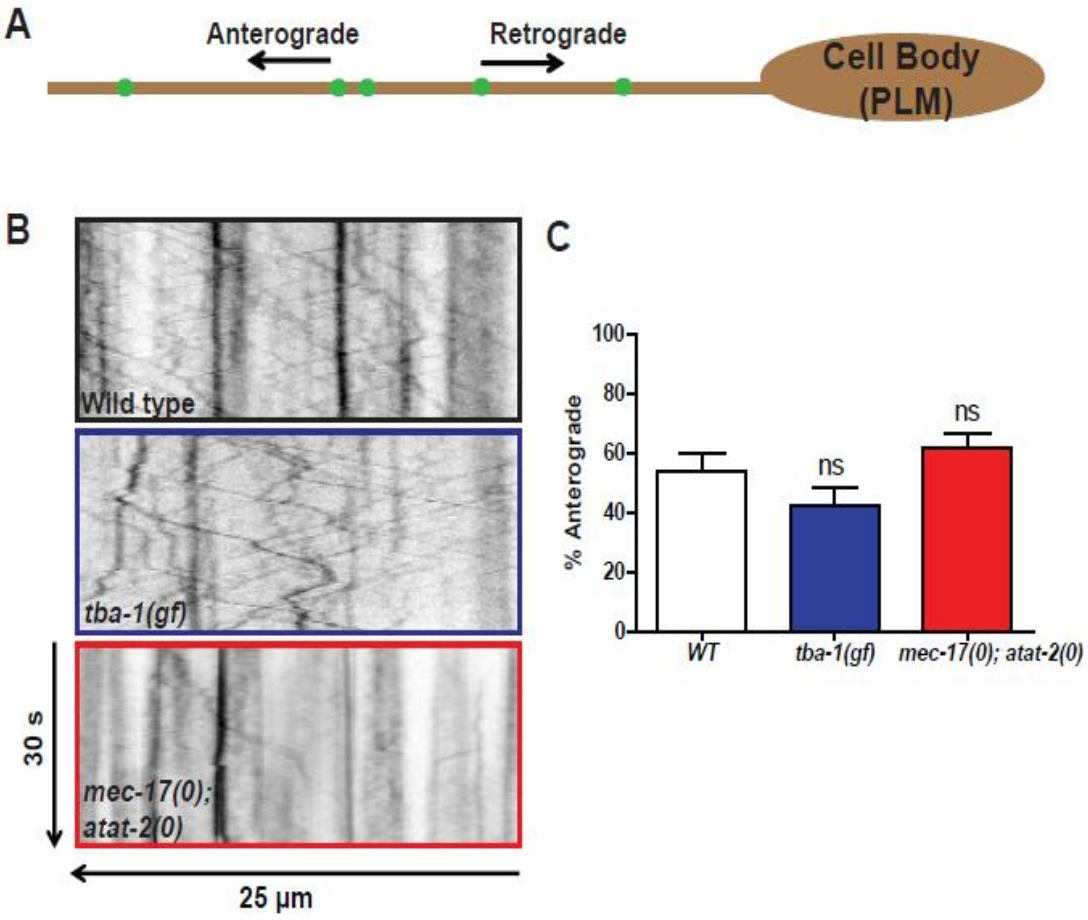

Figure 5.4 Synapse vesicle transport is altered with changes in MT architecture

(A) Schematic diagram of RAB-3-GFP tagged synaptic vesicle transport along the anterior PLM process in both the anterograde (towards axon tip) and retrograde (towards cell body) directions. (B) Kymographs of synaptic vesicle movement in wild type, *tba-1(gf)* and *mec-17(0); atat-2(0)* animals, representing a total time of 30 seconds and a total distance of 25 µm. (C-E) Quantification of particle directionality (C), number of stationary particles (D) and velocity of mobile particles (E) in WT, *tba-1(gf)* and *mec-17(0); atat-2(0)* animals. n=9 animals for WT and *tba-1(gf)*, and 11 animals for *mec-17(0); atat-2(0)*. Statistics: One-way ANOVA followed by Tukey's posttest, ***p<0.0001, ns-not significant.

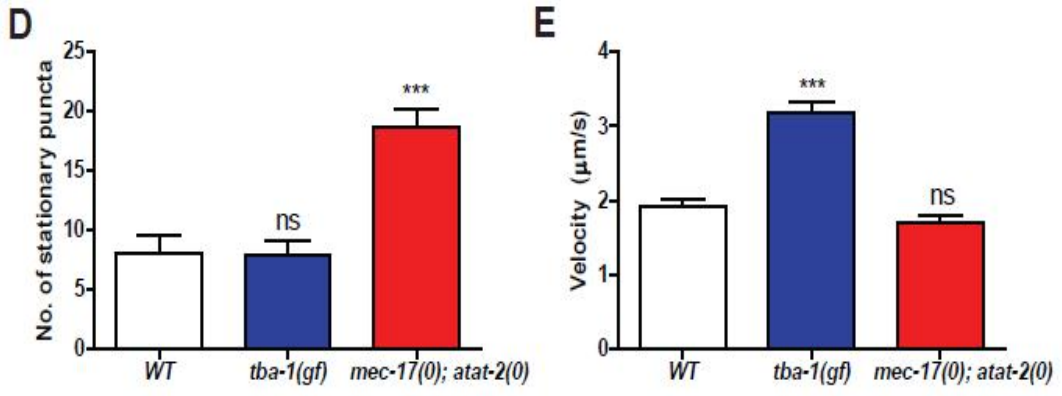

Figure 5.4 (continued) Synapse vesicle transport is altered with changes in MT architecture
(A) Schematic diagram of RAB-3-GFP tagged synaptic vesicle transport along the anterior PLM process in both the anterograde (towards axon tip) and retrograde (towards cell body) directions. (B) Kymographs of synaptic vesicle movement in wild type, *tba-1(gf)* and *mec-17(0); atat-2(0)* animals, representing a total time of 30 seconds and a total distance of 25 µm. (C-E) Quantification of particle directionality (C), number of stationary particles (D) and velocity of mobile particles (E) in WT, *tba-1(gf)* and *mec-17(0); atat-2(0)* animals. n=9 animals for WT and *tba-1(gf)*, and 11 animals for *mec-17(0); atat-2(0)*. Statistics: One-way ANOVA followed by Tukey's posttest, ***p<0.0001, ns-not significant.

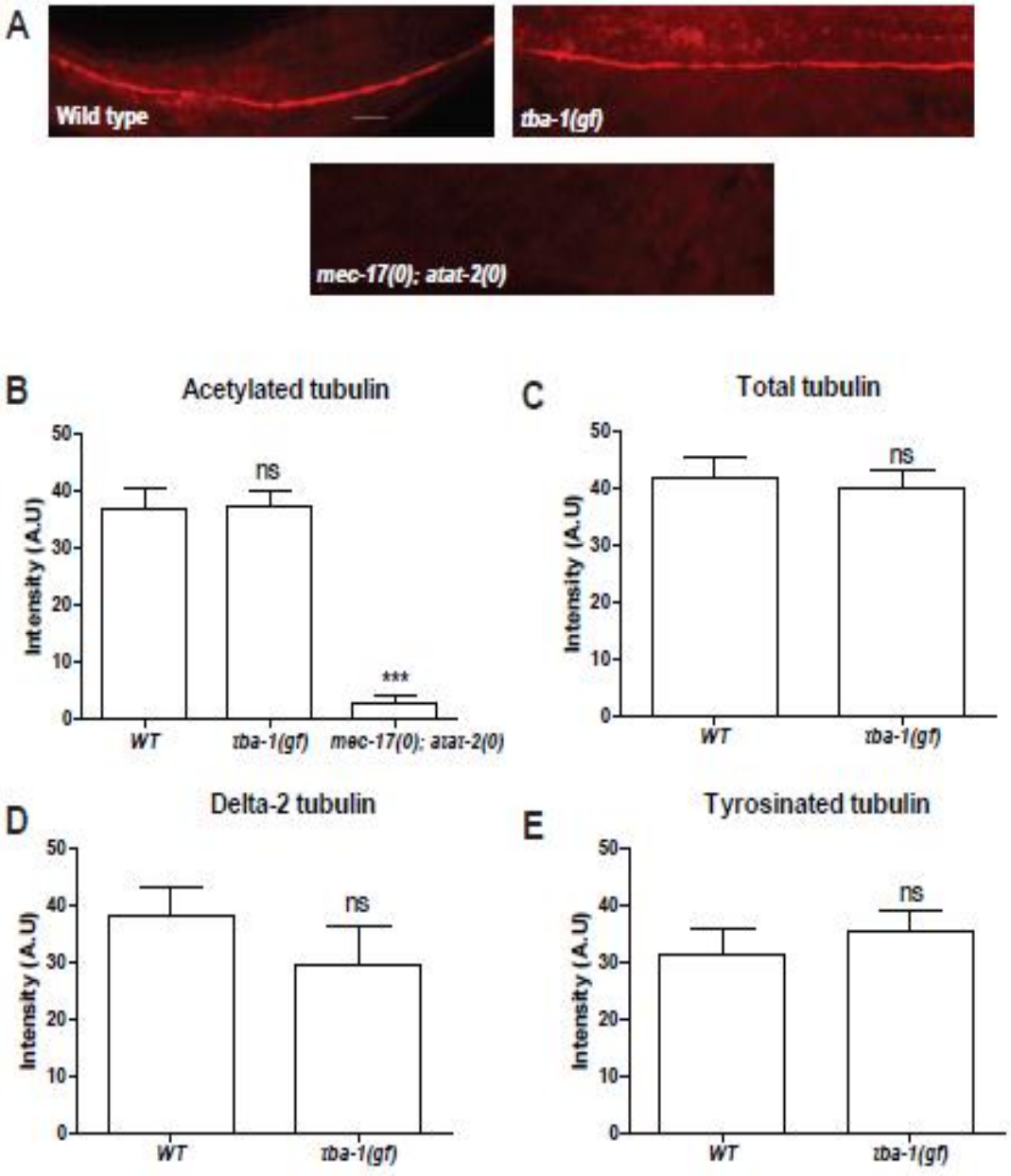

Figure 5.S1 MT-PTMs are unchanged in *tba-1(gf)* animals

(A) Using an antibody specific to acetylated K40 of α-tubulin, images of immunostaining wild type, *tba-1(gf)* and *mec-17(0); atat-2(0)* animals. Scale bar: 20 μm. (B) Quantification of the levels of acetylated tubulin in wild type, *tba-1(gf)* and *mec-17(0); atat-2(0)* animals. n> 10 animals per genotype. Statistics: One-way ANOVA followed by Tukey's posttest, ***p<0.0001, ns-not significant. (C-E) Quantification of total tubulin (C), Δ-2 modified tubulin (D) and tyrosinated tubulin (E) in WT and *tba-1(gf)* animals. n> 10 animals for all genotypes. Statistics: Unpaired t-test, ns-not significant.

Table 5.1 List of strains used in this study

Strain	Genotype	Notes
CZ10969	P*mec-7-GFP(muIs32) II*	
CZ14006	P*mec-7-GFP(muIs32) II ; mec-17(ok2109) IV*	*ok2109*: 1977 bp deletion
CZ14008	P*mec-7-GFP(muIs32) II ; atat-2(ok2415) X*	*ok2415*: 1660 bp deletion
CZ14848	P*mec-7-GFP(muIs32) II ; mec-17(ok2109) IV ; atat-2(ok2415) X*	
CZ14849	*mec-17(ok2109) IV ; atat-2(ok2415) X*	
CZ20215	*tba-1(ju89) I*	*ju89*: Gly414Arg (C1581T) (Baran et al., 2010)
NM2689	P*mec-7-GFP::RAB-3(jsIs821) X*	
CZ15539	*mec-17(ok2109) IV ;* P*mec-7-GFP::RAB-3(jsIs821) X*	
CZ15541	*atat-2(ok2415) X* P*mec-7-GFP::RAB-3(jsIs821) X*	
CZ15846	*tba-1(ju89) I ;* P*mec-7-GFP::RAB-3(jsIs821) X*	
CZ15540	*mec-17(ok2109) IV ; atat-2(ok2415) X* P*mec-7-GFP::RAB-3(jsIs821) X*	

References

Akella, J. S., Wloga, D., Kim, J., Starostina, N. G., Lyons-Abbott, S., Morrissette, N. S., Dougan, S. T., Kipreos, E. T., & Gaertig, J. (2010). MEC-17 is an alpha-tubulin acetyltransferase. *Nature*, *467*(7312), 218-22.

Baran, R., Castelblanco, L., Tang, G., Shapiro, I., Goncharov, A., & Jin, Y. (2010). Motor neuron synapse and axon defects in a C. elegans alpha-tubulin mutant. *PloS one*, *5*(3), e9655.

Brill, M. S., Kleele, T., Ruschkies, L., Bishop, D. L., Kneussel, M., & Misgeld, T. (2016). Branch-specific microtubule destabilization mediates axon branch loss during neuromuscular synapse elimination. *Neuron*, *92*(4), 845-856.

Cai, D., McEwen, D.P., Martens, J.R., Meyhofer, E., Verhey, K.J. (2009) Single molecule imaging reveals differences in microtubule track selection between Kinesin motors. *PLoS Biol* 7: e1000216.

Chalfie, M., Sulston, J.E., White, J.G., Southgate, E., Thomson, J.N., and Brenner, S. (1985). The neural circuit for touch sensitivity in *Caenorhabditis elegans*. J. Neurosci. *5*, 956–964.

Cingolani, L. A, & Goda, Y. (2008). Actin in action: the interplay between the actin cytoskeleton and synaptic efficacy. *Nature reviews. Neuroscience*, *9*(5), 344-56.

Conde, C., & Cáceres, A. (2009). Microtubule assembly, organization and dynamics in axons and dendrites. *Nature reviews. Neuroscience*, *10*(5), 319-32.

Coombes, C., Yamamoto, A., Mcclellan, M., Reid, T. A., Plooster, M., & Luxton, G. W. G. (2016). Mechanism of microtubule lumen entry for the α-tubulin acetyltransferase enzyme αTAT1. *Proceedings of the National Academy of Sciences of the United States of America*, e7176-7184.

Cueva, J. G., Hsin, J., Huang, K. C., & Goodman, M. B. (2012). Posttranslational Acetylation of α-Tubulin Constrains Protofilament Number in Native Microtubules. *Current Biology, 22*, 1-9.

Fischermeier, E., Diez, S., & Walter, W. J. (2012). Tubulin acetylation alone does not affect kinesin-1 velocity and run length in vitro. *PloS one*, *7*(8), e42218.

Fukushige, T., Siddiqui, Z. K., Chou, M., Culotti, J. G., Gogonea, C. B., Siddiqui, S. S., & Hamelin, M. (1999). MEC-12 , an α-tubulin required for touch sensitivity in C . elegans. *Journal of cell science*, *403*(1999), 395-403

Fukushima, N., Furuta, D., Hidaka, Y., Moriyama, R., & Tsujiuchi, T. (2009). Post-translational modifications of tubulin in the nervous system. *Journal of neurochemistry*, *109*(3), 683-93.

Gallegos, M. E., Bargmann, C. I., Hughes, H., Francisco, S., & Cbk, S. (2004). Mechanosensory neurite termination and tiling depend on SAX-2 and the SAX-1 Kinase. *Neuron*, *44*, 239-249.

Ghosh-Roy, A., Goncharov, A., Jin, Y., & Chisholm, A. D. (2012). Kinesin-13 and tubulin posttranslational modifications regulate microtubule growth in axon regeneration. *Developmental cell*, *23*(4), 716-28.

Hammond, J. W., Huang, C.-fang, Kaech, S., Jacobson, C., Banker, G., & Verhey, K. J. (2010). Posttranslational modifications of tubulin and the polarized transport of kinesin-1 in neurons. *Molecular biology of the cell*, *21*, 572-583.

Hilliard, M. A. and Bargmann, C. I. (2006). Wnt signals and Frizzled activity orient anterior-posterior axon outgrowth in C. elegans. *Dev. Cell, 10*, 379-390.

Hu, X., Viesselmann, C., Nam, S., Merriam, E., & Dent, E. W. (2008). Activity-dependent dynamic microtubule invasion of dendritic spines. *The Journal of neuroscience : the official journal of the Society for Neuroscience*, *28*(49), 13094-105.

Janke, C., & Bulinski, J. C. (2011). Post-translational regulation of the microtubule cytoskeleton: mechanisms and functions. *Nature reviews. Molecular cell biology*, *12*(12), 773-86.

Kalebic, N., Martinez, C., Perlas, E., Hublitz, P., Bilbao-cortes, D., Fiedorczuk, K., & Andolfo, A. (2013). Tubulin acetyltransferase αTAT1 destabilizes microtubules independently of its acetylation activity. *Molecular and cellular biology*, *33*(6), 1114-1123.

Kurup, N., Sharifnia, P., & Jin. Y. (2013) Spatial and temporal dynamics of neurite regrowth. *Curr. Opin. Neurobiol.*, *23*, 1011– 1017.

Kurup, N., Yan, D., Goncharov, A., & Jin, Y. (2015). Dynamic microtubules drive circuit rewiring in the absence of neurite remodeling. *Current Biology*, *25*(12), 1594-1605.

Mclaughlin, C. N., Nechipurenko, I. V., Liu, N., & Broihier, H. T. (2016). A Toll receptor – FoxO pathway represses Pavarotti / MKLP1 to promote microtubule dynamics in motoneurons. *Journal of Cell Biology*, *214*(4), 459-474.

Nahm, M., Lee, M.-jung, Parkinson, W., Lee, M., Kim, H., Kim, Y.-jung, Kim, S., Cho, Y. S., Min, B.-moo, Bae, Y. C., Broadie, K., & Lee, S (2013). Spartin Regulates Synaptic Growth and Neuronal Survival by Inhibiting BMP mediated microtubule stabilization. *Neuron*, *77*(4), 680-695.

Neumann, B., & Hilliard, M. A. (2014). Loss of MEC-17 leads to microtubule instability and axonal degeneration. *Cell reports*, *6*(1), 93-103.

Pan, C-L., Peng, C-Y., Chen, C-H., & McIntire, S. (2011). Genetic analysis of age-dependent defects of the Caenorhabditis elegans touch receptor neurons. *Proceedings of the National Academy of Sciences of the United States of America*, *108*(22), 9274-9.

Prasad, B. C., & Clark, S. G. (2006). Wnt signaling establishes anteroposterior neuronal polarity and requires retromer in C. elegans. *Development*, *133*(9), 1757-66.

Reed, N. A., Cai, D., Blasius, T. L., Jih, G. T., Meyhofer, E., Gaertig, J., & Verhey, K. J. (2006). Microtubule acetylation promotes kinesin- 1 binding and transport. *Current biology*, *16*(21), 2166-72.

Shida, T., Cueva, J. G., Xu, Z., Goodman, M. B., & Nachury, M. V. (2010). The major alpha-tubulin K40 acetyltransferase alphaTAT1 promotes rapid ciliogenesis and efficient mechanosensation. *PNAS*, *107*(50), 21517-22.

Stephan, R., Goellner, B., Aberle, H., Pielage, J., Stephan, R., Goellner, B., Moreno, E., Frank, C.A., Hugenschmidt, T., Genoud, C., Aberle, H. & Pielage, J. (2015). Hierarchical microtubule organization controls axon caliber and transport and determines synaptic structure and stability. *Developmental Cell*, (33), 1-17.

Topalidou, I., Keller, C., Kalebic, N., Nguyen, K. C. Q., Somhegyi, H., Politi, K. A., Heppenstall, P., Hall, D. H., & Chalfie, M. (2012). Genetically separable functions of the MEC-17 tubulin acetyltransferase affect microtubule organization. *Current Biology, 22*, 1-9.

White, J. G., Southgate, E., Thomson, J. N. and Brenner, S. (1986). The structure of the ventral nerve cord of *Caenorhabditis elegans*. *Philos. Trans. R. Soc. Lond. B Biol. Sci. 275*, 327-348.

Yu, T. W. and Bargmann, C. I**.** (2001). Dynamic regulation of axon guidance. *Nature Neuroscience, 4*, 1169-1176.